UNIVERSIDAD DE EXTREMADURA

TESIS DOCTORAL

DISEÑO DE UN ROBOT NADADOR DE PEQUEÑAS DIMENSIONES TIPO FLAGELO EUCARIÓTICO ARTIFICIAL. APLICACIONES MÉDICAS

Traver Becerra, José Emilio

Modelización y Experimentación en Ciencia y Tecnología

Conformidad del director y codirectora:

Vinagre Jara, Blas Manuel **Tejado Balsera, Inés**

Esta tesis cuenta con la autorización del director y codirectora de la misma y de la Comisión Académica del programa. Dichas autorizaciones constan en el Servicio de la Escuela Internacional de Doctorado de la Universidad de Extremadura.

2023

UNIVERSIDAD DE EXTREMADURA

Ph.D. Thesis

DESIGN OF AN ARTIFICIAL EUKARYOTIC FLAGELLUM-LIKE SMALL SWIMMING ROBOT. MEDICAL APPLICATIONS

Traver Becerra, José Emilio

Modelización y Experimentación en Ciencia y Tecnología

2023

Dedicated to my parents, my brothers,
and her.

Abstract:

Microrobots, specifically swimming robots, have attracted significant attention in the last decades showing high potential in the biomedical field, such as minimally invasive surgery, drug delivery or monitoring. However, working at the microscale implies a paradigm shift and the need to face new challenges. Conventional design or propulsion methods are no longer adequate at micrometer scales when interacting in environments characterized by a low Reynolds number (*RE*), i.e., environments dominated by viscous forces. However, research lines focused on bio-inspired swimming robots propelled autonomously are in the minority.

In this context, this thesis focuses on the modeling, design and control of an eukaryotic artificial flagellum-like small swimming robot to navigate in conditions similar to those of the human cardiovascular system. Firstly, the model of an *N*-link articulated swimming robot for medium and low *Re* conditions is presented, and a new propulsion waveform is proposed. Secondly, locomotion and control design study of the swimmer is carried out based on the mentioned model, proposing a nested control strategy for path following. Finally, an *N*-segment swimming robot simulator and a flexible 3-link prototype are developed to validate and verify the model and the designed control strategies. Additionally, the modeling and validation of the human cardiovascular system are addressed by presenting a new electrical and hydraulic model.

Resumen:

Los microrobots, y concretamente los robots nadadores, han atraído una gran atención en las últimas décadas mostrando un alto potencial en el campo biomédico, como la cirugía mínimamente invasiva, la administración de fármacos o la monitorización. Sin embargo, trabajar en la microescala implica un cambio de paradigma y la necesidad de afrontar nuevos retos. Los métodos convencionales de diseño o propulsión dejan de ser adecuados a escalas micrométricas al interactuar en entornos caracterizados por un bajo número de Reynolds (*Re*), es decir, entornos dominados por las fuerzas viscosas. Sin embargo, son minoritarias las investigaciones orientadas a robots nadadores de propulsión autónoma con carácter bioinspirado.

En este contexto, esta tesis se centra en el modelado, diseño y control de un robot nadador tipo flagelo artificial eucariótico de pequeñas dimensiones capaz de navegar en condiciones similares a las que se dan en el sistema cardiovascular humano. En primer lugar, se presenta el modelo de un robot nadador articulado de N segmentos para entorno con medio y bajos *Re*, y se propone una nueva forma de onda para la propulsión. Sobre el modelo presentado se lleva a cabo un estudio de la locomoción y el diseño del control, proponiendo una estrategia de control anidada para el seguimiento de trayectorias. Para la validación del modelo, así como de las estrategias de control diseñadas, se desarrolla un simulador de robot nadador de N segmentos y un prototipo de 3 segmentos flexibles. Adicionalmente, se aborda el modelado y validación del sistema cardiovascular humano presentando un nuevo modelo eléctrico e hidráulico.

CONTENTS

LIST OF FIGURES

LIST OF TABLES

ACKNOWLEDGEMENTS

I am pleased to express my gratitude to the many people who have helped or accompanied me over the last five years. I must recognize that without them, today, I would not be me, nor would these words be mine.

First, I would like to thank my supervisors, Blas M. Vinagre and Inés Tejado, for their support and trust from the beginning of the final project of my bachelor's degree in this long and complex research path until today, when I have completed my doctorate. I would also like to extend my sincere gratitude to Dr. Hassan HosseinaNia, associate professor at Delft University of Technology (Delft, Netherlands), for his advice and attention during my stay there.

Secondly, I must thank the members of the small group of young people who started our research career as strangers and ended up as a small family for this thesis. Thanks to Javier Prieto for his support and faithful companionship; Miguel Ángel López for his insatiable restlessness and unexpected friendship; Cristina Nuevo for her patience, continuous willingness to help and ability to put up with me; and Paloma Rodríguez for her constant unbeatable debates, her 24/7 support and unquestionable ability to question and make you doubt everything. Last but not least, I would like to thank Enrique Mancha, Ana Gañan and Begoña Montes, and colleagues from the University of Extremadura, who were also part of my self and my circumstances. Working with these kinds of friends over the years has been a great pleasure.

Finally, I am eternally grateful to my family. My parents and brothers for all their love and support, models of inspiration and self-improvement. Her for her love, support, understanding and help. Ana C. Donoso for her friendship and for always being willing to listen and give her support.

José Emilio Traver

Talavera la Real, December 2022

AGRADECIMIENTOS

Es un placer para mi poder expresar mi gratitud a las numerosas personas que me ha ayudado o acompañado a lo largo de estos últimos cincos años, y a las que debo reconocer que sin ellas, hoy yo no sería yo, ni estas palabras mias.

En primer lugar, agradezco a mis supervisores Blas M. Vinagre e Inés Tejado su apoyo y confianza desde los inicios de mis andaduras con mi proyecto de TFG en esta larga y entramada senda de la investigación, hasta el día de hoy culminado el doctorado. También quiero hacer extensible mi sincera gratitud al Dr. Hassan Hosseinia, profesor asociado de TU Delft en Delft (Holanda), por sus consejos y atención durante mi estancia allí.

En segundo lugar, debo agradecer esta tesis a cada uno de los miembros de ese pequeño grupo de jóvenes que comenzamos nuestra carrera investigadora como desconocidos y terminamos siendo una pequeña familia. Gracias a Javier Prieto, por su apoyo y fiel compañerismos, Miguel Ángel López, por su insaciable inquietud y amistad inesperada, Cristina Nuevo, por su paciencia, continua disposición a ayudar y capacidad de soportarme, y Paloma Rodríguez, por sus continuos debates imbatibles, su apoyo 24/7 y su indudable capacidad de cuestionar y hacerte dudar de todo. Por último y no menos importante, dar las gracias a Enrique Mancha, Ana Gañan y Begoña Montes, así como colegas de la Universidad de Extremadura, que igualmente formaron parte de mi yo y mis circunstancias. Ha sido un gran placer trabajar con esta clase de amigos durante estos años

Por último, estoy eternamente agradecido a mi familia. Mis padres y hermanos por todo su amor y apoyo, modelos de inspiración y superación. Ella por su amor, apoyo, compresión y ayuda. Ana C. Donoso por su amistad y por siempre estar dispuesta a escuchar y dar su apoyo.

José Emilio Traver

Talavera la Real, Diciembre 2022

FINANCIAL SUPPORT

José Emilio Traver would like to thank the Ministerio de Educación, Cultura y Deporte its support through the scholarship no. FPU16/2045 of the FPU Program. This work has been supported in part by the Spanish Agencia Estatal de Investigación (AEI) under project DPI2016-80547-R (Ministerio de Economía, Ciencia y Agenda Digital), in part by the European Social Fund (FEDER, EU), in part by the Consejería de Economía e Infraestructuras (Junta de Extremadura) under the grant “Ayuda a Grupos de Investigación de Extremadura” (no. GR18159) and project IB18109, and in part by the European Regional Development Fund “A way to make Europe”.

1

ABOUT THIS THESIS

"Those who are victorious plan effectively and change decisively.
They are like a great river that maintains its course but adjusts its flow."

The art of war, Sun Tzun

Contents

This chapter presents the motivation, objectives and main contributions of this Thesis.

1.1 Problem statement and motivation

Technological advances in recent years have shown great potential in many applications, encouraging new synergies and the creation of new research areas. Advances in micro/nano-scale science and technology have increased the demand and expectations for new microsystems capable of accessing small spaces, manipulating and interacting directly with entities of equivalent size and with high-impact applications in healthcare, biotechnology and manufacturing, among others. In this scenario, as cross-disciplinary research, microrobots have attracted significant attention, exhibiting high application potential in the biomedical field, such as minimally invasive surgery, drug delivery, and sensing.

However, working at the micro-scale implies a paradigm shift and the need to face new challenges, from mechanical design to the performance of the applications, as well as control strategies. Conventional actuation principles cannot be applied in those applications because microrobots have to navigate within environments characterized by a low Reynolds number, meaning within environments dominated by viscous forces. In this way, many lines of research are currently focused on the study of locomotion methods. However, those focusing on autonomous actuation methods are the minority and reproduce strategies found in nature, that is, bioinspired, to achieve further optimization.

This work constitutes the basis of a line of research in microrobots at the University of Extremadura, directed and supervised by Dr. Blas M. Vinagre Jara and Dr. Inés Tejado Balsera. In other words, the present Thesis presents contributions to propulsion methods and control motion strategy of microrrobots from a bioinspired perspective to improve the motion performance.

1.2 Objectives

The Thesis is considered of interest from several points of view. From a scientific perspective, it is intended to develop a mathematical model and simulation tool to represent an N-link swimming flagellum-type articulated eukaryotic artificial swimming microrobot. In addition, from the viewpoint of control theory, the possible contributions in analysis and methods to control the system mentioned above. Finally, from the engineering and biomedical engineering point of view, in the applications of minimally invasive surgery and search and rescue robots. The general objective can be divided into the following partial aims:

1. Study and simulation of the robot working environment and robot-environment interactions.

2. Mathematical modeling, physical modeling and control of artificial flagellum-type swimming robot with a planar wave.

3. Design of an artificial flagellum-type swimming robot prototype.

4. Modeling of an experimental platform for robot testing in environments that emulate the fundamental characteristics of a swimming robot.

1.3 Contributions and related publications

The main contributions of this Ph.D. Thesis are the following:

1. The proposal of a new beating waveform for propulsion of swimming microrobots based on a fractional order power law for amplitude modulation, as well as validation and the study of the propulsion performance.

2. The development of a simulator and testbed of an N-link flagellum-type articulated eukaryotic artificial swimming microrobot in the MATLAB®/Simulink environment to validate the designed control strategies. Following the literature, it allows the configuration of the swimmer's size, the number of links in which its flagellum is divided, the mode of propulsion among four types of traveling waves and the control strategy applied to the distributed actuators.

3. The fabrication of an IPMC-based flagellum-type articulated eukaryotic artificial swimming robot and design of a controller robust to actuators of different lengths to propel the robot at low *Re* regimes. Also, addressing the design of

a small-scale swimming robot whose links are integrated into the same piece of material and work as actuators or passive flexible links.

4. The proposal of a novel electrical model of the cardiovascular system. It extends the classical Windkessel model of four elements to the left common carotid artery, motivated by 1) having an experimental platform for the development of dimensionless tests with swimming robots and 2) the need to have a complete model from a medical point of view for validation purposes, as well as to describe other cardiovascular phenomena in this area, such as atherosclerosis, one of the main risk factors for cardiovascular diseases.

These results have been spread in the journals, books and conferences cited next.

Journals papers

- J. E. Traver, C. Nuevo-Gallardo, P. Rodríguez, I. Tejado, and B. M. Vinagre, "Modeling and control of IPMC-based artificial eukaryotic flagellum swimming robot: Distributed actuation," *Algorithms*, vol. 15, no. 6, 2022
- J. E. Traver, C. Nuevo-Gallardo, I. Tejado, J. Fernández-Portales, J. F. Ortega-Morán, J. B. Pagador, and B. M. Vinagre, "Cardiovascular circulatory system and left carotid model: A fractional approach to disease modeling," *Fractal and Fractional*, vol. 6, no. 2, p. 64, 2022
- J. E. Traver, I. Tejado, C. Nuevo-Gallardo, M. A. López, and B. M. Vinagre, "Performance study of propulsion of n-link artificial eukaryotic flagellum swimming microrobot within a fractional order approach: from simulations to hardware-in-the-loop experiments," *European Journal of Control*, vol. 58, pp. 340–356, 2021

Book chapters

- J. E. Traver, C. Nuevo-Gallardo, I. Tejado, and B. M. Vinagre, "Frequency domain modeling of an IPMC-based artificial eukaryotic flagellum swimming robot," in *Proceedings of the International Conference on Fractional Differentiation and its Applications (ICFDA'21)*, A. Dzielinski, D. Sierociuk, and P. Ostalczyk, Eds. Cham: Springer International Publishing, 2022, pp. 58–64

- J. E. Traver, I. Tejado, C. Nuevo-Gallardo, J. Prieto-Arranz, M. A. López, and B. M. Vinagre, "Evaluating an AEF swimming microrobot using a hardware-in-the-loop testbed," in *Robot 2019: Fourth Iberian Robotics Conference*, M. F. Silva, J. Luís Lima, L. P. Reis, A. Sanfeliu, and D. Tardioli, Eds. Springer International Publishing, 2020, pp. 524–536

Conference papers

- J. E. Traver, I. Tejado, J. Prieto-Arranz, C. Nuevo-Gallardo, M. A. López, and B. M. Vinagre, "Improved locomotion of an AEF swimming robot using fractional order control," in *2019 IEEE International Conference on Systems, Man and Cybernetics (SMC)*, 2019, pp. 2567–2572

- J. E. Traver, I. Tejado, J. Prieto-Arranz, and B. M. Vinagre, "Comparing classical and fractional order control strategies of a cardiovascular circulatory system simulator," *IFAC-PapersOnLine*, vol. 51, no. 4, pp. 48–53, 2018, 3rd IFAC Conference on Advances in Proportional-Integral-Derivative Control PID 2018

- J. E. Traver, J. F. Ortega, I. Tejado, B. Pagador, F. Sun, R. Pérez-Aloe, B. M. Vinagre, and M. F. Margallo, "Simulador cardiovascular para ensayo de robots de navegación autónoma," in *Actas de las XXXVIII Jornadas de Automática*. Servicio de Publicaciones de la Universidad de Oviedo, 2017, pp. 633–640

- J. E. Traver, I. Tejado, and B. M. Vinagre, "A comparative study of planar waveforms for propulsion of a joined artificial bacterial flagella swimming robot," in *Proceedings of the 2017 4th International Conference on Control, Decision and Information Technologies (CoDIT'17)*, 2017, pp. 550–555

- J. E. Traver, B. M. Vinagre, and I. Tejado, "New waveforms for propulsion of planar artificial bacterial flagella microrobots." VI reunión del Capítulo Español de la Sociedad Europea de Biomecánica, 2016

- J. E. Traver, B. M. Vinagre, and I. Tejado, "Robot nadador tipo flagelo bacteriano plano: estudio y simulación del mecanismo de propulsión," in *Actas de las XXXVII Jornadas de Automática*, 2016, pp. 1075–1082

In all, the work reported in this Thesis has been disseminated in:

- Three journals papers.
- Two book chapters.
- Six conference papers.

1.4 Overview of contents

This Thesis is organized as follows:

- Chapter 1 contains this introduction about the Thesis.
- Chapter 2 presents the current state of the art of microrobots, and their wide variety of applications. In addition, the theoretical foundations on which this Thesis is based are described.
- Chapter 3 states the modeling of the flagellum-type articulated eukaryotic artificial swimming robot for medium and low *Re* environments and a new motion-beating waveform for propulsion.
- Chapter 4 explains the motions and design of the bioinspired swimming robot from an engineering and robotics point of view and how control theory can be used to adapt existing techniques for swimming robot navigational control, specifically path following.
- Chapter 5 details the model and design of the prototypes and experimental platform.
- Chapter 6 contains all the simulated and experimental results obtained in this work.
- Concluding remarks and future works will be presented in chapter 7.
- Appendix A details the variables to describe the articulated eukaryotic flagellum-type swimming robot model.
- Appendix B explains the analysis of the electrical circuit of experimental platform.

2

STATE OF THE ART AND THEORETICAL FOUNDATIONS

"The grass is always greener on the other side."

English proverb

Contents

In this chapter, a brief introduction to the field of microrobotics is given, presenting the most relevant studies since its beginnings in the mid-19th century and discussing the main challenges that this new field must overcome to consolidate and continue to advance. The aim is to provide a snapshot of the current state of research in the field. The lists below are far from aiming at completeness, failing to mention hundreds of other published texts. The main reason they are not mentioned here is that their subjects are of minor importance for this Thesis. As one can see from the surveys below, numerous kinds of microrobots have been reported during the last decades as propulsion and actuation methods. However, few references and works are related to articulated eukaryotic artificial flagellum swimming robots, especially in Spain. This fact justifies the final purpose of this Thesis.

In addition, the theoretical foundations on which this Thesis is based are described. Firstly, the field of microrobotics is explained, especially for robots that must work in fluid environments. Also, the work and research taken as a basis for studying the articulated eukaryotic artificial flagellum swimming robot are introduced. Secondly, the ionic polymer metal composite (IPMC) is presented, which has started a new revolution in soft robotics, with particular attention to micro-swimming robots and soft artificial muscles for medical uses, supporting many current applications. In the third place, a general description of the cardiovascular system (CVS) is realized, and the available models and modeling perspectives are presented.

2.1 Definition of microrobotic

The microscopic, the `small`, is not a new term or concept in popular culture. It is a concept that has been with us since the invention of the microscope in the 17th century and that launched the field of biology, and microbiology, more specifically, with the identification of cells and microorganisms. However, it took several centuries after the invention of the microscope for the scientific community to stop looking at the microscopic and start questioning how to be and operate in the microscopic environment. There is no clear consensus on when microtechnology started. However, an inflection point was the annual meeting of the American Physical Society in Pasadena, USA, where the lecture titled `There'~s Plenty of`

`Room at the Bottom` was given by Richard P. Feynman, the 1965 Nobel Prize Laureate in physics, and he is considered the father of modern nanotechnology. He introduced the concept of manipulating matter at the atomic level and encouraged physicists to explore the possibilities of the microscopic environment. «*Why cannot we write the entire 24 volumes of the Encyclopedia Brittanica on the head of a pin? Could we swallow a mechanical surgeon and put it inside the blood vessel and it goes into the heart and looks around?*» These, among others, are some of the questions he used to reflect on the great possibilities of `the small` and the plenty of room at the bottom.

These crazy ideas, unrealizable until then, were not so for the film industry with the release of *Fantastic Voyage* in 1966, which brought together on the big screen two completely unrelated terms: robotics and microscopic, outlining the field of micorobotics and spreading those crazy ideas of Dr. Feynman to the whole of society. The film narrated the mission of a group of doctors who had to miniaturize themselves to the microscopic scale and enter the brain of a scientist to get him out of the coma that he was in due to an assassination attempt. This film would be the beginning of a new theme that continues to this day with *Innerspace* in 1987, the episode "One little ship" of *Star trek: deep space nine* in 1998 or *Ant-man* in 2015.

However, the field of mobile microrobotics did not begin to develop until the end of the 20th century, when the advances and intensification of the use of microelectromechanical systems (MEMs) have offered the possibilities and tools for development, integration and miniaturization, together with the combination of other fields, such as control theory, materials engineering, artificial vision or image acquisition in the medical field [17]. This has allowed it to establish itself as a discipline in its own right, and it is currently one of the engineering disciplines with the greatest projection. As a result of technological development, in recent decades, it has experienced rapid growth with extraordinary advances that aim to revolutionize the way of working in many fields of application, such as medicine, biotechnology, bioengineering, manufacturing, and mobile sensors networks for environmental and health monitoring. Such microsystems will offer access to confined and/or hard-to-reach spaces, such as inside the human body and manipulate or interact with microscopic entities directly. Working areas where the human or macroscale robot capabilities (sensing, precision and size) do not achieve desired characteristics. To this technological challenge, it is expected to wonder how these microrrobots should be; the answer, as so many other times, can be observed in nature, which has produced centuries-perfected micromachines capable of living, interacting and learning at the microscale. The biomimetic swimming microrobots have attracted the most attention in the development of current microrobotics, and this is why the leading applications are focused on fluidic environments.

But what is a microrobot? There is no standardization of the term microrobot. However, a macroscopic-scale mobile robot could be defined as a self-contained, untethered, programmable robot able to interact with the environment and learn from it. An equivalent definition is employed in [18, 19], stating that a mobile microrobot is «*a mobile robotic system where its untethered mobile component less than* 1 *mm and larger than* 1 *μm and its mechanics is dominated by microscale physical forces and effects*». It is important to remark that the range of dimensions is indicative, since many authors also consider any device with a size close to that of an insect and with biomechanical properties similar to those of an insect. On the other hand, systems close to micrometers can fall into the category of nanorobots. Nanorobotics is a counterpart discipline also on the rise, but more focused on systems below the micrometers or close to the molecular scale. Although there is no clear limit to the dimensions covered by both disciplines, the set of forces and interactions to which robots are subjected is more clearly defined: at the microscopic scale, volume forces have no impact on surface or perimeter forces. In the case of swimming microrobots, viscous forces are much higher in magnitude than inertial forces, implying a low Reynolds number (*Re*), a dimensionless parameter that quantifies the ratio of inertial and viscous forces. The flows developed are practically stationary and defined in Stokes's regime. The motion remains deterministic; a stochastic (Brownian) motion is not identified yet. Therefore, two essential characteristics must be inherent to a microrobot:

1. *Overall size*: a microrobot must be able to access confined and confined spaces with minimal invasion, which implies untethered operations and relatively small dimensions according to the application.

2. *Scaling effect on robot mechanics*: microrobot dynamics and interaction

Table 2.1: Classification of mobile robots according to size and dominant forces.

Robot type	**Overall size**	**Environment forces**
Conventional robots	$\gg$ cm	Volume-based forces. $Re \gg 1$. Classical mechanics, deterministic behavior (no Brownian motion).
Milirobots	from cm to mm	Volume- and Surface-based forces. $Re \sim 1$ or Classical mechanics, deterministic behavior (negligible Brownian motion).
Microrobots	from mm to μm	Surface- or perimeter-based forces. $Re \approx 1$ or $\ll 1$ Classical mechanics, deterministic behavior (negligible Brownian motion).
Nanorobots	$\ll \mu$m	Intermolecular forces. $Re \ll 1$. Quantum mechanics, stochastic behavior (Brownian motion).

> with the environment are governed by the microscale's physical forces and effects. Therefore, volume forces, such as inertia, gravity or buoyancy, will be negligible with respect to the magnitude of surface forces (viscous forces, friction, surface tension or adhesion) [18, 19].

Moreover, the technology required for developing macro, micro or nanoscale robots is also different in each case. Microrobots will be designed with submillimeter scale components (microactuators, microsensors and micromechanisms), applying micromanufacturing methods, at the limits of current engineering, different from those used at the macroscale and nanorobotics techniques, more similar to molecular engineering techniques.

Table 2.1 outlines the different classifications of mobile robots based on their dimensions and the prevailing dynamics and interaction forces. The millirobots cover the range of miniaturized robots that are not yet small enough for volume-based forces not to be considered, but surface forces begin to have the same impact. Fluid dynamics is not completely stationary, reaching turbulent flows, resulting in an environment with *Re* close to unity. It is the interface between classical mobile robots and microrobotics. As for nanorobots, the assumption of continuum mechanics begins to be invalid, so quantum mechanics is necessary to describe their behavior. It changes from deterministic to stochastic due to intermolecular forces and Brownian motion. If fluid dynamics is no longer accurately described by the Navier-Stokes equation, then *Re* is not relevant.

Depending on the application and in a broad sense, there are two approaches for the design, development and control of mobile microrobots:

1. *Off-board*: the mobile and untethered components of the microrobot are remotely actuated, sensed, controlled and/or powered. In this approach, only the tools have reduced dimensions, while the complementary system for management and control has only the restrictions of the application to be performed.

2. *On-board*: analogous to classical robots, the microrobots are autonomous, self-contained and untethered. All components, such as propulsion mechanisms, specific operation tools, sensors, computation, and wireless communication, are integrated into it, so they are designed at smaller scales.

The first approach simplifies the challenges of miniaturization and allows the possibility of taking advantage of technological developments already achieved. However, they only have a mili, micro or nanoprecision in a reduced workspace, but it does not always imply a significant limitation in specific applications, such as single-cell analysis [20], cell orientation control [21, 22], in vitro fertilization [23] or micro/nanorobotic assembly and manufacturing [24, 25, 26]. It is precisely the advantage of reusing existing systems and reducing the number of components to be miniaturized that has encouraged research to focus mainly on this second approach, highlighting magnetic microrobots. In contrast, the second approach requires further technological development of each component in the microrobot, which involves significant challenges in its design and manufacture. Therefore, its development and progress are linked to technological advances in manufacturing, sensing, energy and communication methods. However, it offers great advantages, such as the design of microrobots capable of unrestricted movement (regardless of energy considerations) in large workspaces and any location, without relying on external systems. They have exhibited great potential in various applications, including targeted therapy [27, 28], microsurgery [29, 30], biosensing [31, 32] or pollutant treatment [33, 34] among others [35].

Furthermore, and independently of the previous approaches, microrobots can also be classified according to the type of materials used in their construction as biological, artificial, or biohybrid [36]. The first group employs techniques close to nanorobotics. It integrates natural material in their designs, such as cardiac muscle cells or microorganisms, to achieve a symbiosis that augments or complements the functionalities of the microrobot, which means propulsion, sensing or energy harvesting, and they succeed in being highly biocompatible at the same time. Artificial microrobots refer to those that are manufactured by synthetic materials or materials lacking biological activity, such as polymers, magnetic materials, metals, silicon, as well as alloys. The majority of the designs are based on them due to the versatility of material.Biohybrid microrobots combine the advantages of both latter types, namely biocompatibility and artificial tools' multifunctionality. However, they also present disadvantages in their design, which are restricted by the materials used for their fabrication.

A further classification can be established according to the energy source for robot porpulsion, which mainly considers biohybrid, chemical fuel, thermal gradient, electric field, light, acoustic waves and magnetic fields [37, 38, 39].

2.2 Brief history of mobile microrobotics

The interest and need for manipulation, measurement and interaction at small scales began to acquire great attention in the late 20th century, emerging a new field within robotics, the microrobotics. Although the concept was used in the mid-20th century, the technology was not ready until the end of the 20th century to meet the technological challenges. Thanks to advances in micro- and nanotechnology, the microrobotics field began to respond and established the tools to fill these gaps. Advances in MEMS devices and the increase in their development and implementation have allowed and encouraged research in numerous technical and scientific disciplines. Although it is a relatively new field, its importance has multiplied, as seen in Figure 2.1, which shows the trend of publications and citations of articles related to the field of microrobotics in the last century according to registered data on the Web of Science database. The number of publications has duplicated every decade since 1990, reaching the order of 450 publications per year, which covers a multitude of research lines and a wide range of applications [24, 32, 40, 41, 42, 43, 44, 45, 46].

The first studies that considered the principles on which microrobots would be

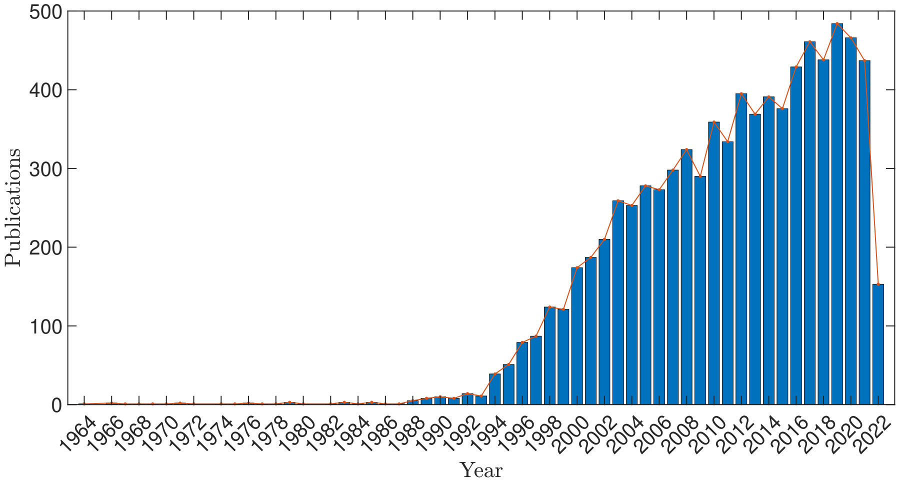

Figure 2.1: The publication trends in the microrobotic field show the number of publications from 1964 to 2021 (including 2021). Data retrieved from the Web of Science. The query used in the search were: microrobot (topic) OR micro-robot (topic) OR micro-machine (topic) OR micro swimmer (topic) OR microswimmer (topic) OR micro-swimmer (topic). On the research areas: Engineering OR Instruments Instrumentation OR Automation Control Systems or Physics OR Robotics OR Mathematics OR Mechanics. For document types: Meeting OR Articles OR Review Articles. The search is available at `https://www.webofscience.com/wos/alldb/summary/12ba7260-5e79-48bb-bda1-f2aedeaf8f5a-1dbe0589/relevance/1`

developed began in the 1950s. In particular, the most popular propulsion methods take nature as inspiration, imitating the flexible behavior of the eukaryotic flagellum and the tail of fishes [47, 48, 49, 50] and the helical motion of the flagellum of bacteria [38, 51, 52]. Within the flexible flagella group, multiple proposals have been studied to generate beating waveforms to propel microrobots from both an off-board [46, 53, 54, 55] and on-board [56, 57, 58, 59, 60, 61, 62] perspective. In the second group, all efforts were focused on developing rigid helical flagella whose motion was imposed by magnetic fields [52, 63, 64, 65, 66, 67, 68, 69]. In addition to the above methods, many other proposals were addressed, such as steerable magnetic dragging [70, 71, 72, 73, 74, 75, 76], where the microrobots are dragged and steered through magnetic fields or electric fields [25, 77, 78, 79]. On the other hand, other types of methods relied on friction forces to achieve propulsion, such as earthworm movement [80, 81, 82, 83, 84, 85, 86, 87, 88] or stick-slip crawling [74, 89].

All these studies continued in the following decades, approaching new features and exploring new technologies that allow miniaturization or the simplification of the propulsion mechanism. Among a large number of proposals, most of them belong to the off-board approach due to the existing methods and techniques that were directly used in developing the microrobots. Methods based on magnetic fields received particular attention and experienced significant advances, and interest due to the scalability of the microrobots [44, 90, 91, 92]. There were also numerous alternatives to the magnetic field approach, but their impact was less significant, such as lasered-powered microwalkers [93], or optically driven bubble microrobots [94, 95], chemically propelled design based on microtubular jet [96], catalytic motor [97], electro-osmotic [98] and even bio-hybdrid cell-driven including magnetic material in cell [99] and chemotactic steering of magnetic microrobots [100].

As for on-board designs, these were mainly technologies whose miniaturization was feasible and easy, such as piezoelectric materials, shape-memory alloy (SMA), ionic polymer-metal composite (IPMC) or ionic conducting polymer film (ICPF). However, the latest studies also focus on the use of biocompatible fuels providing sufficient energy to the microrobots to move without the need for chemical or external fuels, which represents another attractive solution for practical applications due to their biocompatibility and sustainability [39] or even designing microrobots using cardiomyocyte cell as motor [101].

In the last decade, significant progress has been made in developing different designs, fabrication, and actuation techniques for the propulsion of microrobots. However, there are still numerous challenges that need to be addressed to make the `Fantastic Voyage` a reality so that microrobots can perform predetermined tasks for countless industrial, environmental and biomedical applications, such as nano- and microscale object manipulation and assembly, targeted drug and gene delivery, and nanosurgery.

2.3 Challenges of microrobotics

All entities, regardless of size or operation mode, are subject to the same physical forces and governed by the same physical laws as on the macroscopic level. No new laws are used to describe the dynamics of microsystems, but their interpretation and magnitude of phenomena at such dimensions can change dramatically with scale because the magnitude of forces is usually size dependent. Even as sizes continue to decrease further in the microscale, approaching the nanoscale, another limit is encountered. Classical physics will not be able to explain the phenomena and dynamics of robots, and it will be necessary to resort to quantum physics. Likewise, structures will have sizes close to cells so that the assumption of the continuum begins to lose its validity, and it is necessary to go deeper into the behavior of fluids and how external actions affect them [18, 19, 24, 102, 103, 104]. Effects negligible at the macroscopic level become important at the micrometer scale and vice versa.

However, at the technological level, this new field presents a new way of thinking, designing and acting, which involves many new challenges, since the interpretation and meaning of phenomena in these dimensions are radically different. This section describes the main challenges facing this new field. The reader can learn more about the concepts shown below in [32, 36, 45, 91].

2.3.1 Design and modelling

Design and modeling remain an unfinished task despite numerous research whose results provide a wide range of models and designs of microrobots. It will continue to be a challenge as new applications are addressed, as they will demand new models and designs to cover their requirements. Taking biological organisms as a reference again, an integrated system where all components (locomotion principles, material, and power sources) are connected and synchronized is necessary. This challenge has been addressed from many perspectives: from designing a single multitasking robot to a swarm of robots with parallel and distributed functions, allowing them to perform complex tasks. Especially the methodology of programmable modular design is receiving significant interest due to the versatility that the design of individual components offers. Modular microrobots can be assembled into fully equipped multifunctional and larger systems. Despite the complexity of programmable modular design, it is a simple and robust strategy for rapidly adapting the system to dynamic changes in the environment. However, both concepts, programmable and modular assembly, are still in their infancy in this field, and there is a need for thoroughly understanding and controlling them and the related processes. From a global system perspective, they must function by sensing environmental stimuli and reacting to them. Therefore, real-time sensing and feedback control are critical elements for proper functioning, but these are new challenges where traditional knowledge must be adapted to new requirements.

2.3.2 Materials and Fabrication

The fabrication material of microrobots is one of the main concerns in their manufacture and is always influenced by the final application. Likewise, the fabrication material of microrobots is also a fundamental part of locomotion and energy source because their physical properties or design will limit their application and functionalities. Therefore, the material is a vital aspect for optimum performance. However, a critical aspect that all must meet is resistance to interacting with the environment, which is organic in some applications. Mechanical resilience and durability are also highly critical, particularly in load-bearing applications. In addition, in medical applications, it is essential that they meet higher requirements, such as biocompatibility and biodegradability, and are even desired to be multifunctional, smart and compatible with existing micro and nanofabrication processes. According to the most recent research, elastomers or polymeric composites are likely an intermediate alternative to developing more specific and suitable materials.

Regarding to fabrication, microelectromechanical systems (MEMS) technology has been a significant step forward. However, it still requires many custom and novel micro/nanoscale fabrication methods and prototyping tools that could be based on optical lithography, two-photon stereo-lithography, self-folding thin films, micro/nanomachining, micro/nanoprinting, and micro/nanomolding.

2.3.3 Functionality

The most disputed challenge is functionality. The potential applications of microrobots are undoubtedly linked to the development of technology. The case of recognition or diagnostic diseases applications is already viable for milirobots. However, it is still necessary to develop image processing to map the environment or an organ using visual simultaneous localization and mapping (SLAM) or optical flow to predict the movement of organs or tissues accurately. The most common and viable application for microrobots is cargo transport, such as the controlled release of drugs, targeted therapy or gene delivery. For this purpose, a whole microrobot can be fabricated as a big container or porous surface, slowly providing the dose to a specific target. Likewise, the surface can be modified by incorporating biomarkers enabling the sensing of disease diagnosis.

On the other hand, microrobots could also have microtools to perform surgical functions. In the case of microgrippers, they would allow ablation and biopsy for diagnostic purposes. The propulsion mechanisms can be used for a second purpose, such as cauterization or cleaning obstructed blood vessels, in the latter case making use of flexible or helical flagella. This would be a significant advance in the medical field, improving noninvasive surgical operations, such as the extirpation of tumors or biopsy in deep tissue areas. From a collaborative perspective, a great functionality is the coordination of swarms for the formation of scaffolds or joints, which allows the repair or recovery of damaged areas.

2.3.4 Mobility

As discussed above, all entities are subject to the same physical forces and governed by the same physical laws as on the macroscopic level. No new laws are used to describe the dynamics of microsystems, but their interpretation and magnitude of phenomena at such dimensions can change dramatically with scale because the magnitude of forces is usually size dependent. Although numerous locomotion methods have been proposed to overcome the implications of the scale change, there are still many open challenges, such as increasing the locomotion precision and speed for accurate and shorter operations, minimizing the power consumption during locomotion and increasing safety. Of particular interest are medical applications where tissue damage could create an adverse reaction in the body, and precise motion is required near organs with relative movements, such as the lungs. These locomotion methods must ensure a robust adaptation to variations.

In addition, the modes of locomotion are also vital factors in mobility. Therefore, it would also be optimal to have methods to determine the most efficient mode of locomotion based on the characteristics of the environment. Likewise, speed control is another critical factor in the optimal and efficient development of the functions of microrobots.

2.3.5 Powering

Undoubtedly, one of the most challenging issues in the field of microrobotics is power and, obviously, the methods for obtaining or generating the energy necessary for locomotion and performing its corresponding actions, which differ drastically from their macroscopic counterparts. At the same time, it is the main bottleneck in microrobot design and applications, trying to find the optimum balance between maximum power supply to support long operating hours and minimum space. On the other hand, minimizing energy consumption for sensing, locomotion, data transfer, and computation would help this major challenge. However, the latest research is starting to focus on generating the driving force directly from the surroundings, such as self-electrophoresis, self-thermophoresis, self-diffusiophoresis and microbubble-based propulsion.

The first solution proposed is based on traditional methods of using materials capable of storing energy, such as silver oxide batteries, guaranteeing several hours of exclusively maintaining the necessary resources, being reduced to minutes when all functionalities are activated. As an alternative solution to traditional methods, wireless power transmission techniques such as inductive powering and radio frequency, microwave radiation, and piezoelectric ultrasound systems were addressed. However, in all of the above technologies, the performance or ability to transmit energy is strongly dependent on the size of the microrobot or the separation distance, so their efficiency is highly reduced.

In this respect, the concept of energy efficiency plays a crucial role in this field since this could be a limiting step for the overall success of this new field. Therefore, achieving autonomous microrobot actuation for long locomotion periods is a great challenge. Maximizing the power efficiency and minimizing the power consumption of systems are crucial for long-term operations, which could be enabled by optimal design of microrobot locomotion, sensing, and control methods.

2.3.6 Localization

Knowing the position and location is a fundamental part of precise and safe control of the movement of microrobots, especially if they operate in sensitive areas, such as the human body. Numerous methods have been proposed and validated to achieve local localization, but it remains a significant challenge due to the small size of microrobots. In this aspect, robot swarms have the advantage of facilitating their localization by vision or image processing. The main methods used for this aspect are fluoroscopy, Positron emission tomography (PET), Near-infrared spectroscopy (NIR), and ultrasound. These techniques could even be combined to achieve greater accuracy.

2.3.7 Communication

Communication and information transfer are yet to be addressed for microrobots inside the human body or for swarm robots that must receive and send large volumes of data. It is also an essential component for real-time robot manipulation and control. A first proposal was to use magnetic actuation as wireless communication but was discarded because it offered limited bandwidth and only in open loop.

Again, biological organisms can be a reference to establish the principles of social behaviors in swarms of microrobots. For example, microscopic species exhibit collective behaviors in response to environmental stimuli sensed and transmitted between individual species through physical interactions and/or chemical secretions. Quorum sensing is another cell-to-cell communication process used in bacteria to share information among the population and elicit a collective reaction. An intriguing property of quorum sensing is that the population density is monitored in real-time by the whole colony and a communal response is elicited as a result.

2.3.8 Safety

Although it is a very application-dependent concept, safety is a fundamental and mandatory principle. The integrity of the microrobots and the environment must be guaranteed at different levels during all microrobot phases of operation. This safety must be guaranteed from different perspectives: design, manufacturing and integration. Therefore, the correct selection of materials, locomotion, actuation method, and power supply is paramount. On the other hand, the safety principle will restrict manufacturing methods, materials, locomotion methods or some of the positioning techniques indicated above, such as those based on ionizing radiation, which should only be used when necessary. In medical applications, the robotic components, remote or autonomous actuation, or sensing methods should be within the health legislation limits so that they do not cause any discomfort, damage, or pain to the patients. Synthetic microrobots should be made of biocompatible and biodegradable soft materials; whereas biohybrid ones should not be pathogenic or create any negative immunological response. In the case of the magnetic fields generation, they are considered safe, with no significant health risk. However, blood is also conductive, so sufficiently high magnetic fields can reduce blood flow due to induced voltage, according to Faraday's law.

2.3.9 Testbench

The development of test platforms that can emulate the conditions of the environment in which the microrobots will operate is becoming increasingly important. From a medical perspective, it is possible to use medical phantoms for in vitro or ex vivo organ or tissue testing, allowing a closer-to-reality experience. In this sense, organs-on-chips could become test platforms to emulate the clinical and physiological part of the human body environment.

2.4 Theoretical framework

This section aims to explain the concepts, theories, models and research supporting this Thesis's work.

2.4.1 Hydrodynamics at microscale

Many microscale applications involve operating in fluid environments, specifically medical applications. The properties or composition of the fluid environment remain unchanged at any scale, but their dynamics, behavior and interaction with other objects or fluids are affected by shrinking because below scaling laws are also applicable to fluid particles [18, 19, 105, 106, 107, 108].

Drawing on the governing equations of fluid mechanics, the Navier-Stokes equations establish the pressures, viscous and inertial forces governing a fluid flow, expressed in vector form as:

$$\frac{\partial\rho}{\partial t} = -\nabla\left(\rho\mathbf{v}\right), \tag{2.1}$$

$$\underbrace{\frac{\partial\rho\mathbf{v}}{\partial t}}_{\substack{\text{Ratio of momentum}\\ \text{per unit volume}}} + \underbrace{\mathbf{v}\cdot\nabla\rho\mathbf{v}}_{\substack{\text{Ratio of momentum loss}\\ \text{by convection, per unit volume}}} = - \underbrace{\nabla P + \mu\nabla^2\mathbf{v}}_{\substack{\text{surface-based forces}\\ \text{per unit volume}}} + \underbrace{\rho F.}_{\substack{\text{volume-based forces}\\ \text{per unit volume}}}$$

The first equation describes the conservation of mass and the second, the conservation of momentum, where $\mathbf{v}$ is the fluid velocity field, P is the fluid pressure, F denotes other external forces per unit volume and ρ and μ are the density and the dynamic viscosity of the fluid, respectively. Operator to $\nabla(\,\cdot\,)$ denotes the gradient of a scalar function or vector. The conservation of mass offers a description of the density change rate measured by an observer moving along with the fluid [106]. Considering and assuming that fluid is continuous, incompressible and Newtonian (therefore, it has a constant density and viscosity), the conservation of mass principle in equation (2.1) is simplified to

$$\nabla\mathbf{v} = 0. \tag{2.2}$$

The conservation of momentum principle can be interpreted as the external forces exerted by the surroundings on a stationary fluid element equal to the time rate at which momentum is created within the element. The external forces are decomposed by: 1) surface-based forces exerted by the fluid stresses acting over the surface of the element, and 2) volume-based forces, for example, gravity, exerted on the element [106]. Analyzing the momentum conservation principle from a nondimensional perspective offers an easier way to understand how the scale effect influences the fluid dynamics and the interaction with the fluid. If $\mathbf{x}$ defines the position vector field, v_{fc} is the characteristic velocity of the fluid. L is a characteristic length, the following changes of variable can be used $\hat{\mathbf{x}} = \mathbf{x}/L$, $\hat{\nabla} = L\nabla$, $\hat{t} = t/(L/v_{fc})$, $\hat{\mathbf{v}} = \mathbf{v}/v_{fc}$ and $\hat{P} = PL/(\mu v_{fc})$. In addition, if the gravitational force and Brownian motion are not considered, it is permissible to say that there are no external forces applied to the system or microswimmer and the fluid surrounding it, and therefore, $F = 0$. Applying the above change of variables and considerations and arranging the equations, the nondimensional form of the monument conservation principle ca be written as:

$$\left(\frac{\rho v_{fc}L}{\mu}\right)\left(\frac{\partial \hat{\mathbf{v}}}{\partial \hat{t}} + \hat{\mathbf{v}}\cdot\hat{\nabla}\hat{\mathbf{v}}\right) = -\hat{P} + \hat{\nabla}^2\hat{\mathbf{v}}. \tag{2.3}$$

The first term in parenthesis on the left-hand of the above expression is the Reynolds number ($Re = \rho v_{fc}L/\mu$), which is a dimensionless parameter that quantifies the ratio between inertial and viscous forces. There are other definitions more suitable for systems with low amplitude motion in high frequency ($Re_\omega = \rho v_{fc}L^2/\mu$) or when the speed varies rapidly across streamlines on a length scale l_s, but slowly along streamlines on a length scale l_l ($Re_v = \rho v_{fc}l_s^2/(\mu l_l)$) [107]. The Re varies with scale in a proportion of L^4; moreover, if the velocity is considered proportional to L, it varies with L^5. This means inertial effects (volume-based forces) are negligible compared to viscous (surface-based forces) at the microscale. The conservation of momentum equation (2.2) involves that the right-hand term can be neglected, resulting in Stoke's equations of motion that define a creeping flow as

$$\hat{\nabla}\hat{\mathbf{v}} = 0, \tag{2.4}$$

$$-\hat{\nabla}\hat{P} + \hat{\nabla}^2\hat{\mathbf{v}} = 0. \tag{2.5}$$

Creeping flow or Stokes flow has powerful properties, as deduced from its equation. The main statements of the Stokes environment are [106, 107, 108]:

1. Linear relationship for forces and motions. Stokes' equations are linear, so the forces from or into the fluid to a particle will also be linear.

2. Inertialess. The magnitude of the mass makes the inertial forces irrelevant as opposed to the viscous forces ($\sim \hat{\nabla}^2\hat{\mathbf{v}}$), involving a low Re. On the other hand, the time elapsed during the propagation of a disturbance convectively from its origin is typically expressed as $t_{conv} \sim L/v$, while the time for the

diffusion of a perturbation away due to viscosity is $t_{dff} \sim \rho L^2/\mu$. Noting that $Re = t_{diff}/t_{conv}$, it means that the fluid transport is also dominated by viscous diffusion.

3. No dependence on time. The governing equations do not contain time derivatives or other ways of considering past behavior. This involves that the solutions for steady boundary conditions only require determining the fluid state at a single time. In other words, the resulting forces at a specific moment will only depend on other variables at the same instant of time.

4. Reciprocal theorem. It is a consequence of the linearity character of Stokes equations (2.5) and is a particular case of the principle of virtual works. It states that the virtual work developed by two stokes flows in the same region is equal. For example, consider two stokes flows with different velocity and stress fields, (v_1, σ_1) and (v_2, σ_2), the following relation can be written:

$$\int_S \sigma_1 v_2 dS = \int_S \sigma_2 v_1 dS \tag{2.6}$$

   where S is a closed surface bounding any fluid volume V.

5. Kinematic reversibility. A consequence of the above properties is that the response of the fluid to a perturbation or movement of its boundaries is instantaneous, as opposed to macroscale, where any motion or disturbance experiences a propagation time to reach the entire system. This property has an important implication in the motion of solid bodies since if an applied force is reversed, the flow will also be reversed. This also means that if a consecutive sequence of applied forces is reversed, the flow will also reverse in the same sequence so that any solid body will follow backward exactly its trajectory, and the initial state will be the same as the final state. In other words, the fluid particles bounding the surfaces of a moving body follow the same trajectory described by the body.

In conclusion, fluids at the microscale are characterized by low Re and described as a Stokes' flow, with no time dependency and where the evolution of motion only depends on the spatial character of the forces that cause the movement of objects or particles. Refer to [106, 107, 108] for a deeper explanation.

2.4.1.1 Slender body motion

Considering microswimmers propelled in a Stokes' flow, the total rate of momentum must be zero according to the conservation of momentum (equation (2.2)). Then, the fluid's resulting forces exerted on the body must be zero [106, 107, 108, 109]. However, it needs to be clarified how to solve this statement based on the inertial conception, where it is possible to separate the effects due to motion and fluid resistance. Find a solution to the Stoles' equation that provides a relationship between fluid flow and body velocity that yields zero net force and momentum on the body has been approached from many perspectives and by many authors, which has led to the definition of theories and methods that apply different conditions to the body under study [105, 108, 109, 110, 111, 112, 113, 114, 115].

The first studies were carried out by G.I. Taylor, who directly deducted the velocity of a thin sheet as a consequence of its transversal deformation [109]. Although the results are valid, they only apply to small deformations. Alternative approximations for higher amplitudes were studied based on the principle of the smooth and slender body, which considers a body with a thin main dimension that is larger enough than others, such as the flagellum of the microorganism. A few years later, Gray and Hancock introduced local drag theory, denominated as resistive force theory (RFT) [108, 111]. The RTF establishes that the force of an infinitesimal element ds exerts on a fluid at a point s, denotes as ds where s is the arc length along the slender filament of cross-section, is proportional to the local velocity $v(s,t)$, measured in a coordinate frame in which the fluid is at rest at infinity. Decomposing the velocity in its normal and tangential components with respect to the local frame, as shown in Figure 2.2, the force density can be expressed as:

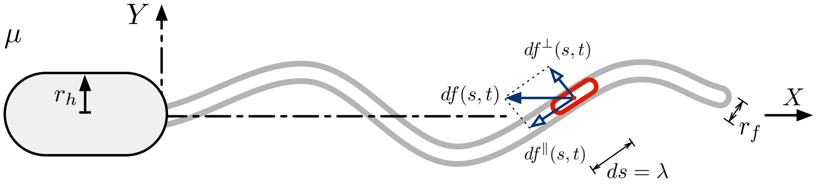

Figure 2.2: Description of Resistive Force Theory for smooth and slender flagellum.

$$\begin{aligned} df^{\perp}(s,t) &= -\mu \; c^{\perp}_{v,s} \; v^{\perp}(s,t) \; ds, \\ df^{\|}(s,t) &= -\mu \; c^{\|}_{v,s} \; v^{\|}(s,t) \; ds, \end{aligned} \tag{2.7}$$

where $c^{\|}_{v,s} \in \Re$ and $c^{\perp}_{v,s} \in \Re$ are the viscous friction coefficients that define the relation between velocity and forces, concretely, in the tangential and normal direction of the infinitesimal element, respectively. As for drag coefficients, Gray and Hancock defined them strictly based on the geometry of the body as follows:

$$\begin{aligned} C^{\perp}_{v,s} &= -\frac{2\pi}{\log(\frac{r_f}{2l}) + \frac{1}{2}}, \\ \frac{C^{\perp}_{v,s}}{C^{\|}_{v,s}} &= 2. \end{aligned}$$

where r_f is the radius of the flagellum and λ is the wavelength of the deformation along the flagellum, although other authors consider it as the infinitesimal element length ($l = \lambda$). Likewise, their definition depends only on the geometrical shape of the body and the fluid characteristics.

However, these coefficients were reviewed and slightly modified by different authors [112, 113, 114]. All of them agree that the coefficients may need to be weighted and that the ratio between them may be lower. Note also that the viscosity parameter is not included in the coefficients as other authors present.

The RFT offers a simple method to determine the resulting forces of the motion of a slender body in a viscous environment. Despite the advances that it is supposed in the study of cell motion, it is a coarse description of the hydrodynamic interaction. A more accurate definition of hydrodynamic interactions between the parts of a smooth and slender body is captured by the general slender body theory (SBT) [108, 113, 114]. It was first described by Hancock [110] and consists of applying the solution of a three-dimensional slender filament to a two-dimensional flagellum using an appropriate distribution of flow singularities.

Two approaches to the SBT have been proposed. The first approach proposes to solve the flow dynamics as a natural extension of RTF and approximate the complete solution as a series of logarithmically small terms. The first logarithmic term corresponds to the RFT coefficient and the rests are calculated to determine the Stokelest distribution, which represents the flow behavior away from the slender body and asymptotically coincides with the flow behavior close to the flagellum. It is worth mentioning that the term Stokelest was first coined by Hancock [110] in reference to the singularity inherent to viscous motion, which induces tangential and normal component velocities. This approach offers accurate results, but due to the small contribution of terms, it is necessary to solve many of them. The second approach is to directly derive the integral equation that satisfies the unknown distribution of singularities along the slender body. It states that *if $F(s)$ is the force per unit length with which a slender body acts on a fluid, then the resulting fluid motion can be represented by a distribution of Stokeslets along the centerline, of strength $\mathbf{F}(s)$ per unit length, accompanied by dipoles. The fluid velocity field closely matches slender body motions v such that the whole cross-section where $s = s_0$ moves with velocity* [113]:

$$v(s_0) = \frac{\mathbf{f}^{\perp}(s_0)}{4\pi\mu} + \int_{x_0>\delta} G(\mathbf{x}_0 - x) \cdot \mathbf{F}(s_0) ds \tag{2.8}$$

where G is the Oseen tensor defined as $G(r) = \frac{1}{8\pi\mu}\left(\frac{1}{|\mathbf{r}|} + \frac{\mathbf{r}\cdot\mathbf{r}}{|\mathbf{r}|^3}\right)$.

Although general SBT offers higher accuracy, a simple method that describes the hydrodynamics at low Re is sometimes required rather than good accuracy. However, restricting to the case of a slender body without a head, a comparison between the two theories shows that the results obtained by RFT are consistent with those obtained by SBT and a slightly weighting of the drag coefficients improves the results [114, 116, 117]. As a complement to the previous theories, methods based on finite element simulations have been developed that allow solving Stokes' equations in a simpler way and with a higher computational cost. On the other hand, it is important to mention that it is not necessary to capture all fluid flow details for control design purposes, since control feedback can compensate for reasonable modeling errors.

2.4.2 Living at low Reynolds number

The previous sections have discussed how the change of scale implies a shift of paradigms in which it is necessary to redefine the traditional methods adapting to the new demands of this new field, where the forms of manufacture, operation, handling and propulsion are no longer completely applicable. Focusing on the locomotion of microrobots in fluid environments, as is mostly the case in medical applications, these will have to swim in low *Re* environments so viscous forces will govern the motion dynamics.

Swimming in a low*Re* environment requires a new interpretation of macroscale propulsion methods. Analyzing the Stokes' equations from the perspective of swimming motion, the following two interrelated conclusions can be stated:

- The propulsion method cannot be based on inertia since there is no temporal dependence on the motion, and it is instantaneous. In other words, the displacement of the swimmer is not influenced by the acceleration at which it is moving.

- The swimming gait or beating waveform has to perform a time-asymmetric motion, also known as nonreciprocal motion, to achieve net propulsion. At low *Re*, the flow is kinematically reversible, which means the net displacement only depends on the geometrical sequence of shapes. However, if the motion is time-symmetric, the average displacement during one period will be zero because the following sequence will cancel displacement due to the first sequence of movements.

Both these statements are captured in the scallop theorem, which was postulated by E. Purcell [118]. The theorem gets its name from the scallop motions, which consist of opening its shell slowly and closing its shell quickly, propelling due to the change of acceleration in the opening and closing movements. Based on the above statements, the theorem states that scallop does not perform a suitable movement for low *Re* environment, because it breaches the two statements. In the first place, the different velocity in the movements does not have any effect, and second, the motion is time-symmetric, so it is the same forward and backward.

E. Purcell introduced with this scallop theorem that any swimmer requires a minimum of two joints with one degree of freedom (DoF) to perform a nonreciprocal motion and thus achieve propulsion at low *Re* environments. A comparison between

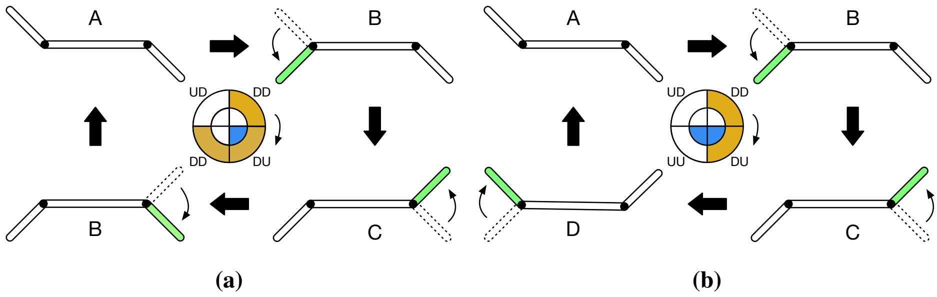

Figure 2.3: Motion comparison in Purcell's three-link swimmer: (**a**) reciprocal (**b**) nonreciprocal.

a nonreciprocal and reciprocal motion is illustrated in Figure 2.3 with the simplest design that could implement those motions, which means Purcell's three-link swimmer. The nonrepetition of any previous and successive movement in a period sequence characterizes nonreciprocal motion. As can be seen, the motion consists of moving the end segments alternatively from an initial position without going back to any previous state until having completed a cycle. The coding to identify the spatial configuration of a nonreciprocal motion is shown in the figure's center, where the letter "U" is used if the displacement is positive, whereas "D" means that it is negative or equal to zero. Therefore, the sequence UD-DD-DU-UU corresponds to nonreciprocal motion, whereas UD-DD-DU-DD identifies a reciprocal motion. Refer to [119] for more details on the coding to identify a nonreciprocal motion.

2.4.2.1 Propulsion methods

The scallop theorem imposes a strong geometrical constraint on the type of swimming motion for propulsion at low *Re*. This reason has motivated the design of most propulsion methods based on biological systems or microorganisms, such as bacteria and eukaryotic cells. Nature offers various methods that perform an inherent nonreciprocal motion, guaranteeing net propulsion and displacement. There are three main types based on eukaryotic, Prokaryotic and Paramecium cells.

The motion of the Paramecium consists of a stick-slip crawling mechanism. Its operation is similar to the action of an oar in a boat (see Figure 2.4a). To push the boat, the oar is used at its widest part and returns to the initial position through the area of minimum opposition to the flow, which means the narrowest area, ensuring that the movement is nonreciprocal. Eukaryotic cells, being spermatozoon an example, perform a different method consisting of producing a beating waveform or traveling wave through a flexible flagellum or tail (see Figure 2.4b). As for prokaryotic cells, like *Escherichia coli* or *Salmonella*, they develop a helical motion similar to a corkscrew (see Figure 2.4c), through a rigid or flexible flagellum. In the last case, the shape is given by the rotational motion.

As it was commented, the last two methods have received great attention in the microrobotics community, and as a result, they have suffered a more extensive development in the previous decades. It should be noted that the term flagellum refers to the flagellum attached to some bacteria conferring mobility capabilities and the fundamental organelles in eukaryotic organisms that play a main role in the locomotion method. However, the bacterial flagellum is utterly different from the eukaryotic one from a structural and mechanical perspective. This thesis will focus on the specific case study of microrobots with a flexible flagellum whose motion is limited in the plane.

2.4.2.2 Flagellum structure

From a macroscopic perspective, the undulatory motions of eukaryotic flagella can be described by flexible behavior. However, if they are observed on a small scale, their structure reveals a completely different behavior. The flagellum structure is based on a fixed geometry called axonema. It is characterized by having nine pairs of microtubules arranged in a circular form and with a central pair (9 + 2), where the microtubules are actin filaments with relatively high stiffness. Coupled and distributed along the flagellum, there are binding proteins and dinein. The proteins act as binding and contraction elements between the microtubules; that is, they

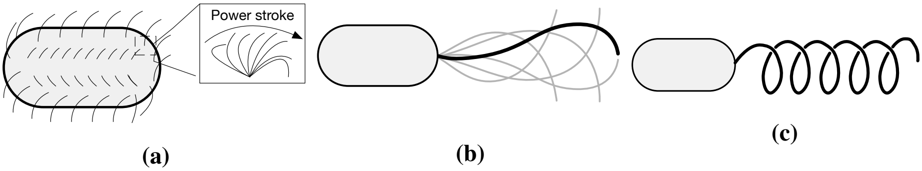

(a) **(b)** **(c)**

Figure 2.4: Propulsion method bioinspired: **(a)** stick-slip crawling, **(b)** flexible flagellum and **(c)** helical flagellum.

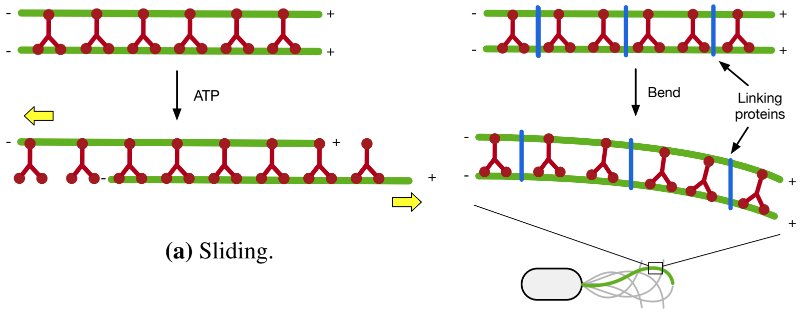

(a) Sliding.

(b) Bending.

Figure 2.5: Deformation produced on microtubules due to active actuation of molecular motor and passive proteins.

perform a function analogous to that of a muscle by producing a bending moment in the flagellum [120]. As for dinein, it is a molecular motor whose action causes the longitudinal sliding between microtubules, as sketched in Figure 2.5a, and whose energy is extracted from the hydrolysis of adenosine triphosphate (ATP). The result of the action of this motor is the longitudinal sliding between microtubules. The action of binding proteins prevents the sliding between microtubules and induces their bending moment (see Figure 2.5b). This moment gives rise to the basic undulatory movement observed in the flagellum of eukaryotic cells. Based on this structure, it may be reasonable that the behavior of the flagellum can be interpreted as an infinite flexible chain of infinitesimal cylindrical segments linked through one DoF that allow an undulatory motion due to a bending moment at each joint [111].

At the macroscopic scale, this type of movement is observed in robot snakes or unrestricted articulated manipulator robot systems. Taking both systems as a reference, numerous dynamics models have developed and can be found in the literature, highlighting the manipulator models [121] and snake robots models [122, 123, 124].

2.4.2.3 Waveforms for propulsion and locomotion

A second crucial factor for locomotion is the undulatory motions performed by the flexible flagellum. In nature, there are numerous examples of self-propelled locomotion strategies from which propulsion methods are inspired [125]. Specifically for low *Re* environments, the movements of bacteria and eukaryotic cells are the most efficient methods from a propulsion perspective. Their motion is characterized by the generation of a continuous beating wave motion (waves) with the flagellum propagated backward from the head to the flagellum. Such motion only dissipates a part of the energy in the environment and the rest of the energy is focused on achieving propulsion through the motions, reaching a high-efficiency ratio [126]. This is why it is considered the most relevant and efficient waveform motion for planar swimming robots. Moreover, this type of motion is exactly an asymmetric and nonreciprocal periodic motion, which Purcell described as necessary for propulsion in low *Re* [118].

The three classical waveforms present in biological swimmers are described next. The first kind of planar wave is based on mimicking the motion of the flagella of eukaryotic cells. It was first reported by Gray and Hancock in [111], and is described as a traveling harmonic wave. The second and third waveforms characterize the Carangiform fish's motion, i.e., the bending of their bodies in a propulsive wave that extends from head to tail end. This motion was classified by Lighthill [127] under the body and caudal fin (BCF) locomotion and is described using a traveling wave function. It should be highlighted that two properties are preserved during the propulsion of Carangiform fishes:

1. The end of the flagellum attached to the swimmer's head is always maintained at zero amplitude. This will be referred to as the boundary condition.
2. The wave amplitude along the flagellum can be modulated. For spermatozoon, it is approximately constant.

The following expression can mathematically describe these three waveforms

$$y_w(x,t) = c_{w,t}x + (c_{w,0} + c_{w,1}x + c_{w,2}x^2)\sin\left(\frac{2\pi}{\lambda}(x - V_p t)\right), \tag{2.9}$$

where x and y_w are the position and transversal displacement of the tail with respect to the swimmer's head, respectively, V_p defines the propagation velocity of the wave and relates the wavelength (λ) and the frequency (f) employing $V_p = \lambda f$, $c_{w,1}$ and $c_{w,2}$ are the coefficients that govern the amplitude growth, and $c_{w,t}$ defines the

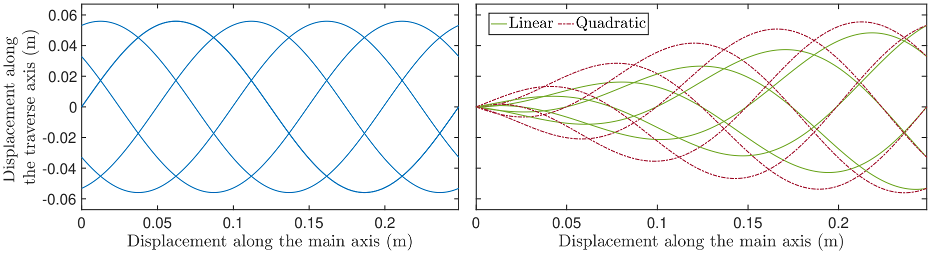

(a) **(b)**

Figure 2.6: Classical traveling waves for bioinspired swimmers with $c_{w,t} = 0$: **(a)** harmonic waveform and **(b)** linear and quadratic Carangiform waveforms

mean amplitude of the motion, and which strongly related to the swimming robot turning ratio. For harmonic waves, the amplitude is only given by coefficient $c_{w,0}$ (thus, $c_{w,1} = c_{w,2} = 0$). This allows the achievement of high propulsion thrust and, consequently, the maximum displacement and velocity since the wave amplitude is maintained along the displacement axis. For Carangiform swimmers, $c_{w,0} = 0$. The two propulsion properties mentioned above are preserved during motion by choosing adequate values for $c_{w,1}$ and $c_{w,2}$ coefficients.

Figure 2.6 depicts the three classical traveling waveforms. As shown in Figure 2.6a, the harmonic wave, unlike the other two, is characterized by a constant amplitude along the flagellum. For the linear Carangiform waveform (Figure 2.6b), the amplitude has a linear growth along the flagellum and the maximum amplitude is reached at the end of this. However, this way of swimming implies a slow forward thrust and velocity. On the other hand, the quadratic Carangiform waveform (Figure 2.6b) allows a second-order polynomial growth of the amplitude, and thus a better modulation of it through the two coefficients $c_{w,1}$ and $c_{w,2}$.

2.4.3 IPMC technology

Within many current applications, the ionic polymer metal composite (IPMC) has revolutionized applications in soft robotics, with particular attention to microswimming robots and soft artificial muscles for medical uses [128]. In this sense, IPMC is presented as an emerging material that stands out for its bending capacity with a relatively low power supply (4–6 V), low density, potential biocompatibility and biodegradability, and underwater actuation, which makes it suitable for the development of swimming microrobots and biomedical applications. However, working with such materials involves multiple challenges, beginning with fabrication techniques, behavior characterization and performance analysis for control, which requires understanding the physical models and the influence of physical parameters [129, 130]. Currently, there are few applications of this material in microsystems, primarily due to a lack of fabrication standards, as well as the reduced number of models that describe its behavior that has been published [131, 132]. Likewise, only of few methods can be found in the specialized literature for manufacturing. For example, an arbitrarily shaped IPMC bulk-machining method is proposed in [133, 134], using MEMS technology [135] or molding and integrating IPMC actuators into a soft silicone tube [136]. The most common method used currently for macro applications is the classical chemical and subsequent mechanical cutting method to fabricate and split an IPMC bulk sheet. Another concern is the variability of material properties depending on the manufacturing process.

This section briefly presents the current state-of-the-art IPMC manufacturing technology and physics-based models, namely, impedance and actuation models.

2.4.3.1 Overview of IPMCs

IPMC units are usually manufactured using Nafion, a thin ion-exchange layer based on a perfluorinated ionomer membrane in a hydrated state with water as a solvent, plated with platinum and establishing a couple of electrodes on both surfaces. The ion-exchange layer is neutralized with Na^+ counteriones to balance the electric charge of the anions attached to the ionomer. Likewise, IPMC sheets can also be manufactured using different types of ionomer membranes, like Flemion, and using different types of counteriones, like Li^+, Rb^+, K^+, Cs^+, Ti^+, Ba^+, with water, ethylene glycol, or glycerol as a solvent, and other organic cations for dry IPMC actuators like TBA^+ and TMA^+. When a positive voltage is applied to one of the electrodes, an ion migration is produced, moving the hydrated cations and water molecules inside the polymer toward the opposite surface. This motion will increase the gradient concentration, producing electrostatic and osmotic forces inside the polymer and forcing the bending. Therefore, IPMCs are electrically driven materials that undergo bending deformations in the presence of external voltages.

2.4.3.2 Physics based models

Impedance and actuation models are usually used to describe the IPMC behaviors [131]. Both models are useful for design and material characterization. Next, governing equations and the mentioned models are presented. Let's start with the basic electrostatic equations:

$$\begin{aligned} E &= -\nabla\phi \\ D &= \kappa_e E \\ \frac{\partial D}{\partial x} &= F(C^+ - C^-) \end{aligned} \tag{2.10}$$

where ϕ, D, E, κ_e, F, C^+, and C^- are the electric potential field in the polymer, electric displacement, electric field, electric permittivity, Faraday's number, and the cation and anion concentration, respectively. The ion-exchange dynamic can be described using the continuity equation:

$$\nabla \cdot \mathbf{J} = -\frac{\partial C^+}{\partial t} \tag{2.11}$$

where $\mathbf{J}$ is the ion flux vector inside the polymer and $\nabla \cdot \mathbf{J}$, the divergence. The ion flux $\mathbf{J}$ is described as:

$$\mathbf{J} = -d\left(\nabla C^+ + \frac{C^+F}{RT}\nabla\phi + \frac{C^+\Delta V}{RT}\nabla P\right) + C^+v \tag{2.12}$$

where d is the ion diffusivity, R is the gas constant, T is the absolute temperature, P is the pressure, and ΔV is the volumetric change. Combining (2.10)–(2.12) and neglecting small term, the following partial differential equation (PDE) for charge density $\rho(x, z, t)$ is obtained:

$$\frac{\partial\rho}{\partial t} + d\frac{\partial^2\rho}{\partial x^2} + \frac{F^2dC^-}{\kappa_e RT}(1 - C^-\Delta V)\rho = 0 \tag{2.13}$$

Reference z axis is defined in the central polymer backbone, being h the distance between the backbone and the electrode layer and parallel to x axis. It is assumed that the induced stress, σ, is proportional to charge density ρ [137]:

$$\sigma = \alpha_0\rho \tag{2.14}$$

where α_0 is the coupling constant. Then, using Laplace transform for $\rho(x,z,t)$, the original PDE (2.13) becomes into the following ordinary differential equation (ODE):

$$s\rho - d\frac{\partial^2\rho}{\partial x^2} + K\rho = 0 \tag{2.15}$$

where $K = \frac{F^2 dC^-}{\kappa_e RT}$. A symmetrical charge distribution is assumed around $x = 0$, thus a solution for the charge density can be obtained as:

$$\rho(x,z,s) = 2c_2(z,s)\sinh(\beta(s)x) \tag{2.16}$$

where $\beta(s) = \sqrt{\frac{s+K}{d}}$, and $c_2(x,s)$ is a generic function that depends on the boundary conditions, which can be obtained from the impedance model in [138].

IPMC actuators can be split into several electrical units and described as an electrical lumped model, where expressions relating current and electric potential are given by:

$$\frac{\partial\phi_\pm}{\partial z} = \pm\frac{r_1'}{W}i_s(z,s) \tag{2.17}$$

$$\frac{\partial i_s(z,s)}{\partial z} = -(i_p(z,s) + i_k(z,s)) \tag{2.18}$$

where $\phi_\pm$ is electric potential, the i_s, i_p and i_k denote the surface current on the electrodes, the distributed current through the polymer due to ion motion and the leaking current, respectively. Surface resistance appears due to the platinum electrodes, generating a drop voltage along z and x axes. Resistances $r_1 = r_1'/W$, $r_2 = r_2'/W$ and $R_p = R_p'/W$ represent the impedances for one electrical unit, being r_1' and r_2' the resistance per unit length ($\Omega \cdot m$) in the electrodes and R_p' representing the polymer resistance per unit length.

From (2.17), and using proper boundary conditions, an expression for the electric potential for $x = \pm h$ can be obtained:

$$\phi(\pm h,z,s) = \frac{\pm V(s)}{2} \mp \int_0^z \frac{r_1'}{W}i_s(\tau,s)d\tau - \frac{r_2'}{W}i_p(z,s) \tag{2.19}$$

where $\pm V(s) = 2\phi_\pm(0,s,)$. Likewise, the electric field can be expressed as:

$$E(h,z,s) = -\frac{\phi(h,z,s)}{h}\frac{\gamma(s)(s+K)}{\gamma(s)s + K\tanh(\gamma(s))} \tag{2.20}$$

where $\gamma(s) = \beta(s)h$. As for ion motion and leaking current can be expressed as follows:

$$\begin{aligned} i_p(z,s) &= -sW\kappa_e E(h,z,s) \\ i_k(z,s) &= \frac{\phi_+(z,s) - \phi_-(z,s)}{R'_p/W} \end{aligned} \tag{2.21}$$

Equations (2.18), (2.20) and (2.21) can be solved to obtain the surface current $i_s(z,s)$ with $i_s(L,s) = 0$, where L is the IPMC length. Total current can be expressed as $I(s) = i(0,s)$. Therefore using an expression for the electric potential regarding the applied voltage, an expression for the global impedance can be obtained as:

$$Z(s) = \frac{V(s)}{I(s)} = \frac{2\sqrt{B(s)}}{A(s)\tanh(\sqrt{B(s)}L)} \tag{2.22}$$

with

$$\begin{aligned} A(s) &= \frac{\theta(s)}{1 + r'_2\theta(s)/W} + \frac{2W}{R'_p}, \quad B(s) = \frac{r'_1}{W}A(s) \\ \theta(s) &= \frac{sW\kappa_e\gamma(s)(s+K)}{h(s\gamma(s) + K\tanh(\gamma(s))} \end{aligned} \tag{2.23}$$

2.4.3.3 Actuation model

Moment bending generation inside of the polymer can be expressed as follows:

$$M(z,s) = \int_{-h}^{h} x\sigma(x,z,s)W\,dx \tag{2.24}$$

An expression for the moment generation can be obtained as:

$$M(z,s) = -\frac{2\alpha_0 KW\kappa_e\left(\gamma(s) - tanh(\gamma(s))\right)\phi(h,z,s)}{\left(s\gamma(s) + Ktanh(\gamma(s))\right)} \tag{2.25}$$

Considering Euler-Bernoulli beam theory for linear displacement, the bending moment can be expressed as:

$$M = -E_m I\frac{\partial^2 w}{\partial x^2} \tag{2.26}$$

where E_m is the elastic modulus, I is the second moment of area, and w is the deflection. Solving w with $w(0,s) = 0$ and $w'(0,s) = 0$ as boundary conditions, and considering that induced stress is proportional to charge density, it is possible to obtain an expression to relate tip deflection with the applied voltage as follows:

$$H(s) = \frac{w(L,s)}{V(s)} = = -\frac{L^2\alpha_0 W}{2EI} \frac{K\kappa_e\,(\gamma(s) - \tanh(\gamma(s)))}{(\gamma(s)s + K\tanh(\gamma(s)))} \frac{2X(s)}{1 + r_2'\theta(s)/W} \tag{2.27}$$

where $X(s)$ is given by:

$$X(s) = -\frac{1 - \operatorname{sech}(\sqrt{B(s)}L) - \tanh(\sqrt{B(s)}L)\sqrt{B(s)}L}{B(s)L^2} \tag{2.28}$$

Additionally, it is necessary to couple a mechanical model to obtain a reliable model of the IPMC dynamics for the first vibration mode, being accurate enough if the bandwidth is relatively low:

2.4.4 Cardiovascular system models

In the medical field, the design of experimental models and platforms that emulate the hemodynamic conditions of the cardiovascular system has been an active topic since the mid-19th century and its interest has increased in recent years. This is motivated by the fact that cardiovascular diseases (CVD) are the leading cause of death worldwide, according to the latest reports from the World Health Organization (WHO). Moreover, the upward trend over the last thirty years continues to increase for almost all countries [139]. In 2019, over 18 million people died from CVDs, which represents 32% of all global deaths; more specifically, 85% of them were due to heart attack and stroke [140]. This fact encouraged, and still does, research on models, where experiments involving computational and mathematical models are much simpler and less expensive to be performed in comparison with in vivo or in vitro experiments. In this sense, this section presents a general description of the CVS and a brief introduction of the main CVS models available in the literature, which will be taken as a basis for modeling a hydraulic platform intended for experimentation with a swimming robot.

2.4.4.1 Overview of the CVS

The following describes the CVS from a functional point of view, with particular attention to the carotid artery. The cardiac cycle is explained through the left ventricle pressure-volume (PV) loops, diagrams that also allow the identification of dysfunctions affecting the CVS.

The CVS can be simply described as a distribution network of blood vessels that supplies blood to all the parts of a body thanks to the heart, which performs as a pump. The path followed by the blood is a closed loop, starting in the heart, continuing through the arteries, passing through the capillaries, where the exchange of substances occurs, and returning to the heart via the veins. From a functional point of view, the distribution network is divided into two stages: 1) systemic circulation, which transports the oxygen and substances; and 2) pulmonary circulation, being responsible for the oxygenation of the blood [141].

The heart, responsible for pumping the blood, is composed of a double atria-ventricle chamber, where the ventricle is the pump and the atria is a preloaded chamber. The compression or contraction of the ventricle generates the necessary pressure to inject blood through the arteries. Specifically, the right side pumps the blood into the pulmonary artery, which carries it to the lungs, and then it returns to the left side, which pumps it again to the rest of the body. It should be noted that the blood only flows in one-way because one-way valves are situated between the chambers to prevent reflux, called atrioventricular valves, and at the output of the ventricles, called semilunar valves.

Regarding systemic circulation, it begins in the ascending aorta, branching into smaller arteries until it reaches the capillaries, covering the entire body. The main branches are: 1) right and left subclavian arteries, supplying blood to the thorax, head, neck, shoulder and arms; 2) right and left common carotid arteries, carrying blood to the head and neck; and 3) descendent aorta, which continues to the abdominal aorta. Finally, the return path is composed of veins that converge in the vena cava, which ends in the heart. Within the systemic circulation, the carotid arteries stand out for their high incidence of strokes [142].

The heart's contraction results from a succession of electrical and mechanical phenomena that occur during a heartbeat, known as the cardiac cycle [141]. The cardiac cycle is divided into two alternate phases: diastole (dilation period) and systole (contraction period), arranged and simplified into four stages. The cardiac cycle starts with the chambers relaxed and the ventricles partially loaded, followed

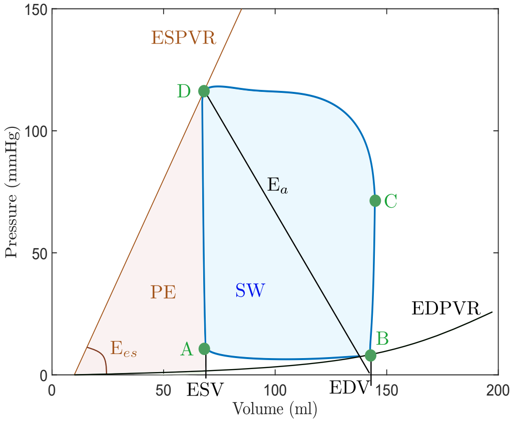

Figure 2.7: Example of PV loop and parameters that can be measured. The meaning of acronyms are detailed in Table 2.2. Image based on [1, 2].

by: 1) the first stage is the atrial systole and ventricular diastole, in which the atrium contracts, filling the ventricles; 2) the second stage is atrial diastole and the beginning of ventricular systole, which means that the atrium relaxes until the next cardiac cycle while the ventricles contract and the atrioventricular valves close, increasing the pressure, but not achieving enough pressure to open semilunar valves; 3) the third stage is the end of ventricular systole, when ventricle pressure rises until it exceeds arterial pressure, opening the semilunar valves and ejecting the blood into the pulmonary and systemic circulation; and 4) the last stage is the ventricular and atrial diastole, when the pressure in the ventricles decreases rapidly and all the chambers are passively loaded due to their relaxation. Then, a new cycle starts with the atrial systole.

A graphical way to describe and characterize the cardiac cycle is by means of a left ventricle PV loop, which represents the left ventricle pressure (LVP) versus the left ventricle volume (LVV) throughout the four stages, allowing to identify changes in heart function, such as preload and afterload factors and contractility of the heart [143]. Another advantage of PV loops is that they allow rapid detection of CVDs, such as heart failure, myocardial and valve diseases. An example of a PV loop is shown in Figure 2.7, where the different stages of a cardiac cycle corresponding to the left ventricle (LV) are represented from a thermodynamic point of view: 1) passive filling (referred to as A-B); 2) isovolumetric contraction (denoted as B-C);

3) ejection (C-D); and 4) isovolumetric relaxation (D-A) [2]. Furthermore, these diagrams also provide information on a wide range of variables, such as those listed in Table 2.2.

Concerning the factors affecting the functioning of the heart, the preload factors refer to the level of distension of the ventricle during diastole and are proportional to end-diastolic volume (EDV) [141, 144]. According to Frank-Starling's law, an increase in ventricular preload leads to an increment of stroke volume (SV), which implies an increase in EDV and the opening pressure of the semilunar valves. These effects are shown in Figure 2.8a. Furthermore, an increase in preload is associated with an increment in physical exercise and acceleration of heart rate (HR), while occlusion of the veins or hemorrhages produces a reduction of preload.

The afterload is related to end-systolic volume (ESV), although preload factors and inotropy also affect it. ESV is the pressure the ventricle must exert to open the semilunar valves and propel the blood. In the PV loops, an increase in afterload involves a reduction in SV and an increment in ESV, which also leads to an increase of the EDV (see Figure 2.8b). An increased systemic resistance usually causes an increase in afterload due to damage of the semilunar valves, stenosis or obstructions in the circulation, as well as a loss of elasticity in the aortic artery.

With respect to inotropy, understood as the capacity of the ventricles to contract, a rise of this factor implies a higher slope of the end-systolic PV relationship (ESPVR)

Table 2.2: Parameters measured from PV loops. Data extracted from [2].

Abbreviation	**Parameter**	**Meaning**
EDV	End-diastolic volume	Left ventricle volume in diastole.
ESV	End-systolic volume	Left ventricle volume in systolic.
ESPVR	End-systolic PV relationship	Maximal pressure of left ventricle.
EDPVR	End-diastolic PV relationship	Left ventricle pressure in diastole.
E_{es}	End-systolic elastance	Peak chamber elastance during a beat.
E_a	Effective arterial elastance	Relates EDP and EDV to ESV.
SV	Stroke volume	The difference between ESV and EDV.
SW	Stroke work	The area within the loop.
PE	Potential energy	The area within the loop and ESPVR.
PVA	Pressure-volume area	Sum of SW and potential energy PE.
ME	Mechanical efficiency	The ratio between SW and PVA.

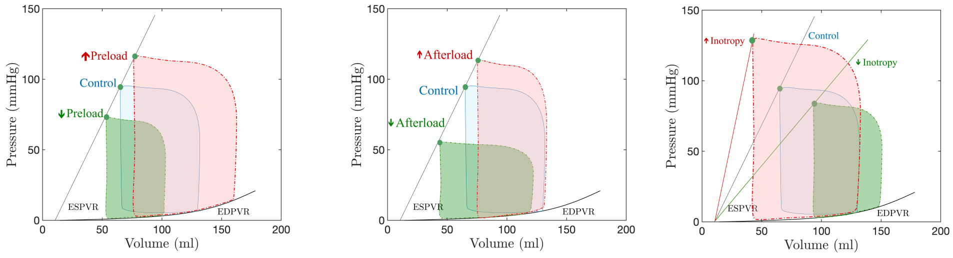

(a) **(b)** **(c)**

Figure 2.8: Effects on PV diagrams due to changes in: (a) preload, (b) afterload, and (c) inotropy on left ventricular.

line, represented in Figure 2.8c. This variation allows to have a higher SV and reduces EDV and ESV. Reduced ability to contract is observed as a consequence of a prolonged state of hypoxia, hyponatremia or hypercapnia.

2.4.4.2 Approaches of CVS modeling

The CVS is a relatively complex system that needs knowledge from several branches of physics and chemistry to understand all its behavior, which has led to the development of models or simulators, in greater or lesser detail, to achieve a global understanding of its operation. Numerous models have been proposed and approached from different perspectives, such as the study of neuroregulation mechanisms, gas exchange or the hemodynamics of the system. The models offer the possibility to diagnose or predict the behavior of the CVS when a patient suffers a cardiovascular dysfunction or pathology [145, 146, 147, 148, 149], or to study the performance of auxiliary devices [4, 150, 151]. This reduces the diagnostic time for certain pathologies or research time of functional evaluation devices under development while reducing animal experimentation. On the other hand, they allow to emulate the hemodynamic conditions and/or working conditions of the robots. However, existing models have limitations at the level of both clinical use and implementation on a real platform, due to their physical and computational complexity. In addition, if modeling of pathologies, or even medical assistance devices, is desired, it usually requires modification of numerous parameters of the model, which are firmly related to each other, making it necessary sometimes to perform new validations. This fact makes the models with a great number of parameters undesirable for real applications. In this regard, lumped parameter models offer an advantage over the others, demonstrating a higher accuracy to execution time ratio, which is suitable for real-time simulations and applications [152, 153]. Despite this, lumped models are reduced to describe the main arteries of the CVS [4, 147, 154, 155] or the entire circulatory system [156], complicating the study of certain vascular areas due to a greater number of parameters. This is the case of the carotid artery, for which no studies model its behavior simply and accurately. Despite this, it is one of the main arteries affected by stenosis according to clinical studies [157]. On the other hand, the development of real platform or mock circulatory loops (MCL) has also received a great deal of attention due to the advantages they offer in the clinical and engineering fields, allowing costly and problematic clinical and animal testing to be avoided. Their possibilities of use cover a large number of applications, which are not only limited to in vitro testing of ventricular assist diseases (VAD) [158] or artificial heart ventricle (AHR) [159], but also to the study of vascular grafts and lung or heart prostheses. It also supports other disciplines, such as tissue engineering, by creating bioreactors, or education by emulating physiological conditions and the anatomical structure of the circulatory system and, in recent years, as a test base for swimming robots.

The MCLs described in the literature can be grouped into two categories according to the type of flow developed: pulsed or nonpulsed system. The type of category will be determined by the type of actuator. Nonpulsating flow systems use centrifugal or axial pumps, while pulsating flow systems use piston pumps, eccentric pumps, diaphragm pumps or pneumatic and hydraulic pressure chambers. The first MCLs in the mid-20th century were focused on evaluating heart valve prostheses. They tried to reproduce the CVS through discrete elements that emulated peripheral resistance, the elasticity of the arteries through a conduit of different dimensions or flexible tubes, and the atria as open deposits. An example of this is reported in[160], where a pulsatile flow mechanism that imitates the heart's contraction to push the blood through a hydraulic compression circuit was presented. On the other hand, other research aimed at developing more complete systems recreating the pulmonary and systemic circulation, where elasticity was emulated through pressurized deposits and resistance with membrane tubes [161, 162]. The subsequent studies published addressed different implementation methods, although all of them were based on the approaches mentioned. It was not until the last few decades that there was a change in the approach. As a result, research focused on studying a mechanism that emulates the left ventricle, controlling its elastance and/or complying with Frank-Starling's law. In this way, it is possible to emulate not only normal hemodynamic conditions, but also pathological ones [163, 164].

2.4.4.3 Electrical equivalences

To describe the CVS using a zero dimension (0-D) global parameter model, it is firstly required to understand how it is possible to transfer the fluid dynamics of an environment to a discrete system, such as electrical circuits. The key concept is to analyze the CVS through segments or compartments, which means defining the relationship between their output and input, which can be calculated either empirically or theoretically.

Applying the Navier-Stokes' equations to a blood vessel segment and taking into account the considerations given in [165, 166], it is possible to define the relationship between pressure and flow within the segment as:

$$\begin{aligned} K_c l \frac{d\hat{p}}{dt} + q_2 - q_1 &= 0 \\ \frac{\rho l}{A}\frac{d\hat{q}}{dt} + \frac{\rho K_R l}{A^2}\hat{q} + p_2 - p_1 &= 0, \end{aligned}$$

where $\hat{p}$ and $\hat{q}$ are the average segment pressure and flow rate, respectively, p_1 and p_2 and q_1 and q_2 are the pressures and the flow rate at the inlet and outlet, respectively, A denotes the average section of the blood vessel, l is the length of the segment, ρ is the density of the blood, and K_c and K_R are variables dependent on the elastic properties of the blood vessel and the viscosity of the blood (see [165, 167] for more information).

The system of equations (2.29) implies that the flow and pressure of the segment considered is limited by the boundary conditions ($q_{1,2}$ and $p_{1,2}$). However, the 0-D model does not have boundary conditions, since there is no continuous dependence on space, but rather an input/output relationship. Therefore, to solve such a system of equations, it is necessary to establish initial conditions ($p_0 = p_1$ and $q_0 = q_1$) and also to make the following simplifications: $\hat{p} \approx p_2$ y $\hat{q} \approx q_1$. These assumptions,

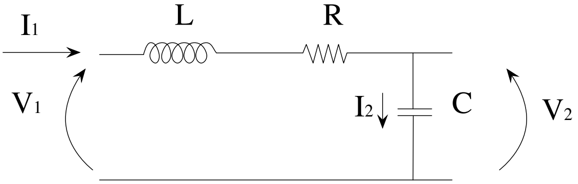

Figure 2.9: Lumped electrical model equivalent to a short blood vessel segment.

valid for relatively short blood vessel segments, result in a 0-D global parameter model [165].

Equations of this type are found in the analysis of resistor-inductor-capacitor (RLC) electrical circuits, which demonstrate the same dynamics [167]. This is shown by analyzing the circuit depicted in Figure 2.9, whose dynamics is defined by the following relationships:

$$\begin{aligned} C\frac{dV_2}{dt} + I_2 - I_1 &= 0 \\ L\frac{dI_1}{dt} + RI_1 + V_2 - V_1 &= 0 \end{aligned}$$

By analogy to an electrical circuit, current represents blood flow, while pressure corresponds to voltage. Likewise, from the sets of equations (2.29) and (2.29) it is possible to establish the equivalence of the electrical components with the variables that define the characteristics of the blood vessel considered as follows: the resistances emulate the opposition of vessel to flow due to viscosity and variation in the diameter of the vessels; the inductance shows the inertial effects that the blood flow experiences as a result of flow variations; and the capacitor represents the conservative term of the principle of mass conservation due to the elasticity of the blood vessels. Assuming that the blood behaves like a Newtonian fluid, i.e., a flow developed under a constant pressure gradient, the following definitions of the equivalent electrical components can be written [165]:

$$R = \frac{8\pi\mu l}{A^2}, \qquad L = \frac{\rho l}{A}, \qquad C = \frac{3\pi r^3 l}{2Eh}, \tag{2.29}$$

where μ is the viscosity of the blood, E is the Young modulus , and h and r are the thickness and the radius of the vessel, respectively.

3

PLANAR SWIMMING ROBOT MODELING

"If you want to find the secrets of the universe, think in terms of energy, frequency and vibration."

Nikola Testa

Contents

This chapter describes the dynamic model of a flagellum-type articulated artificial eukaryotic swimming robot for medium and low *Re* environments. The medium *Re* case is when inertial effects cannot be ignored and have an influence equivalent to viscous forces. As for the low *Re* case, inertial forces become negligible compared to viscous forces. The above cases correspond precisely to mili and micro-scale robots, respectively. Nonlinear control strategies will be applied to both models to simplify them and reduce their strong nonlinearity. In addition, a new motion-beating waveform is proposed to improve the propulsion efficiency concerning classical waveforms.

3.1 Model for medium *Re* environments

The motion of biological swimmers is essentially performed in two dimensions. For this reason, the swimming robot motions described next will be constrained to such dimensions. The general case on three dimensions can be handled with similar techniques, although it is slightly more complex [168]. The global frame (inertial frame) is restricted to two dimensions and defined by the vectors $(\mathbf{e}_\mathrm{x}, \mathbf{e}_\mathrm{y})$, and obtaining $\mathbf{e}_\mathrm{z}$ as result of their cross product. Similarly, the body frame for the local coordinates of the links from the center of mass (CM) is given by the vectors $(\mathbf{e}_{||}, \mathbf{e}_{\perp})$, which define the tangential and normal directions to the link orientation, and it is also the result of their cross product. Taking this premise as a basis, the following sections will analyze the kinematics and dynamics of the articulated robot.

3.1.1 Kinematic

Let's consider a swimming robot whose flagellum is formed by N_u links plus the head and each link has up to N_f DoF. The flexibility of each link is modeled by a spring-damper system except the last link, which is rigid and represents the head, as shown in Figure 3.1. The robot presents $(N_u \cdot N_f) + 3$ DoF; $N = (N_u \cdot N_f) + 1$ degrees correspond to the angles of the link and the head, and 2 degrees to the flat position of the head. Let $\mathbf{q}_i = (x_i, y_i) \in \Re^2$ denote the (CM) of i-link in the global frame with $i \in \{1, \ldots, N\}$, l_i is the length, r_i is the link radius, θ_i is the angle that forms with the horizontal $\mathbf{e}_\mathrm{x}$ axis with counterclockwise positive directions, and α_i is the joint angle defined as $\alpha_i = \theta_{i+1} - \theta_i$. The local coordinates of each link are related to the global frame through the following rotation matrix, being able to express the robot kinematics in both reference frames:

$$\mathbf{R}^{\mathrm{I}}_{\mathrm{B},i} = \begin{bmatrix} \mathbf{e}_{\parallel,i} & \mathbf{e}_{\perp,i} \end{bmatrix} = \begin{bmatrix} \cos\theta_i & -\sin\theta_i \\ \sin\theta_i & \cos\theta_i \end{bmatrix}. \tag{3.1}$$

It should be noted that links' angles represent the orientation with respect to the global horizontal axis. In contrast, joint angles are the difference between the link angle of two consecutive links. Additionally, the swimmer robot velocity along its forward or tangential direction is defined as [123, 124]:

$$v_x = \dot{q}_x \cos\psi + \dot{q}_y \sin\psi \tag{3.2}$$

that means the projection of the robot velocity vector onto the robot orientation vector. Likewise, the coordinates of any link can be expressed as a linear function of the swimmer head position $\mathbf{q_N} = (q_x, q_y) \in \Re^2$ in the global frame, where the geometric dependence between them is:

$$\mathbf{q_i} = \begin{bmatrix} x_i \\ y_i \end{bmatrix} = \begin{bmatrix} q_x - \sum_{j=i}^{N-1}\left(\frac{l_j}{2}\cos\theta_j + \frac{l_{j+1}}{2}\cos\theta_{j+1}\right) \\ q_y - \sum_{j=i}^{N-1}\left(\frac{l_j}{2}\sin\theta_j + \frac{l_{j+1}}{2}\sin\theta_{j+1}\right) \end{bmatrix} \tag{3.3}$$

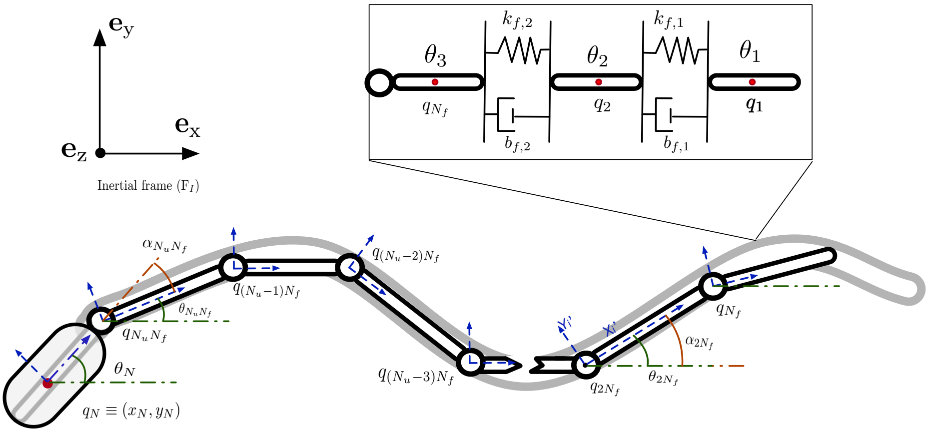

Figure 3.1: Diagram of planar flagellum-type articulated artificial eukaryotic swimming robot.

and whose matrix form is

$$\mathbf{X} = \mathbf{e}\mathbf{q}_x - \frac{1}{2}\mathbf{L}\mathbf{W}\mathbf{C}_\theta \tag{3.4a}$$

$$\mathbf{Y} = \mathbf{e}\mathbf{q}_y - \frac{1}{2}\mathbf{L}\mathbf{W}\mathbf{S}_\theta \tag{3.4b}$$

where $\mathbf{X} = [x_1, \ldots, x_N]^T \in \Re^N$, $\mathbf{Y} = [y_1, \ldots, y_N]^T \in \Re^N$, $\mathbf{e} = [1, \ldots, 1]^T \in \Re^N$ is a summation vector, $\mathbf{L} = \mathrm{diag}(l_i) \in \Re^{N\times N}$, $\mathbf{C}_\theta = \mathrm{diag}(\cos\boldsymbol{\theta}) \in \Re^{N\times N}$, $\mathbf{S}_\theta = \mathrm{diag}(\sin\boldsymbol{\theta})$ $\in \Re^{N\times N}$, $\boldsymbol{\theta} = [\theta_1, \ldots, \theta_N]^T \in \Re^N$ is the angle link vector, $\mathrm{diag}(\,\cdot\,)$ is an operator that produces a diagonal matrix with each individual element of its argument along its diagonal and $\mathbf{W} \in \Re^{N\times N}$ is a matrix defined by:

$$\mathbf{W}_{(i,j)} = \begin{cases} 1 & \text{if } i = j \\ 2 & \text{if } j > 1 \\ 1 & \text{if } j = N \\ 0 & \text{Otherwise.} \end{cases} \tag{3.5}$$

where i and j denote its row and columns, respectively. If the link position is differentiated with respect to time, linear velocities are obtained as:

$$\dot{\mathbf{X}} \;\; = \mathbf{e}\dot{\mathbf{q}}_x + \tfrac{1}{2}\mathbf{L}\mathbf{W}\mathbf{S}_\theta\dot{\boldsymbol{\theta}} \tag{3.6a}$$

$$\dot{\mathbf{Y}} \;\; = \mathbf{e}\dot{\mathbf{q}}_y - \tfrac{1}{2}\mathbf{L}\mathbf{W}\mathbf{C}_\theta\dot{\boldsymbol{\theta}}. \tag{3.6b}$$

Similarly, differentiating the link velocity, link acceleration can be found expressed in terms of link angle and the swimmer's head acceleration:

$$\ddot{\mathbf{X}} \;\; = \mathbf{e}\ddot{\mathbf{q}}_x + \tfrac{1}{2}\mathbf{L}\mathbf{W}\Big(\mathbf{C}_\theta\dot{\boldsymbol{\theta}}^2 + \mathbf{S}_\theta\ddot{\boldsymbol{\theta}}\Big) \tag{3.7a}$$

$$\ddot{\mathbf{Y}} \;\; = \mathbf{e}\ddot{\mathbf{q}}_y - \tfrac{1}{2}\mathbf{L}\mathbf{W}\Big(\mathbf{C}_\theta\ddot{\boldsymbol{\theta}} - \mathbf{S}_\theta\dot{\boldsymbol{\theta}}^2\Big) \tag{3.7b}$$

where $\dot{\boldsymbol{\theta}}^2 = \mathrm{diag}(\dot{\boldsymbol{\theta}})\,\dot{\boldsymbol{\theta}}$. Additionally, the swimming geometry imposes two holonomic constraints resulting from the connections between two neighboring links at joint $i \in 1, \ldots, N-1$ as:

$$x_{i+1} - x_i \;\; = \tfrac{l_i}{2}\cos\theta_i + \tfrac{l_{i+1}}{2}\cos\theta_{i+1} \tag{3.8a}$$

$$y_{i+1} - y_i \;\; = \tfrac{l_i}{2}\sin\theta_i + \tfrac{l_{i+1}}{2}\sin\theta_{i+1} \tag{3.8b}$$

Using a matrix notation, the holonomic constraints for all the links can be expressed in a more intuitive way by

$$\mathbf{DX} = \tfrac{1}{2}\mathbf{AL}\cos\boldsymbol{\theta}, \tag{3.9a}$$

$$\mathbf{DY} = \tfrac{1}{2}\mathbf{AL}\sin\boldsymbol{\theta}, \tag{3.9b}$$

where $\cos\boldsymbol{\theta} = [\cos\theta_1, \ldots, \cos\theta_N]^T \in \Re^N$, $\sin\boldsymbol{\theta} = [\sin\theta_1, \ldots, \sin\theta_N]^T \in \Re^N$, and the matrices $\mathbf{D} \in \Re^{(N-1)\times N}$ and $\mathbf{A} \in \Re^{(N-1)\times N}$ represent a difference and a summation matrix, respectively, defined by:

$$\mathbf{D}_{(i,j)} = \begin{cases} -1 & \text{if } i = j \\ 1 & \text{if } (i+1) = j \\ 0 & \text{Otherwise.} \end{cases} \quad \text{and} \quad \mathbf{A}_{(i,j)} = \begin{cases} 1 & \text{if } i = j \\ 1 & \text{if } i = (j+1) \\ 0 & \text{Otherwise.} \end{cases} \tag{3.10}$$

Hence, the set of equations corresponding to the position (3.4a), velocity (3.6a) and acceleration (3.7a) describes the direct kinematic problem of the swimmer's robot, taking also in account that the coordinates of any link can be expressed as a linear function of the other link or the head position.

3.1.2 Environment interaction

As discussed in sections 2.4.1 and 2.4.2, self-propulsion of biological microorganisms and swimmer robots is the result of a combination of two main factors: 1) the resulting forces exerted on the body by the fluid environment, and 2) the swimming pattern motion. Therefore, a correct description of fluid-body interaction is crucial to the swimming robot dynamics. For that purpose, the environment dynamics is based on the RFT. Although it offers lower accuracy than other theories discussed, it is sufficient for control strategies design. Moreover, if the environment characteristic or the swimming robot size cannot ultimately ensure the properties of a Stokes' flow, even if the system is in a low *Re* environment, inertial effects may affect the swimming robot dynamics. Thus, a complete model requires considering two types of forces resulting from the fluid-body interaction: 1) resistive forces due to creeping flow, and 2) reactive forces result from a fluid mass's change in velocity.

Recalling the hydrodynamics simplifications mentioned in section 2.4.1, the description of the above forces is also supported by the following assumptions:

1. *The fluid is viscid, incompressible, and irrotational in the inertial frame.*
2. *The relative velocity in the surrounding of the CM is equal to the relative velocity of the respective CM of each link.*
3. *The flagellum is circular in cross-section.*
4. *Each segment is considered isolated.*
5. *The border effects are neglected.*

On the other hand, the fluid velocity is assumed to be known and defined by $\mathbf{v}_f = (v_{f,x}, v_{f,y}) \in \Re^2$ in the $\mathbf{e}_\mathrm{x}$ and $\mathbf{e}_\mathrm{y}$ directions, respectively. The swimming robot is modeled in a neutrally buoyant position concerning the gravitational force. Thus the buoyant force (Archimedes' principle) compensates for the gravitational forces. Although, without loss of generality, the interaction forces described below can be extended to a tilted plane, considering further the gravitational and buoyant forces in that case.

3.1.2.1 Resistive forces

The particularization of the RFT to a flexible articulated swimming robot also implies that the resistive forces or viscous drags are only proportional to the relative velocity of links to the fluid velocity, expressed in local-frame coordinates [111, 112, 123]. Taking s as the arc-length coordinate in the i-th link with $0 \leq s \leq l_i$, as depicted Figure 3.2, the local coordinates of a point from the CM link are:

$$\mathbf{q}_i(s) = \mathbf{q}_i + s\mathbf{e}_{\|,i} \tag{3.11}$$

and the velocity is obtained by differentiating with respect to time, which means

$$\dot{\mathbf{q}}_i(s) = \dot{\mathbf{q}}_i + s\dot{\theta}_i\mathbf{e}_{\perp,i}. \tag{3.12}$$

Then, it follows that the viscous force density function based on the RFT (2.7) applied to i-th link of a swimming robot is

$$\begin{aligned} df_{v,i}(s) = &- c^{\|}_{v,i}\Big(\big(\dot{\mathbf{q}}_i(s) - \mathbf{v}_f\big)\cdot \mathbf{e}^T_{\|,i}\Big)\mathbf{e}_{\|,i} \\ &- c^{\perp}_{v,i}\Big(\big(\dot{\mathbf{q}}_i(s) - \mathbf{v}_f\big)\cdot \mathbf{e}^T_{\perp,i}\Big)\mathbf{e}_{\perp,i}\, ds, \end{aligned} \tag{3.13}$$

where the coefficients $c^{\|}_{v,i}$ and $c^{\perp}_{v,i}$ are defined in the tangential ($\mathbf{e}_{\|,i}$) and normal ($\mathbf{e}_{\perp,i}$) direction of the link, respectively. It is worth mentioning that the terms within the large parentheses refer to the local relative velocity expressed in the global frame.

Finally, integrating the force density function (3.13) over the link length of the link (l_i) with respect to s, including the length terms within the friction coefficients, and using a matrix notation, the viscous forces actuating on the i-link CM are defined as

$$\begin{bmatrix} \mathbf{F}_{v,x} \\ \mathbf{F}_{v,y} \end{bmatrix} = -\mathbf{R}^{\mathrm{I}}_{\mathrm{B},i} \begin{bmatrix} \mathbf{c}^{\|}_{v} & 0 \\ 0 & \mathbf{c}^{\perp}_{v} \end{bmatrix} \left(\mathbf{R}^{\mathrm{I}}_{\mathrm{B},i}\right)^T \begin{bmatrix} \dot{\mathbf{X}} - \mathbf{V}_{f,x} \\ \dot{\mathbf{Y}} - \mathbf{V}_{f,y} \end{bmatrix}, \tag{3.14}$$

where $\mathbf{F}_{v,x} = [f_{v,x,1}, \dots, f_{v,x,N}]^T \in \Re^N$ and $\mathbf{F}_{v,y} = [f_{v,y,1}, \dots, f_{v,y,N}]^T \in \Re^N$ are the viscous forces in the $\mathbf{e}_{\mathrm{x}}$ and $\mathbf{e}_{\mathrm{y}}$ directions, respectively, $\mathbf{c}^{\|}_{v} = \mathrm{diag}(c^{\|}_{v,i}) \in \Re^{N\times N}$, $\mathbf{c}^{\perp}_{v} = \mathrm{diag}(c^{\perp}_{v,i}) \in \Re^{N\times N}$ and $\mathbf{V}_{f,x} = \mathbf{e}v_{f,x} \in \Re^N$ and $\mathbf{V}_{f,y} = \mathbf{e}v_{f,y} \in \Re^N$ are the fluid

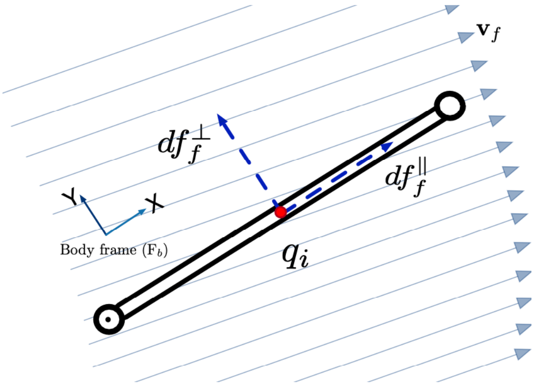

Figure 3.2: Interaction between body and environment: viscous forces.

velocity vectors. Developing and arranging the above matrix product results in

$$\begin{bmatrix}\mathbf{F}_{v,x}\\ \mathbf{F}_{v,y}\end{bmatrix} = \begin{bmatrix} -\mathbf{c}_v^{\parallel}(\mathbf{C}_\theta)^2 - \mathbf{c}_v^{\perp}(\mathbf{S}_\theta)^2 & (\mathbf{c}_v^{\perp} - \mathbf{c}_v^{\parallel})\mathbf{S}_\theta\mathbf{C}_\theta \\ (\mathbf{c}_v^{\perp} - \mathbf{c}_v^{\parallel})\mathbf{S}_\theta\mathbf{C}_\theta & -\mathbf{c}_v^{\parallel}(\mathbf{S}_\theta)^2 - \mathbf{c}_v^{\perp}(\mathbf{C}_\theta)^2\end{bmatrix}\begin{bmatrix}\dot{\mathbf{X}} - \mathbf{V}_{f,x}\\ \dot{\mathbf{Y}} - \mathbf{V}_{f,y}\end{bmatrix}, \tag{3.15}$$

where it can already be observed, considering only the resistive forces, the swimming robot propulsion. This means a positive force or thrust in the direction $\mathbf{e}_\mathrm{x}$ can only be developed if $\mathbf{c}_v^{\perp} > \mathbf{c}_v^{\parallel}$ and, consequently, if $(\dot{\mathbf{Y}} - \mathbf{V}_{f,y}) > \mathbf{c}_v^{\perp}(\mathbf{c}_v^{\perp} - \mathbf{c}_v^{\parallel})^{-1}\mathbf{T}_\theta(\dot{\mathbf{X}} - \mathbf{V}_{f,x})$, where $\mathbf{T}_\theta = \mathrm{diag}(\tan\boldsymbol{\theta}) \in \Re^{N\times N}$. This will be explained in more detail in a later section.

Furthermore, resistance forces also induce a moment in each link due to the flagellum division into a finite joint segment robot. By contrast, other studies neglect the contribution of torque produced by the environment [123], because they assume that it does not significantly affect the swimming robot's motion. However, when the modeling approach is based on a finite joint segment robot, [122, 124, 169, 170, 171], the fluid moments should be present in the model because: 1) they affect the accuracy of the model, 2) their influence is strictly related to the required actuation torques at the joint, and thus in the available technology to fulfill the technical requirements, and 3) the torque is also proportional to the system's power consumption. Then, the moment caused by the interaction between the swimming robot's motion and the environment is calculated by

$$\mathbf{e}_\mathrm{z}\cdot\tau_{v,i}(s) = \int_{\frac{-l_i}{2}}^{\frac{l_i}{2}} \mathbf{e}_\mathrm{z}\cdot\Big((\mathbf{q}_i(s) - \mathbf{q}_i)\times df_{v,i}(s)\Big)\,ds \tag{3.16}$$

Developing and solving the above expression, it is observed that the resistive viscous torque is only due to the normal forces actuating during its rotation, which can be expressed as

$$\mathbf{T}_v = -\mathbf{c}_v^{\circ}\dot{\boldsymbol{\theta}}, \tag{3.17}$$

where $\mathbf{T}_v = [\tau_{v,1},\ldots,\tau_{v,N}]^T \in \Re^N$ and $\mathbf{c}_v^{\circ} = \mathrm{diag}(c_{v,i}^{\circ}) \in \Re^{N\times N}$ are the viscous friction torque coefficients.

3.1.2.2 Reactive forces

The reactive or added masses forces aim to model the inertial effects resulting from the acceleration of the surrounding fluid. For this purpose, the employed approach is based on Morison's equations, which describe the force exerted on a differential section as a function of the relative acceleration of the link with respect to the fluid, expressed in the local-frame coordinates as [172]

$$\begin{aligned} df_{a,i}(s) = &-c^{\|}_{a,i}\Big(\big(\ddot{\mathbf{q}}_i(s)-\dot{\mathbf{v}}_f\big)\cdot\mathbf{e}^T_{\|,i}+\big(\dot{\mathbf{q}}_i(s)-\mathbf{v}_f\big)\cdot\frac{d}{dt}\mathbf{e}^T_{\|,i}\Big)\mathbf{e}_{\|,i} \\ &-c^{\perp}_{a,i}\Big(\big(\ddot{\mathbf{q}}_i(s)-\dot{\mathbf{v}}_f\big)\cdot\mathbf{e}^T_{\perp,i}+\big(\dot{\mathbf{q}}_i(s)-\mathbf{v}_f\big)\cdot\frac{d}{dt}\mathbf{e}^T_{\perp,i}\Big)\mathbf{e}_{\perp,i}\,ds, \end{aligned} \tag{3.18}$$

where $c^{\|}_{a,i}$ and $c^{\|}_{a,i}$ are the added mass coefficients in the tangential ($\mathbf{e}_{\|,i}$) and normal ($\mathbf{e}_{\perp,i}$) direction of the link, respectively. These coefficients also depend on the environmental properties and the swimming robot's shape.

Regarding the derivative of the local frame vector basis, it is given by

$$\frac{d}{dt}\mathbf{R}^{\mathrm{I}}_{\mathrm{B},i}=\frac{d}{dt}\begin{bmatrix}\mathbf{e}_{\|,i} & \mathbf{e}_{\perp,i}\end{bmatrix}=\begin{bmatrix}\dot{\theta}_i & 0\\ 0 & \dot{\theta}_i\end{bmatrix}\begin{bmatrix}-\sin\theta_i & -\cos\theta_i\\ \cos\theta_i & -\sin\theta_i\end{bmatrix} \tag{3.19}$$

In the same way as the resistive forces, the differential force function (3.18) can be integrated over the link length (l_i) with respect to s to obtain the added masses forces actuating on the CM of i-link, in matrix form, as

$$\begin{bmatrix}\mathbf{F}_{a,x}\\ \mathbf{F}_{a,y}\end{bmatrix}=-\mathbf{R}^{\mathrm{I}}_{\mathrm{B},i}\begin{bmatrix}\mathbf{c}^{\|}_a & 0\\ 0 & \mathbf{c}^{\perp}_a\end{bmatrix}\left(\left(\mathbf{R}^{\mathrm{I}}_{\mathrm{B},i}\right)^T\begin{bmatrix}\ddot{\mathbf{X}}-\dot{\mathbf{V}}_{f,x}\\ \ddot{\mathbf{Y}}-\dot{\mathbf{V}}_{f,y}\end{bmatrix}+\left(\frac{d}{dt}\mathbf{R}^{\mathrm{I}}_{\mathrm{B},i}\right)^T\begin{bmatrix}\dot{\mathbf{X}}-\mathbf{V}_{f,x}\\ \dot{\mathbf{Y}}-\mathbf{V}_{f,y}\end{bmatrix}\right), \tag{3.20}$$

where $\mathbf{F}_{a,x}=[f_{a,x,1},\dots,f_{a,x,N}]^T\in\mathfrak{R}^N$ and $\mathbf{F}_{a,y}=[f_{a,y,1},\dots,f_{a,y,N}]^T\in\mathfrak{R}^N$ are the added masses forces in the $\mathbf{e}_{\mathrm{x}}$ and $\mathbf{e}_{\mathrm{y}}$ directions, respectively, $\mathbf{c}^{\|}_a=\mathrm{diag}(c^{\|}_{a,i})\in\mathfrak{R}^{N\times N}$ and $\mathbf{c}^{\perp}_a=\mathrm{diag}(c^{\perp}_{a,i})\in\mathfrak{R}^{N\times N}$. The above expression can also be expressed as

$$\begin{aligned}\begin{bmatrix}\mathbf{F}_{a,x}\\ \mathbf{F}_{a,y}\end{bmatrix}=&\begin{bmatrix}-\mathbf{c}^{\|}_a(\mathbf{C}_\theta)^2-\mathbf{c}^{\perp}_a(\mathbf{S}_\theta)^2 & (\mathbf{c}^{\perp}_a-\mathbf{c}^{\|}_a)\mathbf{S}_\theta\mathbf{C}_\theta\\ (\mathbf{c}^{\perp}_a-\mathbf{c}^{\|}_a)\mathbf{S}_\theta\mathbf{C}_\theta & -\mathbf{c}^{\|}_a(\mathbf{S}_\theta)^2-\mathbf{c}^{\perp}_a(\mathbf{C}_\theta)^2\end{bmatrix}\begin{bmatrix}\ddot{\mathbf{X}}-\dot{\mathbf{V}}_{f,x}\\ \ddot{\mathbf{Y}}-\dot{\mathbf{V}}_{f,y}\end{bmatrix}\\ &+\begin{bmatrix}(\mathbf{c}^{\|}_a-\mathbf{c}^{\perp}_a)\mathbf{S}_\theta\mathbf{C}_\theta\dot{\boldsymbol{\theta}} & -\mathbf{c}^{\|}_a(\mathbf{C}_\theta)^2\dot{\boldsymbol{\theta}}-\mathbf{c}^{\perp}_a(\mathbf{S}_\theta)^2\dot{\boldsymbol{\theta}}\\ \mathbf{c}^{\|}_a(\mathbf{S}_\theta)^2\dot{\boldsymbol{\theta}}+\mathbf{c}^{\perp}_a(\mathbf{C}_\theta)^2\dot{\boldsymbol{\theta}} & (\mathbf{c}^{\perp}_a-\mathbf{c}^{\|}_a)\mathbf{S}_\theta\mathbf{C}_\theta\dot{\boldsymbol{\theta}}\end{bmatrix}\begin{bmatrix}\dot{\mathbf{X}}-\mathbf{V}_{f,x}\\ \dot{\mathbf{Y}}-\mathbf{V}_{f,y}\end{bmatrix}.\end{aligned} \tag{3.21}$$

Similarly to viscous forces, the first term indicates that the relative transversal accelerations of the flagellum also contribute to the swimming robot's propulsion. However, from the second term, it can be deduced that if the robot's velocity is greater than that of the fluid, that means greater kinetic energy. The propulsion will be reduced due to some energy being transferred to the environment to equal the velocity. In other works, the fluid acceleration is considered equal to zero because they assumed that the flow in the global frame is constant and irrotational, meaning the swimming robot is immersed in a stationary flow or can be interpreted as such. In addition, in slender bodies, the tangential coefficient ($\mathbf{c}_a^{\|}$) is usually considered to be zero because its influence is negligible compared to normal one [171, 173].

The consideration of the added masses forces also implies a moment as a result of the normal forces induced on the flagellum, which can be calculated as

$$\mathbf{e}_{\mathrm{z}} \cdot \tau_{a,i}(s) = \int_{-\frac{l_i}{2}}^{\frac{l_i}{2}} \mathbf{e}_{\mathrm{z}} \cdot \Big((\mathbf{q}_i(s) - \mathbf{q}_i) \times df_{a,i}(s) \Big)\, ds \,. \tag{3.22}$$

Solving the previous equation, the added masses torque is, in matrix form, defined as

$$\mathbf{T}_a = \quad -\mathbf{c}_a^{\circ} \ddot{\boldsymbol{\theta}}, \tag{3.23}$$

where $\mathbf{T}_a = [\tau_{a,1}, \ldots, \tau_{a,N}]^T \in \Re^N$ and $\mathbf{c}_a^{\circ} = \mathrm{diag}(c_{a,i}^{\circ}) \in \Re^{N \times N}$ are the viscous friction torque coefficients.

3.1.3 Motion dynamics

The description of the swimming robot dynamics is based on the free body diagram illustrated in Figure 3.3, where it can be observed that the forces involved in the motions are mainly the following: 1) resistive and reactive forces due to environment interaction, which act on the CM of the links, 2) internal constraint forces ($h_{x,i}$ and $h_{y,i}$) that keep the links together, 3) torques resulting from the springs and dampers that represent the link flexibility, and 4) the torque resulting from the actuators to move links. Using the second Newton's law, the force balance for each link in the global frame is:

$$m_i \ddot{x}_i = f_{v,x} + f_{a,x} - h_{x,i} + h_{x,(i-1)}, \tag{3.24a}$$

$$m_i \ddot{y}_i = f_{v,y} + f_{a,y} - h_{y,i} + h_{y,(i-1)}, \tag{3.24b}$$

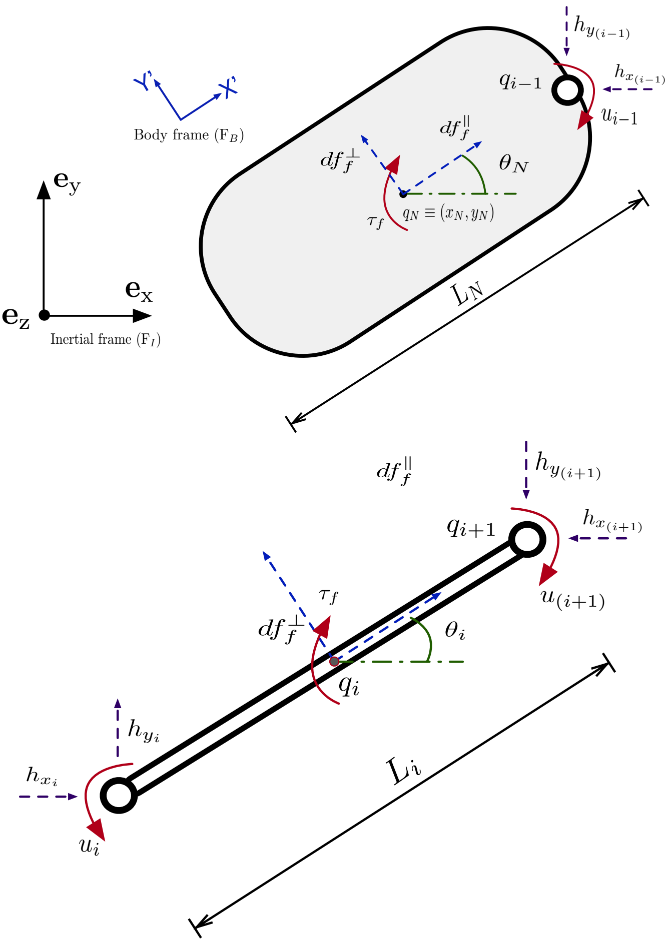

Figure 3.3: Free body diagram of head and link of a flagellum-type articulated artificial eukaryotic swimming robot.

where m_i is the mass of i-link. Expressing the force balance equations in matrix form, the following form is adopted when all the links are considered:

$$\mathbf{M}\,\ddot{\mathbf{X}} = \mathbf{F}_{v,x} + \mathbf{F}_{a,x} + \mathbf{D}^T\mathbf{H}_x \tag{3.25a}$$

$$\mathbf{M}\,\ddot{\mathbf{Y}} = \mathbf{F}_{v,y} + \mathbf{F}_{a,y} + \mathbf{D}^T\mathbf{H}_y \tag{3.25b}$$

where $\mathbf{M} = \mathrm{diag}(m_i) \in \Re^{N\times N}$, $\mathbf{H}_x = [h_{x,1}, \dots, h_{x,N-1}]^T \in \Re^{N-1}$ and $\mathbf{H}_y = [h_{y,1}, \dots, h_{y,N-1}]^T \in \Re^{N-1}$ are the vector joint constraint forces in the $\mathbf{e}_{\mathrm{x}}$ and $\mathbf{e}_{\mathrm{y}}$ directions, respectively.

Now, the head acceleration can be expressed as a function of the external forces actuating on the head, described in the equations (3.25a) and (3.25b) , and constraint forces, obtaining:

$$m_n\ddot{q}_x = f_{v,x,N} + f_{a,x,N} + h_{x,N} = \mathbf{e}^T\Big(\mathbf{F}_{v,x} + \mathbf{F}_{a,x}\Big) \tag{3.26a}$$

$$m_n\ddot{q}_y = f_{v,y,N} + f_{a,y,N} + h_{y,N} = \mathbf{e}^T\Big(\mathbf{F}_{v,y} + \mathbf{F}_{a,y}\Big) \tag{3.26b}$$

It should be noted that the head constraint forces are equivalent to the sum of all the reaction forces to which the other links are subjected. For its part, the torque balance for i-link is given by

$$\begin{aligned} j_i\,\ddot{\theta}_i = u_i - u_{(i+1)} + \tau^{\circ}_{v,i} + \tau^{\circ}_{a,i} - k_{f,i}(\theta_i - \theta_{i+1}) + k_{f,(i-1)}(\theta_{i-1} - \theta_i) \\ -b_{f,i}(\dot{\theta}_i - \dot{\theta}_{i+1}) + b_{f,(i-1)}(\dot{\theta}_{i-1} - \dot{\theta}_i) + \frac{l_i}{2}\sin\theta_i\Big(h_{x,i} + h_{x,(i+1)}\Big), \\ -\frac{l_i}{2}\cos\theta_i\Big(h_{y,i} + h_{y,(i+1)}\Big) \end{aligned} \tag{3.27}$$

where j_i is the moment of inertia of i-link, u_i is the actuator torque exerted at the ends of the link, and $k_{f,i}$ and $b_{f,i}$ are the bending stiffness and damping of flexible links, respectively. Using a matrix notation, the torque balances can be expressed as

$$\mathbf{J}\ddot{\boldsymbol{\theta}} = \mathbf{D}^T\mathbf{Q}\mathbf{U} + \mathbf{T}_a + \mathbf{T}_v - \mathbf{D}^T\mathbf{K}_f\mathbf{D}\boldsymbol{\theta} - \mathbf{D}^T\mathbf{B}_f\mathbf{D}\dot{\boldsymbol{\theta}} + \frac{1}{2}\mathbf{L}\mathbf{S}_\theta\mathbf{A}^T\mathbf{H}_x - \frac{1}{2}\mathbf{L}\mathbf{C}_\theta\mathbf{A}^T\mathbf{H}_y, \tag{3.28}$$

where $\mathbf{J} = [j_1, \dots, j_N] \in \Re^N$ and $\mathbf{U} = [u_1, \dots, u_{N-1}] \in \Re^{N-1}$. As for the matrix

$\mathbf{Q} \in \Re^{N\times N_u}$, $\mathbf{K}_f \in \Re^{N\times N}$ and $\mathbf{B}_f \in \Re^{N\times N}$ are defined as follows;

$$\begin{aligned}
\mathbf{Q}_{(i,j)} &= \begin{cases} 1 & \text{if } (k\cdot N_f) = j \text{ for } i = 1,\dots,N_u \\ 0 & \text{Otherwise.} \end{cases} , \\
\mathbf{K}_{f(i,j)} &= \begin{cases} k_{f,i} & \text{if } i = j \text{ and } i \neq N_f\cdot k \text{ for } k = 1,\dots,N_u \\ 0 & \text{Otherwise.} \end{cases} \quad \text{and} \\
\mathbf{B}_{f,(i,j)} &= \begin{cases} b_{f,i} & \text{if } i = j \text{ and } i \neq N_f\cdot k \text{ for } k = 1,\dots,N_u \\ 0 & \text{Otherwise.} \end{cases}
\end{aligned} \tag{3.29}$$

Note that the matrix $\mathbf{Q}$ establishes which links are driven by the actuators.

In the same way, the torque balance can also be expressed as a function of the external forces. For this purpose, the constraint forces can be calculated from the force balance (3.25a). Unlike before, the relation can be determined premultiplying by $\mathbf{DM}^{-1}$ to convert the matrix to a square and nonsingular one, and thereby invertible. After that, they are solved for $\mathbf{H}_x$ and $\mathbf{H}_y$, obtaining:

$$\mathbf{H}_x = \left(\mathbf{DM}^{-1}\mathbf{D}^T\right)^{-1}\left(\mathbf{D\ddot{X}} - \mathbf{DM}^{-1}\left(\mathbf{F}_{v,x} + \mathbf{F}_{a,x}\right)\right), \tag{3.30a}$$

$$\mathbf{H}_y = \left(\mathbf{DM}^{-1}\mathbf{D}^T\right)^{-1}\left(\mathbf{D\ddot{Y}} - \mathbf{DM}^{-1}\left(\mathbf{F}_{v,y} + \mathbf{F}_{a,y}\right)\right), \tag{3.30b}$$

where $\mathbf{D\ddot{X}}$ is the acceleration difference between links, which can be followed from the holonomic constraints (3.9a). If they are differentiated twice with respect to time, it is obtained:

$$\mathbf{D\ddot{X}} = \tfrac{1}{2}\mathbf{AL}\left(\mathbf{C}_\theta\dot{\boldsymbol{\theta}}^2 + \mathbf{S}_\theta\ddot{\boldsymbol{\theta}}\right), \tag{3.31a}$$

$$\mathbf{D\ddot{Y}} = \tfrac{1}{2}\mathbf{AL}\left(\mathbf{S}_\theta\dot{\boldsymbol{\theta}}^2 - \mathbf{C}_\theta\ddot{\boldsymbol{\theta}}\right). \tag{3.31b}$$

Then, inserting the kinematics acceleration (3.31a) and the constrains force equations (3.30a) on torque balance (3.28), the expression can be rewritten as

$$\begin{aligned}
\mathbf{J}\ddot{\boldsymbol{\theta}} =& \mathbf{D}^T\mathbf{QU} + \mathbf{T}_v + \mathbf{T}_a - \mathbf{D}^T\mathbf{K}_f\mathbf{D}\boldsymbol{\theta} - \mathbf{D}^T\mathbf{B}_f\mathbf{D}\dot{\boldsymbol{\theta}} \\
&+ \frac{1}{2}\mathbf{LS}_\theta\mathbf{A}^T\left(\mathbf{DM}^{-1}\mathbf{D}^T\right)^{-1}\left(\frac{1}{2}\mathbf{AL}\left(\mathbf{C}_\theta\dot{\boldsymbol{\theta}}^2 + \mathbf{S}_\theta\ddot{\boldsymbol{\theta}}\right) - \mathbf{DM}^{-1}\left(\mathbf{F}_{v,x} + \mathbf{F}_{a,x}\right)\right) \\
&- \frac{1}{2}\mathbf{LC}_\theta\mathbf{A}^T\left(\mathbf{DM}^{-1}\mathbf{D}^T\right)^{-1}\left(\frac{1}{2}\mathbf{AL}\left(\mathbf{S}_\theta\dot{\boldsymbol{\theta}}^2 - \mathbf{C}_\theta\ddot{\boldsymbol{\theta}}\right) - \mathbf{DM}^{-1}\left(\mathbf{F}_{v,y} + \mathbf{F}_{a,y}\right)\right).
\end{aligned} \tag{3.32}$$

Therefore, the complete dynamics of the swimming robot is described by the head of the swimming robot dynamics (3.26a) and the link dynamics (3.32). Developing the above expression according to the environment forces described in section 3.1.2 and the robot kinematics studied in section 3.1.1, the model is written as follows:

$$\begin{aligned} &\underbrace{\begin{bmatrix} \mathbf{M}_\theta & -\mathbf{P}_x\mathbf{e} & \mathbf{P}_y\mathbf{e} \\ \mathbf{e}^T\boldsymbol{\sigma}_{x,2} & \mathbf{M}_x + \mathbf{e}^T\boldsymbol{\sigma}_{x,3}\mathbf{e} & -\mathbf{e}^T\boldsymbol{\sigma}_{x,4}\mathbf{e} \\ -\mathbf{e}^T\boldsymbol{\sigma}_{y,2} & -\mathbf{e}^T\boldsymbol{\sigma}_{y,3}\mathbf{e} & \mathbf{M}_y + \mathbf{e}^T\boldsymbol{\sigma}_{y,4}\mathbf{e} \end{bmatrix}}_{\boldsymbol{\Psi}} \begin{bmatrix} \ddot{\boldsymbol{\theta}} \\ \ddot{q}_x \\ \ddot{q}_y \end{bmatrix} = \underbrace{\begin{bmatrix} \omega_\theta\dot{\boldsymbol{\theta}}^2 - \mathbf{V}_\theta\dot{\boldsymbol{\theta}} - \mathbf{D}^T\mathbf{K}_f\mathbf{D}\boldsymbol{\theta} \\ \mathbf{e}^T\boldsymbol{\sigma}_{x,1}\dot{\boldsymbol{\theta}}^2 + \mathbf{e}^T(\boldsymbol{\sigma}_{x,5} - \boldsymbol{\delta}_{x,1})\dot{\boldsymbol{\theta}} \\ \mathbf{e}^T\boldsymbol{\sigma}_{y,1}\dot{\boldsymbol{\theta}}^2 + \mathbf{e}^T(\boldsymbol{\sigma}_{y,5} + \boldsymbol{\delta}_{y,1})\dot{\boldsymbol{\theta}} \end{bmatrix}}_{\boldsymbol{\Omega}(\boldsymbol{\theta},\dot{\boldsymbol{\theta}})} \\ &+ \underbrace{\begin{bmatrix} -\mathbf{P}_x\dot{\mathbf{V}}_{f,x} + \mathbf{P}_y\dot{\mathbf{V}}_{f,y} \\ \mathbf{e}^T\boldsymbol{\sigma}_{x,3}\dot{\mathbf{V}}_{f,x} - \mathbf{e}^T\boldsymbol{\sigma}_{x,4}\dot{\mathbf{V}}_{f,y} \\ \mathbf{e}^T\boldsymbol{\sigma}_{y,4}\dot{\mathbf{V}}_{f,y} - \mathbf{e}^T\boldsymbol{\sigma}_{y,3}\dot{\mathbf{V}}_{f,x} \end{bmatrix}}_{\boldsymbol{\Pi}(\dot{\mathbf{V}}_{f,x},\dot{\mathbf{V}}_{f,y})} + \underbrace{\begin{bmatrix} \mathbf{N}_x(\mathbf{e}\dot{q}_x - \mathbf{V}_{f,x}) + \mathbf{N}_y(\mathbf{e}\dot{q}_y - \mathbf{V}_{f,y}) \\ \mathbf{e}^T(\boldsymbol{\sigma}_{x,6} - \boldsymbol{\delta}_{x,2})(\mathbf{e}\dot{q}_x - \mathbf{V}_{f,x}) + \mathbf{e}^T(\boldsymbol{\delta}_{x,3} - \boldsymbol{\sigma}_{x,7})(\mathbf{e}\dot{q}_y - \mathbf{V}_{f,y}) \\ \mathbf{e}^T(\boldsymbol{\sigma}_{y,6} + \boldsymbol{\delta}_{y,2})(\mathbf{e}\dot{q}_x - \mathbf{V}_{f,x}) + \mathbf{e}^T(\boldsymbol{\sigma}_{y,7} - \boldsymbol{\delta}_{y,3})(\mathbf{e}\dot{q}_y - \mathbf{V}_{f,y}) \end{bmatrix}}_{\mathbf{E}(q_x,q_y,\mathbf{V}_{f,x},\mathbf{V}_{f,y})} + \underbrace{\begin{bmatrix} \mathbf{D}^T\mathbf{Q} \\ 0 \\ 0 \end{bmatrix}}_{\mathbf{B}}\mathbf{U} \end{aligned} \tag{3.33}$$

where the used variables for simplifications are defined in the Appendix A. The model can also be expressed in an abbreviated form for ease of use as:

$$\boldsymbol{\Psi}\begin{bmatrix} \ddot{\boldsymbol{\theta}} \\ \ddot{q}_x \\ \ddot{q}_y \end{bmatrix} = \boldsymbol{\Omega}(\boldsymbol{\theta},\dot{\boldsymbol{\theta}}) + \boldsymbol{\Pi}(\dot{\mathbf{V}}_{f,x},\dot{\mathbf{V}}_{f,y}) + \mathbf{E}(q_x,q_y,\mathbf{V}_{f,x},\mathbf{V}_{f,y}) + \mathbf{BU}. \tag{3.34}$$

However, the complexity of the model makes it unsuitable for analysis and control design purposes. In addition, it is an underactuated system of which $N + 2$ DoF only N_u can be actuated, those corresponding to the angle driven by actuators. The position and the angle of the head of the swimming robot position and angle have to be indirectly controlled. Hence, to simplify the model, two actions are done: first, to separate the model into actuated and nonactuated dynamic equations, and second, to reduce the link behavior to a second-order linear system. Both steps are explained below.

In the case where only the inertial effects due to the motion of the robot are considered, that means the fluid acceleration is neglected, and the model (3.34) can be simplified: Φ becomes only nonzero terms on the diagonal, Π is equal to zero, and Ω does not depend on the acceleration of the link angle.

3.1.4 Decoupling dynamics

The swimming robot model given by (3.34) has a quite complex form for analysis and control design purposes because there is no clear relationship between the inputs and the output of the model. A more straightforward model form where a clear relation between input-output can be analyzed and is more suitable for these purposes. To this objective, a partial feedback linearization method will be applied. This method is widely used for underactuated systems [121, 174], such as industrial articulated robots and mobile robots [123, 124]. However, before applying the method, the model must be divided into two parts representing the actuated and nonactuated DoF.

Analyzing the model (3.34, it represents three clearly differentiated dynamics: 1) the head of the swimming robot accelerations, $\ddot{\mathbf{q}}$, affected by the motion of links, 2) $(N_f - 1)N_u$ flexibility DoF, which depends directly on the material properties and indirectly on the driven link and fluid-body interaction; and 3) the link angular acceleration, $\ddot{\boldsymbol{\theta}}$, which is directly driven by the actuators. Based on these dynamics, the nonactuated part is composed of the first two dynamics, whereas the actuated part is the third one, where the inputs $\mathbf{U}$ directly influence the link dynamics. There are only N_u actuated DoFs, corresponding to actuator inputs, compared with $(N_f - 1) \cdot N_u + 3$ nonactuated DoFs. Both dynamics are strongly related due to the geometrical structure of the system and $\mathbf{B}$ matrix of the model. Hence it is not feasible to separate the model into the nonactuated and actuated parts. Consequently, a transformation or base change is necessary to establish a direct relationship between each input to a single link. This is achieved by considering relative joints instead of the angle links, which are related through the following expression:

$$\begin{bmatrix} \alpha_u \\ \alpha_f \\ \theta_N \end{bmatrix} = \mathbf{\Phi} = \mathbf{T}\boldsymbol{\theta} \tag{3.35}$$

where $\boldsymbol{\alpha}_u = [\alpha_{N_u}, \alpha_{(2 \cdot N_f)}, \ldots, \alpha_{(N_u N_f)})]^T \in \Re^{N_u}$ are the N_u joint angles, $\boldsymbol{\alpha}_f = [\alpha_1, \ldots, \alpha_{(N_u-1)}, \alpha_{(N_u+1)}, \ldots, \alpha_{(2N_u-1)}, \alpha_{(N_f N_u+1)}, \ldots, \alpha_{(N_f N_u-1)}]^T \in \Re^{(N_f-1)N_u}$, are the joint angles corresponding to flexible links, and θ_N is the link angle of the head. Respect to the transformation matrix, $\mathbf{T} \in \Re^{N\times N}$, is defined by

$$\mathbf{T}_{(i,j)} = \begin{cases} -1 & \text{if } i \leq N_u \text{ and } j = iN_f \\ 1 & \text{if } i \leq N_u \text{ and } j = iN_f + 1 \\ -1 & \text{if } i > N_u \text{ and } j = 1 + (i-1-N_u)N_f \\ 1 & \text{if } i > N_u \text{ and } j = 2 + (i-1-N_u)N_f \\ 1 & \text{if } i = N \text{ and } j = N \\ 0 & \text{Otherwise.} \end{cases} \tag{3.36}$$

In addition to applying the base change to the swimming robot model (3.34), if the model (3.34) is also premultiplied by $(\mathbf{T}^{-1})^T$, the input matrix takes the desired form. The first N_u variables (α_u) are influenced directly with each control input and the last variables $(\alpha_f, \theta_N, q_x, q_y)$ are totally independent of the control input, that means

$$\mathbf{\Psi}_{\mathbf{T}} \begin{bmatrix} \ddot{\alpha}_u \\ \ddot{\alpha}_f \\ \ddot{\theta}_N \\ \ddot{q}_x \\ \ddot{q}_y \end{bmatrix} = \mathbf{\Omega}_{\mathbf{T}}(\mathbf{T}^{-1}\mathbf{\Phi}, \mathbf{T}^{-1}\dot{\mathbf{\Phi}}) + \mathbf{\Pi}_{\mathbf{T}}(\dot{\mathbf{V}}_{f,x}, \dot{\mathbf{V}}_{f,y}) + \mathbf{E}_{\mathbf{T}}(q_x, q_y, \mathbf{V}_{f,x}, \mathbf{V}_{f,y}) + \mathbf{B}_{\mathbf{T}}\mathbf{U} \tag{3.37}$$

where the modified matrix are given as:

$$\mathbf{\Psi}_{\mathbf{T}} = \begin{bmatrix} (\mathbf{T}^{-1})^T\mathbf{M}_\theta\mathbf{T}^{-1} & -(\mathbf{T}^{-1})^T\mathbf{P}_x & (\mathbf{T}^{-1})^T\mathbf{P}_y \\ \mathbf{e}^T\sigma_{x,2}\mathbf{T}^{-1} & \mathbf{M}_x + \mathbf{e}^T\sigma_{x,3} & -\mathbf{e}^T\sigma_{x,4}\mathbf{e} \\ -\mathbf{e}^T\sigma_{y,2}\mathbf{T}^{-1} & -\mathbf{e}^T\sigma_{x,3}\mathbf{e} & \mathbf{M}_y + \mathbf{e}^T\sigma_{y,4} \end{bmatrix}, \quad \mathbf{B}_{\mathbf{T}} = \begin{bmatrix} \mathbf{I}_{N_u\times N_u} \\ 0_{(N_f-1)N_u} \\ 0 \\ 0 \\ 0 \end{bmatrix},$$

$$\mathbf{\Omega}_{\mathbf{T}}(\mathbf{T}^{-1}\mathbf{\Phi}, \mathbf{T}^{-1}\dot{\mathbf{\Phi}}) = \begin{bmatrix} (\mathbf{T}^{-1})^T\omega_\theta(\mathbf{T}^{-1}\dot{\mathbf{\Phi}})^2 - (\mathbf{T}^{-1})^T\mathbf{V}_\theta\mathbf{T}^{-1}\dot{\mathbf{\Phi}} - (\mathbf{T}^{-1})^T\mathbf{D}^T\mathbf{K}_f\mathbf{D}\mathbf{\Phi} \\ (\mathbf{T}^{-1})^T\mathbf{e}^T\sigma_{x,1}(T^{-1}\dot{\mathbf{\Phi}})^2 + \mathbf{e}^T(\sigma_{x,5} - \delta_{x,1})\mathbf{T}^{-1}\dot{\mathbf{\Phi}} \\ \mathbf{e}^T\sigma_{y,1}(T^{-1}\dot{\mathbf{\Phi}})^2 + \mathbf{e}^T(\sigma_{y,5} + \delta_{y,1})\mathbf{T}^{-1}\dot{\mathbf{\Phi}} \end{bmatrix},$$

$$\mathbf{\Pi}_{\mathbf{T}}(\dot{\mathbf{V}}_{f,x}, \dot{\mathbf{V}}_{f,y}) = \begin{bmatrix} -(\mathbf{T}^{-1})^T\mathbf{P}_x\dot{\mathbf{V}}_{f,x} + (\mathbf{T}^{-1})^T\mathbf{P}_y\dot{\mathbf{V}}_{f,y} \\ \mathbf{e}^T\sigma_{x,3}\dot{\mathbf{V}}_{f,x} - \mathbf{e}^T\sigma_{x,4}\dot{\mathbf{V}}_{f,y} \\ \mathbf{e}^T\sigma_{y,4}\dot{\mathbf{V}}_{f,y} - \mathbf{e}^T\sigma_{y,3}\dot{\mathbf{V}}_{f,x} \end{bmatrix} \text{ and}$$

$$\mathbf{E}_{\mathbf{T}}(q_x, q_y, \mathbf{V}_{f,x}, \mathbf{V}_{f,y}) = \begin{bmatrix} (\mathbf{T}^{-1})^T\mathbf{N}_x(\mathbf{e}\dot{q}_x - \mathbf{V}_{f,x}) + (\mathbf{T}^{-1})^T\mathbf{N}_y(\mathbf{e}\dot{q}_y - \mathbf{V}_{f,y}) \\ \mathbf{e}^T(\sigma_{x,6} - \delta_{x,2})(\mathbf{e}\dot{q}_x - \mathbf{V}_{f,x}) + \mathbf{e}^T(\delta_{x,3} - \sigma_{x,7})(\mathbf{e}\dot{q}_y - \mathbf{V}_{f,y}) \\ \mathbf{e}^T(\sigma_{y,6} + \delta_{y,2})(\mathbf{e}\dot{q}_x - \mathbf{V}_{f,x}) - \mathbf{e}^T(\sigma_{y,7} - \delta_{y,3})(\mathbf{e}\dot{q}_y - \mathbf{V}_{f,y}) \end{bmatrix}.$$

Note that the result of $(\mathbf{T}^{-1})^T\mathbf{B}$ is the identity matrix and is the key to obtaining the desired mapping input.

Now, the actuated and nonactuated dynamics are represented by independent equations with the new coordinates and the model may be partitioned for simplification purposes. Introducing the state variable $\gamma = [\boldsymbol{\alpha}_f, \theta_N, q_x, q_x]^T$, which arranges the nonactuated DoFs, the partitioned model is

$$\mathbf{\Psi}_{\mathbf{T}}^{\alpha,1}\ddot{\boldsymbol{\alpha}}_u + \mathbf{\Psi}_{\mathbf{T}}^{\gamma,1}\ddot{\boldsymbol{\gamma}} - \mathbf{\Omega}_{\mathbf{T}}^{\alpha} - \mathbf{\Pi}_{\mathbf{T}}^{\alpha} - \mathbf{E}_{\mathbf{T}}^{\alpha} = \mathbf{U} \tag{3.38a}$$

$$\mathbf{\Psi}_{\mathbf{T}}^{\alpha,2}\ddot{\boldsymbol{\alpha}}_u + \mathbf{\Psi}_{\mathbf{T}}^{\gamma,2}\ddot{\boldsymbol{\gamma}} - \mathbf{\Omega}_{\mathbf{T}}^{\gamma} - \mathbf{\Pi}_{\mathbf{T}}^{\gamma} - \mathbf{E}_{\mathbf{T}}^{\gamma} = \mathbf{0}_{(N_f-1)N_u+3} \tag{3.38b}$$

where $\mathbf{\Psi}_{\mathbf{T}}^{\alpha,1} \in \Re^{N_u \times N_u}$, $\mathbf{\Psi}_{\mathbf{T}}^{\gamma,1} \in \Re^{N_u \times ((N_f-1)N_u+3)}$, $\mathbf{\Omega}_{\mathbf{T}}^{\alpha} \in \Re^{N_u}$, $\mathbf{\Pi}_{\mathbf{T}}^{\alpha} \in \Re^{N_u}$, $\mathbf{E}_{\mathbf{T}}^{\alpha} \in \Re^{N_u}$ are the terms of matrix corresponding to the actuated dynamics (3.37), that means the first N_u rows, and $\mathbf{\Psi}_{\mathbf{T}}^{\alpha,2} \in \Re^{((N_f-1)N_u+3) \times N_u}$, $\mathbf{\Psi}_{\mathbf{T}}^{\gamma,2} \in \Re^{((N_f-1)N_u+3) \times ((N_f-1)N_u+3)}$, $\mathbf{\Omega}_{\mathbf{T}}^{\alpha} \in \Re^{((N_f-1)N_u+3)}$, $\mathbf{\Pi}_{\mathbf{T}}^{\alpha} \in \Re^{(N_f-1)N_u+3}$, $\mathbf{E}_{\mathbf{T}}^{\alpha} \in \Re^{(N_f-1)N_u+3}$ are the part belonging to the nonactuated dynamics, in this case the last three rows. Here, it is worth noting that $\mathbf{\Psi}_{\mathbf{T}}(\alpha)$ only depends on the relative joint angles and not on the absolute orientation of the head, θ_N, because the head angle is a cyclic coordinate [123, 175].

Finally, the swimming robot dynamics is expressed through the equations (3.38a) and (3.38b), which capture the links and head of the swimming robot dynamics, respectively, making the latter independent the system inputs.

3.1.5 Partial feedback linearization

Let us consider the partitioned model of the previous section. Now, it will be simplified by applying feedback linearization. The main idea of this technique is to transform the system into a linear one and simplify it, making a state representation change that will allow the cancellation of the nonlinearities of the system. Concretely, an input will be chosen that linearizes the dynamics of the actuated DoF (3.38a) into a second-order linear system. This linearization will make the analysis of the system more convenient. However, it should be remarked that this methodology also involves a significant limitation: it is very sensitive to parameter and modeling uncertainties [174].

Firstly, the unactuated dynamics (3.38b) is solved for γ:

$$\ddot{\boldsymbol{\gamma}} = \left(\boldsymbol{\Psi}_{\mathbf{T}}^{\gamma,2}\right)^{-1}\left(\boldsymbol{\Omega}_{\mathbf{T}}^{\gamma} + \boldsymbol{\Pi}_{\mathbf{T}}^{\gamma} + \mathbf{E}_{\mathbf{T}}^{\gamma} - \boldsymbol{\Psi}_{\mathbf{T}}^{\alpha,2}\ddot{\alpha}\right). \tag{3.39}$$

Secondly, substituting $\ddot{\boldsymbol{\gamma}}$ into in the actuated dynamics (3.38a) gives

$$\left(\boldsymbol{\Psi}_{\mathbf{T}}^{\alpha,1} - \boldsymbol{\Psi}_{\mathbf{T}}^{\gamma,1}\left(\boldsymbol{\Psi}_{\mathbf{T}}^{\gamma,2}\right)^{-1}\boldsymbol{\Psi}_{\mathbf{T}}^{\alpha,2}\right)\ddot{\alpha} + \boldsymbol{\Psi}_{\mathbf{T}}^{\gamma,1}\left(\boldsymbol{\Psi}_{\mathbf{T}}^{\gamma,2}\right)^{-1}\left(\boldsymbol{\Omega}_{\mathbf{T}}^{\gamma} + \boldsymbol{\Pi}_{\mathbf{T}}^{\gamma} + \mathbf{E}_{\mathbf{T}}^{\gamma}\right) - \boldsymbol{\Omega}_{\mathbf{T}}^{\alpha} - \boldsymbol{\Pi}_{\mathbf{T}}^{\alpha} - \mathbf{E}_{\mathbf{T}}^{\alpha} = \mathbf{U} \tag{3.40}$$

Observing the above expression of the link dynamics, the following law control is defined:

$$\mathbf{U} = \left(\boldsymbol{\Psi}_{\mathbf{T}}^{\alpha,1} - \boldsymbol{\Psi}_{\mathbf{T}}^{\gamma,1}\left(\boldsymbol{\Psi}_{\mathbf{T}}^{\gamma,2}\right)^{-1}\boldsymbol{\Psi}_{\mathbf{T}}^{\alpha,2}\right)\boldsymbol{\nu} + \boldsymbol{\Psi}_{\mathbf{T}}^{\gamma,1}\left(\boldsymbol{\Psi}_{\mathbf{T}}^{\gamma,2}\right)^{-1}\left(\boldsymbol{\Omega}_{\mathbf{T}}^{\gamma} + \boldsymbol{\Pi}_{\mathbf{T}}^{\gamma} + \mathbf{E}_{\mathbf{T}}^{\gamma}\right) - \boldsymbol{\Omega}_{\mathbf{T}}^{\alpha} - \boldsymbol{\Pi}_{\mathbf{T}}^{\alpha} - \mathbf{E}_{\mathbf{T}}^{\alpha} \tag{3.41}$$

where $\boldsymbol{\nu} = [\nu_1, \dots, \nu_{N_u}]^T \in \Re^{N_u}$ is the new control input, which enables to define the swimming robot model dynamics (3.38) as:

$$\begin{aligned} \ddot{\alpha} &= \boldsymbol{\nu}, \\ \ddot{\boldsymbol{\gamma}} &= \mathcal{J}(\boldsymbol{\gamma}, \dot{\boldsymbol{\gamma}}, \alpha, \dot{\alpha}) + \mathcal{E}(\boldsymbol{\gamma}, \alpha)\boldsymbol{\nu} \end{aligned} \tag{3.42}$$

where

$$\begin{aligned} \mathcal{J}(\boldsymbol{\gamma}, \dot{\boldsymbol{\gamma}}, \alpha, \dot{\alpha}) &= \left(\boldsymbol{\Psi}_{\mathbf{T}}^{\gamma,2}\right)^{-1}\left(\boldsymbol{\Omega}_{\mathbf{T}}^{\gamma} + \boldsymbol{\Pi}_{\mathbf{T}}^{\gamma} + \mathbf{E}_{\mathbf{T}}^{\gamma}\right) \in \Re^{(N_f-1)N_u+3}, \\ \mathcal{E}(\boldsymbol{\gamma}, \alpha) &= -\left(\boldsymbol{\Psi}_{\mathbf{T}}^{\gamma,2}\right)^{-1}\boldsymbol{\Psi}_{\mathbf{T}}^{\alpha,2} \in \Re^{(N_f-1)N_u+3\times N_u} \end{aligned} \tag{3.43}$$

Finally, introducing the state variable $\mathbf{x} = [\boldsymbol{\alpha}_u^T, \boldsymbol{\gamma}^T, \dot{\boldsymbol{\alpha}}_u^T, \dot{\boldsymbol{\gamma}}^T]^T \in \Re^{2N+4}$, the swimming robot model may be rewritten in a control-affine system structure as:

$$\dot{\mathbf{x}} = \begin{bmatrix} \dot{\alpha}_u \\ \dot{\gamma} \\ \ddot{\alpha}_u \\ \ddot{\gamma} \end{bmatrix} = \begin{bmatrix} \dot{\alpha}_u \\ \dot{\boldsymbol{\gamma}} \\ \boldsymbol{\nu} \\ \mathcal{J}(\boldsymbol{\gamma}, \dot{\boldsymbol{\gamma}}, \alpha_u, \dot{\alpha}_u) + \mathcal{E}(\alpha, \boldsymbol{\gamma})\boldsymbol{\nu} \end{bmatrix} = f(\boldsymbol{\gamma}, \dot{\boldsymbol{\gamma}}, \alpha_u, \dot{\alpha}_u) + \sum_{i=1}^{N-1} g_i(\alpha_u, \boldsymbol{\gamma})\nu_i \tag{3.44}$$

where

$$f(\boldsymbol{\gamma}, \dot{\boldsymbol{\gamma}}, \boldsymbol{\alpha}_u, \dot{\boldsymbol{\alpha}}_u) = \begin{bmatrix} \dot{\boldsymbol{\alpha}}_u \\ \dot{\boldsymbol{\gamma}} \\ \mathbf{0}_{(N-1\times1)} \\ \mathcal{J}(\boldsymbol{\gamma}, \dot{\boldsymbol{\gamma}}, \boldsymbol{\alpha}_u, \dot{\boldsymbol{\alpha}}_u) \end{bmatrix}, \quad g_i(\boldsymbol{\alpha}_u, \boldsymbol{\gamma}) = \begin{bmatrix} \mathbf{0}_{(N-1\times1)} \\ \mathbf{0}_{(3\times1)} \\ \mathbf{e}_i \\ \mathcal{E}_i(\boldsymbol{\alpha}_u, \boldsymbol{\gamma}) \end{bmatrix}, \tag{3.45}$$

with $i \in [1, \ldots, N_u]$, $\mathbf{e}_i$ is the unit vector of the ith column of the identity matrix I_{N_u}, and $\mathcal{E}_i(\boldsymbol{\alpha}, \boldsymbol{\gamma})$ denotes the ith column of $\mathcal{E}(\boldsymbol{\alpha}, \boldsymbol{\gamma})$.

In summary, the swimming model described in (3.34) has been transformed into a simpler form (3.44) and canceling the nonlinearities of the dynamics of the links by doing a partial feedback linearization through the input transformation. As will be seen in the following sections, this new description of the system will facilitate its study and analysis.

3.2 Modeling for low *Re* environment

In the previous section, the swimming robot dynamics was analyzed under the assumption that a strictly low *Re* environment cannot be guaranteed and, therefore, it cannot be assured that inertial effects do not influence the dynamics. However, if the above assumptions are met, the model changes drastically from underdamped to overdamped dynamics, a behavior that characterizes the system without inertia.

In this case, the second Newton's law must be equal to zero because the forces resulting from inertial contribution are neglected. Only the resistive and joint constraint forces are considered since they are the only ones that do not depend on acceleration. Therefore, the force balance for each link (3.25a) results in

$$0 = \mathbf{F}_{v,x} + \mathbf{D}^T \mathbf{H}_x \tag{3.46a}$$

$$0 = \mathbf{F}_{v,y} + \mathbf{D}^T \mathbf{H}_y \tag{3.46b}$$

Similarly, dynamics of the swimming robot head (3.26a) is deducted for a strictly low *Re* and expressed as:

$$0 = f_{v,x,N} + h_{x,N} = \mathbf{e}^T \mathbf{F}_{v,x} \tag{3.47a}$$

$$0 = f_{v,y,N} + h_{y,N} = \mathbf{e}^T \mathbf{F}_{v,y} \tag{3.47b}$$

With the torque equation of balances (3.27) is reduced to

$$0 = \mathbf{D}^T \mathbf{Q} \mathbf{U} + \mathbf{T}_v - \mathbf{D}^T \mathbf{K}_f \mathbf{D} \boldsymbol{\theta} - \mathbf{D}^T \mathbf{B}_f \mathbf{D} \dot{\boldsymbol{\theta}} + \frac{1}{2} \mathbf{L} \mathbf{S}_\theta \mathbf{A}^T \mathbf{H}_x - \frac{1}{2} \mathbf{L} \mathbf{C}_\theta \mathbf{A}^T \mathbf{H}_y. \tag{3.48}$$

Now, the joint constraint forces (3.30a) are only functions of the viscous forces as a result of link motions since the inertial effects vanished from (3.46a), obtaining:

$$\mathbf{H}_x = -\left(\mathbf{D}\mathbf{D}^T\right)^{-1}\mathbf{D}\mathbf{F}_{v,x}, \tag{3.49a}$$

$$\mathbf{H}_y = -\left(\mathbf{D}\mathbf{D}^T\right)^{-1}\mathbf{D}\mathbf{F}_{v,y}. \tag{3.49b}$$

Inserting the constraint forces into the torque balance equation, the link dynamics is described in a strictly low *Re* as

$$\begin{aligned}\Big(-T_v + \mathbf{D}^T\mathbf{B}_f\mathbf{D} - \frac{1}{2}\mathbf{L}\mathbf{S}_\theta\mathbf{K}^\star\boldsymbol{\delta}_{x,1} - \frac{1}{2}\mathbf{L}\mathbf{C}_\theta\mathbf{K}^\star\boldsymbol{\delta}_{y,1}\Big)\dot{\boldsymbol{\theta}} = \mathbf{D}^T\mathbf{Q}\mathbf{U} - \mathbf{D}^T\mathbf{K}_f\mathbf{D}\boldsymbol{\theta}& \\ + \Big(\frac{1}{2}\mathbf{L}\mathbf{S}_\theta\mathbf{K}^\star\boldsymbol{\delta}_{x,2}\frac{1}{2}\mathbf{L}\mathbf{C}_\theta\mathbf{K}^\star\boldsymbol{\delta}_{y,2}\Big)(\mathbf{e}\dot{q}_x - \mathbf{V}_{f,x})& \\ - \Big(\frac{1}{2}\mathbf{L}\mathbf{S}_\theta\mathbf{K}^\star\boldsymbol{\delta}_{x,3}\frac{1}{2}\mathbf{L}\mathbf{C}_\theta\mathbf{K}^\star\boldsymbol{\delta}_{y,3}\Big)(\mathbf{e}\dot{q}_y - \mathbf{V}_{f,y}),&\end{aligned} \tag{3.50}$$

where $\mathbf{K}^\star$, among other variables, are defined in the Appendix A. Finally, the complete dynamics of the swimming robot (3.33) is redefined as

$$\underbrace{\begin{bmatrix} \mathbf{V}^\star{}_\theta & -\mathbf{N}^\star{}_x\mathbf{e} & \mathbf{N}^\star{}_y\mathbf{e} \\ \mathbf{e}^T\boldsymbol{\delta}_{x,1} & \mathbf{e}^T\boldsymbol{\delta}_{x,2}\mathbf{e} & -\mathbf{e}^T\boldsymbol{\delta}_{x,3}\mathbf{e} \\ -\mathbf{e}^T\boldsymbol{\delta}_{y,1} & -\mathbf{e}^T\boldsymbol{\delta}_{y,2}\mathbf{e} & -\mathbf{e}^T\boldsymbol{\delta}_{y,3}\mathbf{e} \end{bmatrix}}_{\boldsymbol{\Psi}^\star}\begin{bmatrix}\dot{\boldsymbol{\theta}} \\ \dot{q}_x \\ \dot{q}_y\end{bmatrix} = \underbrace{\begin{bmatrix}-\mathbf{D}^T\mathbf{K}_f\mathbf{D}\boldsymbol{\theta} \\ 0 \\ 0\end{bmatrix}}_{\boldsymbol{\Omega}^\star(\boldsymbol{\theta},\dot{\boldsymbol{\theta}})} + \underbrace{\begin{bmatrix}-\mathbf{N}^\star{}_x\mathbf{V}_{f,x} + \mathbf{N}^\star{}_y\mathbf{V}_{f,y} \\ \mathbf{e}^T\boldsymbol{\delta}_{x,2}\mathbf{V}_{f,x} - \mathbf{e}^T\boldsymbol{\delta}_{x,3}\mathbf{V}_{f,y} \\ -\mathbf{e}^T\boldsymbol{\delta}_{y,2}\mathbf{V}_{f,x} + \mathbf{e}^T\boldsymbol{\delta}_{y,3}\mathbf{V}_{f,y}\end{bmatrix}}_{\mathbf{E}^\star(q_x,q_y,\mathbf{V}_{f,x},\mathbf{V}_{f,y})} + \underbrace{\begin{bmatrix}\mathbf{D}^T\mathbf{Q} \\ 0 \\ 0\end{bmatrix}}_{\mathbf{B}}\mathbf{U}. \tag{3.51}$$

The model confirms that the swimming robot dynamics, and hence the propulsion, at a strictly low *Re* level, is only established by the viscous forces resulting from the movements of the links, focusing on the crucial role played by the waveform in the motion of the swimming robot.

3.2.1 Decoupling dynamics

Despite the swimming robot model for low *Re* described in (3.51) being simpler, it is still rather complex for study, analysis and design control purposes. Therefore, the same procedure used in sections 3.1.4 and 3.1.5 is applied to this model next.

Applying the change of variable defined in (3.35), the partitioned model is

$$\begin{aligned} \boldsymbol{\Psi}^{\star\alpha,1}_{\mathbf{T}}\ddot{\boldsymbol{\alpha}} + \boldsymbol{\Psi}^{\star\gamma,1}_{\mathbf{T}}\ddot{\boldsymbol{\gamma}} - \boldsymbol{\Omega}^{\star\alpha}_{\mathbf{T}} - \mathbf{E}^{\star\alpha}_{\mathbf{T}} &= \mathbf{U} && \text{(3.52a)} \\ \boldsymbol{\Psi}^{\star\alpha,2}_{\mathbf{T}}\ddot{\boldsymbol{\alpha}}_u + \boldsymbol{\Psi}^{\star\gamma,2}_{\mathbf{T}}\ddot{\boldsymbol{\gamma}} - \boldsymbol{\Omega}^{\star\gamma}_{\mathbf{T}} - \mathbf{E}^{\star\gamma}_{\mathbf{T}} &= \mathbf{0}_{(N_f-1)N_u+3\times 1}\,. && \text{(3.52b)} \end{aligned}$$

3.2.2 Partial feedback linearization

Now, as in the case of medium *Re*, the partitioned model is considered to be simplified. The design control input to apply a feedback linearization is:

$$\mathbf{U} = \left(\boldsymbol{\Psi}^{\star\alpha,1}_{\mathbf{T}} - \boldsymbol{\Psi}^{\star\gamma,1}_{\mathbf{T}}\left(\hat{\boldsymbol{\Psi}}^{\gamma,2}_{\mathbf{T}}\right)^{-1}\boldsymbol{\Psi}^{\star\alpha,2}_{\mathbf{T}}\right)\hat{\boldsymbol{\nu}} + \boldsymbol{\Psi}^{\star\gamma,1}_{\mathbf{T}}\left(\hat{\boldsymbol{\Psi}}^{\gamma,2}_{\mathbf{T}}\right)^{-1}\left(\boldsymbol{\Omega}^{\star\gamma}_{\mathbf{T}} + \mathbf{E}^{\star\gamma}_{\mathbf{T}}\right) - \boldsymbol{\Omega}^{\star\alpha}_{\mathbf{T}} - \mathbf{E}^{\star\alpha}_{\mathbf{T}} \tag{3.53}$$

where $\boldsymbol{\nu}^\star$ is the new input control that enables to define the swimming model dynamics (3.52) as

$$\begin{aligned} \dot{\boldsymbol{\alpha}}_u &= \boldsymbol{\nu}^\star, \\ \ddot{\boldsymbol{\gamma}} &= \mathcal{J}^\star(\boldsymbol{\gamma}, \dot{\boldsymbol{\gamma}}, \boldsymbol{\alpha}, \dot{\boldsymbol{\alpha}}) + \mathcal{E}^\star(\boldsymbol{\gamma}, \boldsymbol{\alpha})\boldsymbol{\nu}^\star \end{aligned} \tag{3.54}$$

with

$$\begin{aligned} \mathcal{J}^\star(\boldsymbol{\gamma}, \dot{\boldsymbol{\gamma}}, \boldsymbol{\alpha}_u, \dot{\boldsymbol{\alpha}}_u) &= \left(\boldsymbol{\Psi}^{\star\gamma,2}_{\mathbf{T}}\right)^{-1}\left(\boldsymbol{\Omega}^{\star\gamma}_{\mathbf{T}} + \mathbf{E}^{\star\gamma}_{\mathbf{T}}\right) \in \mathfrak{R}^{(N_f-1)N_u+3}, && \text{(3.55a)} \\ \mathcal{E}^\star(\boldsymbol{\gamma}, \boldsymbol{\alpha}_u) &= -\left(\boldsymbol{\Psi}^{\star\gamma,2}_{\mathbf{T}}\right)^{-1}\boldsymbol{\Psi}^{\star\alpha,2}_{\mathbf{T}} \in \mathfrak{R}^{(N_f-1)N_u+3\times N_u} && \text{(3.55b)} \end{aligned}$$

Finally, introducing the state variable $\mathbf{x}^\star = [\boldsymbol{\alpha}_u^T, \boldsymbol{\gamma}^T]^T \in \mathfrak{R}^{N+2}$ the swimming robot model ca be rewritten in a control-affine system structure as

$$\dot{\mathbf{x}^\star} = \begin{bmatrix} \dot{\boldsymbol{\alpha}}_u \\ \dot{\boldsymbol{\gamma}} \end{bmatrix} = \begin{bmatrix} \boldsymbol{\nu} \\ \mathcal{J}^\star(\boldsymbol{\gamma}, \dot{\boldsymbol{\gamma}}, \boldsymbol{\alpha}_u, \dot{\boldsymbol{\alpha}}_u) + \mathcal{E}^\star(\boldsymbol{\alpha}_u, \boldsymbol{\gamma})\boldsymbol{\nu} \end{bmatrix} = f^\star(\boldsymbol{\gamma}, \dot{\boldsymbol{\gamma}}, \boldsymbol{\alpha}_u, \dot{\boldsymbol{\alpha}}_u) + \sum_{i=1}^{N-1} g^\star{}_i(\boldsymbol{\alpha}_u, \boldsymbol{\gamma})\nu_i \tag{3.56}$$

where

$$f^\star(\boldsymbol{\gamma}, \dot{\boldsymbol{\gamma}}, \boldsymbol{\alpha}_u, \dot{\boldsymbol{\alpha}}_u) = \begin{bmatrix} \mathbf{0}_{(N-1\times 1)} \\ \mathcal{J}^\star(\gamma, \dot{\gamma}, \alpha_u, \dot{\alpha}_u) \end{bmatrix}, \quad g^\star{}_i(\boldsymbol{\alpha}_u, \boldsymbol{\gamma}) = \begin{bmatrix} \mathbf{e}_i \\ \mathcal{E}^\star{}_i(\boldsymbol{\alpha}_u, \boldsymbol{\gamma}) \end{bmatrix}. \tag{3.57}$$

3.3 Fractional waveform for propulsion and locomotion

The section 2.4.2.3 has described the classical waveforms used for the propulsion of flagellum-type articulated robots. These require defining a set of coefficients to define their geometry, which are intimately linked to the propulsion velocity, as will be seen in later chapters. A new alternative beating waveform is the fractional beating waveform, which is based on a fractional-order power law for amplitude modulation as follows

$$y_w(x,t) = c_{w,t}x + (c_{w,3}x^{\alpha_w})\sin\left(\frac{2\pi}{\lambda}(x - V_p t)\right), \tag{3.58}$$

where $c_{w,3}$ defines the amplitude at the end of the tail, and $\alpha_w \in \mathbb{R}^+$ $(0 < \alpha < 1)$ is the fractional order coefficient of the wave, whose value determines the form of growth. This one retains the motion properties obtained with the classical traveling waveforms but presents some advantages in terms of propulsion. In particular, when $\alpha_w = 0$, the resulting waveform is harmonic, whereas when $\alpha_w = 1$, it results in the Carangiform waveform. The way of swimming with this waveform can also be viewed as a generalization of those given by previous waves, merging the features from harmonic to Carangiform waveforms.

Figure 3.4 shows the waveform obtained for different parameter values α_w. It can be seen that the waveform is similar to a traveling harmonic wave for values

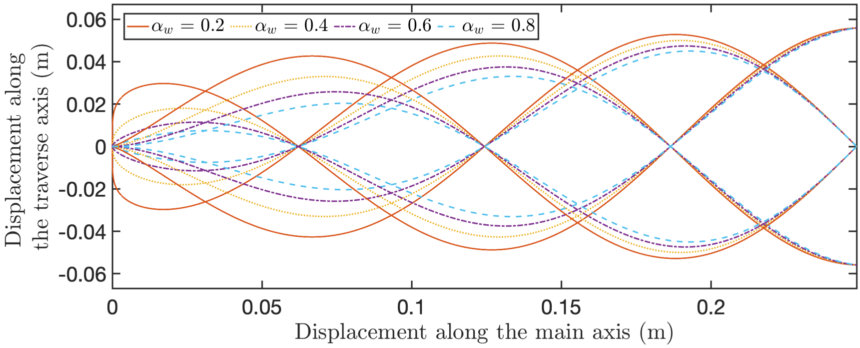

Figure 3.4: Appearance of the fractional growth waveform for different values of α_w and with $c_{w,3} = 0$.

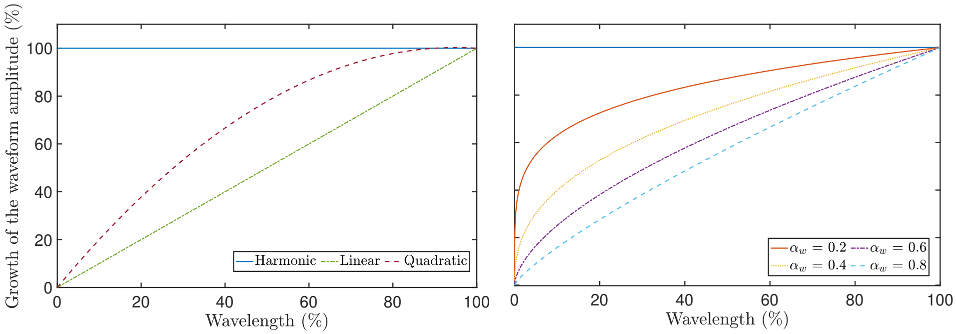

Figure 3.5: Comparison of amplitude growth for the different beating waveforms.

of α_w close to zero. However, for values close to one, the obtained waveform is closer to Carangiform swimming, whereas values between zero and one merge the characteristics of both waves. Therefore, the wave growth can be equal to or faster than the classical waveforms, as illustrated in Figure 3.5. Furthermore, considering that the maximum amplitude of the waveform is achieved in one wavelength, at the point corresponding to the 20% of the wavelength, the wave given by (3.58) reaches the 72% of the maximum desired amplitude for $\alpha_w = 0.2$, whereas with the waveform given by (2.9) only a percentage of 20% and 37% is reached for linear and quadratic Carangiform waveforms, respectively. Likewise, the lower the value of α_w, the higher the percentage of amplitude growth achieved at the considered point. Notice that the growth of the waveform amplitude is always of 100% for the harmonic case.

3.4 Summary

This chapter has presented a mathematical model of a planar swimming robot model with N_u flexible links plus the head and driven by $N_u - 1$ actuated joints suitable for medium Re environment. Likewise, the model is particularized for a strictly low Re environment, where inertial forces are negligible and brownian effects are not yet present. For better handling and analysis of the model for design control purposes, the models are partially feedback linearized to a simpler form after making a variable change that allows handling the actuated and nonactuated dynamics separately. Moreover, modeling the dynamics of an articulated swimming robot has highlighted the importance of flagellum or tail motion, which is a crucial factor in improving mechanical design, locomotion and performance. For this purpose, a novel beating waveform is presented. It is based on a fractional order power law for amplitude modulation, which makes it possible to preserve the motion properties obtained by applying classical traveling waveforms and controlling the stroke and propulsion with a single parameter.

4

LOCOMOTION ANALYSIS AND CONTROL

"You have to make the rules, not follow them."

Isaac Newton

Contents

The motivation to understand and reproduce the movement of biological swimmers and reptiles, such as eukaryotic cells and snakes, respectively, has given rise to numerous works and research focused on the mathematical description of their behavior. However, the primary studies are based on empirical studies and simulations of fishes [176, 177, 178] and snakes [123, 179, 180, 181] at the macroscale. At the micro-scale, on the other hand, the studies are reduced to a mathematical description and analysis of the forces resulting from swimmer motion and interaction with the environments, always from a mathematical or biological point of view [111, 113, 182, 183]. Likewise, technological development and miniaturization in recent years have increased the interest in this type of swimmer and the possibility of reproducing how they can move. Even so, understanding this type of motion still needs to be fully covered. There are still many gaps in the design of bioinspired artificial swimming robots reproducing the functionalities of biological systems. In this scenario, this chapter aims to contribute to the understanding of the motions and design of bioinspired swimming robots from an engineering and robotics point of view and how existing control techniques can be adapted for the swimming robot navigation, namely path following.

4.1 Propulsion

Turning the attention to the beating waveform presented in the section 2.4.2.3, this section discusses what effect the beating waveform has on propulsion and locomotion and how the type of motion influences these. For this purpose, the motion will be considered to occur in an environment with a low *Re* enough to entirely neglect the forces arising from the inertial effects. Likewise, this is a common assumption for slowly moving underwater vehicles [184] and bioinspired robots [123, 124].

The propulsion of swimming robots is defined to be along the $\mathbf{e}_x$ direction. Therefore, the force propelling the robot's head can be expressed as the sum of all forces actuating on it. Recalling the force balances at the head of the swimming robot described in equation (3.46a), the propulsive force is expressed as a function of the viscous forces acting along the tail, which are directly proportional to the motion velocity according to the definition of the RFT give by (3.13). Then, the propulsive force density is

$$df_{p,x}(s) = \Big(\big(c^{\perp}_{v,s} - c^{||}_{v,s}\big)\dot{q}_{y,s} \sin\theta\cos\theta - \dot{q}_x\big(c^{\perp}_{v,s}\sin^2\theta + c^{||}_{v,s}\cos^2\theta\big) \Big)\, ds, \tag{4.1}$$

where $\dot{q}_{y,s}$ is the velocity displacement of the considered infinitesimal element in the $\mathbf{e}_\mathrm{x}$ direction and $\dot{x}_n$ is the propulsion velocity in such a $\mathbf{e}_\mathrm{x}$ direction, which also corresponds to the head velocity. Then, the total propulsive force exerted by the flagellum over one wavelength, λ, propelling the head forward is

$$F_{p,x} = \int_0^{\lambda} \big(c^{\perp}_{v,s} - c^{||}_{v,s}\big)\dot{q}_{y,s} \sin\theta\cos\theta - \dot{q}_x\big(c^{\perp}_{v,s}\sin^2\theta + c^{||}_{v,s}\cos^2\theta\big)\, ds \tag{4.2}$$

From expression (4.2) is deducted that the propulsive force consists of two clear terms: the first one is proportional to the velocity of the infinitesimal element, or of the links, if it were discretized, in the $\mathbf{e}_\mathrm{y}$ direction, normal to the direction of motion, and the second term is a function of the velocity in the $\mathbf{e}_\mathrm{x}$ direction, coincident with the direction of motion. Moreover, taking the common factor $\cos^2\theta$ from (4.2), the propulsive force can be written in a more readable form as:

$$F_{p,x} = \int_0^{\lambda} \Big(\big(c^{\perp}_{v,s} - c^{||}_{v,s}\big)\, \dot{q}_{y,s} \tan\theta \, - \big(c^{\perp}_{v,s}\tan^2\theta + c^{||}_{v,s}\big)\, \dot{q}_x \Big) \frac{1}{1+\tan^2\theta} ds. \tag{4.3}$$

In this form, the contribution of each term to propulsive force can be observed easier. Focusing on the second term, it never contributes to the forward propulsion of the swimming robot but rather opposes it because the waveform is assumed to involve motion in the $\mathbf{e}_normalx$ direction and the viscous drag coefficients are always positive, by definition. Then, if the swimming robot moves with a positive velocity, the term is always positive and then its contribution is negative to the propulsion. However, this is an expected behavior since the swimmer's motion is naturally subjected to a force opposite to the motion direction due to viscous drag. Therefore, any propulsive force in the $\mathbf{e}_\mathrm{x}$ direction must be produced by the transversal motion of the flagellum. Analyzing the first term of (4.3), several assumptions must be met to achieve a positive thrust force and, consequently, a net horizontal displacement:

- The friction must be anisotropic and $c^{\perp}_{v,s} > c^{||}_{v,s}$, a property that also appears to be inherent in the smooth and slender bodies observed in nature [109, 111, 122, 123, 169, 170]. In the case of isotropic friction, the normal and transversal contribution of sideways motions cancel one another, not contributing to propulsion. It is worth mentioning that isotropic friction also implies an uncontrollable system because any input cannot generate a motion that moves the system from one state to another.

- Transverse movements of the flagellum contribute to maintaining propulsion, while the sign of sign(θ) and sign($\dot{q}_{y,s}$) does not change.

- The transverse velocity must be greater than the normal velocity, satisfying the relation $\dot{q}_{y,s} > \dot{q}_x \tan\theta$.

- The waveforms must be time-varying to produce a continuous contribution to propulsive propulsion.

In compliance with the above considerations, the propulsion forces described in (4.3) establish that anisotropic friction forces map transversal velocity of flagellum into force components in the direction of motion, achieving the maximum thrust of each infinitesimal element or link when the tilted angle reaches the $\pm\pi/2$ rad.

Knowing that the resulting thrust during an entire period must cancel the drag force of the head, the following expression can calculate the forward speed reached by the swimmer:

$$n_w \; F_{p,x} = c^{\|}_{v,n} \; \dot{q}x, \tag{4.4}$$

where $c^{\|}_{v,n}$ is the viscous drag coefficient of the head and n_w is the number of simultaneous waves along the flagellum. Substituting the propulsive force (4.3) into the head drag force per wave cycle (4.4), the swimming robot velocity per wave cycle is obtained. Two approaches can be used to solve this relation according to the ratio between the transverse amplitude and the flagellum length. The first approach uses small deformations if the amplitude displacement is relatively small and the flagellum length is comparable to the wavelength. The second approach uses large deformations when both conditions cannot be fulfilled. Both cases are detailed below, considering that the swimming robot moves only forward, i.e., $c_{w,t} = 0$.

Small deformations

In the case of small oscillations, the transverse velocity is interpreted as the derivative of the waveform with respect to time, $\frac{d}{dt}y_w$, and the tangent of the angle as the derivative with respect to space, $\frac{d}{dx}y_w$. Then, the force (4.3) is written as

$$F_{p,x} = \int_0^\lambda \left(\left(c_{v,s}^\perp - c_{v,s}^\parallel \right) \frac{d}{dt}y_w \frac{d}{dx}y_w - c_{v,n,s}^\parallel \dot{q}_x \right) ds. \tag{4.5}$$

In addition, it can be assumed that the infinitesimal element of length can approximate that of surface, $ds \approx dx$, and the infinitesimal terms of second order are neglected, without making a large error [111, 185, 186]. Hence, arranging (4.3) and (4.4) the forward swimming robot velocity per wave cycle is

$$\dot{q}_x = \left(\frac{c_v^\perp - c_v^\parallel}{c_v^\parallel} \right) \left(\lambda + \frac{c_{v,n}^\parallel}{n_w \, c_v^\parallel} \right)^{-1} \int_0^\lambda \frac{d}{dt}y_w \, \frac{d}{dx}y_w \, dx. \tag{4.6}$$

From the above expression, it follows that the velocity is, regardless of the beating waveform, proportional to the relative ratio of normal to tangential viscous resistance. Moreover, it is inversely proportional to wavelength and head drag, although the latter's influence is less dependent on the number of simultaneous waves along the flagellum. In other words, velocity increases as the wavelength decreases and the number of simultaneous waves increases. It is worth remarking that the swimmer head's design also has a key role in the velocity [55]. Regarding the integral term, it indicates that beating waveform must not only be time-varying but also must be space-varying.

Big deformations

However, if the deformations cannot be considered small enough, the infinitesimal element of surface is replaced by $ds = \sqrt{1 + y_w'^2}\; dx$. For this assumption, the swimming robot velocity per wave is

$$\dot{q}_x = (c_v^\perp - c_v^\parallel) \frac{\int_0^\lambda \frac{d}{dt}y_w \; \frac{d}{dx}y_w \left(1 + \left(\frac{d}{dx}y_w\right)^2\right)^{-1/2} dx}{\frac{c_{v,n}^\parallel}{n_w} + \int_0^\lambda \Big(c_v^\parallel + c_v^\perp\Big(\frac{d}{dx}y_w\Big)^2\Big)\Big(\Big(1 + \Big(\frac{d}{dx}y_w\Big)^2\Big)^{-1/2} dx}. \tag{4.7}$$

In this case, the space-varying behavior becomes of even greater importance.

4.1.1 Classical beating waveform

Applying the above analysis to the classical beating waveforms, described in the section 2.4.2.3, a direct expression that relates the geometrical parameters of the planar wave motion with the forward velocity of the swimming robot can be obtained. In particular, solving the velocity (4.6) for classical beating waveforms (2.9) in the case of small deformations, the theoretical forward velocity has the following form:

$$\begin{aligned}\dot{q}_x = V_p \left(\frac{c_v^{\perp} - c_v^{\parallel}}{c_v^{\parallel}}\right)\left(\lambda + \frac{c_{v,n}^{\parallel}}{n_w\, c_v^{\parallel}}\right)^{-1} &\left(\left(\frac{1}{\lambda}c_0c_1 + c_0c_2 + \lambda c_1c_2 + \frac{1}{2}c_1^2 + \frac{\lambda^2}{2}c_2^2\right)\pi \sin(4\pi f t)\right.\\ &\left.-2\pi^2\left(c_0c_1 + \frac{1}{3}c_0c_2 + \frac{\lambda}{2}c_1c_2 + \frac{1}{\lambda^2}c_0^2 + \frac{\lambda}{2}c_1^2 + \frac{\lambda^2}{5}c_2^2\right)\right).\end{aligned} \tag{4.8}$$

From the above result, there exists a strong dependency between the geometrical parameters of the waveform and the forward velocity. Concretely, the velocity is proportional to the wave's squared amplitude and propagation velocity. In addition, the velocity has a harmonic component associated with the linear and quadratic Carangiform motion, producing an oscillating speed.

4.1.2 Fractional beating waveform

The same principles applied to classical waveforms can be extended to the fractional order growth waveform to determine the forward thrust and velocity according to the shape of the beating motion. However, the integration of (4.6) with (3.58) presents analytical difficulties involving to use of numerical integration to calculate the corresponding forward velocity. Thus, a numerical integration algorithm is required for this purpose, as explained next.

The numerical integration algorithm is based on the adaptive Gauss-Kronrod quadrature, which approximates the definite integral of a function as a weighted sum of function values at optimum and specific points (referred to as "Kronrod points") within the integration interval [187]. It establishes that differential equations can be handled as parametric functions and applies an iterative integration process over time and space sequentially. This allows obtaining the solution of expression (4.7) with no simplifications.

It should be mentioned that this method was developed and implemented in MATLAB®. In order to validate the numerical integration algorithm, it was first applied to classical waveforms so that numerical results could be compared with the analytical ones. For that purpose, the normalized root mean square error (NRSME) was considered as a performance index. The value of NRSME obtained for the three waveforms was of the order of 10^{-16}, a result that can be neglected. Consequently, the algorithm was validated to obtain forward propulsion thrust and velocity corresponding to the proposed fractional waveform.

Figure 4.1 shows the forward velocity for the waveform given by (3.58) obtained when applying the numerical integration algorithm for solving (4.7) for different values of parameter α_w. The velocities corresponding to the three classical beating waveforms are plotted for comparison purposes. As can be observed, the maximum velocity during swimming is reached with the harmonic wave, whereas the lowest corresponds to the linear Carangiform. These results endorse the strong relationship that exists between forward velocity and the growth profile of the amplitude. With respect to the waveform with fractional growth, changes in the value of α_w allow achieving any velocity within the range established by the harmonic waveform and the linear Carangiform, evincing a direct relation between the forward velocity, propulsion, and parameter α_w.

The forward velocities in Figure 4.1 were obtained for the parameters given in Table 4.1. It is important to emphasize that, to achieve comparable results, the following criterion was established. Taking into account that the wave reaches

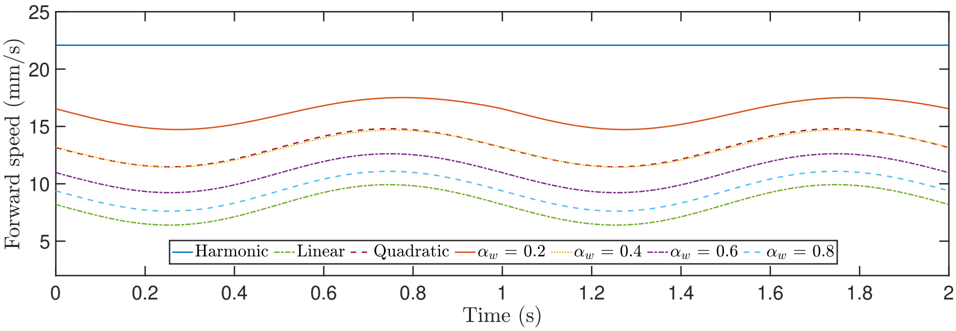

Figure 4.1: Comparison of forward velocity for different waveforms.

Table 4.1: Waveform and environment parameters.

Parameter	Value	Description	Unit	Parameter	Value	Description	Unit
$c_{w,0}$	94	Amplitude of the harmonic wave	mm	f	0.5	Frequency	Hz
r_f	12.5	Radius of the flagellum	mm	λ	600	Wavelength	mm
r_n	12.5	Radius of the head	mm	n_w	1	Simultaneous waves	
ρ	964	Density of the environment	kg/m^3	μ	0.1	Viscosity of the environment	Pa · s
n_q	0.9	Modulation coefficient of Quadratic Carangiform		m_q	1	Modulation coefficient of Quadratic Carangiform	
$c_{v,n}^{\parallel}$	$6\pi\mu r_7$	Head normal viscous drag coefficient					

the maximum desired amplitude at the end of the flagellum, for a given value of parameter $c_{w,0}$ for the harmonic wave and the length of the flagellum (value of $n_w\lambda$), the coefficients of the remainder waveforms were calculated as a function of the parameters mentioned above as follows:

- Linear Carangiform waveform:

$$c_{w,1} = \frac{c_{w,0}}{n_w\lambda} \tag{4.9}$$

- Quadratic Carangiform waveform: the second coefficient was set to modulate the wave amplitude from n_q to m_q percent of wavelengths (see Figure 2.6 for $n_q = 0.9$ and $m_q = 1$). According to that, the coefficients $c_{w,1}$ and $c_{w,2}$ were defined as a function of $c_{w,0}$ by:

$$c_{w,1} = \frac{c_{w,0}}{n_q\lambda} + \frac{m_q}{m_q - n_q}\left(\frac{c_{w,0}}{m_q\lambda} - \frac{n_q c_{w,0}}{m_q^2\lambda}\right), \tag{4.10}$$

$$c_{w,2} = \frac{m_q}{m_q - n_q}\left(\frac{c_{w,0}}{m_q^2\lambda^2} - \frac{c_{w,0}}{n_q m_q\lambda^2}\right), \tag{4.11}$$

  where $n_q, m_q \in \Re^+$ and $m_q > n_q$.

- Fractional waveform:

$$c_{w,3} = \frac{c_{w,0}}{(n_w\lambda)^\alpha} \tag{4.12}$$

The proposed fractional waveform defines a motion whose growth and amplitude modulation can be controlled by only one parameter, α_w. This can be an essential and valuable property to be considered when searching for optimal propulsion waveform, simplifying such a problem.

4.1.3 Waveform discretization

In the analysis of previous sections, it has been considered that the flagellum or tail of the swimming robot is composed of a relatively high number of small rigid links, that behave similarly to a continuous flexible flagellum. However, this assumption can only sometimes be realized in the physical implementation of a swimming robot due to current technological and manufacturing limitations. Therefore, a discretization method must be applied to the desired beating waveform to translate such a motion from a continuous space to a discrete one based on N links. It is worth mentioning that the analysis is still applicable to relatively large links, although it comes at the cost of losing accuracy in the results.

Two discretization methods that address motion splitting are presented below, considering the motion amplitude and the computational power required to perform this splitting. However, for both cases, the method result will be the references of the swimming robot's actuators.

4.1.3.1 Projection method

The projection method is based on the assumption that the angular positions of the links are sufficiently small. Therefore the projection of each link over the propulsion axis is constant and approximately equal to the segment length. Then, the link angle at each instant time is deduced as:

$$\theta_{j,t} \quad = \quad \tan^{-1}\left(\frac{y_w(x_j,t) - y_w(x_{(j-1),t})}{x_{j,t} - x_{(j-1),t}}\right), \tag{4.13}$$

where $j \in [0, N_u]$ means the considered link. This discretization method implies light computational capacity, allowing online and offline execution. For the first implementation, the equation (4.13) will be calculated for each link and time instant. On the other hand, the offline implementation method requires defining the sampling time and waveform period by providing a matrix, $\Theta[N_u][T]$, which contains the trajectory in time and space for the N_u links and which must be repeated for each period of the waveform, where T is the number of samples for the waveform period and the defined sampling time. Hence, $\Theta[N_u][T]$ allows the reproduction of the desired waveform with distributed actuators since it is the reference for the control of each actuator. As for the rotation term, it can be considered implicit in the definition of the beating waveform or excluded from the discretization and added later as a displacement in the motion, simplifying the implementation of the control algorithm. It should also be remarked that this method involves a reduction of amplitude by increasing the angle range; consequently, the projection of each link is reduced and does not hold constant. However, it ensures the recreation of the complete motion within one wavelength, even if the total length of the links is less than one wavelength.

This method can also be described from an analytical perspective, providing a continuous function that describes the angle of each link rather than a data set containing the movements during a wave period and for a specific sampling time. The link motion function has the same form as the beating waveform (2.9) and (3.58). However, the amplitude and the space phase are calculated considering the maximum amplitude with the link position along the flagellum. Then, the angle links for classical beating waveform can also be described by:

$$\theta(j,t) = \phi_{w,t} + \left(\phi_{w,0} + \phi_{w,1} \sum_{i=1}^{j} l_i \frac{1}{L} + \phi_{w,2} \left(\sum_{i=1}^{j} l_i \right)^2 \frac{1}{L} \right) \sin\left(\frac{2\pi}{\lambda} \left(\sum_{i=1}^{j} l_i - V_p t \right) \right), \tag{4.14}$$

and the fractional beating waveform is

$$\theta(j,t) = \phi_{w,r} + \phi_{w,3} \left(\sum_{i=1}^{j} l_i \right)^{\alpha_w} \frac{1}{L} \sin\left(\frac{2\pi}{\lambda} \left(\sum_{i=1}^{j} l_i - V_p t \right) \right), \tag{4.15}$$

where now $\phi_{w,r}$ defines the mean angle over which the motion is performed, whereas $\phi_{w,0}$, $\phi_{w,1}$, $\phi_{w,2}$ and $\phi_{w,3}$ are the angles that sweep the links, instead of the amplitude of the motion and L refers to the total length of the flagellum.

For illustration purposes, let's consider a 6-link swimming robot. Figure 4.2 shows the desired (ideal) waveform and its discretization for the fractional wave (3.58) with $\alpha_w = 0.2$. From this example, some shortcomings of the method can be seen. First, the amplitude of the discretized wave is slightly smaller than that of the ideal wave; specifically, it is reduced by a percentage of around 15% in this case. Likewise, the length of the flagellum resulting after applying the method is also slightly smaller than the original. In fact, the greater the amplitude of the

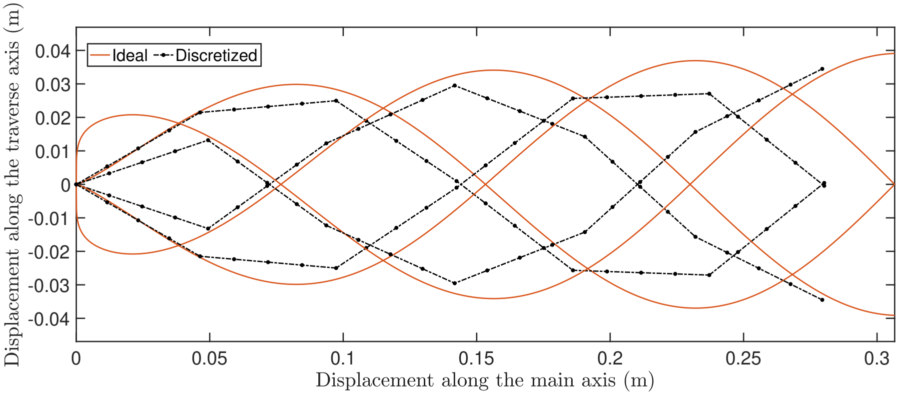

Figure 4.2: Comparison of the ideal and discretized waveform by the projection method for a 4-link swimming robot. Fractional beating waveform case for $\alpha_w = 0.2$.

desired waveform and the number of segments, the shorter the length. However, these differences will become smaller as the link angle reduces or the number of links increases, so its length will be shortened for a fixed length of the flagellum.

On the other hand, Figure 4.3 shows the angles of each link, where the phase difference between the angles makes it possible to deduce how the wave advances along the flagellum and the references for each link are sine waves with different amplitude and phase. It must be said that, although the results analyzed above correspond to a fractional waveform for $\alpha_w = 0.2$, they are entirely extensible to the

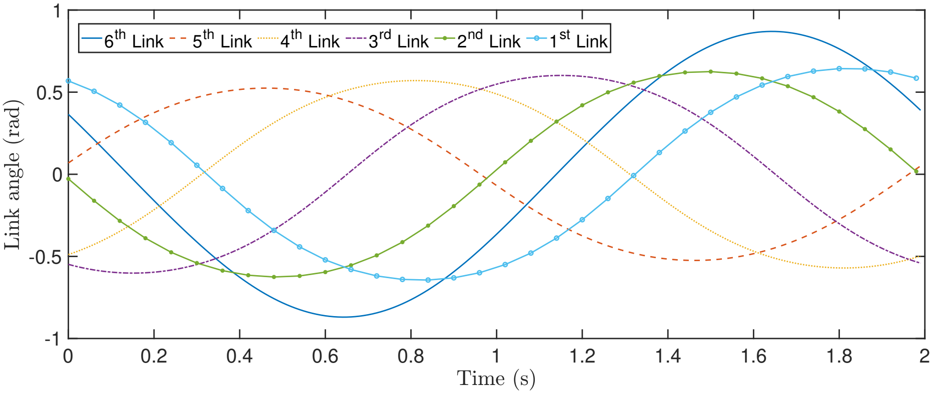

Figure 4.3: Angle of link for a 6-link swimming robot. Fractional beating waveform case for $\alpha_w = 0.2$.

obtained with other values of α, waveforms and number of links from the viewpoint of the discretization method.

4.1.3.2 Fitting method

The fitting method, in contrast to the previous one, provides a more accurate discretization of the waveform because it does not consider any assumptions about the length of the links. Moreover, it offers a more suitable discretization for swimming robots whose links have different lengths or when the wavelength is longer than the length of the swimming robot. However, the increase in accuracy produces an increased computational cost and consequently, the longer calculation time requires the method to be performed offline.

As in the previous method, the angle for each link is calculated by applying (4.13) and imposing the spacial length constraint of each link as:

$$l_j = \sqrt{(x_{(j+1)} - x_j)^2 + (y_w(x_{(j+1)}, t) - y_w(x_j, t))^2}, \tag{4.16}$$

The result, similarly to the other method, is a dataset, $\Theta[N_u][T]$, containing the angle of each link for each time instant. However, to achieve such results, a numerical resolution algorithm must be applied to solve the equation successfully. An iterative process was implemented based on the Nelder-Mead's simplex search method (means of the command *fminsearch* in MATLAB$^{\circledR}$) considering a maximum error of ±10% of the link length.

The fitting method applied to the fractional waveform for $\alpha_w = 0.2$ is illustrated in Figure 4.4 in comparison with the ideal waveform motion. In this case, the links are more closely matched to the waveform, achieving a shape closer to the ideal and reaching the maximum amplitude. Recalling the expression for the propulsive velocity (4.7), this method implies a higher velocity, not only because of the increase in amplitude but also because of the higher contribution of the term corresponding to the spatial derivative since the method reproduces more closely the waveform.

Regarding the link angles, shown in Figure 4.5, they lose their pure sinusoidal behavior, although they still maintain an oscillating behavior, which is smoother with this method.

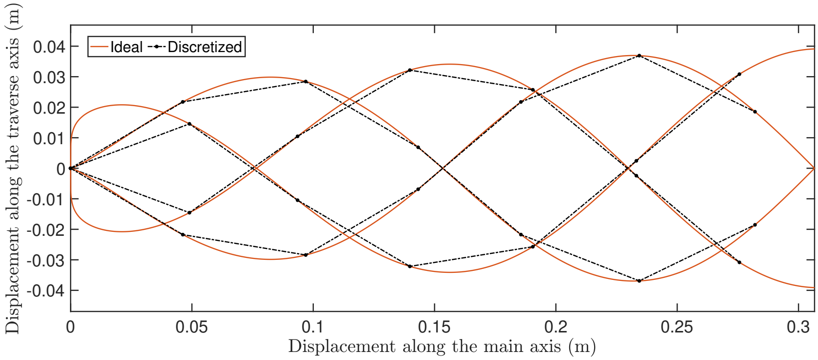

Figure 4.4: Comparison of the ideal and discretized waveform by the fitting method for a 6-link swimming robot and fractional beating waveform case for $\alpha_w = 0.2$.

4.1.3.3 Comparison of methods

A comparison between the two methods is depicted in Figure 4.6, where it can be seen that the projection method exhibits a larger deviation from the desired waveform as the link angle increases.

Figure 4.7 represents the link angles obtained by applying both methods and shows how the link angles are more similar the closer to the first link, so that the difference increases as the link considered is closer to the last one. In addition, the error of each link also affects the consecutive links, as seen in the last link. This error also impacts the phase lag between the link angles. Despite the fitting

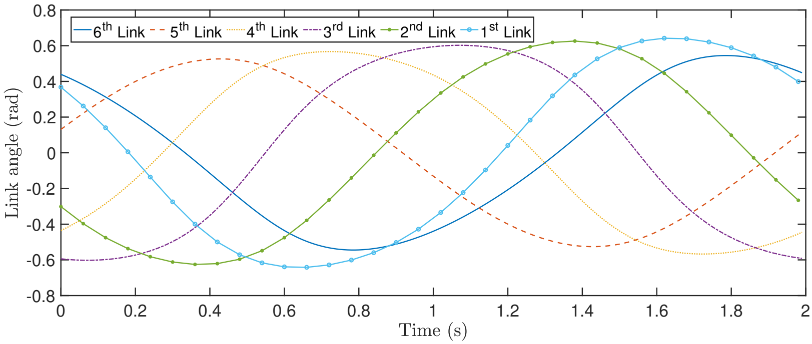

Figure 4.5: Angle of link for a 6-link swimming robot and fractional beating waveform case for $\alpha_w = 0.2$.

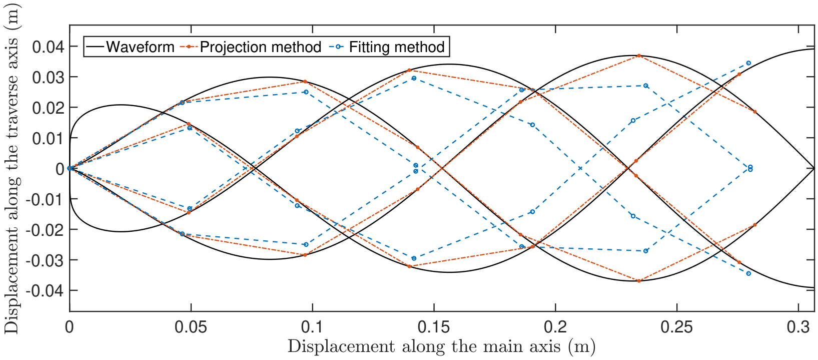

Figure 4.6: Comparison between methods for a 6-link swimming robot and fractional beating waveform case for $\alpha_w = 0.2$.

method providing more accuracy, the projection method allows recalculating real-time changes in waveform types, amplitude and frequency. The analysis still applies to relatively large links, although it supposes the cost of losing accuracy in the results.

4.2 Turning motion

It has been discussed how the definition of the waveform influences the propulsion force and speed. The turning motion is the third characteristic determined by the waveform. Primarily, turning motions are controlled by the coefficient $c_{w,t}$, which defines the average amplitude over which the beating waveform is realized. In

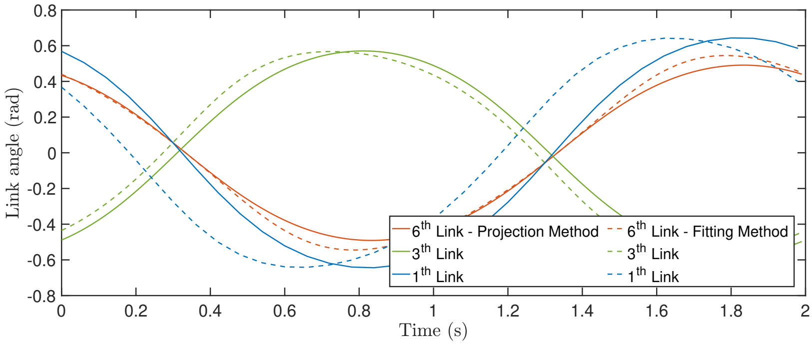

Figure 4.7: Comparison link angle obtained from both methods for a 6-link swimming robot and fractional beating waveform case for $\alpha_w = 0.2$.

order to understand how the turning motion is produced, the tangential and normal forces must be analyzed when $c_{w,t}$ is nonzero.

For simplicity, the case of the harmonic beating waveform will be analyzed without loss of generality since the analysis is extensible and equivalent to other beating waveforms. Moreover, if small deformation is considered, the viscous forces generated on an infinitesimal element of the flagellum in the $\mathbf{e}_\mathrm{x}$ direction is given by (4.5) and in the $\mathbf{e}_\mathrm{y}$ is

$$F_{p,y} = \int_0^\lambda \left(\left(c^\perp_{v,s} - c^\parallel_{v,s} \right) \frac{d}{dx} y_w \, \dot{x}_n \; - c^\perp_{v,s} \frac{d}{dt} y_w \right) dx. \tag{4.17}$$

Solving the above expression for a flagellum of length λ and the harmonic beating waveform (2.9), which means with $c_{w,1} = c_{w,2} = 0$, the resistive forces in $\mathbf{e}_\mathrm{x}$ and $\mathbf{e}_\mathrm{y}$ direction, respectively, are

$$F_{p,x} = \left(c^\perp_{v,s} - c^\parallel_{v,s} \right) \frac{2\pi^2 c^2_{w,0} V_p}{\lambda} - c^\perp_{v,s} \lambda \dot{x}_n \tag{4.18a}$$

$$F_{p,y} = \left(c^\perp_{v,s} - c^\parallel_{v,s} \right) c_{w,t} \, \dot{x}_n \tag{4.18b}$$

From the propulsive forces resulting from the harmonic beating waveforms, it shows that the turning term involves a force contribution in the $\mathbf{e}_\mathrm{y}$ direction, which is directly proportional to the turning coefficient $c_{w,t}$. Likewise, it does not influence the propulsive force in $\mathbf{e}_\mathrm{x}$ direction. However, for the other beating waveforms, it also contributes to the propulsion in the $\mathbf{e}_\mathrm{x}$ direction. This analysis can also be deduced from Figure 4.8, where the two cases are represented: a motion with a rotation coefficient equal to zero (Figure 4.8a) and another different from zero (Figure 4.8b). When the undulatory motion of the elements or links of the flagellum is produced over a line parallel to forward motion, the net propulsion forces are also

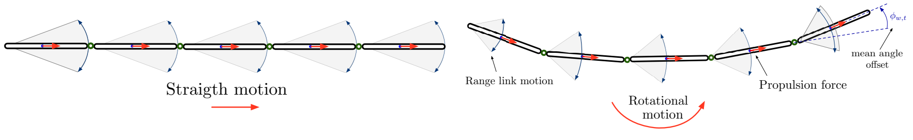

(a) (b)

Figure 4.8: Graphical description of turning motion: **(a)** straight motion and **(b)** rotational motion.

in that direction. However, if the beating motion is performed over a nonzero mean amplitude, the contribution of the net vertical forces is not compensated during the motion. Thus, the motion gives rise to two forces: one parallel to the forward motion and the other normal to it, which induces a rotation.

Therefore, it can be stated that a nonzero turning coefficient, $c_{w,t}$, produces a force normal to the forward motion, steering the motion of the swimming robot. A positive value of the turning coefficient, $c_{w,t} > 0$, produces a rightward turn, whereas a negative one, $c_{w,t} < 0$, implies a leftward turn. Moreover, the steering rate is directly proportional to the turning coefficient and the forward velocity.

4.3 Locomotion

The control design for a swimming robot supposes a significant challenge. Due to their strong under-actuated dynamics, the system only has N_u input with respect to $N + 2$ DoF, making it impossible to control the heading and the position directly. However, before establishing a locomotion control strategy, it is necessary to study the controllability and observability of the system, in this case, of a swimming robot. Both concepts play a crucial role in the choice and definition of the control strategy. They will allow for discerning if it is possible to control the system to obtain the desired behavior, in this case, to reach a predetermined destination and if the system's dynamics can be estimated using models (observers) without the need to measure all its variables. Both aspects require differential geometry techniques for the analysis of nonlinear systems from the point of view of control theory, so a brief introduction to differential geometry techniques is given in Appendix A.3.

Therefore, the following sections will analyze the controllability and observability of a swimming robot and propose a control strategy for path following.

4.3.1 Controllability

One of the properties more relevant in the study and design of a system in control theory is its controllability. In plain words, it is described as *the capacity of admissible control input to do whatever we want with the given dynamic system*. Thus, this property ensures that a system can move from one configuration or operation point to another due to an external input performing specific admissible manipulations.

Let consider the structure of the nonlinear system given by (3.44). Formally, it is said controllable if, for an initial state $\mathbf{x}_i \in \Re^n$ and final $\mathbf{x}_f \in \Re^n$, there exists a time interval $t_1 > t_2$ and a set control functions $\mathbf{u}(t)$ such that $\mathbf{x}(t_1) = \mathbf{x}_i$ and $\mathbf{x}(t_2) = \mathbf{x}_f$, where $\mathbf{x}(t)$ is a unique solution [188]. In contrast to linear systems, where controllability is proved by checking whether the system satisfies the Kalman rank condition, nonlinear systems require more complex studies, which are still an active area of research. General conditions are not necessary or sufficient to ensure system controllability. Instead, it is studied by analyzing the local behavior of the system near the equilibrium points ($\mathbf{x}_e$,$\mathbf{u}_e$), for which there are necessary and sufficient conditions and different methods.

The most straightforward approach to verifying a nonlinear system's controllability is linearizing the system around an equilibrium point. However, in the case of under-actuated systems, they usually do not have a controllable linearized system. Even the structure can become an unmanageable canonical expression, but that does not imply that the nonlinear system cannot be controllable (for example, the model of maneuvering a car). Therefore, this approach is often unsatisfactory and can result in a lack of much of the system's information. A second approach relies on Lie group theory, especially the accessibility algebra, which is quite a helpful tool for finite dimension, but is useless for infinite-dimensional control systems. However, first of all, some formal concepts related to controllability and accessibility of nonlinear systems are need to be recalled [123, 188, 189, 190, 191]:

- *Small-time local controllability* (STLC). It is a stronger property than controllability and defines that a system is small-time locally controllable at the equilibrium point ($\mathbf{x}_e$,$\mathbf{u}_e$) if, for every real number $\eta > 0$, there exists a real number $\varepsilon > 0$ such that, for every $\mathbf{x}_1 := \{\mathbf{x} \in R^n; |\mathbf{x} - \mathbf{x}_e|\} < \varepsilon$ and for every $\mathbf{x}_2 := \{\mathbf{x} \in R^n; |\mathbf{x} - \mathbf{x}_e| < \varepsilon\}$, there exists a measurable function $\mathbf{u} : [0, \eta] \longrightarrow \Re^m$ such that

$$|\mathbf{u} - \mathbf{u}_e| \leq \eta, \forall t \in [0, \varepsilon],$$

$$\left(\dot{\mathbf{x}} = f(\mathbf{x}) + \textstyle\sum_{i=1}^{m} g_i(\mathbf{x}) u_i(t), \mathbf{x}(0) = \mathbf{x}_1\right) \Longrightarrow (\mathbf{x}(\varepsilon) = \mathbf{x}_2).$$

Therefore, if a system is STLC, then it can reach any state or configuration in an arbitrary period of time with a suitable control input. However, it is a property only considered from the equilibrium point since, in certain systems, it is generally not possible to move instantaneously in one direction if it is already moving in the opposite direction. For example, an aircraft in flight is not STCL because there is no suitable control input to allow it to move instantaneously in the opposite direction to its current one. Despite this, it is a fundamental property in systems to which it is desired to apply a motion planner control because it is always possible to find a suitable control input or move the system to a state that satisfies the requirements of the motion planner.

- *Locally accessibility (LA).* It is a weaker form of controllability that corresponds to being able to reach, from $\mathbf{x}_i$, a set of n-dimension space (not necessarily the entire space) within some time $t > 0$. In the particular case of a driftless system, when the drift field vector is zero ($f(\mathbf{x}) = 0$), this property coincides with the STLC property by the Rashevsky–Chow's theorem.

- *Strong accessibility (SA).* It is a slightly stronger property than the former and imposes a fixed time t_2 with $t_2 > 0$ to reach the n-dimension space by the system.

A simple illustration of above concepts is depicted in Figure 4.9 for a two-dimensional configuration space.

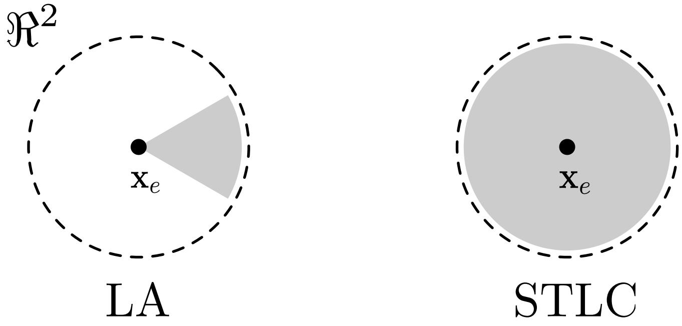

Figure 4.9: Illustrations of local accessibility (LA) and small-time local controllability (STLC) in a two-dimensional space.

The study of these concepts is performed by analyzing the drift, f, and control, g, vector fields that define the directions in which the system can move or which states can be reached from an initial state. Generally, these vectors only span a subset of the entire accessible state space. However, through the motion combinations along these vector fields, the system can cover other subsets that are not spanned by the initial vector fields of the system. At this point, the distribution concept takes particular interest allowing the study of the space that can reach with the combinations of the drift and control vector fields. Lie brackets operator, which is defined in the equation (A.17) of the Appendix A, approximates the net motion resulting from the alternating combination of two vector fields.

Recalling some geometry control theory results, two conditions to go deeper into the analysis and study of controllability are established.

1. A necessary, but not sufficient, condition meets the Lie algebra rank condition (LARC) or accessibility rank condition at state ($\mathbf{x}_i$), defined as:

   $$\dim \Delta(\mathbf{x}_i) = n. \tag{4.19}$$

   Let Δ be the distribution constructed using the vector fields of the system, $\{f, g_1, \ldots, g_m\}$, and all vector fields that can be obtained through the drift vector, $f(\mathbf{x})$, control vector fields, $g(\mathbf{x})$, and taking any number of Lie bracket of them (see Appendix A for more information). Δ is the accessibility distribution generated by

   $$\Delta(\mathbf{x}) = \operatorname{span}\Big\{ad_f^k g_i(\mathbf{x}), ad_{g_i}^k g_j(\mathbf{x}) \in S\,; k \in \mathbb{N}, i, j \in \{1, \ldots, m\}\Big\}. \tag{4.20}$$

   If the system satisfies the LARC at state $\mathbf{x}_i$, it is locally accessible from $\mathbf{x}_i$. If the drift vector field is not included in the accessibility algebra, then the system is strongly accessible. In addition, if the state $\mathbf{x}_i$ is an equilibrium point, the system is also susceptible to being STLC.

   A particular case is the driftless systems. Systems with drift vector fields involve greater complexity than those without drift, since systems have dynamics that are not directly influenced by the input control, imposing restriction motions. However, it may only be possible to move in specific directions for an arbitrarily small time interval due to the imposed behavior of the drift vector fields. When the system is driftless, there are no such constraint motions in any direction. In these cases, it is possible to prove that LARC becomes necessary and sufficient to ensure STLC since all the states are directly proportional to the input control.

2. A sufficient condition is to satisfy the LARC by good Lie bracket terms up to degree i and that all bad Lie brackets of degree $j \leq i$ are θ-neutralized.Let define $B \subset \Delta$ as the set of formal iterated Lie brackets and $B(\mathbf{x}) \in \Re^n$ as the evaluation of B at $\mathbf{x}$. The degree of a bracket with respect to a vector field f and g_i, denoted by $\delta_f(B)$ and $\delta_g^i(B)$, respectively, is the number of times that the corresponding vector fields defined by subscript and superscripted appear in the bracket. A bracket is said to be bad if $\delta_f(B)$ is odd and $\delta_g^i(B)$ are all even (including zero). A bracket is good if it is not bad. The classification of good and bad bracket is strongly related to the occurrence of the drift vector field because the latter may involve directional constraint that obstructs the controllability, despite the systems being accessible. An example is the drift vector, which is bad because it only allows motion in its positive direction and not in the negative. Nevertheless, the bad brackets may be θ-neutralized if they can be written as a linear combination of good brackets of lower degree. Moreover, a bad Lie bracket is also assumed to be neutralized if it is zero at the equilibrium point. The θ-degree for the vector field B is defined by

$$\delta_\theta(B) = \frac{1}{\theta_0}\delta_f(B) + \sum_{i=0}^{m} \delta_g^i(B) \tag{4.21}$$

where $\theta_0 \in (1, \infty]$ is an arbitrary number. For example, given the following set of lie brackets

$$\begin{aligned}
LB_1 &= [f, g_1],\\
LB_2 &= [f, [f, g_1]],\\
LB_3 &= \big[[f, g_1], [f, g_2]\big],\\
LB_4 &= \big[[f, [f, g_1]], [f, g_1]\big],\\
LB_5 &= \Big[\big[[f, g_1], [f, g_2]\big], \big[[f, [f, g_1]], [f, g_1]\big]\Big],
\end{aligned}$$

Table 4.2 indicates what their θ-degree is and whether they are good or bad. The brackets that meet some premise for being bad are highlighted in bold. It is shown that only LB_4 is bad since δ_f is odd and all δ_g^i are even. Regarding its θ-neutralization, it can be neutralized by a set of brackets whose θ-degree is less than 5, in the case that LB_4 would not be neutralized by itself because it is zero at the equilibrium point.

Table 4.2: Example of Lie bracket analysis

Bracket	$\delta_\theta(B)_{(\theta_0=1)}$	$\delta_f(B)$	$\delta_g^1(B)$	$\delta_g^2(B)$	$\delta_g^i(B),(i>3)$	Type
LB_1	2	**1**	1	0	0	Good
LB_2	3	2	1	0	0	Good
LB_3	4	2	1	1	0	Good
LB_4	5	**3**	**2**	0	0	**Bad**
LB_3	9	**5**	3	1	0	Good

4.3.1.1 Medium *Re* environment case

Once the differential geometry tools have been presented and the necessary and sufficient conditions for controllability have been stated, the controllability of the swimming robot model described in section 3.1 can be studied and analyzed.

Recalling the swimming robot model defined in (3.44), first, the equilibrium points are calculated. For this purpose, the flow is considered at rest, which means that the fluid velocity is zero ($\mathbf{V}_f = 0$), then the system has the equilibrium point:

$$(\mathbf{x}_e, \boldsymbol{\nu}_e)_1 = \left([\boldsymbol{\alpha}_e, \boldsymbol{\theta}_e, q_{x,e}, q_{y,e}, \mathbf{0}_N, 0, 0]^T, \mathbf{0}_{N_u}^T\right) \tag{4.22}$$

where the variables $\boldsymbol{\alpha}_e, \boldsymbol{\theta}_e$ can take any value between $[0, 2\pi]$ and the robot position $(q_{x,e}, q_{y,e})$ can take any value in the space $\Re^2$. In other words, the swimming robot is at a point of equilibrium whenever it is at rest, regardless of its geometrical configuration and global position. On the other hand, if the environment is turbulent ($\dot{\mathbf{V}}_f \neq 0, \mathbf{V}_f \neq 0$) or stationary ($\dot{\mathbf{V}}_f = 0, \mathbf{V}_f \neq 0$) the model does not have equilibrium point as a consequence of the flow dragging the robot. Therefore, the swimming robot velocity, $\dot{q}_x \neq 0$ and $\dot{q}_y \neq 0$, will never be zero. In terms of controllability, this also implies that the system is not STLC when subjected

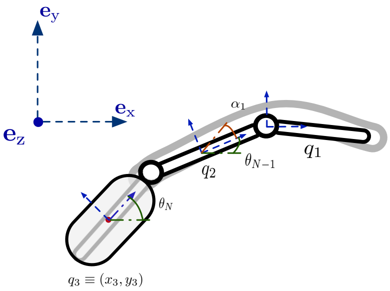

Figure 4.10: The simplest configuration of a swimming robot, based on three links.

to environmental movements. However, it should be remembered that STLC is a stronger property than controllability, so this condition supports that the system is not STLC in such a scenario but cannot prove it is not controllable. On the other hand, if the relative velocity is zero as a consequence of the fluid velocity coinciding with the velocity of the swimming robot, there will be no admissible control input to move the system from one state to another since the swimming acceleration is zero. Therefore, the system is uncontrollable in this case.

The simplest configuration of a swimming robot is made of three rigid links, which means two rigid links plus the head ($N = 3$, see Figure 4.10). This has the minimum number of active joints to generate a nonreciprocal motion, as discussed by E. Purcell [118] and described through Purcell's swimmer, which is composed of three links. An additional consequence of the rigid links is that the control vector field is only a function of the angles of the actuated joints, $g(\boldsymbol{\alpha})$. On the other hand, it is also considered that the movements are slow enough not to consider the added forces due to the fluid. The controllability analysis will focus on such configuration. Likewise, the results will also be valid and applicable to swimming robots with a greater number of links. This is because any robot configuration with $N > 3$ can behave as a 3-link by fixing some joint angles at zero degrees and allowing only the motion to three joints irrespective of different link lengths. Therefore, the controllability of a 3-link swimming robot is sufficient, although not necessary, condition for controllability with $N > 3$.

Taking as a starting point an environment at rest, that means, from every position and shape of the swimming robot, the distribution Δ should span a 10-dimensional space in order to satisfy the necessary LARC given by (4.19). In Table 4.3, all

Table 4.3: Accessibility distribution, Δ, for a swimming robot model with $N = 3$ (two links plus the head) in medium Re case.

$\delta_\theta(B)_{(\theta_0=1)}$	Vectors		
1	f, g_1,	g_2;	
2	$[f, g_1]$,	$[f, g_2]$;	
3	$\left[f, [f, g_1]\right]$,	$\left[f, [f, g_2]\right]$,	
	$\left[g_1, [f, g_1]\right]$,	$\left[g_1, [f, g_2]\right]$,	
	$\left[g_2, [f, g_1]\right]$,	$\left[g_2, [f, g_2]\right]$;	
4	$\left[f\left[f, [f, g_1]\right]\right]$,	$\left[f\left[f, [f, g_2]\right]\right]$,	$\left[f\left[g_1, [f, g_1]\right]\right]$,
	$\left[f\left[g_1, [f, g_2]\right]\right]$,	$\left[f\left[g_2, [f, g_1]\right]\right]$,	$\left[f\left[g_2, [f, g_2]\right]\right]$;
	$\left[g_1\left[f, [f, g_1]\right]\right]$,	$\left[g_1\left[f, [f, g_2]\right]\right]$,	$\left[g_1\left[g_1, [f, g_1]\right]\right]$,
	$\left[g_1\left[g_1, [f, g_2]\right]\right]$,	$\left[g_1\left[g_2, [f, g_1]\right]\right]$,	$\left[g_1\left[g_2, [f, g_2]\right]\right]$;
	$\left[g_2\left[f, [f, g_1]\right]\right]$,	$\left[g_2\left[f, [f, g_2]\right]\right]$,	$\left[g_2\left[g_1, [f, g_1]\right]\right]$,
	$\left[g_2\left[g_1, [f, g_2]\right]\right]$,	$\left[g_2\left[g_2, [f, g_1]\right]\right]$,	$\left[g_2\left[g_2, [f, g_2]\right]\right]$;

vector functions than can be obtained through the drift vector field are gathered, $f(\alpha, \dot{\alpha}, \gamma, \dot{\gamma})$ and the control vector field $g_i(\alpha)$ with $i \in \{1, 2\}$, which could span the dimensional space with the minimum θ-degree in (4.21). Moreover, the bad brackets are highlighted in green.

From the Lie Algebra distribution presented above it can be observed that there are 29 vectors to span the complete space of the system and only 3 bad brackets that will have to be θ-neutralized. However, 10 independent vectors from these vectors must be chosen to construct the accessible distribution. In particular, the vectors chosen are as follows:

$$\Delta(\mathbf{x_e}) = \Big[g_1,\ g_2,\ [f, g_1],\ [f, g_2],\ \left[f,\ [f, g_1]\right],\ \left[f, [f, g_2]\right],$$
$$\left[g_1, [f, g_2]\right],\ \left[f\left[f, [f, g_1]\right]\right],\ \left[f\left[f, [f, g_2]\right]\right],\ \left[f\left[g_1, [f, g_2]\right]\right]\Big]_{(\mathbf{x}_e, \boldsymbol{\nu}_e)}$$
$$= \begin{bmatrix} \mathbf{0} & \mathbf{0} & -\mathbf{e}_1 & -\mathbf{e}_2 & \mathbf{0} & \mathbf{0} & \mathbf{0} & \mathbf{0} & \mathbf{0} & \mathbf{0} \\ \mathbf{0} & \mathbf{0} & -\mathcal{E}_1 & -\mathcal{E}_2 & \mathcal{K}_1 & \mathcal{K}_2 & \mathcal{K}_5 & \mathcal{K}_7 & \mathbf{0} & \mathcal{K}_{10} \\ \mathbf{e}_1 & \mathbf{e}_2 & \mathbf{0} & \mathbf{0} & \mathbf{0} & \mathbf{0} & \mathbf{0} & \mathbf{0} & \mathbf{0} & \mathbf{0} \\ \mathcal{E}_1 & \mathcal{E}_2 & -\mathcal{K}_1 & -\mathcal{K}_2 & \mathcal{K}_3 & \mathcal{K}_4 & \mathcal{K}_6 & \mathcal{K}_8 & \mathcal{K}_9 & \mathcal{K}_{11} \end{bmatrix}_{(\mathbf{x}_e, \boldsymbol{\nu}_e)} \in \Re^{10\times 10},$$

where $\mathcal{K}_i \in \Re^{3x1}$ is a nonzero matrix whose value is calculated from the Lie bracket. The matrix is denoted in this form to make it more readable. The accessible distribution, $\Delta(\mathbf{x_e})$, has full rank if it can be shown that all vectors are linearly independent, and thereby, the $\det(\Delta(\mathbf{x_e})) \neq 0$ (where det() denotes determinant of a matrix). This can be verified through a mathematical analysis software, such as *Wolfram Mathematica*, due to the length and complexity of the equations.

Therefore, the necessary, but not sufficient, Lie algebra rank condition is satisfied. Lie algebra rank condition satisfaction allows to claim that a 3-link swimming robot is strongly accessible in $(\mathbf{x}_e, \boldsymbol{\nu}_e)$ (strongly, because the drift vector field is not included in Δ). However, to guarantee the system's STLC, the second condition must be verified, which implies that the bad brackets highlighted in Table 4.3 must be θ-neutralized. In other words, the three bad brackets must be a linear combination of other vectors with an equal or lower θ-degree, if they are not zero at the equilibrium point. The first bad bracket, f, vanishes at the equilibrium point as a consequence of the equilibrium point definition. Regarding the other bad brackets $\left[g_1, [f, g_1]\right]_{(\mathbf{x}_e, \boldsymbol{\nu}_e)}$ and $\left[g_2, [f, g_2]\right]_{(\mathbf{x}_e, \boldsymbol{\nu}_e)}$ are checked that they cannot be obtained from a linear combination of the good brackets, consequently, the system does not satisfy the sufficient condition to STLC.

In summary and as a conclusion of the above results, an N-link swimming robot is not small-time locally controllable. However, it is important to remark that STLC is a stronger property than controllability, which means that nonSTLC does not imply that the system is not controllable, rather that its controllability cannot be analyzed by this method. In addition, in the particular case when the equilibrium point fulfills the condition $\alpha_1 = \ldots = \alpha_{N-1}$, that means when all the links follow the head in parallel ($\alpha = 0$) or the swimming robot takes a C-shape configuration, a singular conclusion results from the above analysis: the dimensions of the accessible algebra Δ drop below the space dimension, implying that specific (geometric) configurations make the system uncontrollable. This result is, in turn, consistent with claims in the literature [111, 113, 123], which said that propulsion or locomotion of swimming robots is the result of the motion of links when they are out of phase.

4.3.1.2 Low *Re* environment case

A paradigm shift occurs as described in section 3.2 when the swimming robot is in a low *Re* environment. This has a significant impact on the controllability of the system. Therefore, based on the results obtained above, where the absence of inertial effects implies the lack of the drift vector, and therefore, according to the Rashevsky–Chow's Theorem, it is only necessary to show that system complies with LARC to prove that it is STLC.

Considering the same assumptions as in the previous case, the Lie Algebra distribution, $\hat{\Delta}$ should span a 5-dimensional space in order to satisfy the necessary LARC given by (4.19). In the Table 4.4, the main are vector functions are gathered can be obtained through the control vector field $g_i(\gamma, \alpha)$ with $i \in \{1, 2\}$. In addition, all are good brackets.

The vector chosen to proof the controllability of the swimming robot is

$$\begin{aligned}\Delta(\mathbf{x_e}) &= \Big[g_1,\ g_2,\ [g_1, g_2],\ \big[g_1,\ [g_1, g_2]\big],\ \big[g_2, [g_1, g_2]\big], \Big]_{(\mathbf{x}_e, \nu_e)} \\ &= \begin{bmatrix} \mathbf{e}_1 & \mathbf{e}_2 & \mathbf{0} & \mathbf{0} & \mathbf{0} \\ \mathcal{E}_1 & \mathcal{E}_2 & \hat{\mathcal{K}}_1 & \hat{\mathcal{K}}_2 & \hat{\mathcal{K}}_3 \end{bmatrix}_{(\mathbf{x}_e, \nu_e)} \in \Re^{5\times 5},\end{aligned}$$

where $\hat{\mathcal{K}}_i \in \Re^{3x1}$ is a nonzero matrix whose value is calculated from the Lie bracket. The above distribution has a full range can be verified through a mathematical software like *Wolfram Mathematica*.

Finally, it is, therefore, demonstrated that an N-link swimming robot is small-time locally controllable in low *Re* environments, even in the particular case when the equilibrium point fullfils the condition: $\alpha = 0$.

4.3.2 Observability

This section turns to the notion of observability, which is also one of the most fundamental properties in the study and design of systems in control theory (for

Table 4.4: Accessibility distribution, $\hat{\Delta}$, for a swimming robot model with $N = 3$ (two links plus the head).

$\delta_\theta(B)_{(\theta_0=1)}$	Vectors
1	$g_1, g_2;$
2	$[g_1, g_2];$
3	$\big[g_1, [g_1, g_2]\big], \big[g_2, [g_1, g_2]\big];$

a more profound and rigorous explication, the readers are encouraged to consult [191, 192, 193, 194]). This property describes the possibility of inferring the system states from observing its inputs and outputs. Therefore, this section is focused on the output of the affine control system defined in (3.44).

First, it is necessary to introduce the indistinguishable concept of a state in order to understand the observability definition. A pair of states $\mathbf{x}_1$ and $\mathbf{x}_2$ are said to be indistinguishable (expressed as $\mathbf{x}_1\mathrm{I}\mathbf{x}_2$) for system (3.44), if for every admissible input function $\mathbf{u}$, the system output $\mathbf{y}(t, \mathbf{x}_1, \mathbf{u}), t > 0$, for initial state $\mathbf{x}_1$ and the system output $\mathbf{y}(t, \mathbf{x}_2, \mathbf{u}), t > 0$ for initial state $\mathbf{x}_2$, are the same on their common domain of definition. Then, the system is said to be observable if $\mathbf{x}_1\mathrm{I}\mathbf{x}_2$ implies strictly $\mathbf{x}_1 = \mathbf{x}_2$ [191, 192, 193].

The considered definition of observability does not imply that every input function $\mathbf{u}$ distinguishes points of $\mathcal{M}$. If the output is a linear combination of the initial state and the input (as it is for the linear systems) and if some input distinguishes between two initial states, then every input will do. On the other hand, note that observability is a global concept that requires showing the above definition for the entire system domain since a nonlinear system may not be observable, but may contain observable local domains. Therefore, the local concept of observability is introduced, which is also stronger than the global one.

Let $\mathcal{U}$ be a subset of $\mathcal{M}$ ($\mathcal{U} \subset \mathcal{M}$) and $\mathbf{x}_1, \mathbf{x}_2 \in \mathcal{U}$. $\mathbf{x}_1$ is $\mathcal{U}$-indistinguishable from $\mathbf{x}_2$ ($\mathbf{x}_1\mathrm{I}^{\mathcal{U}}\mathbf{x}_2$) if for every admissible constant control $\mathbf{u} := u(t), [t_0, t_1]$, with the property that the solutions $\mathbf{x}(t, \mathbf{x}_1, \mathbf{u})$ and $\mathbf{x}(t, \mathbf{x}_2, \mathbf{u})$ both remain in $\mathcal{U}$, the output $\mathbf{y}(t, \mathbf{x}_1, \mathbf{u})$ and $y(t, \mathbf{x}_2, \mathbf{u})$, respectively, are the same for $t_0 < t < t_1$ on their common domain of definition. A system is locally observable at $\mathbf{x}_1$ if there exists a neighborhood $\mathcal{W}$ of $\mathbf{x}_1$ such that for every neighborhood $\mathcal{U} \subset \mathcal{W}$ of $\mathbf{x}_1$ the relation $\mathbf{x}_1\mathrm{I}^{\mathcal{U}}\mathbf{x}_2$ implies that $\mathbf{x}_1 = \mathbf{x}_2$ [191, 192, 193]. Local observability also implies observability if the subset $\mathcal{U}$ is defined equal to $\mathcal{M}$, but generally it does not imply observability. However, if a system is not locally observable at some $\mathbf{x}_1$, then it is not observable.

For the study of accessibility and small local time controllability, the accessibility algebra of the system was an essential tool. Analogously, for the study of local observability, the observation space is also necessary to show this property. Let considers the system (3.44) with the output map defined by $h(\mathbf{x})$. The observation space $\mathcal{O}$ is the linear space (over $\Re$) of functions on $\mathcal{M}$ containing $\mathbf{h}$ and all repeated Lie derivatives (see Appendix A for more information), such as:

$$\mathcal{O}(\mathbf{x}) = \text{span}\left\{\mathcal{L}_{v_i}^{k} h_j; i, k \in \mathbb{N}, j = \{1, \ldots, p\}\right\}, \tag{4.23}$$

where v_i with $i = \{1, 2, \ldots\}$ is a vector field of the set $\{f, g_i, \ldots, g_m\}$ and p is the number of system outputs. The observation space defines the observability codistribution by the gradients of the elements of $\mathcal{O}$, denoted as $\nabla\mathcal{O}$ and defined by

$$\nabla_{\mathbf{x}}\mathcal{O}(\mathbf{x}) = \text{span}\left\{\nabla_{\mathbf{x}}\xi(\mathbf{x}) : \xi \in \mathcal{O}\right\}, \tag{4.24}$$

where ξ are functions (vector fields) belonging to the observation space and form the smallest linear subspace.

Once the observation space and observability codistribution of the system given by the expression (A.11) of the Appendix A, are defined, the observability rank condition (ORC) is defined as well. The ORC constitutes necessary and sufficient condition to demonstrate the observability and it determines that:

$$\dim \nabla_{\mathbf{x}}\mathcal{O}(\mathbf{x_1}) = n. \tag{4.25}$$

Then, a system is said to be locally observable at $\mathbf{x}_1$ if it satisfies the observability rank condition [191, 192, 193]. It should be noted that the above definition of observation space was formulated in terms of an admissible constant input. However, it was shown in [194] that the observation space could be defined equally well in terms of analytic inputs. Moreover, when the study of the system is focused on input-output, an alternative observation space is more suitable, considering differentiable controls and time derivatives. Especially, it is formed taking the successive derivatives of the output system $(h(\mathbf{x}), \mathcal{L}_f h(\mathbf{x}), \ldots, \mathcal{L}^p h(\mathbf{x}))$ as a function of initial states, over all inputs and their successive derivatives $(\mathbf{u}, \mathcal{L}_{g_1} h(\mathbf{x}), \ldots, \mathcal{L}_{g_m}^{p} h(\mathbf{x}))$. This alternative observation space is formally defined as:

$$\mathcal{O}^{\star}(\mathbf{x}) = \text{span}\left\{\frac{d^k}{dt^k} y_j; k \in \mathbb{N}, j = \{1, \ldots, p\}\right\} \tag{4.26}$$

where the time derivative is actually the Lie derivative defined in the earlier sections and can also be rewritten as:

$$\mathcal{O}^{\star}(\mathbf{x}) = \text{span}\left\{\mathcal{L}_{\mathbf{z}_i}^{k} h_j; k \in \mathbb{N}, j = \{1, \ldots, p\}, i \in k, \right\} \tag{4.27}$$

with $\mathbf{z}_i(\mathbf{x}) = f(\mathbf{x}) + \sum_{i=1}^{m} g_i(\mathbf{x}) u_j^k$, where u^k is the k-derivative evaluated at $t = 0$. In [194] is shown that the above observation space (4.27) spans the same space as that defined by the first definition of observation space (4.23), which means:

$$\mathcal{O}(\mathbf{x}) = \mathcal{O}^{\star}(\mathbf{x}). \tag{4.28}$$

On this basis, the observability codistribution (4.24) can also be formed from the space (4.26) as

$$\nabla_{\mathbf{x}}\mathcal{O}^{\star}(\mathbf{x}) = \text{span}\left\{\nabla_{\mathbf{x}}\xi^{\star}(\mathbf{x}) : \xi^{\star} \in \mathcal{O}^{\star}\right\}. \tag{4.29}$$

Therefore, it redefines the observability rank condition (ORC) as

$$\dim \nabla_{\mathbf{x}}\mathcal{O}^{\star}(\mathbf{x_1}) = n. \tag{4.30}$$

where n is the system dimension.

4.3.2.1 Medium *Re* environment case

Once the necessary and sufficient condition for observability of a nonlinear system has been stated, the observability of the swimming robot model described in section 3.1 is addressed. For this purpose, the simplest configuration of a swimming robot is again considered, namely two rigid links plus the head ($N = 3$) and the motions are slow enough not to consider the added forces due to the fluid.

Defining the output vector of the swimming robot given by (3.44) in the function of the position and velocity of the robot, $\mathbf{y} = \mathbf{h}(\mathbf{x}) = [\dot{q}_x, \dot{q}_y, \dot{\theta}_N, q_x, q_y, \theta_N]^T \in \Re^6$. The observation space (4.26) is drawn up as:

$$\mathcal{O}(\mathbf{x}_0) = \left[h_1, h_2, h_3, h_4, h_5, h_6, \mathcal{L}_f h_1, \mathcal{L}_{g_1} h_1, \mathcal{L}_{g_2} h_1, \mathcal{L}_f^2 h_1, \right]_{(t_0)} \tag{4.31}$$

where h_i is the i-element of the vector $h(\mathbf{x})$.

The system is locally observable whether the ORC is satisfied, which implies that codistribution has a full rank dimension equal to $2N + 4$ (see equation (4.30)). From the above observation, it can be obtained the following codistribution of observability:

$$\nabla_{\mathbf{x}}(\mathbf{x}_0) = \begin{bmatrix} \mathbf{0}^{3\times3} & \mathbf{0}^{3\times2} & \mathbf{0}^{3\times3} & \mathbf{I}^{3\times3} \\ \mathcal{K}_1^{3\times3} & \mathcal{K}_2^{3\times2} & \mathbf{0}^{3\times2} & \mathcal{K}_3^{3\times3} \\ \mathcal{K}_4^{4\times3} & \mathbf{0}_{4\times3} & \mathcal{K}_5^{4\times2} & \mathcal{K}_6^{2\times3} \end{bmatrix}_{(t_0)} \in \Re^{(10\times10)} \tag{4.32}$$

where $\mathcal{K}_i$ is a nonzero matrix whose value is calculated by applying the gradient to observation space (4.31). By analyzing the observability codistribution and using a mathematical analysis software, it can be shown that codistribution 4.32 has a full range, satisfying the ORC (see equation (4.25)).

Therefore, it proves that an N-link swimming robot is observable, which means that the complete state of the system can be determined through the inputs and output variables of the system.

4.3.2.2 Low *Re* environment case

The observability analysis also changes when the swimming robot is within a strictly low *Re* environment. A new output vector is defined for system (3.44), which only considers the position in this case: $\hat{\mathbf{y}} = \hat{\mathbf{h}}(\mathbf{x}) = [\theta_N, q_x, q_y]^T \in \Re^3$. Therefore, the observation space is also modified, defining it as

$$\mathcal{O}(\mathbf{x}_0) = \left[\hat{h}_1, \hat{h}_2, \hat{h}_3, \mathcal{L}_{g_1}\hat{h}_1, \mathcal{L}_{g_2}\hat{h}_1, \right]_{(t_0)}. \tag{4.33}$$

As in the previous section, it is shown that the observability codistribution resulting from the previous observability space satisfies the ORC.

4.4 Path following control

The previous analyses conclude that an N-link swimming robot system is not small-time local controllable (STLC) at a medium *Re* environment but is observable. However, it should be remarked that STLC is a stronger property than controllability, which means that a nonSTLC system does not imply that it is not controllable, simply that its controllability cannot be analyzed by this method. It is also confirmed that the movements of the links must be out of phase for propulsion. Statements consistent with the claims in the literature [111, 113, 123]. On the other hand, it has been shown that a swimming robot in a low *Re* environment is STLC and observable due to the absence of inertial forces. It is, therefore, reasonable to address the problem of controlling the propulsion, heading and position and, in particular, to consider the problem of allowing the robot to follow a path.

In designing a trajectory tracking control strategy, it is first necessary to clarify that path following is understood as the task of following a predefined path independent of time. In other words, there are no temporal constraints, and where a trajectory or path describes the position of a moving object in 2 or 3-dimensional space over time, by whatever the object is. Unlike conventional control strategies for mobile robots, swimming robots require a new strategy because they are self-propelled by the beating of the flagellum rather than by wheels or actuators that act directly on the speed and heading of the system. This implies discarding the typical control strategies of regulation or tracking. In order to address this type of control for a swimming robot, a cascade control strategy approach is suggested, which is schematized in Figure 4.11. The strategy is based on three lower control strategies that divide the path following problem into simpler control tasks. The loops from the inner to the outer are:

1. Joint controller, to ensure the correct link motion of the swimming robot according to the desired beating waveform to reach the desired propulsion speed.

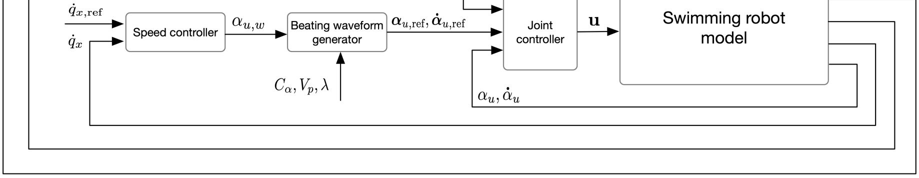

Figure 4.11: Path following control strategy.

2. Speed controller, which aims to set the swimming robot's speed through modifying the beating waveform.

3. Heading controller, to steer the swimming robot following the desired path.

4. Path generation, that decomposes a given trajectory into points and straight lines

4.4.1 Joint control

A nonreciprocal motion is only guaranteed when all the robot actuators follow their reference with the same dynamics and tracking error. For this purpose, the joint controller plays a key role. It is the first control law applied to the swimming robot and must ensure tracking specifications regardless of the position of the actuator along the flagellum (i.e., independently of its load) or the way of swimming (i.e., the kind of beating waveforms selected). On the other hand, the joint controller is close to the hardware implementation of the swimming robot. Therefore, it has a second objective: to make the following control strategies hardware-independent. It also means that if the technology of the swimming robot is changed, only the joint controller needs to be adjusted, and all other controllers remain unchanged.

For comparison purposes, three types of controllers are considered in order to analyze the power efficiency of motion based on them: 1) proportional-integral-derivative (PID) controller, 2) noninteger order derivative (PD$^{\mu}$) controller, and 3) reference model strategy. Not all control strategies will be applied to each of the prototypes described in later chapters. Furthermore, for tuning the proposed controllers, the following assumptions will be made: 1) the dynamics for velocity of the links is slow enough to consider that the influence between them is small enough to be neglected, and 2) their dynamics was identified as an isolated first-order system with the following transfer function:

$$P(s) = \frac{\dot{\alpha}_{u,i}(s)}{v_i(s)} = \frac{k_{l,i}}{\tau_{l,i}s + 1} \tag{4.34}$$

where $k_{l,i}$ and $\tau_{l,i}$ are each actuator's gain and time constant, respectively.

4.4.1.1 PID controller

A classical PID controller is considered to control the position of the links, defined in parallel form as follows

$$\nu_{\mathrm{PID}}(t) = \mathbf{K}_p\mathbf{e}(t) + \mathbf{K}_d\frac{d\mathbf{e}(t)}{dt} + \mathbf{K}_i\int_0^t \mathbf{e}(\tau)d\tau \tag{4.35}$$

where $\mathbf{K}_p = [k_{p,1}, \ldots, k_{p,N_u}]^T \in \Re^{N_u}$, $\mathbf{K}_i = [k_{i,1}, \ldots, k_{i,N_u}]^T \in \Re^{N_u}$ and $\mathbf{K}_d = [k_{d,1}, \ldots, k_{d,N_u}]^T \in \Re^{N_d}$ are the proportional, integral and derivative gains, respectively, $\mathbf{e}(t) = (\alpha_{u,\mathrm{ref}}(t) - \alpha_u(t))$, is the error signal and $\alpha_{u,\mathrm{ref}}$ is the joint angle reference obtained from the discretization method detailed in the section 4.1.3 and referred to as the beat waveform generator in the control strategy block diagram. An optimization was carried out to estimate the best controller parameters using two tuning methods: a) minimizing the integral time absolute error (ITAE), to evaluate the performance of the system along the time (it penalizes the errors that are persistent and neglects the initial errors) [195]; and b) minimizing the integral of absolute error (IAE), to quantify the performance to be sensitive at low errors [195].

The tuning procedure for each method was implemented in MATLAB®. The controller's parameters were estimated by evaluating the desired criteria defined as follows:

$$ITAE = \int_0^\infty t|\mathbf{e}(t)|dt \tag{4.36}$$

$$IAE = \int_0^\infty |\mathbf{e}(t)|dt, \tag{4.37}$$

An iterative process was used to determine the optimal parameters based on the Nelder-Mead's simplex search method (implemented by the function `fminsearch`), minimizing the above indices.

4.4.1.2 PD$^\mu$ controller

In the second place, PD$^\mu$ controller is proposed. As is well known, fractional calculus (FC), a branch of mathematical analysis dealing with derivatives and integrals of noninteger order, emerged as an efficient and powerful mathematical tool offering accurate modeling of many complex phenomena and control of complex systems by improving and generalizing well-established control methods and strategies. The controller is designed in the following form:

$$v_{\mathrm{PD}^{\mu}}(t) = \mathbf{K}_p \mathbf{e}(t) + \mathbf{K}_d \frac{d^{\mu}\mathbf{e}(t)}{dt^{\mu}} \tag{4.38}$$

where K_p and K_d are the proportional and derivative gains of the PD$^{\mu}$, and $\mu \in (0, 1]$ is the fractional order. It should be noted that this controller has the same number of parameters as the PID controller, and therefore both are comparable.

The tuning methods used for this controller are the two described in the previous section plus a third method: considering robustness to time constant variations for a desired phase margin, which will be referred to as robustness criterion (RC). This third method establishes three specifications to be satisfied to guarantee robustness to time constant variations. The first two are based on the classic definition of phase margin (ϕ) at a gain crossover frequency (ω_{cp}). The third specification must ensure that time constant variations do not produce changes in the crossover frequency and phase margin, which means that [196]:

$$\left.\frac{\partial\left|G(j\omega)\right|}{\partial\omega}\right|_{(\omega_{cp},\tau_0)} \Delta\omega + \left.\frac{\partial\left|G(j\omega)\right|}{\partial\tau}\right|_{(\omega_{cp},\tau_0)} \Delta\tau = 0, \tag{4.39}$$

$$\frac{\Delta\omega}{\Delta\tau} = -\left.\frac{\partial\left|G(j\omega)\right|/\partial\omega}{\partial\left|G(j\omega)\right|/\partial\tau}\right|_{(\omega_{cp},\tau_0)} \tag{4.40}$$

$$\left.\frac{\partial \arg\left[G(j\omega)\right]}{\partial\omega}\right|_{(\omega_{cp},\tau_0)} \Delta\omega + \left.\frac{\partial \arg\left[G(j\omega)\right]}{\partial\tau}\right|_{(\omega_{cp},\tau_0)} \Delta\tau = 0, \tag{4.41}$$

$$\frac{\Delta\omega}{\Delta\tau} = -\left.\frac{\partial \arg\left[G(j\omega)\right]/\partial\omega}{\partial \arg\left[G(j\omega)\right]/\partial\tau}\right|_{(\omega_{cp},\tau_0)} \tag{4.42}$$

where $G(j\omega)$ is the frequency response of the controlled system, that means $G(j\omega) = C(j\omega)P(j\omega)$ ($C(j\omega)$ denotes that of the controller, and $P(j\omega)$ is that of the model of the considered link) and τ_0 is the time constant to guarantee the controller's robustness.

Hence, the specifications for the RC method are the following:

1. Phase margin:

$$\arg\left[G(j\omega_{cp})\right] = -\pi + \phi \tag{4.43}$$

2. Gain crossover frequency:

$$\left|G(j\omega_{cp})\right| = 1 \tag{4.44}$$

3. Robustness to time constant variations:

$$\left.\frac{\partial\left|G(j\omega)\right|/\partial\omega}{\partial\left|G(j\omega)\right|/\partial\tau}\right|_{(\omega_{cp},\tau_0)} = \left.\frac{\partial\arg\left[G(j\omega)\right]/\partial\omega}{\partial\arg\left[G(j\omega)\right]/\partial\tau}\right|_{(\omega_{cp},\tau_0)} \tag{4.45}$$

To determine the controller parameters for the RC method, the set of nonlinear equations (4.43)–(4.45) was solved using the optimization toolbox of MATLAB®. More precisely, the function `lsqnonlin` was used to find the constrained minimum of a function of several variables. It solves a nonlinear least-squares problem of the form $\min_x \|f(x)\|_2^2$, where $f(x)$ is the function to minimize, and x is the minimum sought.

4.4.1.3 Tuning approach by reference model

The reference model methodology establishes a method for tuning the parameters of a proposed control structure to the desired ideal system dynamics using an optimization method, as depicted in Figure 4.12 and described in [197].

First, the design specifications of the ideal system are defined, whose temporal response will be used as a reference to refine the desired control strategy. Secondly, the cost function to be used in the optimization process is chosen after proposing

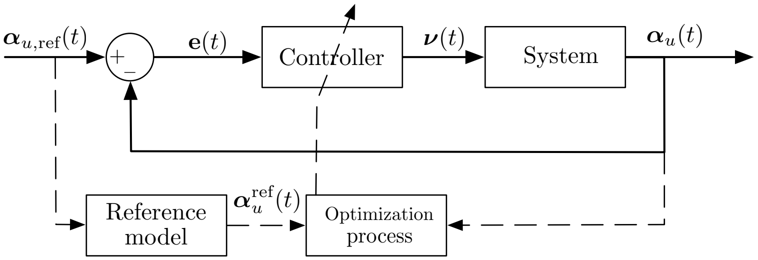

Figure 4.12: Reference model methodology.

the desired control strategy. In this case, the cost function is:

$$J(K_{pc}) = \int_0^\infty \left(\frac{1}{2} + \frac{t}{2}\right)|\mathbf{e}(t)| \tag{4.46}$$

where K_{pc} denotes the control strategy parameters. Note that cost function (4.46) is a combination of ITAE, to evaluate the performance of the system over time, and IAE, to quantify the performance to be sensitive at low errors [195].

The optimization process is divided into two steps and is carried out by combining both MATLAB® and Simulink®. The first step is implementing the system with the proposed control strategy, whose gains are variable, in closed-loop, along with the scheme corresponding to the reference model. The second step is a MATLAB® script that implements an iterative process based on the Nelder–Mead simplex search method, thanks to the function `fminsearch`, that runs the mentioned Simulink® model calculating the cost function J given by (4.46). In particular, this script varies the parameters of the controller until the values that minimize J are found, which means the controller's optimal values. In order to be able to find a globally optimal solution, the iterative process was applied for a wide number of initial conditions, which were randomly changed for each optimization.

4.4.2 Speed control

The speed controller aims to establish and achieve the desired propulsion speed through the variation that defines the beating waveform, mainly the coefficient that defines the beating amplitude and the propagation velocity of the wave. However, it should be noted that the physical limitations of the length links and the actuator dynamics constrain both parameters. Thereunder, the fractional beating waveform performs a crucial role in controlling the speed through the fractional order coefficient, α_w, changing the kind of beating waveform and remaining unchanged in the rest of the parameters. This is why the speed control strategy is only applied to the fractional beat waveform. In addition, this control must take into consideration the discretization method used. As was previously commented, the projection method allows the modification of the beating waveform parameters and recalculates the joint angles online. However, the fitting method does not allow changes in real-time due to the high computational cost. This implies the need to apply different control strategies for each discretization method. Furthermore, as a consequence, the speed propulsion of the swimming robot is proportional to the different parameters that define the beating waveforms; the fractional order coefficient is chosen as the control variable while setting the maximum propagation speed allowed by the actuators.

In this work, the speed control only covers the first discretization method, which is based on a classical proportional-integral (PI) controller whose law control is given by:

$$\alpha_{u,w}(t) = K_{p,\alpha}(\dot{x}_{n,\mathrm{ref}}(t) - \dot{x}_n(t)) + K_{i,\alpha} \int_0^t (\dot{x}_{n,\mathrm{ref}}(\tau) - \dot{x}_n(\tau))d\tau, \tag{4.47}$$

where $\alpha_{u,w}$ is the fractional order coefficient wave resulting from the law control, $K_{p,\alpha}$ and $K_{i,\alpha}$ are the proportional and integral gains, respectively, and $\dot{x}_{n,\mathrm{ref}}(t)$ is the desired swimming robot velocity.

4.4.3 Heading control

The swimming robot heading is the third requirement for the path following. The heading controller aims to ensure the forward motion of the swimming robot towards a given trajectory. It consists of two parts. The first one approaches the problem of determining the turning angle to track a straight path. The second part controls the head offset angle or the mean amplitude over which is performed the beating waveform to generate normal forces to the motion axis and, consequently, induce a rotation, as was commented in section 4.2.

The implementation of this control strategy is based on the assumption that any path can be converted into a set of straight lines, which is the basic operation of a path. Therefore, it is possible to apply the Line-of-sight (LOS) guidance methodology, a popular method for straight line following applied in maritime vehicles and surface-to-air missiles. LOS steers the system towards a straight line, for which it considers three control points: two of them are the starting and target point that form the straight line to follow, and the third is the position of the moving system. Specifically, the angle between the trajectory and the system determines the heading controller reference [123, 184].

Let consider a straight line defined by two points, $\mathbf{w}_k = [x_k^{\mathrm{w}}, y_k^{\mathrm{w}}]^T \in \Re^2$ and $\mathbf{w}_{k-1} = [x_{k-1}^{\mathrm{w}}, y_{k-1}^{\mathrm{w}}]^T \in \Re^2$. The local path frame is defined by the vector ($\mathbf{e}_{\mathrm{x}}^{\mathrm{w,k}}$, $\mathbf{e}_{\mathrm{y}}^{\mathrm{w},k}$, $\mathbf{e}_{\mathrm{z}}^{\mathrm{w},k}$), where the last vector is the result of the cross product of the first ones, with origin in $\mathbf{w}_{k-1}$. X-axis, $\mathbf{e}_{\mathrm{x}}^{\mathrm{w},k}$, is rotated with respect to the global frame an angle of:

$$\beta_k = \tan^{-1}\left(\frac{y_k^{\mathrm{w}} - y_{k-1}^{\mathrm{w}}}{x_k^{\mathrm{w}} - x_{k-1}^{\mathrm{w}}}\right) \tag{4.48}$$

Then, the swimming robot's position in the path frame is

$$\mathbf{q}^{\mathrm{w}} = \mathbf{R}_{\mathrm{I}}^{\mathrm{w},k}(\mathbf{q} - \mathbf{w}_{k-1}) \in \Re^2 \tag{4.49}$$

where

$$\mathbf{R}_{\mathrm{I}}^{\mathrm{w},i} = \begin{bmatrix}\mathbf{e}_{\mathrm{x}}^{\mathrm{w},k} & \mathbf{e}_{\mathrm{y}}^{\mathrm{w},k}\end{bmatrix} = \begin{bmatrix}\cos\beta_k & -\sin\beta_k \\ \sin\beta_k & \cos\beta_k\end{bmatrix}. \tag{4.50}$$

Now, with the transformation to the path frame, the swimming robot's position can be interpreted as

$$\mathbf{q}^{\mathrm{w}} = \begin{pmatrix} q_x^{\mathrm{w},k} \\ q_y^{\mathrm{w},k} \end{pmatrix} = \begin{pmatrix} s_{\mathrm{w}} \\ e_{\mathrm{w}} \end{pmatrix} \tag{4.51}$$

where s_{w} is along-track distance (tangential to path), and e_{w} cross-track error (normal to path) [184]. For guidance purposes, only the second component is relevant since it indicates how far the object is from the straight line, while $e_{\mathrm{w}} = 0$ means that it has converged to it. Therefore, the objective of guidance control is to ensure that

$$\lim_{t\to\infty} e_{\mathrm{w}}(t) = 0 \tag{4.52}$$

This problem is addressed by two different methodologies in the literature: enclosure-based steering and lookahead-based steering. Both methods aim to steer the swimming robot towards the trajectory, guaranteeing the above condition. However, the latter presents computational advantages in contrast to the other. Focusing on the lookahead-based method, it establishes the control law as

$$\theta_{N,\mathrm{ref}}^{\mathrm{w,k}} = \beta + \tan^{-1}\left(\frac{-e_{\mathrm{w}}}{\triangle}\right) \tag{4.53}$$

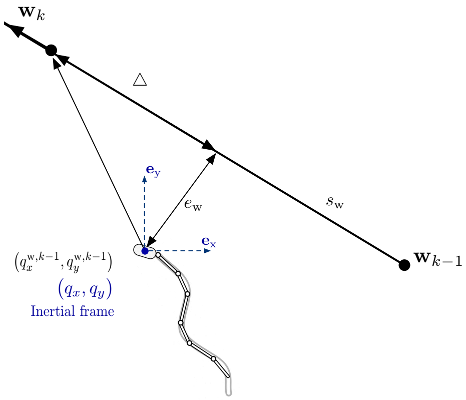

Figure 4.13: Graphical description of line-of-sight guidance.

where the first component corresponds to the path-tangential angle, whereas the second is the velocity-path relative angle, which guarantees that the swimming robot moves towards a point on the path that is located a lookahead distance, $\triangle$, $\triangle > 0$ [184]. The meaning of both components can be observed depicted in Figure 4.13, from which it can be stated that small values of $\triangle$ involve aggressive steering. Once the turning angle is calculated, the next step is to steer the swimming robot toward that angle. For that purpose, a proportional controller is proposed with the following control law:

$$\phi_{w,t} = K_{p,h}\left(\theta_{N,\text{ref}}^{\text{w,k}} - \theta_N^{\text{w,k}}\right) = K_{p,h}\left(\beta + \tan^{-1}\left(\frac{-e_{\text{w}}}{\triangle}\right) - \theta_N^{\text{w,k}}\right) \tag{4.54}$$

where $\theta_{N,\text{ref}}$ is the desired heading, $\overline{\theta}_N$ is the moving average of the head angle, $K_{p,h}$ is an error proportional gain. The reason for considering the moving average of the head angle is motivated by the oscillating motion of the swimming robot. Notice that $\theta_{(N-1),h}$ is the angle offset that is added to the motion of the last link, which is equivalent to the $c_{w,t}x$ term described in the definition of the beating waveform to induce a rotation in the swimming robot motion.

4.4.4 Path generation

Finally, the last step of the trajectory tracking control is the classification of the trajectory by straight or curved sections. In this application, accuracy is less

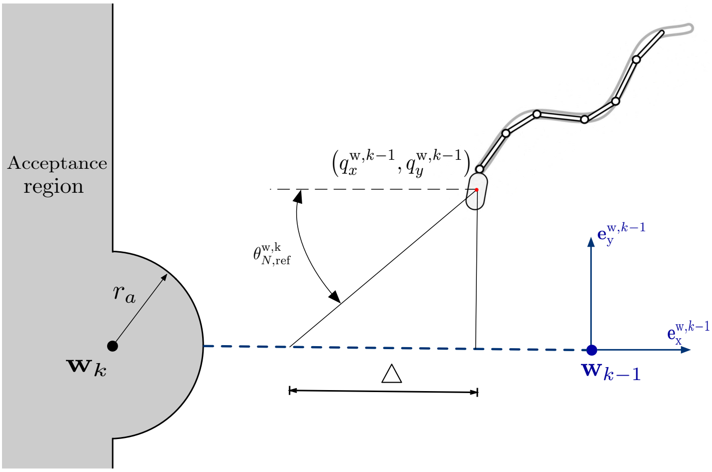

Figure 4.14: Graphical description of acceptance region.

important than reaching the target. Therefore, segmenting a set of points that form straight sections will be adopted as a waypoint guidance methodology. The orientation of these straight sections will be the reference of the heading control, which will ensure trajectory tracking.

The waypoints guidance methodology is thoroughly applied for ships and underwater vehicles. The waypoint selection process can incorporate many factors, such as obstacle avoidance, mission planning, and efficient trajectory from an environmental flow point of view, among others. Furthermore, each waypoint must be feasible in the sense that it must be possible to maneuver to the next waypoint without exceeding the maneuverability of the swimming robot. After decision and optimization processes, the final result will be a trajectory described by a set of waypoints, which are defined in the global frame and stored in an internal memory or in an external device with wireless communication.

Once the trajectory is segmented into points, the swimming robot will follow the straight line from a waypoint until the next one is reached. At that time, a new straight line is defined according to the new waypoint, and the heading controller steers the swimming robot toward the new line. The switching operation between waypoints is based on the acceptance region method [123, 184]. It consists of proceeding to the next waypoint as soon as the system position enters inside an acceptance region. The acceptance region, as illustrated Figure 4.14, is composed of a circle of radius r_a and the right half-plane of the reference system with origin in the current waypoint. Furthermore, when a new waypoint is considered, the path frame is redefined, and the reference of heading control is updated. This method ensures that when the system reaches the acceptance region, it connects to the next waypoint and propels itself along the new straight line, regardless of how the waypoints are defined.

The path following based on waypoints is implemented by the following algorithm:

Algorithm 1 Path following based on waypoints algorithm

```
Define the initial position of the swimming robot, $\mathbf{w}_0$;
Set the straight line between ($\mathbf{w}_0$,$\mathbf{w}_1$) and the path frame ($\mathbf{e}_{\mathrm{x}}^{\mathrm{w},1}$, $\mathbf{e}_{\mathrm{y}}^{\mathrm{w},1}$,$\mathbf{e}_{\mathrm{z}}^{\mathrm{w},1}$);
if $\upsilon_x \neq 0$ then
    Waiting for speed;
end if
Update reference of heading control;
i = 2;
while $i \neq (k+1)$ do
    {where $k$ is the number of waypoints}
    Calculate $q^{\mathrm{w}}$;
    if $q^{\mathrm{w}} \in \mathbf{w}_i^{\text{acceptance region}}$ then
        $i = i + 1$;
        Set the straight line between ($\mathbf{w}_{i-1}$,$\mathbf{w}_i$) and the path frame ($\mathbf{e}_{\mathrm{x}}^{\mathrm{w},i}$, $\mathbf{e}_{\mathrm{y}}^{\mathrm{w},i}$,$\mathbf{e}_{\mathrm{z}}^{\mathrm{w},i}$);
        Update reference of heading control;
        The heading control steers the swimming robot toward the new line;
    end if
end while
```

4.5 Summary

This chapter presents an analysis of the influence of the beating waveform performed by the flagellum on the propulsion and the control strategy for path following. The motion analysis states a strong relationship between the amplitude coefficients of the waveform and the wave propagation velocity with the propulsive velocity of the swimming robot. In this respect, the fractional beating waveform can control the propulsion speed using a single parameter, the fractional coefficient. In particular, this coefficient makes it possible to produce equivalent propulsive forces from harmonic motion to linear Carangiform. Regarding path following, the control strategy is based on nested control loops that address link position control, propulsion speed, and heading control. In addition, path following control is combined with waypoint guidance methodology, which defines the heading control reference by dividing the path into straight segments.

5

PROTOTYPES AND EXPERIMENTAL PLATFORM

"Things don't have to change the world to be important."

Steve Jobs

Contents

This chapter details the model and the design of the prototypes of articulated swimming robot developed based on the model presented in chapter 3. In particular, two prototypes will be presented: the first consists of a series of rigid links of 1 DoF modules that include a DC motor, and the second is a series of flexible links on a IPMC sheet. In addition, a novel CVS model is presented that covers the following three contributions. Firstly, a new electrical model that extends the classical Windkessel model of four elements to the left common carotid artery. This is motivated by the need to have a complete model from a medical point of view for validation purposes, as well as to describe cardiovascular phenomena in this area, such as atherosclerosis, one of the main risk factors for cardiovascular diseases. Secondly, the hydraulic model, equivalent to electrical one, is obtained and, thus, a viable platform for research and clinical trials is designed based on it. Thirdly, the CVS platform allows to emulate low *Re* conditions to test and evaluate the performance of swimming robots.

5.1 6-link swimming robot

This section deals with the design of a flagellum-type articulated artificial eukaryotic swimming robot with six rigid links, starting from its model (as a particularization of the one previously presented), a simulator to validate control strategies before prototyping and, finally, the description of the prototype to be manufactured.

5.1.1 Model

Here, the particular case of the model detailed in Chapter 3 for six rigid links at a medium *Re* environment is presented. Recalling the swimming robot dynamics (3.33) for the swimming robot parameters give in Table 4.1 and Table 5.1, the dynamics model is reduced to:

$$\begin{bmatrix} \Psi_{11} & \Psi_{12} & \Psi_{13} & \Psi_{14} & \Psi_{15} & \Psi_{16} & \Psi_{17} & 0 & 0 \\ \Psi_{12} & \Psi_{22} & \Psi_{23} & \Psi_{24} & \Psi_{25} & \Psi_{26} & \Psi_{27} & 0 & 0 \\ \Psi_{13} & \Psi_{23} & \Psi_{33} & \Psi_{34} & \Psi_{35} & \Psi_{36} & \Psi_{37} & 0 & 0 \\ \Psi_{14} & \Psi_{24} & \Psi_{34} & \Psi_{44} & \Psi_{45} & \Psi_{46} & \Psi_{47} & 0 & 0 \\ \Psi_{15} & \Psi_{25} & \Psi_{35} & \Psi_{45} & \Psi_{55} & \Psi_{56} & \Psi_{57} & 0 & 0 \\ \Psi_{16} & \Psi_{26} & \Psi_{36} & \Psi_{46} & \Psi_{56} & \Psi_{66} & \Psi_{67} & 0 & 0 \\ \Psi_{17} & \Psi_{27} & \Psi_{37} & \Psi_{47} & \Psi_{57} & \Psi_{67} & \Psi_{77} & 0 & 0 \\ 0 & 0 & 0 & 0 & 0 & 0 & 0 & \Psi_{88} & 0 \\ 0 & 0 & 0 & 0 & 0 & 0 & 0 & 0 & \Psi_{99} \end{bmatrix} \begin{bmatrix} \ddot{\theta}_1 \\ \ddot{\theta}_2 \\ \ddot{\theta}_3 \\ \ddot{\theta}_4 \\ \ddot{\theta}_5 \\ \ddot{\theta}_6 \\ \ddot{\theta}_7 \\ \ddot{q}_x \\ \ddot{q}_y \end{bmatrix} = \begin{bmatrix} \Omega_1 \\ \Omega_2 \\ \Omega_3 \\ \Omega_4 \\ \Omega_5 \\ \Omega_6 \\ \Omega_7 \\ \Omega_8 \\ \Omega_9 \end{bmatrix} + \begin{bmatrix} E_1 \\ E_2 \\ E_3 \\ E_4 \\ E_5 \\ E_6 \\ E_7 \\ E_8 \\ E_9 \end{bmatrix} + \begin{bmatrix} -1 & 0 & 0 & 0 & 0 & 0 \\ 1 & -1 & 0 & 0 & 0 & 0 \\ 0 & 1 & -1 & 0 & 0 & 0 \\ 0 & 0 & 1 & -1 & 0 & 0 \\ 0 & 0 & 0 & 1 & -1 & 0 \\ 0 & 0 & 0 & 0 & 1 & -1 \\ 0 & 0 & 0 & 0 & 0 & 1 \\ 0 & 0 & 0 & 0 & 0 & 0 \\ 0 & 0 & 0 & 0 & 0 & 0 \end{bmatrix} \begin{bmatrix} u_1 \\ u_2 \\ u_3 \\ u_4 \\ u_5 \\ u_6 \end{bmatrix} \qquad (5.1)$$

where coefficients Ψ_i, Ω_i and $E_i$are developed in Appendix A.4. As mentioned above, this structure is still quite complex to analyze the dynamics of the swimming robot, even if only six links are considered. Therefore, applying the change of basis and the feedback linearization described in chapter 3, the control-affine system structure is considered again. It represents the actuated and nonactuated DoFs independently and linearizes the input-output dynamics. The considered state vector is $\mathbf{x} = [\alpha_1, \alpha_2, \alpha_3, \alpha_4, \alpha_5, \alpha_6, \theta_7, q_x, q_y, \dot{\alpha}_1, \dot{\alpha}_2, \dot{\alpha}_3, \dot{\alpha}_4, \dot{\alpha}_5, \dot{\alpha}_6, \dot{\theta}_7, \dot{q}_x, \dot{q}_y]^T \in \Re^{18}$ and the swimming robot model dynamics is given as

$$\begin{bmatrix} \dot{\alpha}_1 \\ \dot{\alpha}_2 \\ \dot{\alpha}_3 \\ \dot{\alpha}_4 \\ \dot{\alpha}_5 \\ \dot{\alpha}_6 \\ \dot{\theta}_7 \\ \dot{q}_x \\ \dot{q}_y \\ \ddot{\alpha}_1 \\ \ddot{\alpha}_2 \\ \ddot{\alpha}_3 \\ \ddot{\alpha}_4 \\ \ddot{\alpha}_5 \\ \ddot{\alpha}_6 \\ \ddot{\theta}_7 \\ \ddot{q}_x \\ \ddot{q}_y \end{bmatrix} = \underbrace{\begin{bmatrix} \dot{\alpha}_1 \\ \dot{\alpha}_2 \\ \dot{\alpha}_3 \\ \dot{\alpha}_4 \\ \dot{\alpha}_5 \\ \dot{\alpha}_6 \\ \dot{\theta}_7 \\ \dot{q}_x \\ \dot{q}_y \\ 0 \\ 0 \\ 0 \\ 0 \\ 0 \\ 0 \\ \mathcal{J}_\theta \\ \mathcal{J}_{q_x} \\ \mathcal{J}_{q_y} \end{bmatrix}}_{f(\mathbf{x})} + \underbrace{\begin{bmatrix} 0 & 0 & 0 & 0 & 0 & 0 \\ 0 & 0 & 0 & 0 & 0 & 0 \\ 0 & 0 & 0 & 0 & 0 & 0 \\ 0 & 0 & 0 & 0 & 0 & 0 \\ 0 & 0 & 0 & 0 & 0 & 0 \\ 0 & 0 & 0 & 0 & 0 & 0 \\ 0 & 0 & 0 & 0 & 0 & 0 \\ 0 & 0 & 0 & 0 & 0 & 0 \\ 0 & 0 & 0 & 0 & 0 & 0 \\ 1 & 0 & 0 & 0 & 0 & 0 \\ 0 & 1 & 0 & 0 & 0 & 0 \\ 0 & 0 & 1 & 0 & 0 & 0 \\ 0 & 0 & 0 & 1 & 0 & 0 \\ 0 & 0 & 0 & 0 & 1 & 0 \\ 0 & 0 & 0 & 0 & 0 & 1 \\ \mathcal{E}_{\theta,1} & \mathcal{E}_{\theta,2} & \mathcal{E}_{\theta,3} & \mathcal{E}_{\theta,4} & \mathcal{E}_{\theta,5} & \mathcal{E}_{\theta,6} \\ \mathcal{E}_{q_x,1} & \mathcal{E}_{q_x,2} & \mathcal{E}_{q_x,3} & \mathcal{E}_{q_x,4} & \mathcal{E}_{q_x,5} & \mathcal{E}_{q_x,6} \\ \mathcal{E}_{q_y,1} & \mathcal{E}_{q_y,2} & \mathcal{E}_{q_y,3} & \mathcal{E}_{q_y,4} & \mathcal{E}_{q_y,5} & \mathcal{E}_{q_y,6} \end{bmatrix}}_{g(\mathbf{x})} \begin{bmatrix} v_1 \\ v_2 \\ v_3 \\ v_4 \\ v_5 \\ v_6 \end{bmatrix} \tag{5.2}$$

Table 5.1: Waveform and environment parameters.

Parameter	Value	Description	Unit	Parameter	Value	Description	Unit
N_u	6	Actuated links	-	N_f	0	Flexible links	-
r_i	12.5	Link radius	mm	l_i	100	Link length	mm
r_7	12.5	Head radius	mm	l_7	100	Head length	mm
R	68.7	Link mass	g	n	22.9	Head mass	g
$v_{f,x}$	0	Fluid velocity in x-axis	m/s	$v_{f,y}$	0	Fluid velocity in y-axis	m/s
$\dot{v}_{f,x}$	0	Fluid acceleration in x-axis	m/s	$\dot{v}_{f,y}$	0	Fluid acceleration in y-axis	m/s
$c^{\parallel}_{v,i}$	0.0276	Tangential viscous friction coefficient	-	$c^{\perp}_{v,i}$	0.05530	Normal viscous friction coefficient	-
$c^{\parallel}_{a,i}$	0	Tangential added mass coefficient	-	$c^{\perp}_{v,i}$	0	Normal added mass coefficient	-

In this case, the expression of coefficients $\mathcal{J}_i$ and $\mathcal{E}_i$ are omitted due to length. It is should be remarked that the input is influenced only and directly by the joint angle and the dynamics that are nonactuated.

5.1.2 Controllability and observability

In the previous chapter, it was indicated that an N-link swimming robot does not meet the necessary conditions to verify that it is STLC. However, this property has a more significant implication than the concept of controllability, so it is not possible to rule out that the system is controllable. This section intends to verify the previous study for the specific case of a 6-link swimming robot described by the parameters listed in table 5.1. Considering the following accessibility distribution spanned from the vector fields of system (3.44)

$$\begin{aligned}\Delta_{6-\text{Link}}(\mathbf{x_e}) =\Big[& g_1,\, g_2,\, g_3,\, g_4,\, g_5,\, g_6\, [f, g_1],\, [f, g_2],\, [f, g_3],\, [f, g_4],\, [f, g_5],\, [f, g_6],\\ & \big[f,\, [f, g_1]\big],\, \big[f, [f, g_2]\big],\, \big[f, [f, g_3]\big]\big[f, [f, g_4]\big],\, \big[f, [f, g_5]\big],\, \big[f, [f, g_6]\big]\Big]_{(\mathbf{x}_e, \nu_e)} \in \Re^{19\times 19},\end{aligned} \tag{5.3}$$

where the formulation of Lie brackets is described in section A.3 of the Appendix A, the vectors are linearly independent, meeting the Lie algebra rank condition, as can be verified with a mathematical analysis software. Nevertheless, as mentioned above, this condition is necessary, but not sufficient to demonstrate the system's controllability. In addition, the bad bracket must be θ-neutralized, which means it must be expressed as a linear combination of a bracket with a lower degree. However, this condition is also not met, as it was previously studied for the case of an N-link swimming robot.

In the observability study, the same conclusions are drawn as in the case of an N-link swimming robot: the system is observable; in other words, it is possible to deduce all the system states even if no sensors are available on the variables of interest. The observation space considered for the analysis is the next:

$$\begin{aligned}O_{6-\text{Link}}(\mathbf{x}_0) =& [h_1, h_2, h_3, h_4, h_5, h_6\\ & \mathcal{L}_f h_1, \mathcal{L}_{g_1} h_1, \mathcal{L}_{g_2} h_1, \mathcal{L}_{g_3} h_1, \mathcal{L}_{g_4} h_1, \mathcal{L}_{g_5} h_1, \mathcal{L}_{g_6} h_1,\\ & \mathcal{L}_f^2 h_1, \mathcal{L}_f^3 h_1, \mathcal{L}_f^4 h_1, \mathcal{L}_f^5 h_1,]_{(t_0)},\end{aligned} \tag{5.4}$$

where $\mathbf{y} = \mathbf{h}(\mathbf{x}) = [\dot{q}_x, \dot{q}_y, \dot{\theta}_7, q_x, q_y, \theta_7]^T \in \Re^6$, h_i is the i-element of the vector $h(\mathbf{x})$, and L_f^i denotes the Lie derivative.

It is important to mention that the equilibrium point and initial condition are considered as in N-link swimming robot case: the environment is at rest ($\mathbf{V}_f = 0$), and the swimming robot is at rest in a configuration where all the link angles are different ($\dot{q}_x = \dot{q}_y = 0$ and $\alpha_1 \neq \alpha_i \neq \ldots \neq \alpha_6 \neq 0$ with $i = 1, \ldots, 6$).

5.1.3 Simulator

A simulator based on physical modeling was developed in the MATLAB® and Simulink® environment (using Simscape™ toolbox). The simulator of the swimming robot is a modular design that allows a quick and easy robot configuration through a graphical user interface (GUI, shown in Figure 5.1) where both robot geometry and locomotion can be changed. Physical modeling is a way of modeling and simulating systems with real physical components. It employs a physical network approach, where Simscape blocks correspond to physical elements, such as pumps, motors, and op-amps. These blocks can be joined by lines corresponding to the physical connections that transmit power. This approach allows the description of a system's physical structure rather than using its underlying mathematics. For more information, see basic principles of modeling physical networks. Concerning

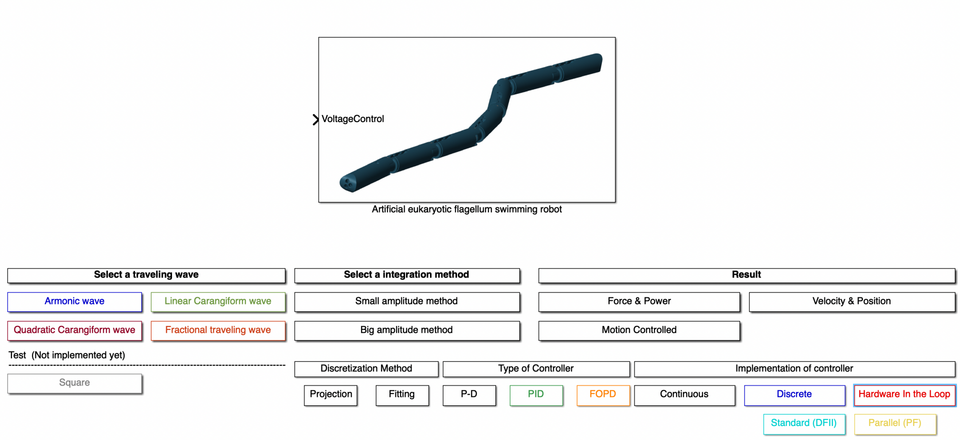

Figure 5.1: GUI of the 6-link eukaryotic flagellum-type swimming robot (configurable options are at the bottom).

geometry, the following parameters can be selected for the robot: size, the number of links the flagellum is divided into (a motor actuates each link), and the length of each link. Furthermore, from a mechanical perspective, it is possible to modify the properties of the actuators and measure the force, velocity, power supplied and consumption of such actuators. Other configurable options, at the bottom of Figure 5.1, are the following:

- *Select a traveling wave*. The desired motion can be selected using this set of buttons. They carry out the discretization method (explained below) and show a brief animation of the microrobot's motion according to the rest of the configuration parameters.

- *Select an integration method.* This option allows the selection of the integration method desired to calculate the forward propulsion thrust and velocity following (4.3). Particularly, "Small amplitude" method considers small displacements along the traversal axis and, consequently, the simplifications made in Section 4.1 are applied. In the case of "Big amplitude" method, the forward propulsion is calculated with no simplifications following (4.7).

- *Type of controller*. It shows the controller that will be applied to track the references obtained from applying the discretization method to the selected waveform. Three different controllers are available: a) P-D, b) PID and c) PD$^{\mu}$, as explained in the above chapters.

- *Implementation of controller*. The above-chosen controller can be implemented in five different forms in both continuous or discrete-time domains, together with hardware, to perform hardwre-in-the-loop (HIL) experiments. Moreover, for the case of a digital implementation, a direct or parallel form can be chosen.

- *Results*. This set of buttons allows to show and analyze different variables and parameters after simulations or HIL experiments. In particular, the button "Force and power" plots the forward propulsion thrust generated due to simulated motion and the energy supplied to the actuator of each link, calculated as the product of the voltage applied by the current demanded. "Motion controlled" shows an animation of both the ideal and the simulated waveform and presents the reference and response of each actuator to evaluate the controller. Likewise, “Velocity and position” represents the forward velocity obtained for the simulated motion and the velocity calculated for the ideal discretized motion.

The flagellum is implemented through distributed actuators, which means a set of links with 1 DoF joints. The link set is developed from a basic unit, repeated as many times as the desired number of joints. The full description of the simulator can be found in section A.5 of Appendix A

From a control perspective, the simulator allows a quick and easy check of the goodness of the waveform, the discretization method and the different stages of the path following control. Likewise, it allows the evaluation of the robot’s performance from different perspectives. In addition, it is important to remark that the simulator can be used as a HIL testbed (see more details also in A.5.3 of Appendix A).

5.1.4 Prototype

This section details the design and architecture of the swimming robot. Although thanks to its modular design, the description will be centered on the head and a link, the latter being replicated as many times as there are links. The design is inspired by the flagella of eukaryotic cells and snake-type robots existing in the literature, consisting of a series of links of 1 DoF modules actuated by motors that control the position and a head that contains the wireless communication module. Figure 5.2 illustrates the prototype of the 6-link swimming robot designed.

5.1.4.1 Mechanical overview

A design requirement of the swimmer prototype is the ease of customization, which is why the reason the design is based on a modular structure from mechanical perspective, but also from the electrical and software points of view. Therefore, links can be connected and disconnected quickly and repeatedly. In addition, not only actuation modules are supported, any other device that matches the mechanical connector, a 5V power supply and I^2C bus compatibility can be connected between modules, allowing freedom in design customization.

Figure 5.2: 6-link eukaryotic flagellum swimming robot.

Each driving link module is a self-contained 1 DoF joint with a rotation operating range of 180°. A micro metal high-power brushed Maxon motor DCX 08M, with a nominal speed of 11600 rpm, drives the modules. The pinion gear on the motor's output shaft transfers rotation through a 64:1 gearbox to increase joint torque. Consecutively, the gearbox shaft is connected to a miter gear that transfers the rotation to a 90° axis in accordance with the swimming robot's dorsal axis. The above combination provides an output torque of 41 mNm and a maximum speed of 181 rpm. Additional information on the characteristics of the motors is given in Table 5.2.

The housing of each link of the prototype is machined from thermoplastic aliphatic polyester (PLA), providing a light and strong structure. Each link is composed of three parts: top, middle and bottom. The connection point between one link and the next is made at the top. The joint axis connects the top part to the following link's middle part. The middle part, which is designed to contain all the components (miter gear, gearbox, bearing, motor, control board and power supply and communication connector). The bottom part seals the middle part, allowing the latter to be opened for easy installation of components and the connection point

Table 5.2: Actuator parameters.

Parameter	Value	Description	Unit	Parameter	Value	Description	Unit
R_m	12.3	Armature resistance	Ω	B_m	9.09×10^{-7}	Rotor damping	Nm/(rad/s)
L_m	41.1×10^{-6}	Armature inductance	H	J_m	3.79×10^{-9}	Rotor inertia	kgm^2
K_{em}	0.0034	Back-emf constant	V/(rad/s)	J_g	4×10^{-10}	Gear head inertia	
n_g	64	Gear ratio		η_g	0.73	Gear efficiency	

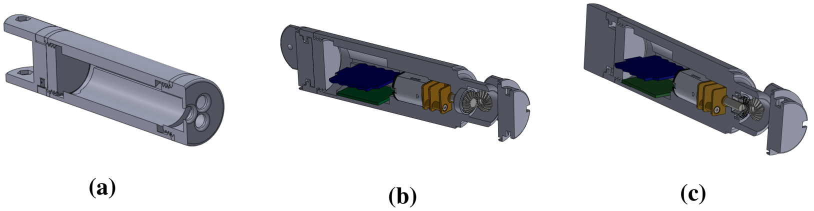

Figure 5.3: Cross-section of the swimming robot: (**a**) head, (**b**) link, and (**c**) last link.

through a custom plug-and-play connector. The watertightness between the parts is ensured by sealant, which guarantees that the prototype can be immersed without water intrusion. On the other hand, the mechanical and electronic components are assembled inside, minimizing the space and, therefore the swimming robot's dimensions. Figure 5.3b illustrates a cross-section of the prototypes modules.

As for the head and last link (see Figure 5.3a, Figure 5.3c, respectively), these are the only modules that differ from other links. Both are based on the same design, although they only allow connection at one end. With respect to the last link, it contains the same components, but, in the lower part, a closing cap is connected. Likewise, unlike other modules, it also contains a power connector to an external cable that powers the swimming robot.

Lastly, concerning the mechanical design, the prototype was designed to scale the microscopic behavior at the macroscale, considering current technology. That implies two issues. Firstly, the value of *Re* has to be preserved to guarantee that the results are comparable for both scales. Secondly, there were limitations concerning the minimum possible size (it was limited due to the dimensions of the required motors) and the maximum number of segments for a defined size. Thus, for the prototype size given in Figure 5.2, to guarantee a low *Re* conditions, it is required to increase the viscosity of the fluid where the robot navigates.

5.1.4.2 Electronic overview

The prototype electronics were designed to minimize the printed circuit board (henceforth, PCB) footprint while facilitating software development. To this end, each link has the same electronic design, mainly based on a dedicated microcontroller and the necessary peripherals for motor control tasks, except for the head, whose purpose differs from the others. The head has a microcontroller with more resources to manage the control of all links and communication with a control software running on an external platform. Likewise, it includes the LEDs to visually notify the operating mode and warnings of malfunction.

The electronics of the link is schematized in Figure 5.4, where it can be seen that it is composed of an Atmel ATmega32u4 microcontroller, a driver motor board, a encoder and a limit switch. The microcontroller has an 8-bit architecture, a capability of 16 million instructions per second (MIPS) at a clock frequency of 16 MHz, and a hardware multiplier that improves the time of arithmetic operations. Its capacity to execute the control task in the desired sampling time makes it suitable for this application. The microcontroller is connected to the motor board and the encoder. It allows to control the voltage applied to the motor through a pulse-width modulation (PWM) signal, the rotation direction, and measure both the speed and the position of the motor. On the other hand, the data exchange between the microcontroller and the main board is done by means of two wires through I^2C bus serial communication bus. All links are connected via the power bus and the data communication bus, which comprises a connection of 4 wires. As for the motherboard electronics, it incorporates a dual processor. The first of these is a low-power 32-bit Arm® Cortex®, which performs all the calculations and control of the link. The second is a NINA-W10, a low-power chipset whose purpose is to interface between the previous

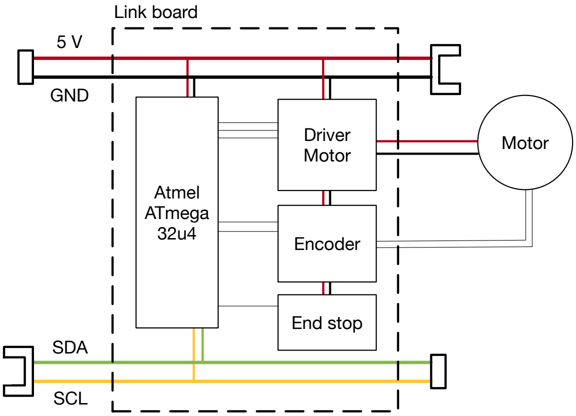

Figure 5.4: Electronic schematics of the links.

microcontroller and the WiFi connectivity module. In addition, it integrates an inertial sensor technology featuring a single chip solution with a 3-axis gyro, 3-axis accelerometer, and 3-axis magnetometer to facilitate the measurement of the relative positioning of the swimming robot. Likewise, as commented, three color LEDs are also added externally to provide immediate feedback on module status.

It is worth mentioning that only the communication between the links is wired. Communication with external control software takes place wirelessly. However, in the current design, it is necessary to use a wired connection for the power supply at 5 V, although a battery could be used instead.

5.1.4.3 Firmware overview

The firmware of the prototype was designed from a research perspective, which means it should be constantly reconfigured to support new physical configurations, module types, and sensor types, allowing an easy adaptation for research in controls, perception and planning. This is why the firmware was developed with a modular structure.

In particular, the firmware was designed according to the mechanical design of the swimming robot, that means the links and the head were implemented dedicated and independent firmware. Therefore, from a control and computing perspective, it is possible to divide the firmware into two abstraction layers, a low-level and a high-level abstraction layer. The low-level abstraction layer refers to the firmware implemented in the links, which has the purpose of controlling the link position. For this purpose, it interacts with the prototype hardware, namely the sensors and actuators, and implements the desired control strategy. On the other hand, the high-level abstraction layer performs the control coordination between the set of coupled links and manages the transmission of information between the links and the external platform.

The link's firmware can implement the desired control strategy for the link position. In this sense, the control strategies are executed by allowing the selection of the desired one, which operates at a sampling frequency of 125 Hz. However, setpoints could be updated less frequently, typically at 20 – 50 Hz. On the other hand, it is also possible to implement the controller in an external control software device that performs the computational load; in this case the firmware would acts only as an interface between the external platform and the sensors and actuators. Position feedback is measured through an optical encoder. The position reading is performed by dedicated hardware that detects the motor rotation. The velocity is estimated by differentiating numerically the position for a fixed period of time and smoothing the result with a Kalman filter to reduce noise. Regarding the position controller implementation, additional features are added to help to compensate common gear-train nonlinearities and sensor noise, such as dead-band and friction. The dead band helps to reduce oscillations due to gear backlash and sensor noise, whereas the friction compensation to overcome static friction.

As for the high-level abstraction layer, it refers to the spindle firmware, whose purpose is to transmit the reference of the link position controllers (or control signal to be applied to the motors) independently of the control strategy employed. Unlike the link's firmware, it has a higher computational load, although it exclusively establishes an interface between the links and the external control software. To this end, the core of the head firmware implements an real-time operating system (RTOS) software, concretely the FreeRTOS distribution, where the firmware is divided into three main tasks: 1) executing motion control commands received from the external control software, 2) sending the sensor measurement, and 3) calculating the relative position of the head by means of the inertial measurement unit. The two first tasks are the primary function that head firmware performs.

To ensure proper communication between the modules without interrupting programmed actions, a master-slave communication hierarchy was established. All communications are always initiated by a clearly defined master role assigned to the external control software. On the other hand, the head and link modules are configured as slaves, waiting for a communication to be initiated to execute the received command and transmit the information from the sensors.

Communication packets are defined as a single meta-message containing all the necessary and desired information for the swimming robot's configuration and actuation. As for the return packets, they only contain information about the status of the swimming robot. Additionally, these messages could contain codes or coding characters that allow the type of information received to be classified and the recipient of the information. Packets consist of three sections: header, payload and CRC. The packet header contains the destination and payload size. The payload section includes the commands or requests to be transmitted. Finally, the cyclic redundancy check (CRC) section is used to verify the integrity of the packet data.

Communication is vital from a control dynamic perspective, in which the latency time plays a key role, and therefore it must be minimal for the command execution and sending of the sensor measurements. This reason has promoted the use of a dual-processor system. On the one hand, the NINA-W10 module manages the wireless communication with the external control software, and. on the other hand, the communication with the link is performed by 32-bit Arm®Cortex®. Between them, a parallel communication based on the (serial peripheral interface) SPI protocol.

As for the external control software, it is developed and implemented in C/C++. It is an extension of the simulator described above, allowing the selection of the output and source of information for the swimming robot prototype or the swimming robot simulator. As in a simulation, recording any information sent or received from the prototype is possible. The communication between the robot and the software is done through UDP protocol, primarily to establish low-latency and loss-tolerating connections and a WiFi connection.

5.2 IPMC-based 3-link swimming robot

This section deals with the design of a flagellum-type articulated artificial eukaryotic swimming robot with three flexible links fabricated on an unique IPMC sheet.

5.2.1 Description

This second prototype is also based on an artificial eukaryotic flagellum. It consists of three flexible planar links. Unlike the previous prototype, the links are flexible based on IPMC technology, so the same links constitute the housing and actuators. This technology offers the advantage of needing to be immersed in an aqueous medium to function correctly, so it is optional to guarantee its watertightness. However, due to its flat geometry, all the electronics needed to drive and monitor

Table 5.3: Geometrical parameters of the IPMC-based AEF swimming robot.

Parameter	**Description**	**Value**	**Unit**
L_T	Length of robot	31	mm
W	Width of robot	3	mm
h	Thickness	250	µm
L_i	Length of actuator	10	mm
N	Number of links	3	-

the prototype is external. A picture of the prototype is shown in Figure 5.5. It was manufactured over the same IPMC sheet attending to the mechanical design depicted in Figure 5.5a. For that purpose, a micro laser etching machine was used to cut the robot flagellum and isolate each of the segments electrically. The dimensions are given in Table 5.3.

It is important to remark that each segment of the flagellum can behave as an independent actuator when it is electrically powered or as a passive flexible link when it is not. Inn this respect,, only the first segment will be used as a robot actuator for robot modeling, so the rest will behave as passive links. On the contrary, for control purposes, each link will be driven in order to reproduce a nonreciprocal motion for propulsion. The deflection of any of the links can be measured at its tip in both cases.

5.2.2 Experimental setup

The experimental setup used in this work for identification and control purposes of the manufactured swimming robot is illustrated in Figure 5.6a, which consists of:

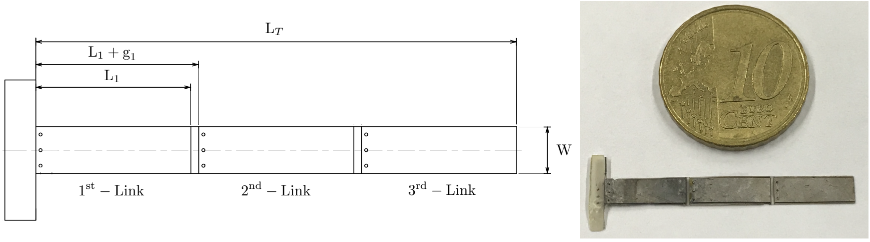

(a) **(b)**

Figure 5.5: The three-link IPMC-based AEF swimming robot: (**a**) mechanical design, (**b**) image of the real prototype.

- A water tank, used as an environment since the ultimate goal of the swimming robot is to be able to swim in a fluid.

- Laser distance meters (OADM 20U2441), to measure the deflection of the links.

- Gold electrodes, attached both sides of an actuator by means of a clamp, to transmit the voltage from the supplier to the IPMC surface.

- A USB multifunction I/O data acquisition board of National Instruments (NI-USB6259), which is connected to a computer in which LabVIEW™ 2020 SP1 runs to collect the data and generate the desired excitation voltage.

- A power stage, to provide sufficient power to the actuator from a power DC supplier and the desired voltage indicated by the computer.

The laser distance meter is calibrated for a resolution of 0.8 mm/V and pointed at the end of the desired link. Furthermore, the swimming robot is positioned in the middle of the range, allowing it to measure a maximum displacement of 4 mm. On the other hand, the voltage applied to the actuator is sampled with the USB multifunction I/O data acquisition board at a frequency of 1 kHz. Likewise, the output signal of the laser distance meter and the excitation voltage applied to IPMC are measured at the same sampling frequency and then sent to the computer in order to collect the data. Figure 5.6b shows an actual image of the robot pointed by the laser during one of the experiments. Note that, although in the scheme only one

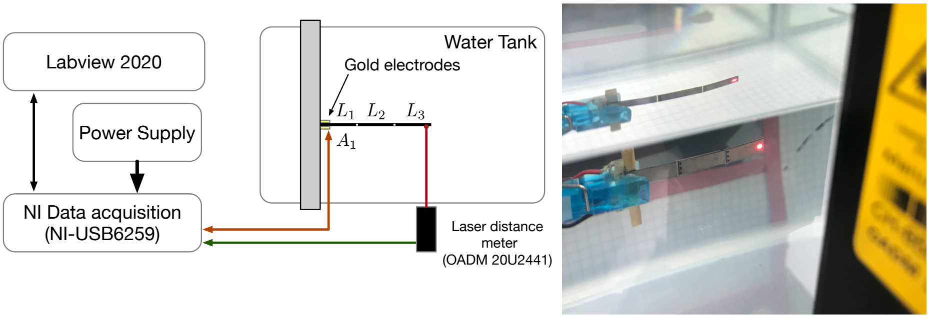

(a) **(b)**

Figure 5.6: Experimental setup: (**a**) scheme, (**b**) swimming robot prototype pointed by the laser distance meter during an experiment.

laser meter is shown pointing to the flagellum end, there are other two to measure the deflection at each of the other two segments' end, depending on the needs of the application to be developed. Likewise, two additional pairs of electrodes are also available for distributed actuation.

5.3 Cardiovascular system platform

A fundamental aspect for research and clinical diagnosis and validation of the performance of swimming robots in low *Re* environments, and specifically within the CVS, is to have a platform that allows emulating the such same conditions so that the macroscopic results are equivalent to those at microscale. Given this motivation, firstly this section presents an electrical model of the CVS extended to the left common carotid artery. It is developed from the classical four-element Windkessel model and the modifications introduced in [4]. Secondly, the electrical model is reinterpreted from a fluid mechanics perspective by developing a hydraulic simulator that allows to build a experimental platform to test swimming robots of small dimensions, i.e. to emulate the conditions in which swimming robots would navigate in the human circulatory system.

5.3.1 Electrical model

The model on which this work is based on the Windkessel model proposed in [198, 199] and the modifications suggested in [4, 5, 200]. Moreover, this work presents a model that extends the model of [4] to the left common carotid artery. The choice of this kind of artery is motivated by the need to have a more complete model from a medical point of view for validation purposes, as well as to describe other cardiovascular phenomena in this area, such as atherosclerosis, one of the main risk factors for CVDs [157]. It should be also noted that the whole model defined based on the anatomic structure of the circulatory system, respecting the criteria used in [199] for the definition of the four element Windkessel model.

The equivalent electrical circuit of the CVS and left common carotid artery is shown in Figure 5.7, where a clear distinction is made between dynamics of the systemic circulation and left carotid dynamic. The cardiovascular model focuses mainly on the left chambers of the heart, assuming that the right ventricle and the

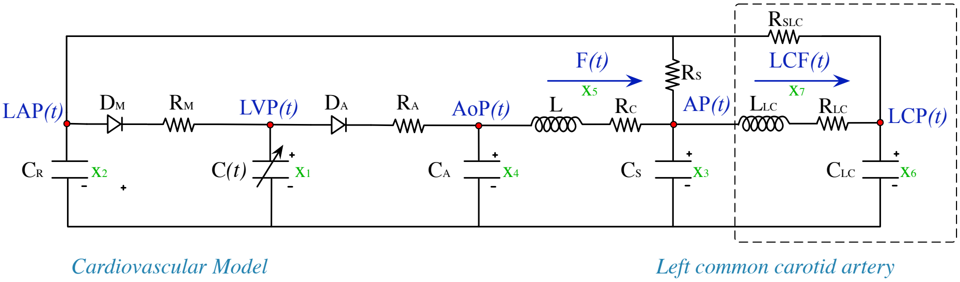

Figure 5.7: Electrical model equivalent to the CVS with extension to left common carotid artery.

pulmonary circulation act correctly and, hence, they are omitted. Resistance to flow from the descending aorta through the capillary vessels, venous and pulmonary circulation to reach the left atrium is identified through the resistors that feedback the electrical system: R$_S$ denotes the systemic resistance, whereas R$_{SLC}$ represents the resistance from the left common carotid. The contractile capacity of the heart is modeled by the variable capacitor, $C(t)$, whose capacitance is the inverse of the LV elastance ($E(t)$). The elastance defines the elasticity of the heart as a function of the pressure that it supports, according to the Frank-Starling's law. A more detailed description is provided in subsection 5.3.2. The aortic and mitral valves are modeled as ideal diodes, D$_A$ and D$_M$, in series with a resistance, R$_A$ and R$_M$, respectively. However, to achieve a more accurate response, the capacitor C$_A$ is added to the first valve, which reflects the elasticity of ascending aorta and models the pressure variation due to the open-close operation of the aortic valve. The rest of elements model the elasticity, inertia and resistance of the descending aorta (C$_S$, L and R$_C$) and the left common carotid artery (C$_{LC}$, L$_{LC}$ and R$_{LC}$). These elements, in combination with R$_S$ and R$_{SLC}$, define the afterload factors.

With respect to the dynamics of the CVS, it is described choosing as state variables the ones listed in Table 5.4 (which correspond to those indicated in Figure 5.7) and applying Kirchhoffs' laws to the electric circuit, except for the state x_1, which depends on the working mode of the diodes and the contractile capacity of the heart $C(t)$. The diodes allow to define the behavior of heart valves and give the system its nonlinear character.

The combination of the conduction state of the diodes allows to describe the four

Table 5.4: State variables of the cardiovascular model.

Variable	Abbreviation	Clinical meaning (unit)
$x_1(t)$	LVP(t)	Left ventricular pressure (mmHg).
$x_2(t)$	LAP(t)	Left atrial pressure (mmHg).
$x_3(t)$	AP(t)	Descending aorta pressure (mmHg).
$x_4(t)$	AoP(t)	Ascending aorta pressure (mmHg).
$x_5(t)$	F(t)	Total flow (ml/s).
$x_6(t)$	LCP(t)	Left common carotid artery pressure (mmHg).
$x_7(t)$	LCF(t)	Carotid artery flow rate (ml/s).

stages of the cardiac cycle, establishing four different equivalent electrical circuits for each stage and, therefore, a set of linear differential equations. This implies a different analysis of the circuit for each of the stages of the cardiac cycle. To overcome this drawback, the diodes are described as a ramp function, $d(x)$, with which the system can be described by a single definition throughout the entire cardiac cycle. Taking into account these considerations, the complete model can be expressed as:

$$\begin{aligned}
\dot{x}_1 &= \frac{1}{C(t)}\Big(-\dot{C}(t)x_1 + \frac{1}{R_M}d(x_1 - x_2) - \frac{1}{R_A}d(x_4 - x_1)\Big)\\
\dot{x}_2 &= \frac{1}{C_R}\Big(\frac{1}{R_S}d(x_3 - x_2) + \frac{1}{R_{SLC}}(x_6 - x_2) - \frac{1}{R_M}d(x_2 - x_1)\Big)\\
\dot{x}_3 &= \frac{1}{C_S}\Big(x_5 - x_7 - \frac{1}{R_S}d(x_3 - x_2)\Big)\\
\dot{x}_4 &= \frac{1}{C_A}\Big(\frac{1}{R_A}d(x_4 - x_1) - x_5\Big)\\
\dot{x}_5 &= \frac{1}{L}(x_4 - x_3 - R_C x_5)\\
\dot{x}_6 &= \frac{1}{C_{LC}}\Big(\frac{1}{R_{SLC}}(x_2 - x_6) + x_7\Big)\\
\dot{x}_7 &= \frac{1}{L_{LC}}(x_3 - x_6 - R_{LC}x_7)
\end{aligned} \tag{5.5}$$

The detailed analysis of the electrical circuit in Figure 5.7 can be found in Appendix B. It should be remarked that the above model defines an autonomous switched time-varying system over different phases within the cardiac cycle. As for the values of the parameters involved in the CVS for the different simulations, they are included in Table 5.5.

Table 5.5: Values of the parameters of the CVS model for validation purposes.

Parameter	Value	Physiological meaning	Parameter	Value
	Resistors (Ω)		**Stergiopulos' elastance**	
R$_S$	1	Total peripheral resistance	A	1.17
R$_{SLC}$	10	Left common carotid peripheral resistance	B	0.7
R$_M$	0.005	Mitral valve resistance	C	1.55
R$_A$	0.001	Aortic valve resistance	α_E	1.9
R$_C$	0.0398	Characteristic resistance	β_E	21.9
R$_{LC}$	0.2	Left common carotid resistance		
	Capacitors (F)		**Atilios' elastance**	
C$_R$	8.8	Left atrial compliance	A	1.23
C$_S$	1.33	Systemic compliance	B	3.50
C$_A$	0.08	Aortic compliance	C	3.02
C$_{LC}$	0.09	Left common carotid		
	Inductors (H)		**Sheffer's elastance**	
L	0.0005	Inertia of blood in aorta	A	1.84
L$_{LC}$	0.03	Inertia of blood in left common carotid	B	2.68
	Left ventricle		C	0.15
E_{max}	2	Maximum volume in diastole	**Elastance based on Mittag-Leffler**	
E_{min}	0.06	Minimum volume in diastole	A	14.45
V_0	10	Reference volume at zero pressure (ml)	B	4.58
HR	75	Heart rate (bpm)	C	1.11
			α_E	0.24

5.3.2 Elastance

The elastance represents the state of contraction of the LV, relating the pressure and volumes of the LV according to the Frank-Starling's law, which is defined as [4, 201]:

$$E(t) = \frac{LVP(t)}{LVV(t) - V_0}, \tag{5.6}$$

where $LVV(t)$ is the left ventricle volume, $LVV(t)$ is the left ventricle pressure, and V_0 is the reference volume that corresponds to the theoretical ventricular volume at zero pressure.

The definition of elastance was addressed in different studies [3, 202, 203] trying to adjust it empirically to a standard function. In particular, most of them agree that the definition can be normalized and scaled between the points of maximum and minimum functioning of the LV as:

$$E_H(t) = (E_{max} - E_{min})E_n(t_n) + E_{min}, \tag{5.7}$$

where E_{max} and E_{min} are constants related to ESV, EDV and ESPVR, and $E_n(t_n)$ is the normalized elastance, with $t_n = t/T_{max}$, being $T_{max} = 0.2 + 0.15t_c$, where t_c,

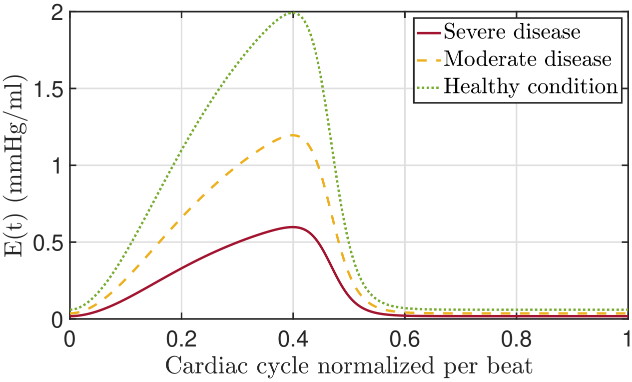

Figure 5.8: Elastance according to Stergiopulos's work [3]. The parameters used are shown in Table 5.6.

calculated as $t_c = 60/HR$, is the time period of the heart cycle. In certain pathologies, the elastance can have the same morphology for a healthy or sick heart [204]. Then, for some cardiac conditions, the elastance model (5.7) is modified to $E(t) = \delta E_H(t)$, with $0 \leq \delta \leq 1$, where lower values of δ represent CVDs (the more severe the disease, the lower the value of δ), whereas $\delta = 1$ corresponds to the healthy state.

The elastance can be described mainly according to four different definitions as detailed next: 1) Stergiopulos' elastance, 2) Atilio's elastance, 3) Sheffer's elastance, and 4) elastance based on the Mittag-Leffler function.

The Stergiopulos' elastance definition is based on the studies carried out in [3], where it is described it for a healthy person as:

$$E_n(t_n) = C\left(\frac{\left(\frac{t_n}{B}\right)^{\alpha_E}}{1+\left(\frac{t_n}{B}\right)^{\alpha_E}}\right)\left(\frac{1}{1+\left(\frac{t_n}{A}\right)^{\beta_E}}\right) \tag{5.8}$$

and whose waveforms are depicted in Figure 5.8. The first term in the brackets describes the ascending part of the curve and the second, the descending part one. The parameter C is the amplitude of elastance, related to the maximum arterial pressure, α_E and β_E denote the ascending and descending slopes through the LV relaxation time, respectively, and A and B are constants to define the relative appearance of each curve within the heart period.

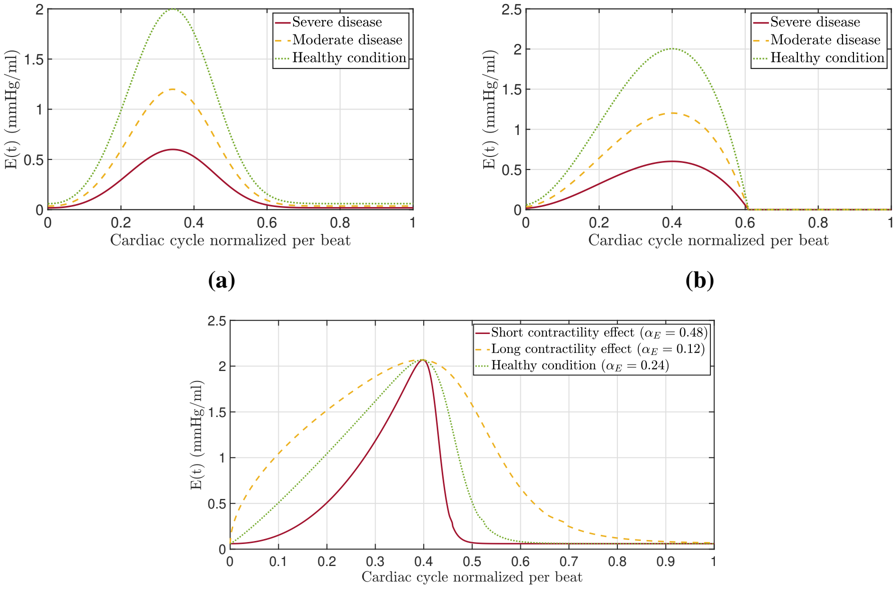

(a) **(b)**

(c)

Figure 5.9: Elastance according to: (**a**) Atilio, (**b**) Sheffers, and (**c**) Mittag-Leffler function.

The second definition was proposed in [202]. The Atilio's elastance is defined by (see Figure 5.9a):

$$E_n(t_n) = C t_n^{B-1} e^{-A t_n^B} \tag{5.9}$$

A similar form was proposed in [203], but defining elastance as a polynomial of increasing powers. The Sheffer's elastance is depicted in Figure 5.9b, which is given by:

$$E_n(t_n) = -A t_n^3 + B t_n + C t_n. \tag{5.10}$$

The last type of studied elastance is modelled based on the Mittag-Leffler function, which has been proved to be effective to model the time-dependent relaxation behaviour of viscoelastic materials. The Mittag-Leffler elastance is given by:

$$E_n(t_n) = C t_n^{(B\alpha_E)} \mathcal{E}_{\alpha_E}\Big(\frac{-t_n^{(B/\alpha_E)}}{A}\Big), \tag{5.11}$$

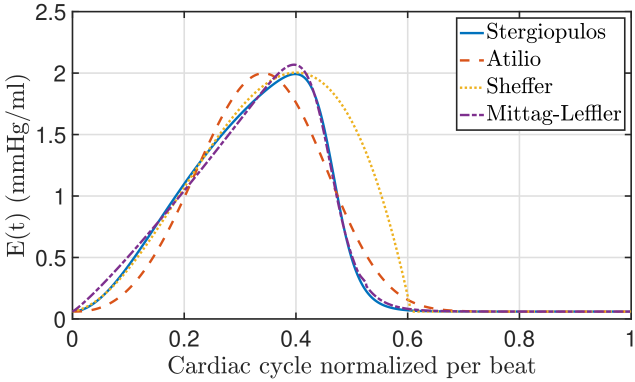

Figure 5.10: Elastance comparation.

where $\mathcal{E}$ is the one parameter Mittag-Leffler function. In this case, parameter α_E modifies the ascending and descending part of the curve, as illustrated in Figure 5.9c.

Finally, a comparison between the four types of elastances is shown in Figure 5.10, where it can be seen that all the definitions are strongly related to each other, but there are small differences between them, such as the slopes and the time that the maximum elastance is reached. These small differences may define pathologies or malfunctions of the heart. All of them have in common that the maximum elasticy of contractile capacity is pondered by parameter δ, but the modification of the slope requires a more complex adjustment. In this respect, the elastance based on the Mittag-Leffler function allows both slopes to be easily modified thanks to a single parameter (α_E), as was shown in Figure 5.9c.

5.3.3 Hydraulic model

This section explains the equivalences between the electrical and hydraulic elements, allowing to model the CVS from a mechanical point of view. Once the relationships and equivalences between the electrical and hydraulic domains are established, the modeling of the CVS, as well as the contractile behavior of the heart, are addressed.

5.3.3.1 Equivalences

In order to describe the hydraulic model through discrete elements, the following set of equivalencies between the electric and hydraulic domains, among other considerations, was defined.

The main electrical elements that are used are resistors, capacitors and inductances, whose behaviour can be modelled by changes in section, tanks or long pipes [205], as detailed below (see Figure 5.11). With respect to the diodes, they are replaced by unidirectional flow valves. Hydraulic resistance occurs whenever there is a difference in pressure, as in the situation of a fluid circulating from one pipe to another with a smaller diameter. If the pressure on both sides of the narrowing is P_1 and P_2 and the flow is Q (see Figure 5.11a), the hydraulic resistance can be defined as:

$$P_1 - P_2 = R_H Q \tag{5.12}$$

Capacitors in hydraulic terms are reservoirs, since they are capable of accumulating energy in the form of potential energy. Considering the tank of Figure 5.11b, if q_1 and q_2 are the input and output flows, respectively, and V is the volume of fluid inside the tank, it is deduced that:

$$q_1 - q_2 \quad = \quad \frac{dV}{dt} = A\frac{dh}{dt}, \tag{5.13}$$

where h denotes the tank level and A is the tank section. On the other hand, the

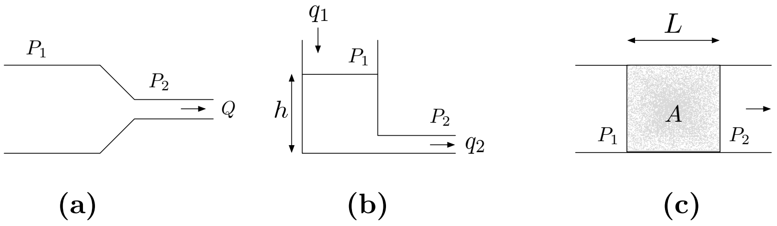

Figure 5.11: Hydraulic elements. (**a**) Resistor. (**b**) Capacitor. (**c**) Inductance.

difference of pressure is:

$$P_1 - P_2 = h\rho g \quad \text{or} \quad h = \frac{P_1 - P_2}{\rho g}, \tag{5.14}$$

where g represents the acceleration due to gravity and ρ is the density of fluid. Therefore, substituting (5.14) into (5.13), the following expression is obtained:

$$q_1 - q_2 = \frac{A}{\rho g}\frac{dP}{dt}, \tag{5.15}$$

which has great similarity with the definition of a capacitor, being able to identify the constant of the equivalent capacity as:

$$C_H = \frac{A}{\rho g} \tag{5.16}$$

With regard to electrical inductance, it is similar to hydraulic inductance. It is deduced from the inertial force required to accelerate the fluid in a pipe. Considering $P_1 - P_2$ the pressure gradient to be generated as a consequence of the acceleration for a section of area A (see Figure 5.11c), a fluid of mass m and with velocity v, applying Newton's second law it can be defined:

$$m\frac{dv}{dt} = A(P_1 - P_2) \tag{5.17}$$

If the pipe has a length of l, then the mass can be calculated as $m = L\rho A$. In this case, equation (5.17) can be rewritten as follows:

$$l\rho\frac{dv}{dt} = (P_1 - P_2), \tag{5.18}$$

where $q = Av$, so equation (5.18) becomes:

$$(P_1 - P_2) = \frac{l\rho}{A}\frac{dq}{dt} \tag{5.19}$$

As this expression has the same relationship as the definition of an inductance, it

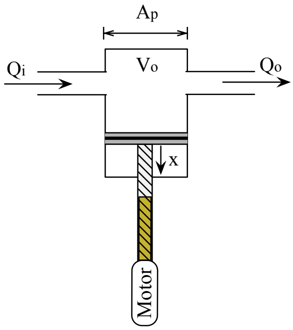

Figure 5.12: Diagram of the left ventricle implemented by piston pump.

is deduced that the equivalent hydraulic inductance constant is:

$$L_H = \frac{l\rho}{A} \tag{5.20}$$

However, the pressure loss or inertia caused by relatively short pipe sections may be considered irrelevant compared to the magnitudes studied.

With regard to the muscle contraction of the left ventricle, it is proposed to emulate it through a piston pump, which will reflect a behaviour similar to that of the heart, ignoring considerations related to morphology. The pump will be driven by a motor and worm drive mechanical transmission. This configuration defines a linear transmission and self-locking nature, that means the translation movement can be only driven by the motor, while the movement is prevented from the opposite side. In addition, it reduces the workload on the engine, since it does not have to continuously support the load generated by the pressure variations, thus facilitating subsequent control tasks. The pump dynamics can be described as a variable volume tank, where the generated pressure (P_P) and permissible volume (V_p) are determined by:

$$\begin{aligned} \dot{P}_p &= \frac{1}{C_p}(Q_i - Q_o - A_p \dot{x_p}), \\ V_p &= V_0 + A_p \int \dot{x}_p dt, \end{aligned} \tag{5.21}$$

where C_p defines the piston capacity according to (5.16); Q_i and Q_o are the inlet and outlet flows, respectively; A_p is the piston section, as shown in Figure 5.12; x_p

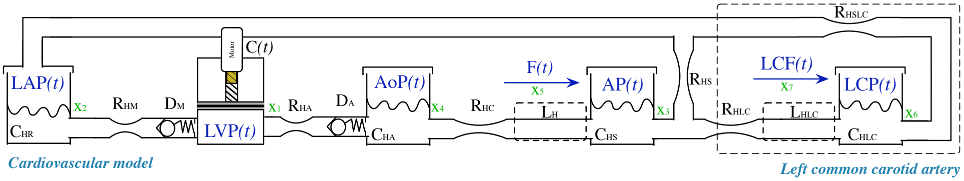

Figure 5.13: Hydraulic cardiovascular model.

is the position of the piston according to the adopted sign criteria in the above figure; and $\dot{x}_p$ corresponds to the travel speed of the piston.

5.3.3.2 Model

Taking into account the considerations explained in the previous sections, the following equivalences are considered so as ([205]): electric resistors, capacitances and inductances are replaced by hydraulic resistors (denoted as R_{Hi}, where the subscript i refers to the name used in the electric model), tanks with constant sections (C_{Hi}) and long pipes (L_{Hi}, where l is the length of the pipe), respectively. The diodes are changed by one-way valves. The hydraulic model of the CVS is illustrated in Figure 5.13 and all their parameters are given in Table 5.6.

Regarding muscular contraction of the left ventricle, in the hydraulic model $C(t)$ is modelled by a pump with piston (tank of variable volume depending on the position of the piston), as shown in Figure 5.12, in such a way that a control strategy is required to emulate the behaviour of the heart [206]. Thus, the derivative of state x_1 in this case can be expressed as:

$$\dot{x}_1 = \frac{1}{\mathrm{C}_p}(Q_i - Q_o - A_p v), \tag{5.22}$$

where C_p is the capacitance of the piston, A_p is the sectional area of the piston, and $v = \dot{x}_p$ is the displacement speed of the piston (this parameter modifies the pressure of the piston chamber). Equation (5.22) can be also written as:

$$\begin{aligned} \dot{x}_1 \quad = \quad & \frac{1}{\mathrm{C}_p}\left(\frac{1}{\mathrm{R}_{H_M}} r(x_2 - x_1) - \frac{1}{\mathrm{R}_{H_A}} r(x_1 - x_4)\right) \\ & - \frac{A_p}{C_p} v \end{aligned} \tag{5.23}$$

The other state equations describing the hydraulic model of the CVS remain inalterable. In contrast to the electric model, now the system has non autonomous nature. Therefore, as commented, it is needed to apply a control strategy to the displacement speed of the piston in order to emulate the contraction of the left ventricle according to Frank-Starling's law.

5.3.4 Control

The main control strategies in the literature are based on classical methodologies, such as PID (Proportional, Integral and Derivative control) [206]. Although studies have also been developed using more modern methodologies, which focus on linearized nonlinear [206] or sliding mode [207] controllers. In this section, two strategies will be considered to obtain normal conditions of a cardiac cycle with the cardiovascular model, concretely feedback linearization and PID. In both cases, fractional dynamics will be introduced into the controller substituting the derivative

Table 5.6: Parameters of the CVS model. Taken from [4, 5].

Parameter	**Value**	**Physiological meaning (unit)**
	Resistors	
R_{HS}	133.32 (MPa/(m^3/s))	Total peripheral resistance
R_{HSLC}	133.32 (MPa/(m^3/s))	Left common carotid peripheral resistance
R_{HM}	0.67 (MPa/(m^3/s))	Mitral valve resistance
R_{HA}	0.13 (MPa/(m^3/s))	Aortic valve resistance
R_{HC}	5.30 (MPa/(m^3/s))	Characteristic resistance
R_{HCLS}	26.67 (MPa/(m^3/s))	Left common carotid resistance
	Capacitances	
C_{HR}	$6.933 \cdot 10^{-2}$ (m^3/MPa)	Left atrial compliance
C_{HS}	$6 \cdot 10^{-4}$ (m^3/MPa)	Systemic compliance
C_{HA}	$9.97 \cdot 10^{-3}$ (m^3/MPa)	Aortic compliance
C_{HLC}	$6.75 \cdot 10^{-4}$ (m^3/MPa)	Left common carotid
	Inductances	
L_{HS}	$6.66 \cdot 10^{-2}$ (MPa/(m^3/s^2))	Inertance of blood in aorta
L_{HSLC}	3.99 (MPa/(m^3/s^2))	Inertance of blood in left common carotid
	Left ventricle	
E_{max}	266.64 (MPa/m^3)	Maximum volume in diastole
E_{mix}	0.79 MPa/m^3)	Minimum volume in diastole
V_0	10 (ml)	Reference volume at zero pressure
HR	75 (bpm)	Heart rate

by the fractional order operator. In order to develop a simple, low-computer load controller, a linearized controller will be used.

5.3.4.1 Feedback linearization controller

The main idea of this approach is to algebraically transform a nonlinear system dynamics into a (fully or partly) linear one, so that linear control techniques can be applied (see for example [174]).

Then, to linearize state variable x_1, (equation (5.23)), it is possible to take the system input v as follows:

$$v = -\frac{\mathrm{C}_p}{A_p}\left(u - \frac{1}{\mathrm{C}_p}\left(\frac{r(x_2 - x_1)}{\mathrm{R}_{H_M}} - \frac{r(x_1 - x_4)}{\mathrm{R}_{H_A}}\right)\right) \tag{5.24}$$

This allows to consider a linear relation between the system output ($y = x_1$) and variable u, being u the equivalent input of the linearized dynamics, and which is considered of relative order one due to the fact that an integration between the output and the equivalent input, that means $\dot{y} = u$, is obtained. Taking into account this linear relation, the control law to be designed is:

$$u = \dot{y}_d - \dot{y} + \lambda(y_d - y) = \dot{e} + \lambda e, \tag{5.25}$$

where y_d is the desired output, e is the error, defined as $e = y_d - y_1$, and $1/\lambda$ is the time constant of the error.

Hence, substituting (5.25) in (5.24), the following expression is obtained:

$$v = -\frac{\mathrm{C}_p}{A_p}\left(\dot{e} - \frac{1}{\mathrm{C}_p}\left(\frac{r(x_2 - x_1)}{\mathrm{R}_{H_M}} - \frac{r(x_1 - x_4)}{\mathrm{R}_{H_A}}\right) + \lambda e\right), \tag{5.26}$$

which allows to follow the reference in accordance with the control law established. This controller will be referred henceforth to as FBL.

For this strategy, fractional dynamics is also introduced by doing

$$u = \mathrm{D}^{\alpha} e + \lambda e, \tag{5.27}$$

where D is the fractional operator, and $\alpha \in \mathbb{R}^+$ the differentiation order. This controller will be referred henceforth to as FBL+FD.

5.3.4.2 PID controller

A PID controller proposed in [206] is used with gains: $k_p = 0.5$, $k_i = 0.6$, and $k_d = 0.003$. It is applied directly over the controlled variable x_1. This controller will be referred henceforth to as PID.

In order to compare with the previous PID controller and the PD control law used in FBL, in this case fractional dynamics is introduced by using a three-parameter fractional controller, namely, a fractional proportional-derivative (FPD) controller.

5.4 Summary

This chapter has described two swimming robot prototypes and an experimental platform designed for swimming robot testing. The design of both prototypes is based on the articulated artificial eukaryotic flagellum. The first prototype consisted of six rigid links plus the head. In addition, a simulator of this prototype in MATLAB®/Simulink® environment was developed for testing purposes. The second prototype consists of three IPMC-based flexible links. Unlike the previous one, all the associated electronics are external and the prototype is essentially the flagellum. A novel electrical model of the CVS has been presented to complement both prototypes. This model extends the classic Windkessel model to the left common carotid artery, motivated by the need to have a complete model from a medical point of view for validation. The model also serves as a simulator, based on physical modeling, of a realizable platform as a testbed for swimming robots. In addition, it allow to emulate a low *Re* environment and hemodynamic conditions of the CVS.

6

SIMULATIONS AND EXPERIMENTS

"We are trying to prove ourselves wrong as quickly as possible, because only in that way can we find progress"

Richard Feynman

Contents

This chapter presents the simulation and experimental results obtained from the two artificial eukaryotic flagellum swimming robot prototypes and the CVS model. The experiments and simulations consist of a set of tests to analyze and evaluate the performance of control strategies and propulsion according to the design beating waveform. Regarding the CVS model, it is validated with experimental data obtained from clinical trials performed on a pig and clinical indices that can be found in the specialized literature.

6.1 6-link swimming robot

This section focuses on the analysis of propulsion performance and the trajectory tracking control strategy based simulations, addressing each of the control loops. In addition, an analysis of how the number of links influences the beating waveform and propulsion is presented.

6.1.1 Joint controller

The joint control is the internal control loop required that must ensure to fulfill tracking specifications. This section details the results of the application this control by addressing actuator modeling, controller design and performance comparison of the control strategies proposed in sections 4.4.1.1 and 4.4.1.2, namely PID and PD$^{\mu}$.

6.1.1.1 Actuator modeling

The dynamics of each actuator depends on its position in the flagellum since the supported load varies accordingly. This is because of the flagellum, but also because of the viscous forces of the environment. Therefore, the actuators are described from model 4.34 in position form, that means considering a pole at origin. For this purpose, the described robot simulator was used with the properties of the actuators, links and environment given in Tables 4.1, 5.1 and 5.2. In particular, to identify the dynamics of each actuator, only the link under study was excited, with an unit step input, considering a rigid link immersed in a viscous environment as the actuator load. To be realistic, the length of this rigid link was set equal to the rest of the links'

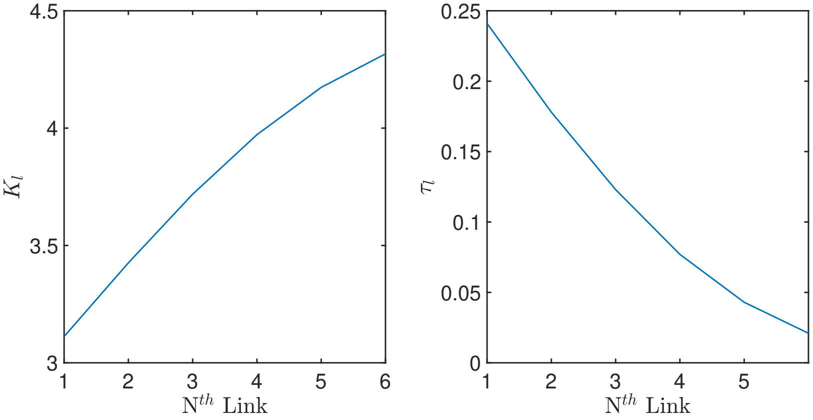

Figure 6.1: Sensitivity of parameters of system (4.34) with respect to the position of the actuator along the flagellum.

length until the free end of the flagellum. The remaining actuators were fixed at zero position.

Figure 6.1 illustrates the sensibility of parameters K_l and τ_l of (4.34) with respect to the position of the actuator along the flagellum and, consequently, the change of actuator load. As observed, the following relation between the system parameters and the actuators' position exists: the closer the actuator is to the robot's head, the smaller the value of K and the slower the actuator dynamics (that is, the higher the value of τ). Therefore, robust control is necessary to allow each actuator to follow its reference with the exact specifications of the remaining actuators to accurately emulate the (nonreciprocal) motion of the desired waveform.

6.1.1.2 Design

The parameters of both the integer and the fractional order controllers obtained after tuning are given in Table 6.1. The design specifications for the RC tuning method were: a phase margin $\phi = 76°$ at the gain crossover frequency of $\omega_{cp} = 200$ rad/s (similar to those obtained with the other methods). The value used for parameter τ_0 corresponds to the first actuator, which means the most disadvantaged case for the three tuning methods described in section 4.4.1.

The optimization procedures were applied to the most disadvantaged case in

Table 6.1: Parameters of the continuous-time controllers.

Controller	Method	K_p	K_i	K_d	Controller	Method	K_p	K_d	μ
PID	IAE	382.55	3.89	3.43	PD^{μ}	IAE	499.93	7.79	0.95
	ITAE	466.69	25.56	3.43		ITAE	499.68	30.31	0.78
	RC	330.47	109.98	5.18		RC	382.32	24.50	0.90

the same way as the dynamics of actuators was identified, i.e., the first actuator, considering the other joints fixed at zero position and tracking a sine wave motion with the maximum allowed amplitude ($\pi/2$ rad) and velocity (2 Hz).

6.1.1.3 Joint control evaluation

Next, the performance of the designed controllers is evaluated in simulation in terms of efficiency, which means the ratio between the mechanical power (P_m) exerted by the link and the electrical power (P_e) supplied to the actuator, as follows:

$$\eta = \frac{P_m(t)}{P_e(t)} = \frac{F_{p,x}(t)\upsilon_x}{V(t)I(t)}, \tag{6.1}$$

where I refers to the current demanded by the motor, and V is the voltage applied to the actuator. Notice that the higher the index η, the higher the efficiency of the control strategy under evaluation.

The performance of a the swimming robot with the simulator when applying the designed continuous-time controllers is summarized in Table 6.2. This table includes not only ITAE and IAE but also the average of the electrical and mechanical powers and the robot's efficiency for the fractional waveform with the parameters given in Tables 4.1, 5.1 and 5.2. The best results are in bold.

From these results, the following conclusions can be stated:

Table 6.2: Performance of the 6-link swimming robot when applying the designed continuous-time controllers (simulation).

Controller		**1st Link**		**2nd Link**		**3rd Link**		**4th Link**		**5rd Link**		**6th Link**		$\mathbf{P_e}$	$\mathbf{P_m}$	η^{**}
		ITAE*	IAE*	ITAE*	IAE*	ITAE*	IAE*	ITAE*	IAE*	ITAE*	IAE*	ITAE*	IAE*	(W)	(μW)***	
PID	IAE	5.89	12.47	10.60	14.85	9.16	26.36	8.01	6.18	7.41	15.08	8.96	21.40	0.55	6.19	11.47
	ITAE	**5.28**	**11.90**	**8.85**	**13.62**	**9.04**	**26.13**	**6.61**	**5.27**	**6.52**	**14.27**	**8.30**	**20.76**	**0.47**	**6.19**	**13.44**
	RC	9.32	15.85	12.95	16.51	21.04	35.82	9.33	7.01	11.34	18.71	16.65	28.18	0.52	6.19	12.20
PD^{μ}	IAE	4.39	11.30	7.94	12.71	6.92	25.39	6.05	4.99	5.53	13.55	6.74	**20.24**	0.47	6.19	13.17
	ITAE	**4.18**	**12.06**	**7.27**	**12.01**	**6.80**	**27.41**	**5.62**	**4.82**	**5.21**	**14.24**	**6.50**	21.89	**0.30**	**6.19**	**20.63**
	RC	5.51	14.03	9.39	13.74	8.93	30.81	7.27	6.01	6.84	16.67	8.57	25.13	0.38	6.19	16.28

Notes: * Values $\times 10^{-3}$. ** Values $\times 10^{-6}$. *** Values $\times 10^{4}$.

- All control strategies, regardless of the chosen tuning method, perform successfully.

- The best tracking in terms of errors for the six actuators is achieved with the controllers designed by minimizing ITAE, in contrast to what one would expect when applying the robust tuning method. Among these results, the lowest tracking error is obtained when applying the robust PD$^{\mu}$ controller.

- From what locomotion performance of the robot is concerned, the six controllers provide approximately the same average of mechanical power, independently of the tuning method applied. However, regarding the electrical power, the PD$^{\mu}$ designed by the ITAE method stands out against the others: the robot controlled with this strategy can perform a nonreciprocal motion with the lowest control requirements, reducing electrical consumption.

In terms of ITAE and IAE, notice that the tuning methods for both the PID and the PD$^{\mu}$ were applied to the actuator transfer function (4.34) with the time constant corresponding to the first link (the worst case).

For illustration purposes, Figure 6.2 shows a comparison of the angle and tracking error for both the first and sixth links of the robot when applying the robust PD$^{\mu}$ controller and the PID designed by minimizing ITAE (the best controllers in terms of efficiency and tracking, respectively). It can be observed that both controllers allow the link actuator to follow the reference correctly, regardless of the link. However, the tracking error is higher with the PD$^{\mu}$, but with lower energy requirements.

6.1.2 Waveform evaluation

Once the joint control is designed, this section presents a simulation study about how the number of segments and the value of parameter α_w of the fractional traveling wave (3.58) affect both the forward velocity and the propulsion thrust. Alternatively, in other words, a performance study based on the waveforms is presented next. First of all, it is essential to remark that the results given below were obtained using the robot simulator with the parameters and properties given in Tables 4.1, 5.1 and 5.2. Likewise, only the forward velocity was considered, but the conclusions are also applicable to the forward propulsion since both variables are

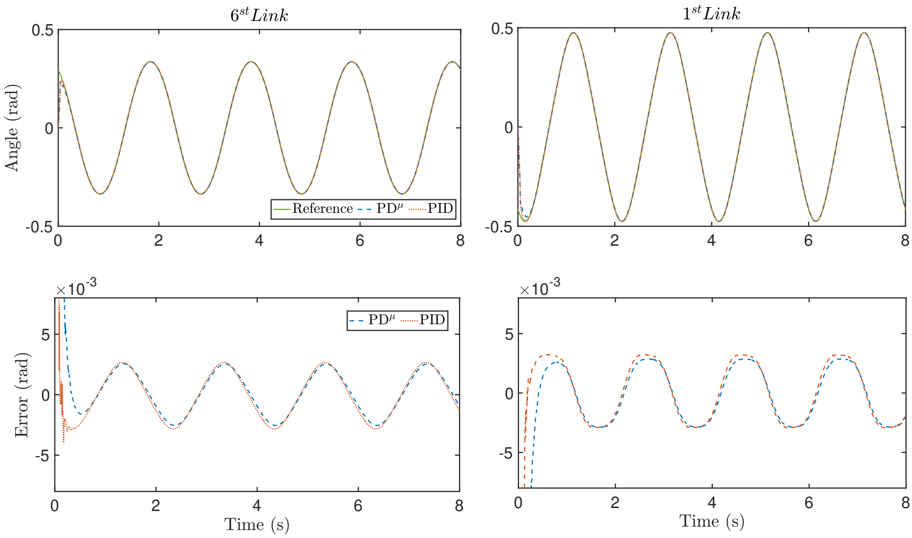

Figure 6.2: Error tracking for fractional waveform for different controllers and links.

directly proportional according to (4.2). The forward velocity of each waveform is plotted in Figure 6.3 for both the ideal case (the ideal velocity for the discretized waveform in Figure 6.3a) and the simulated case (the waveform carried out by the robot in simulation in Figure 6.3b). As observed, only slight differences can be found between the ideal and simulated results. However, a more significant difference exists when comparing with those shown in Figure 4.1: the forward velocity is slower; in fact, the reduction percentage is about $30 - 40\%$. This arises from the limitations of real implementation, which means the finite length of the flagellum and the discretization method established. However, the results are consistent since the harmonic and linear Carangiform waveforms develop the highest and lowest forward velocity, respectively. In contrast, a forward velocity within that range can be obtained with the fractional waveform depending on the value α_w to be set. These results emphasize the importance of the oscillations' growth at the beginning of the flagellum. It should be noted that the oscillating character of velocity in the harmonic wave is caused by the discretization method; theoretically, this value is constant.

Concerning the influence of the number of links on the velocity, it can be stated that the higher the number of links, the higher the velocity (see Figure 6.4a).

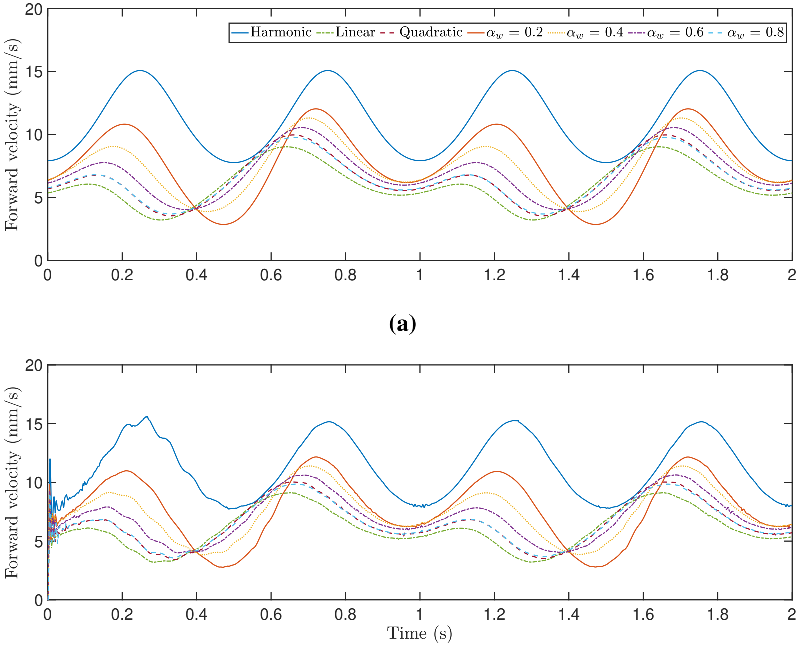

(a)

(b)

Figure 6.3: Forward velocity generated by the four different kinds of waveforms: (**a**) ideal motions, (**b**) simulated motions.

Increasing the number of links reduces the difference between the original waveform and the simulated one caused by the applied discretization method and, consequently, emulates a more faithful motion than the original. However, a high number of links is not necessary to achieve near-ideal speed: as can be stated from Figure 6.4b, it is possible to obtain a percentage of about $70 - 90\%$ of the ideal velocity with a set between four and eight links, respectively. This figure plots the ratio between the forward velocity and the ideal motion versus the number of links for the seven waveforms. Let us now focus on the fractional order waveform. For a given velocity, this waveform achieves that velocity with a smaller number of segments, saving energy. Thus, it can produce a higher velocity than the obtained with other waveforms with a lower number of segments due to faster growth of oscillations. Despite that, and due to the used discretization method, it requires a higher number of links to achieve a velocity closer to the ideal, unlike the other waveforms. This is because the beginning of the flagellum is not perfectly discretized, which causes the growth to be smoothed and the amplitude to be reduced.

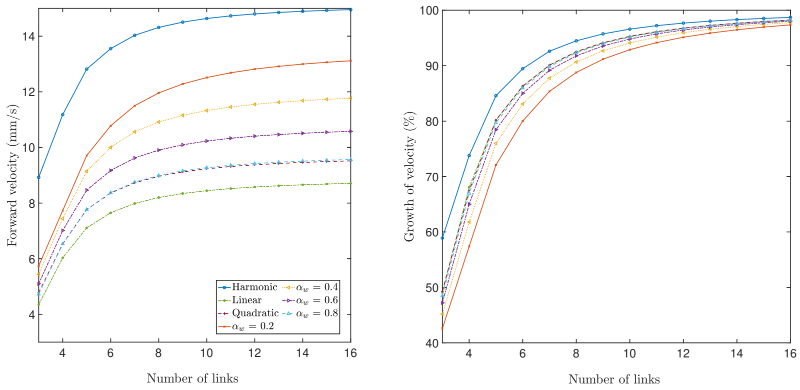

(a) **(b)**

Figure 6.4: Influence of the number of links on the forward velocity generated by the seven different kinds of waveforms: (**a**) forward velocity, (**b**) growth ratio of velocity regarding ideal discretized motion.

To sum up, the way of swimming with fractional growth proposed in this thesis achieves the same velocity as classical waveforms with a lower number of links or higher velocity with the same number of segments. The behavior is the same for the ideal motion, but with slight differences.

6.1.3 Heading control

This section focuses on validating the turning motion and heading orientation control proposed in chapter 4. For this purpose, two trials were simulated. The first one consists of modifying the mean angle over which the motion is performed so as to study the effect of $\phi_{w,t}$ as follows: the variable was set to $\phi_{w,t} = 5°$ during the time interval $t \in [10, 30]$s, $\phi_{w,t} = -5°$ in the time interval $t \in [50, 70]$s and $\phi_{w,t} = 0$ otherwise. The second test implements the heading controller and sets different head angle references: concretely, it was set to $\theta_{7,\mathrm{ref}} = 5°$ during the time interval $t \in [10, 60]$s, $\theta_{7,\mathrm{ref}} = -5°$ for $t \in [110, 160]$s and $\theta_{7,\mathrm{ref}} = 0$ in the rest of the time. Regarding the heading proportional gain, $K_{p,h}$ was set to twice times the length of the swimming robot, that meas $K_{p,h} = 2(N_u + 1)l_i$, for this second scenario.

Figure 6.5 shows the results corresponding to the first trial. As can be seen the swimming robot moves forward, keeping the mean heading close to zero while $\phi_{w,t}$ is zero because the normal reaction forces compensate each other. By contrast, when

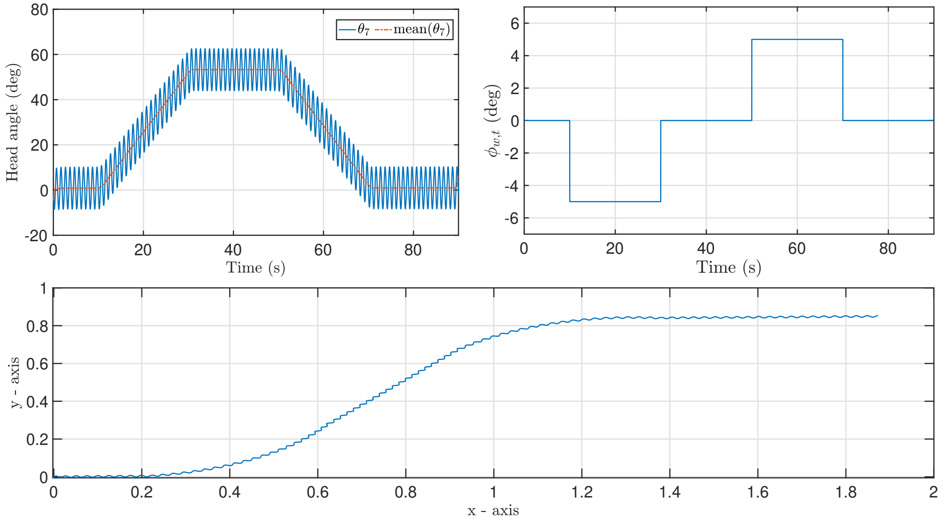

Figure 6.5: Turning motion trial.

$\phi_{w,t} \neq 0$, they do not compensate each other, and a normal contribution appears, producing a rotation of the swimming robot, as explained in section 4.2. It is also observed that a stable orientation is not achieved due to the undulating motion of the flagellum. However, the average value of the head angle presents propulsion over a midline. Finally, the first simulation verifies that a positive (or negative) mean angle produces a rotation.

In turn, Figure 6.6 shows the results of the second trial, which validate the heading control. In this case, the heading control sets the mean angle $\phi_{w,t}$ to generate normal reaction forces that induce the rotation necessary to turn swimmer about the desired head angle. In addition, slow dynamics equivalent to an overdamped second-order system is observed.

6.1.4 Path following controller

This section presents simulation results to evaluate the waypoint guidance methodology, as well as the nested control loops proposed for path following in chapter 4.

In order to test the path following control for waypoints, $k = 7$ was defined

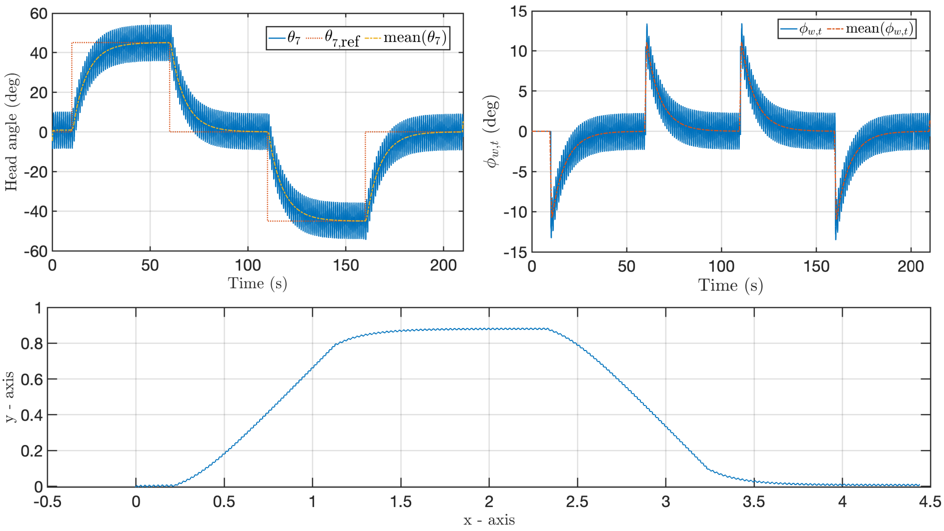

Figure 6.6: Heading control trial.

with global frame coordinates $(0,0)$, $(0.2,0)$, $(0.2,1)$, $(1,1)$, $(1.5,0)$, $(2,-0.5)$ and $(2.5,-1)$, respectively. Figure 6.7 shows the motion of the CM of the swimming robot; waypoint is indicated with a red cross. The figure also shows the heading angle, θ_7, the mean angle, $\phi_{w,t}$, and their mean. At the transition between waypoints, it is observed that the swimming robot experiences a jump state due to the waypoints algorithm, which redefines the global frame at each new waypoint.

The path following strategy provides good results. The swimming robot has a an adequate and smooth movement toward each waypoint. In addition, the mean angle converges to zero, and the heading is achieved after each waypoint change. In summary, the simulation results show that the proposed path following strategy successfully steers the swimming robot toward each specified waypoint.

6.2 IPMC-based 3-link swimming robot

This section deals with the modeling control of the flexible 3-link swimming robot fabricated in IPMC to perform a desired motion. For this purpose, a frequency domain identification is performed, from which a model of each robot link is obtained. The results are discussed to determine what type of actuation can be

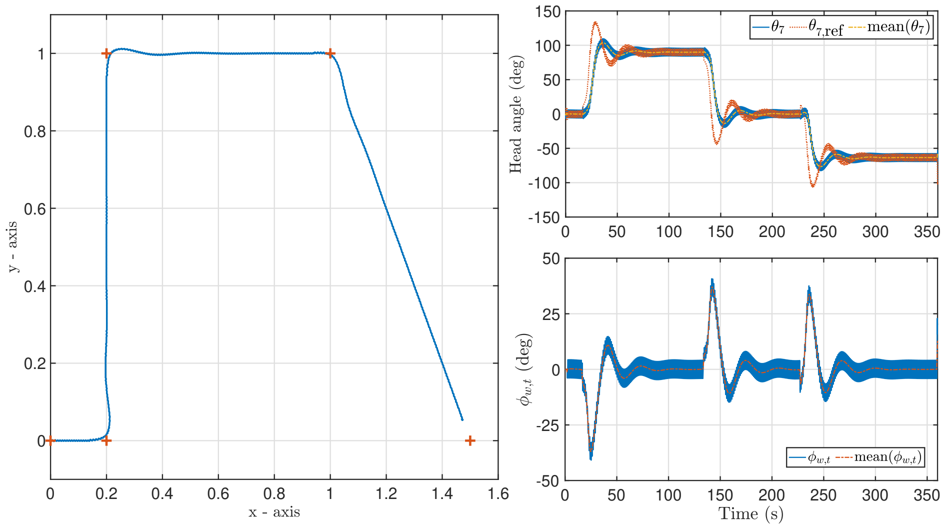

Figure 6.7: Path following trial.

applied to the swimmer to generate a planar waveform for propulsion. As a results, two controllers are tuned to PID and a fractional-order integrator. Simulations are carried out to analyze and compare the motion of the swimming robot.

6.2.1 Measuring frequency responses

The procedure described below was carried out by measuring the deflection of each link when the first actuator was excited exclusively. To measure frequency responses, a frequency sweep is programmed by meas of through a chirp signal with an amplitude of 3 V, a frequency range from 100 mHz to 200 Hz, and a duration of 200 s, to capture all possible dynamics of the system and decide which of them can be neglected for control purposes. The chirp signal is applied directly to the electrodes attached to the first actuator (A_1) and the system response is the tip deflection of the link under study (see Figure 5.6). Note that this experiments is repeated for each of robot's links to characterize their behavior. Figure 6.8 shows the excitation signal and the deflection measured at the third link (L_3). Likewise, every experiment was repeated ten times to guarantee reproducibility and improve the model parameter estimation. The time response shows that the swimming robot reaches the maximum relative deflection in the resonance conditions and then

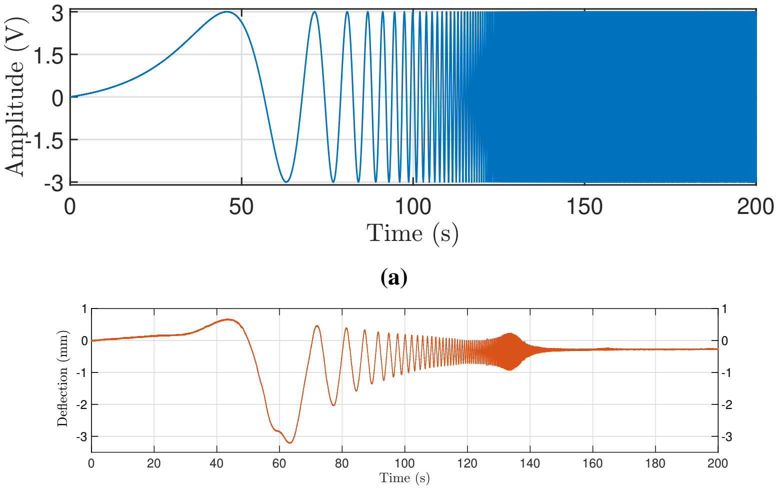

(a)

(b)

Figure 6.8: Example of experimental signals: (**a**) excitation signal applied to the first actuator for identification, (**b**) deflection measured at tip of the third link.

decreases.

Processing these data in MATLAB®, each frequency response was obtained using Welch's method dividing the data set into eight sections with a 50% overlap, where each section was processed with a Hamming window. The eight modified periodograms were computed and averaged. The average frequency response of the experiments set obtained for each flagellum segment is shown in Figure 6.9. Likewise, the maximum and minimum standard deviation is depicted for the response of the third link (gray lines).

6.2.2 Dynamic model identification

The theoretical models of IPMC actuators that can be found in the literature stand out for their complexity and the vast variability of their chemical parameters due to the lack of technical standards in manufacturing methods. More precisely, the existing models can be categorized as: 1) black-box models, based on empirical responses [132]; 2) gray-box models, which combine the knowledge about materials with experimental data, i.e., they are formulated based on physical principles while empirical results are used to define more complex physical processes [131]; and 3)

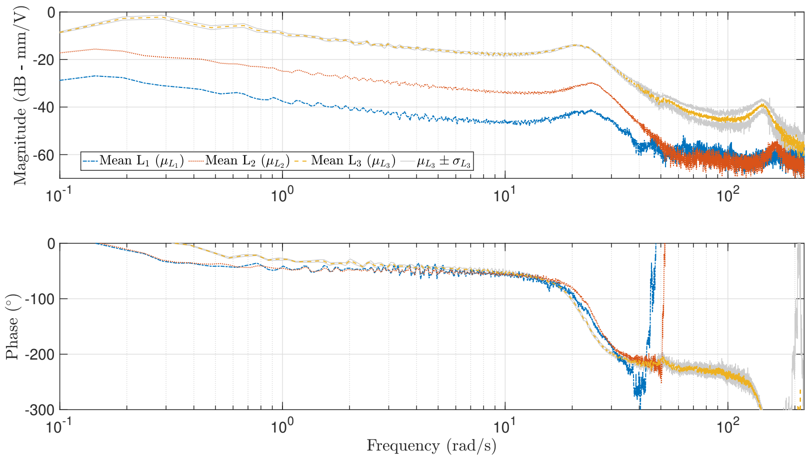

Figure 6.9: Frequency responses of the AEF swimming robot when exciting the first segment the tip deflection of each IPMC link.

white-box models, whose components explain the physics and actuation responses by partial differential equations [137, 208]. Considering that the last method is not practical for real-time control due to the high computational efforts required, the second approach was used as described below.

The measured frequency responses show that the system has two resonance frequencies in the frequency range under study, regardless of the considered link. Moreover, the farther a link is from the first link, the lower the resonance peak. On the other hand, the magnitude curves are not flat at low frequencies: they fall with a slope of -10 dB/dec, being the phase approximately $45°$. This behavior matches perfectly with a fractional integrator of order 0.5, i.e.:

$$H(s) \approx s^{-0.5} \tag{6.2}$$

It is worth mentioning that this low-frequency dynamic was also tested for other prototypes in [131, 132, 137, 209, 210], whose theoretical models present root square of the Laplacian variable to define the electrical dynamics of IPMC. Based on them, preliminary identification results of this swimmer prototypes were reported in [211].

Theoretical studies on IPMCs usually model mechanical behavior and hydrodynamic interactions when the actuator is submerged by coupling a resonant system for the first vibration mode in order to obtain a more reliable model. This consideration can be accepted in this case since, as seen from the experimental frequency responses, the first resonance mode predominates for frequencies below 50 rad/s, which are high enough for the frequency range of interest for this application. Therefore, that dynamics could be given by a second-order spring-mass-damper system of the form:

$$G_1(s) = \frac{a_0}{b_2 s^2 + b_1 s + 1} \tag{6.3}$$

or by a fractional order system as

$$G_2(s) = \frac{a_0}{b_1 s^{\alpha} + 1} \tag{6.4}$$

with $\alpha \in \mathbb{R}^+$ ($\alpha \in (1, 2)$), and being a_0, b_1, and b_2 constants. Notice that both models have the same number of parameters (i.e., three). Hence, the global dynamics of the system will be obtained as the fractional-order integrator cascaded with the mechanical model, that means $P_i(s) = H(s)G_i(s)$, with $i = \{1, 2\}$, for the frequency range of interest of $[0.2, 50]$ rad/s.

For simplicity, the dynamics corresponding to the integrator was removed from the measured frequency responses. Consequently, the identification procedure was reduced to identify models of the form of (6.3) and (6.4) in the mentioned frequency range. In particular, the average frequency response of the ten measurements was used for identification. Concerning the identification process, Levy's method is implemented in MATLAB® (with function `levy` [212]) for both the integer and the fractional-order models. The adjustment was performed by minimizing $J = (G(j\omega)D(j\omega) - N(j\omega))^2$, i.e., the quadratic error per sampling frequency ($N(j\omega)$ and $D(j\omega)$ are the numerator and denominator of the transfer function of the model to be identified, respectively). Fractional models were found sweeping α in the interval $(1, 2)$, with a step of 0.01, and choosing the best result from among the stable models obtained. The model parameters derived from the above-described identification process are indicated in Table 6.3. From these results, it can be stated that: 1) as expected, the two models $G_i(s)$ obtained for each link are stable; 2) gains of the models (coefficient a_0) are of the same order of magnitude; and 3) the values obtained for parameter α for each of the models are very similar. Figure 6.10

Table 6.3: Model parameters obtained from identification procedure

Model		α	a_0 ($\times 10^{-3}$)	b_2 ($\times 10^{-3}$)	b_1 ($\times 10^{-3}$)
First link	G_1	-	13.70	1.62	12.60
	G_2	1.79	13.33	-	3.30
Second link	G_1	-	51.00	1.61	12.72
	G_2	1.81	48.10	-	3.10
Third link	G_1	-	376.09	2.13	23.31
	G_2	1.71	352.80	-	5.80

shows a comparison of the experimental data and the frequency response of the identified model for each robot link (denoted as $P_{L_q}(j\omega) = H(j\omega)G1_{L_q}(j\omega)$, being $L_q = \{L_1, L_2, L_3\}$ the link and $G1_{L_q}(s)$ the dynamics of each link with the form of (6.3)). As can be observed, differences between experimental and model frequency responses appear at frequencies higher than 50 rad/s, i.e., outside of the range of interest.

In order to compare and evaluate the goodness of the obtained models, besides J, additional performance indices were calculated:

1. Mean square error (MSE) per sampling frequency, defined as

$$\mathrm{MSE} = \left(\sum_{k=1}^{N} (g_k - \hat{g}_k)^2 \right) / N, \tag{6.5}$$

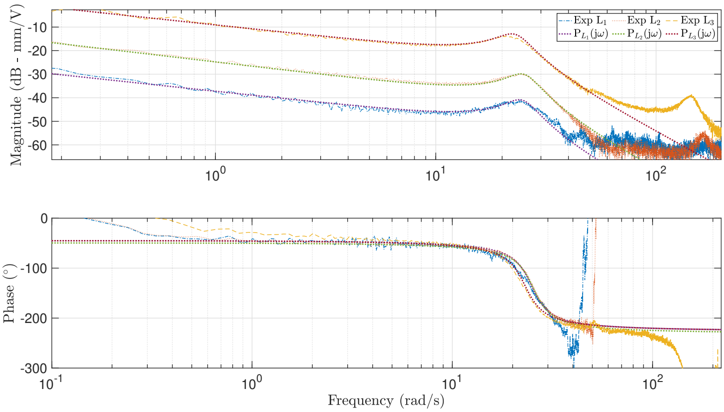

Figure 6.10: Comparison of experimental and model frequency responses of the AEF swimming robot by exciting the first actuator and measuring the deflection at the end of each link.

where g_k and $\hat{g}_k$ are the experimental and estimated frequency responses, respectively, and N is the number of frequency samples.

2. Mean absolute deviation (MAD), defined as

$$\text{MAD} = \left(\sum_{k=1}^{N} |g_k - \hat{g}_k| \right) / N. \tag{6.6}$$

3. Maximum deviation (MD), defined as

$$\text{MD} = \max |g_k - \hat{g}_k|. \tag{6.7}$$

4. Coefficient of determination ($\text{R}^2 \in (0, 1)$), defined as

$$\text{R}^2 = 1 - \left(\sum_{k=1}^{N} (g_k - \hat{g}_k) \right) / \left(\sum_{k=1}^{N} (g_k - \bar{g}) \right). \tag{6.8}$$

where $\bar{g}$ is the mean of the experimental frequency response.

The values of there indices are given in Table 6.4, where the best fits are in bold. To this respect, except for the third link, the best results are obtained using the model $G_1(s)$ given by (6.3). However, for the third link, that model is also the best in terms of J and MD, but not if another of the remaining indices is considered.

Table 6.4: Performance indices after fitting models $P_1(s)$ and $P_2(s)$. Numbers in bold correspond to the best fit.

Model		***J*** **(x10^{-5})**	**MSE (x10^{-7})**	**MAD (x10^{-4})**	**MD (x10^{-3})**	**R^2**
First link	P_1	**2.4884**	**4.5210**	**5.4392**	**2.800**	**0.9153**
	P_2	3.4992	5.0188	5.7149	3.3000	0.9059
Second link	P_1	**4.9163**	**59.7630**	**13.0000**	**24.0000**	**0.9630**
	P_2	12.3680	104.2300	19.0000	28.5000	0.9354
Third link	P_1	**530.0000**	1654.7000	69.0000	**126.5000**	0.9796
	P_2	550.0000	**1392.7200**	**45.000**	186.4000	**0.9828**

6.2.2.1 Discussion of modeling results

According to the above results, it can be stated that the links have similar dynamics regardless of their position. However, there are differences in the gain; that is, the displacement (deflection) increases across the flagellum. Specifically, the tip displacement of the second link shows an increase in gain. In contrast, the tip displacement of the third link also presents a lag with respect to the first link as a consequence of the length, the flexible behavior of IPMC and the interaction with the environment. These conclusions are illustrated in Figure 6.11, which schematizes the relation between the first and the rest of the links. (At this point, it should be recalled that the first link is active, while the other two behave as passive links). The values of the gains and the phase lag of the third link can be directly deducted from Table 6.3 as follows: $K_2 = 3.72$, $K_3 = 7.37$, and $\phi = 4°$. It should be noted that the gain does not increase linearly due to the fact that the IPMC bends into a C-shape, so the closer to the end is measured, the higher the displacement.

Hence, the displacement of each flagellum segment end, or any IPMC point, is characterized by the same dynamics, which remains unchanged across the link with mere gain variations for low-frequency applications. This conclusion is also consistent with other studies reported in the literature, where IPMCs show changes in model gain when the links do not have the same length or are manufactured from different substrates (see, for example, [130, 132, 211, 213]).

Moreover, from the above conclusion, a nonreciprocal motion can be only achieved with a single actuation if the geometrical and mechanical design of the swimming robot has been analyzed previously and designed for that purpose. Otherwise, the dynamics of consecutive links are subjected to the active link. In other

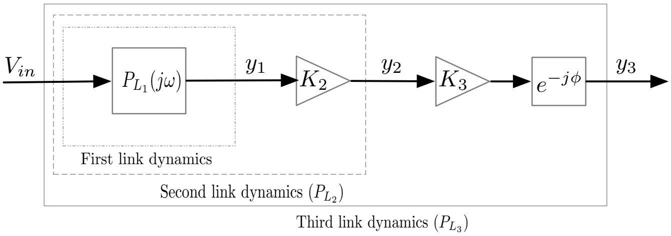

Figure 6.11: Diagram block of a swimming robot model for single actuation.

words, the swimming robot cannot perform a nonreciprocal motion with a single actuation; a distributed actuation is needed to obtain the desired waveform and, consequently, for robot propulsion.

Finally, the dynamics considered for the control design is the one corresponding to the third link, which takes the form:

$$P_{L_3}(s) = \frac{1}{s^{0.5}} \frac{376.09 \times 10^{-3}}{2.13 \times 10^{-3} s^2 + 23.31 \times 10^{-3} s + 1} \tag{6.9}$$

It is worth mentioning that this dynamics is chosen because it represents the worst case. A further increase in the third link gain may cause the system to become unstable, as the gain variation is not linear. On the contrary, a decrease in gain does not compromise the system's stability.

6.2.3 Propulsion control

As commented, two main issues are addressed when generating a nonreciprocal motion, especially a planar traveling wave. Firstly, the desired waveform must be adapted to the swimming robot dynamics and discretized for its geometry, considering that it is necessary to define a reference for each of the robot's links. This adaptation will fulfill the capabilities of the swimming robot in terms of amplitude and velocity. The resulting waves will be the references of the IPMC links. Secondly, a tracking controller must be applied to each link to follow the desired deflection. The following consideration are necessary prior to the design of the control fro the swimmer's propulsion.

6.2.3.1 Preliminary issues

The methodology applied to discretize the motion is based on the projection method described in section 4.1.3. The method divides the flagellum into the same number of segments and lengths as the swimming robot, providing a matrix, $\Theta[N_u][T]$, that contains the trajectory as a function of time and space for the N_u links of the robot. However, the above method is modified for this swimming robot prototype to obtain the waveform amplitude instead of the link angle. The type of waveform chosen is the linear Carangiform due to the physical limitations of IPMCs (slow dynamics and low amplitude responses). Therefore, the linear Carangiform

Table 6.5: Linear Carangiform waveform parameters for IPMC-based swimming robot.

Parameter	Value	Description	Unit
c_0	0	Amplitude coefficient	µm
c_1	200	Amplitude coefficient	-
c_2	0	Amplitude coefficient	1/µm
f	0.01	Frequency	Hz
λ	32	Wavelength	mm

waveform could be the most suitable for this type of material in contrast to others requiring a greater range of motion, which means very low frequencies or the impossibility of performing the motion. The values of the parameters that define the linear Carangiform motion according to the waveform expression (2.9) are collected in Table 6.5. The wavelength was defined using the criterion applied in the chapter 4: it is equal to the robot's length.

In order to track the calculated references, as commented above, a controller for each link takes into account the following considerations is required. Firstly, from the identification procedure, it has been deduced that the dynamics of the IPMC links are very similar and that only variations in the gain are observed due to its strong dependence on the link length. Secondly, it has been found that an equal link length does not provide the optimal waveform and, consequently, the optimal drive for a given number of links [55]. With this motivation, a controller robust to variations in the system gain is considered to overcome the robot propulsion so that it can also be applied after a link length optimization process.

6.2.3.2 Controller design

The methodology applied to design the controller for robot's propulsion is based on the reference model strategy and described in section 4.4.1, which adjusts the step response of the controlled system to an ideal closed-loop system. The frequency domain specifications for the ideal closed-loop are:

1. Gain crossover frequency: $\omega_{cp} = 5$ rad/s.
2. Phase margin: $\phi = 75°$.

Based on the above specifications, the ideal Bode transfer function of a noninteger integrator is taken as the ideal reference model, whose open- and closed-loop forms are, respectively:

$$L_{ol}(s) = \left(\frac{\omega_c}{s}\right)^{\gamma} \tag{6.10}$$

$$L_{cl}(s) = \frac{1}{(s/\omega_c)^{\gamma} + 1} \tag{6.11}$$

where ω_c denotes the gain crossover frequency, that is $|L_{ol}(s)| = 1$, and $\gamma \in (0, 2]$ is the noninteger-order of the reference system. The gain and phase of the ideal reference model (6.10) are given by [197, 214]:

$$|L_{ol}(j\omega)| = -20\gamma \log_{10}\left(\frac{\omega}{\omega_c}\right) \quad \text{dB/dec}$$

$$\arg[L_{ol}(j\omega)] = -\gamma\pi/2 \quad \text{rad}$$

The reference model has a constant phase at any frequency to ensure that the controlled system is robust to gain variations and exhibits an iso-damping property at a step response. Then, based on the above relationships, the system must have a crossover frequency of $\omega_c = \omega_{cp} = 5$ rad/s and a noninteger order of $\gamma = 1.16$ to meet the desired specifications.

In order to achieve this dynamics with the IPMC link model identified (model (6.9)), a PID controller is considered in parallel form as:

$$C_{\text{PID}}(s) = K_p + \frac{K_i}{s} + K_d s \tag{6.12}$$

where K_p, K_i, and K_d are the proportional, integral, and derivative gains, respectively. The controller parameters were determined by the optimization process described in section 4.4.1 as follows: $K_p = 8.12$, $K_i = 53.36$ and $K_d = 0.61$. It is important to remark that other performance indices were tested, but results with minor variations were obtained with respect to the ones presented.

Upon analyzing the design method for the IPMC link model, which also contains noninteger order dynamics, the conclusion is drawn that the PID controller attempts to approximate the dynamics of a noninteger order integrator to approach the system to the desired dynamics. On this basis, a noninteger integrator is also considered for

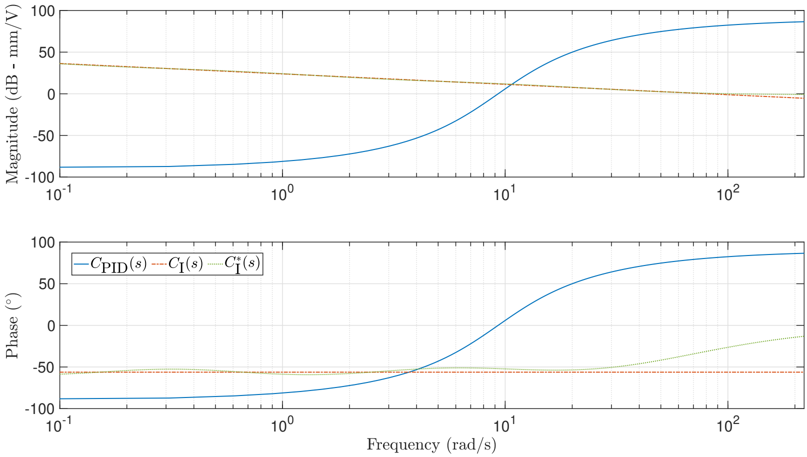

Figure 6.12: Frequency response of the designed integer and fractional order controllers.

comparison purposes with the form:

$$C_{\rm I}(s) = \frac{K}{s^{\lambda}} \tag{6.13}$$

where $\lambda \in (0, 1]$ is its order. Unlike PID, the parameters of fractional integrator are calculated analytically from the design specifications, which results in $K = 15.62$ and $\lambda = 0.62$. Moreover, this controller was approximated by the Oustaloup method with four poles and four zeros in the frequency range $[0.001, 100]$ rad/s as follows:

$$C_{\rm I}^{*}(s) = \frac{32.08s^4 + 1981s^3 + 6511s^2 + 1196s + 11.7}{36.47s^4 + 372.9s^3 + 202.9s^2 + 6.175s + 0.01} \tag{6.14}$$

The Bode plots of the three designed controllers, namely $C_{\rm PID}(s)$, $C_{\rm I}(s)$, and $C_{\rm I}^{*}(s)$, are shown in Figure 6.12. As can be seen, the PID controller provides a phase of 44° at 5 rad/s and a positive gain to the system at relatively high frequencies, which will increase the speed of the system, but at the same time, the crossover frequency specification will not be met. In contrast, the noninteger integrator has a bit higher phase at 5 rad/s, namely 56°, and a positive gain of 15 dB so that the design specifications can be better fulfilled. As for the approximation of the fractional integrator, it should be noted that it performs very close to $C_{\rm I}(j\omega)$, with only a small variation in the phase from the desired ω_{cp} being observed.

Figure 6.13 illustrates Bode plots of the open-loop system when applying the designed controllers and the approximation. From these frequency responses, the first remark that can be stated is that the PID controller does not meet the design specifications. As it was noted, the controller increases the speed of the system (ω_{cp} = 38 rad/s) and the phase margin is 75°. The reason for the frequency response mismatch is that the optimization process was approached from a time perspective to adjust the system's time response for a step input. On the contrary, the system fulfills the design specifications perfectly when applying the fractional-order integrator. Furthermore, the phase is flat at crossover frequency and almost constant within an interval around it. In other words, the system is robust to gain variations and the overshoot of the response will be almost constant close to ω_{cp}.

The issues mentioned above can also be observed from the results plotted in Figure 6.14, which illustrates the step response of the reference model and that corresponding to each link of the robot when applying the PID (see Figure 6.14a) and the fractional integrator and its approximation (see Figure 6.14b). Regarding the PID controller, the response for the third link shows a good fit with respect to the reference model response. However, the characteristics do not hold for the other links: the overshoot increases as the gain decreases, although the system is faster for the second and third links compared to the other control strategies. This behavior is not observed in the system for the fractional integrator, which also approximates the

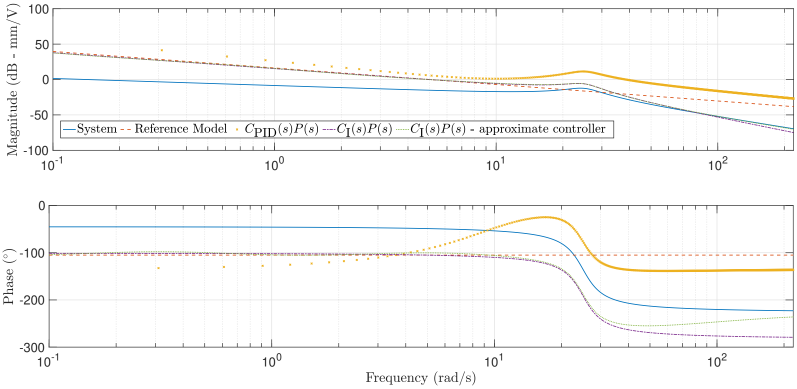

Figure 6.13: Frequency response of the reference model and the controlled system in open-loop.

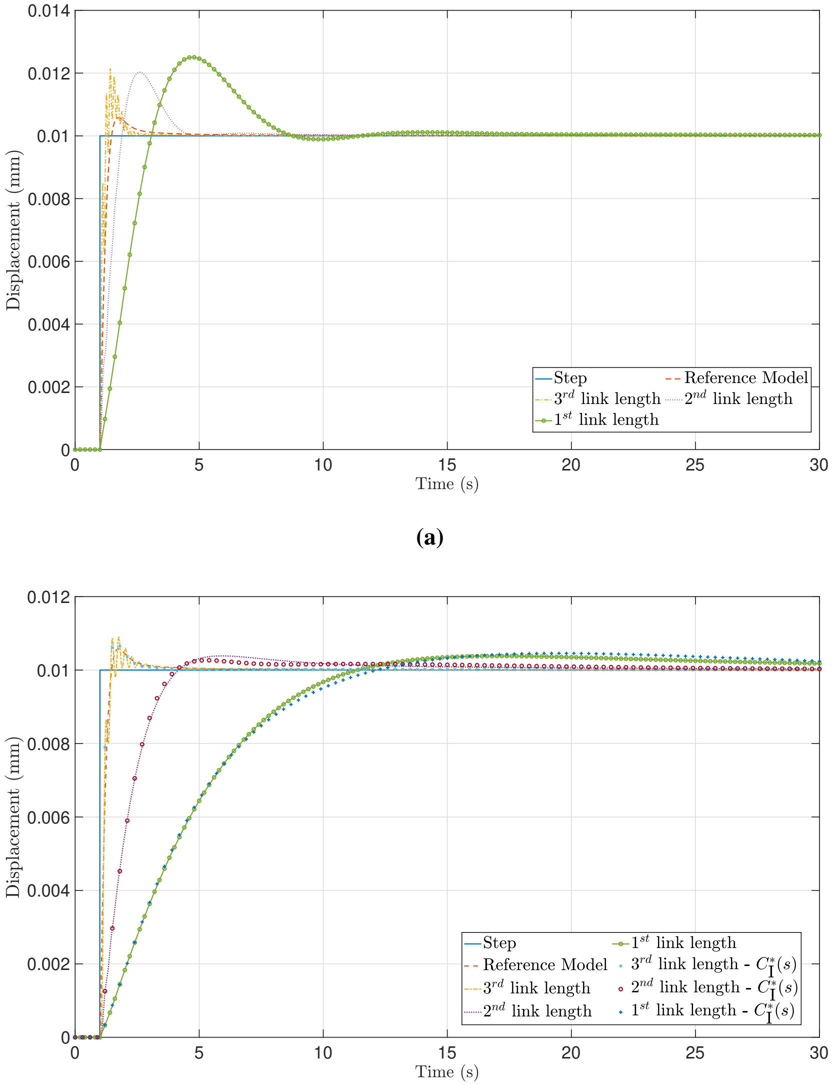

(a)

(b)

Figure 6.14: Step response of each robot link when applying: (**a**) PID controller, (**b**) noninteger-order integrator and its approximation.

step response of the reference model. In the case of applying the controller to other links, the overshoot is maintained, ensuring robustness to gain variations. Regarding the integrator, the responses show slight differences with respect to the ideal case, with the system velocity and overshoot remaining unchanged for all three links.

Table 6.6: Tracking performance indices.

Link	IAE		ITAE	
	$C_{\mathbf{I}}(\mathbf{s})$	$C_{\mathbf{PID}}(\mathbf{s})$	$C_{\mathbf{I}}(\mathbf{s})$	$C_{\mathbf{PID}}(\mathbf{s})$
First link	4.67	0.68	434.90	42
Second link	13.87	2.28	1283.50	140.75
Third link	18.04	3.97	1861.70	269.74

6.2.4 Motion analysis

The swimming robot model was implemented in Simulink® on the basis of the description given in the above section. Three equal IPMC links are concatenated and modeled with the same dynamics since they have the same length. Specifically, the link dynamics is defined as $P_{L_q}(s) = H(s)G1_{L_q}(s)$, where the model parameters of $G1_{L_q}(s)$ for each link are contained in Table 6.3. A link's total displacement is calculated using its relative displacement and the angle of the previous link end.

Figure 6.15 shows the displacement of each link tracking its reference for the designed control strategies (see Figure 6.15a) and the comparison between the ideal linear Carangiform motion and the motion resulting from the distributed actuation (see Figure 6.15b).

Firstly, let comment on the results of Figure 6.15a. Independently of the flagellum segment, both controllers track the references closely, although the PID controller achieves better tracking as the controller increases the system's speed. However, the tracking error increases due to the reference signal's amplitude rise and the motion of the previous link. In order to evaluate tracking performance of the controllers, the ITAE and IAE indices were calculated. The results of these performance indices obtained from the simulation are given in Table 6.6. It is important to remark that the results of the noninteger-order controller correspond to its approximation. Therefore, the indices validate the previous statement: the best performance is achieved at the first link, where the effort demanded by the reference is lowest, and the second and third links obtain worse tracking, although the error between them is similar, which shows the robustness of the controller. In addition, the PID controller exhibits a better tracking performance, although its behavior for a step response is worse.

Concerning the results of Figure 6.15b, the ideal linear waveform, the discretized waveform obtained from the projection method described in section 4.1.3 and the realized waveform are illustrated. The swimming robot can perform a nonreciprocal motion through a distributed actuation. However, a higher amplitude error and lag exist on the response when applying the fractional integrator, which will affect the robot's propulsion. The nonreciprocal motion for the ideal waveform and the obtained by applying each designed controller can be observed more clearly in Figure 6.16, which represents a three-dimensional graph showing time, the normal and transverse axis of the swimming robot. The ideal and simulated results for the three cases show that the flagellum motions perform a wave that travels along the flagellum and over time.

6.3 Cardiovascular system platform

This section presents the validations of the electrical CVS model and simulator presented in chapter 5. Firstly, the electrical model is validated by three approaches: 1) a first validation in terms of the main hemodynamic indices and clinical waveform data; 2) evaluating the model response to variations in the preload and afterload factors; and 3) comparing the simulation results with experimental data obtained

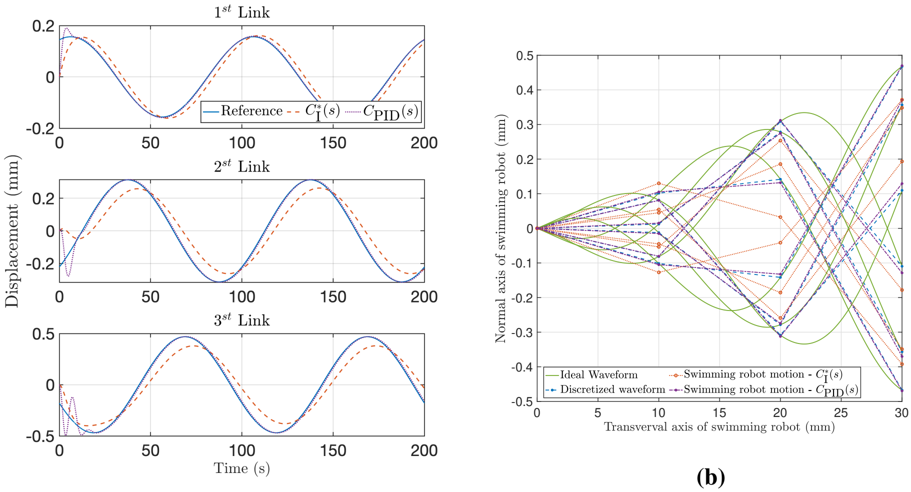

(b)

(a)

Figure 6.15: Swimming robot motion: (**a**) tracking results for the three robot links, (**b**) comparison of the ideal, discretized, and realized linear Carangiform waveform.

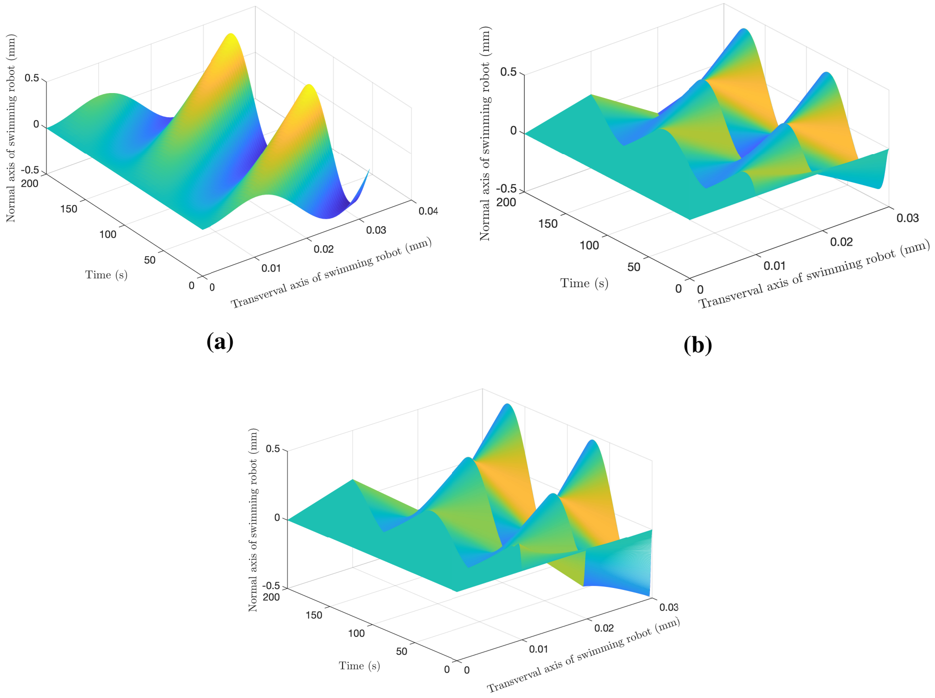

(a)

(b)

(c)

Figure 6.16: Three-dimensional representation of nonreciprocal motion for: (**a**) ideal waveform, (**b**) simulated motion with $C_{\mathrm{PID}}(s)$, (**c**) simulated motion with $C_{\mathrm{I}}^{*}(s)$.

from a pig. Secondly, the hydraulic simulator is analyzed applying different control strategies.

6.3.1 Electrical model validation

The models will be validated verifying that the results offered in nominal conditions correspond to those indicated in section 2, and comparing with experimental results. Secondly, the response to perturbations of preload and after-load conditions will be evaluated.

6.3.1.1 Clinical parameters and experimental waveforms

Next, the model is validated comparing the hemodynamic parameters resulting from the model simulation and those collected in the clinical literature, as well as from experimental data. Hence, this first validation will allows to conclude whether the model provides reasonable and coherent results. Likewise, cardiovascular waveforms corresponding to simulated and experimental data are compared to confirm whether the dynamics is correct.

As for the experimental data, they were obtained from a clinical trial performed on a pig, due to its similarities with human anatomy and hemodynamics. For data collection, the animal was under sedation during the whole process and catheterization methods were used to measure the variables listed in Table 5.4, with the exception of the flow rate, which was measured indirectly by means of cardiac output and the carotid artery flow rate because the specific instrumentation for such a measurement was not available. In order to improve the reproducibility of data and reduce signal noise at the post-processing step, the pressure signals and the cardiac output were collected ten and five times, respectively. To make the experimental data usable, they were previously filtered and, then, synchronized, since all the signals were not collected at the same time, taking for the analysis the mean of the ten repetitions. Data was collected with a sampling time of 4 ms.

On the one hand, the main indices used in the literature to describe the hemodynamic status of a patient are listed in Table 6.7 and Tables 6.8 , as well as their range of acceptable values according to the clinical literature [215]. The table also contains the values obtained from the model simulation and the experiments. It can be seen that the indices corresponding to both the model and the experiments are close, consistent and within the range suggested in the literature.

On the other hand, cardiovascular waveforms of the model and the experiments are shown in Figure 6.17 for a healthy state with the HR given in Table 5.6. As can be observed, waveforms are consistent as explained next. The systolic LAP

Table 6.7: Hemodynamic parameters: comparison between values from literature, proposed model and experiments.

Data from	Heart rate pressure (mmHg)	Systolic arterial pressure (mmHg)	Diastolic arterial pressure (mmHg)	Mean arterial pressure, MAP (l/s)	Cardiac output CO (ml/beat)	Stroke volume SV (mmHg)
Literature	50 - 90	90 - 140	60 - 90	70 - 105	4 - 8	60 - 100
Model	68	112	77	92	5.90	78.71
Experiments	67 - 70	89	62	68	3.18	46.83

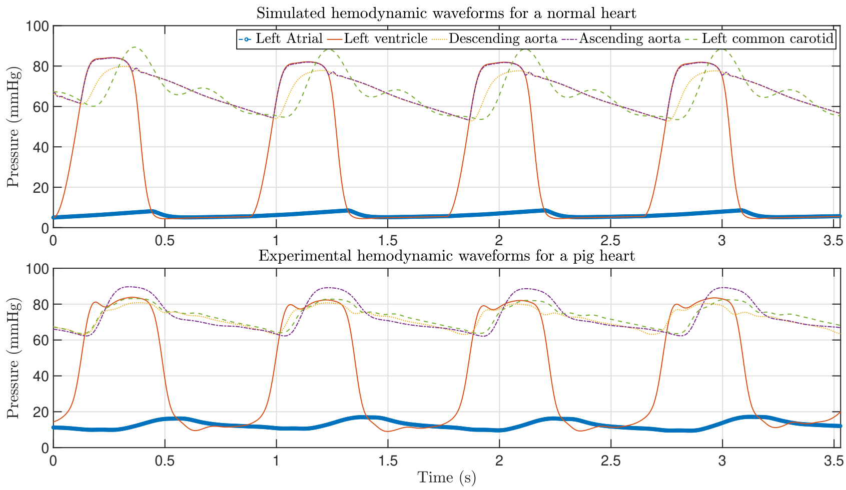

Figure 6.17: Hemodynamic waveforms of the CVS model (5.5) compared with experimental data.

coincides with the diastolic LVP. In the case of the model response, the behavior is close to the ideal case.

The AoP is delayed with respect to LVP as a consequence of the opening and closure of the aortic valve and the propagation of the pressure wave along the artery. In the model, the delay is lower because the AoP is modeled close to the aortic valve, whereas in experiments the pressure sensor was relatively far away from it, the wave propagation time is longer and, consequently, the delay between the LVP and the AoP increases. The same behavior is observed in the LCP. However, small differences can be noticed: the simulated waveforms magnify the pressure fluctuation, especially in the ascending aorta and the LCP, in contrast to the experimental one, where these fluctuations are smoother, and the AoP is higher during the systole contraction. It is important to remark that these discrepancies are strongly related to the point

Table 6.8: Hemodynamic parameters: comparison between values from literature, proposed model and experiments.

Data from	**Systolic LVP (mmHg)**	**Diastolic LVP (ml)**	**Max LVV (ml)**	**Min LVV (mmHg)**	**Systolic LAP (mmHg)**	**Diastolic LAP (mmHg)**
Literature	100 - 140	4 - 15	77 - 195	19 - 72	~ 12	~ 12
Model	117	7	137	67	12	7
Experiments	82	9	–	–	16	10.5

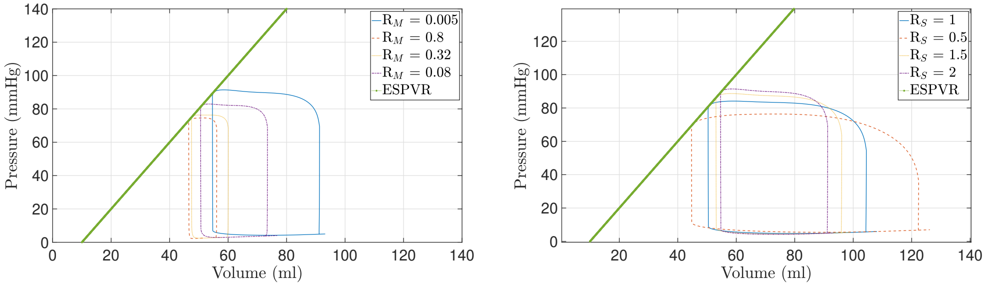

(a) **(b)**

Figure 6.18: PV diagrams for different pre and afterload conditions: (a) variation of preload conditions through R_M, and (b) variation of afterload conditions through R_S.

where the pressure was measured, obtaining greater or lesser delay and variation in pressure. Likewise, the contraction time is longer in the experimental data.

Regarding the pressure and flow waveforms in the left common carotid artery, the main characteristics that are observed are the following: 1) a time lag with respect to LVP; 2) a slight increase in pressure; 3) a greater dicrotic wave; and 4) a negative flow and a second impulse of blood in ventricular diastole. Again, the differences between the experimental and simulated data are mainly due to the point at which the pressure was measured.

To sum up, the model results are consistent with hemodynamic parameters obtained from the literature and experimental data, concluding that the proposed model is valid and provides results comparable with medical data. However, a larger study with a greater number of tests would allow more accurate results to be obtained.

6.3.1.2 Preload and afterload dynamics

The second method of model validation consists of modifying the components that are related with pre and afterload factors. If the model behaves as expected, the ESPVR determined by E_{max} must be maintained for the different conditions, despite the changes for pre and afterload.

To check this feature, a total of eight pre and afterload conditions, four of each, have been performed and represented in Figure 6.18 using PV loops. Figure 6.18a shows the behavior of the model when variations in preload conditions are introduced, in particular by modifying the value of the mitral valve resistance, R_M. The obtained dynamics corresponds with that explained in section 2.4.4.1: a reduction of the EDV and a slight reduction of the opening and closure pressures of the semilunar valves is observed. On the other hand, the variation of afterload conditions through the parameter R_S, shown in Figure 6.18b, results in a reduction of the ejection volume and an increase of the opening and closure pressures of the semilunar valves.

Finally, it should be noted that the ESPVR, the line joining the V_0 and ESV points, shows the same slope under all conditions, and its value is consistent with the characteristics of the LV (E_{max} and V_0). Therefore, the results confirm the validity of the model to reproduce the dynamics of the CVS and the behavior of the LV under different conditions.

6.3.2 Hydraulic model validation

The previous section has demonstrated the validity of the model to represent the dynamics of the CVS. This section aims to analyze the performance of different controls and demonstrate how an appropriate waveform and control strategy allows emulating a dysfunction in the CVS. The strategies that will be compared to obtain normal conditions of a cardiac cycle were described in the section 5.3.4. Likewise, it is necessary to mention that the following considerations were performed to improve the performance of the simulations:

- Fractional derivatives were approximated by Oustaloup method with four poles and four zeros in the frequency range $[0.01, 100]$ rad/s.
- In order to avoid chattering, the controlled variable was filtered before applying the control strategy by the low-pass filter

$$F(s) = \frac{100}{s + 100} \tag{6.15}$$

- For comparison purposes, the following hemodynamic parameters will be measured in the waveforms obtained: systolic and diastolic pressure, mean aortic pressure (MAP), cardiac ouput (CO), SV, systolic and diastolic pressure

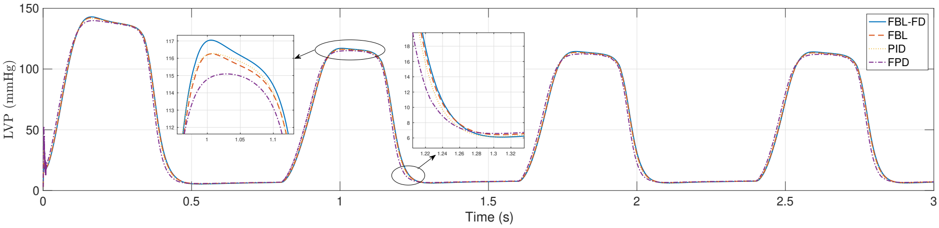

Figure 6.19: Tracking performance of the LVP when applying the proposed strategies with reference provided by the elastance function.

of left ventricle, maximum and minimum volume of left ventricle, and systolic and diastolic pressure of left atrial.

The waveforms of the hemodynamics obtained when applying the four strategies are illustrated in Figure 6.19 and the parameter values are included in Table 6.9, whereas the indices measured are given in Table 6.10. From the simulations results, it can be stated that all strategies, even proportional control law in FBL, that means $u = \lambda e$, provide good enough tracking and hemodynamic performance. So, a fractional-order $\alpha = 0.2$ is chosen for comparison purposes. For all cases, the hemodynamic parameters are coherent with real hemodynamics (see for example [141, 215, 216, 217]).

The results obtained by replacing the reference waveform LVP$_d$ by the electric model of the CVS, that means the theoretical model, are plotted in Figure 6.20 for integer-order controllers, and in Figure 6.21 for fractional order ones. As can be observed, the tracking performance is better when using fractional derivatives.

With regard to the pressure in the common left carotid and the flow, shown in Figure 6.22, they also show the expected behaviour.

The above results show that: 1) the control strategy applied shapes the resulting

Table 6.9: Controller parameters.

Strategy	λ **or** k_p	k_i	k_d	α
FBL	40	–	–	–
FBL+FD	40	–	–	0.2
PID	0.5	0.6	0.003	–
FPD	0.5	–	0.6	0.2

Table 6.10: Hemodynamic parameters and MSE when applying the proposed strategies.

Controller	Systolic pressure (mmHg)	Diastolic pressure (mmHg)	Mean arterial pressure (mmHg)	Cardiac output CO (l/s)	Stroke Volume SV (ml/beat)	Systolic LVP (mmHg)	Diastolic LVP (mmHg)	Max LVV (ml)	Min LVV (ml)	Systolic LAP (mmHg)	Diastolic LAP (mmHg)
FBL	107.6	71.2	83.33	5.47	73	116.2	6.42	138	65	13.12	8.74
FBL+FD	108.2	71.56	83.77	5.50	73.34	117	6.15	138.2	64.96	13.05	8.5
PID	107.8	71.28	83.45	5.48	73.1	116.2	6.16	138.3	65.21	13.03	8.56
FPD	107	71.05	83	5.44	72.57	115.1	6.58	137.9	65.33	13.04	8.79

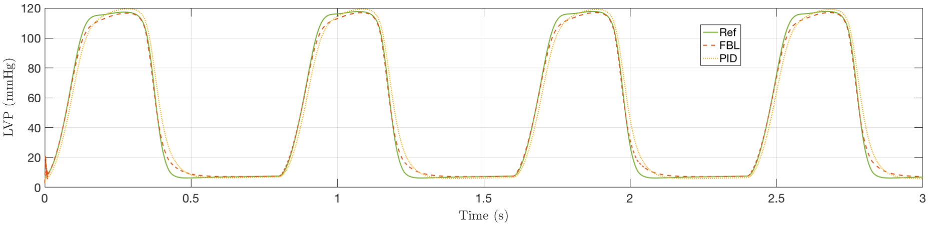

Figure 6.20: Tracking performance of the LVP when applying integer order controllers with the reference provided by the electrical model.

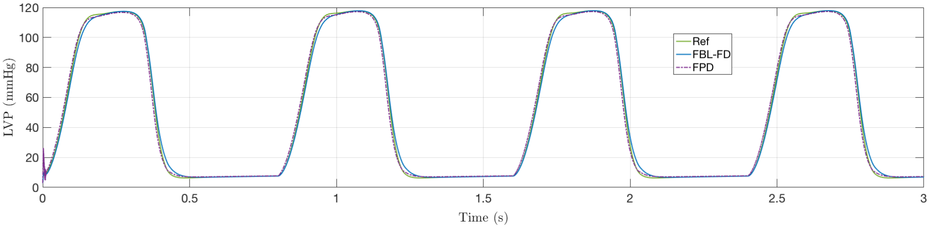

Figure 6.21: Tracking performance of the LVP when applying fractional-order controllers with the reference provided by the electrical model.

reference waveform (LVP_d) when using system-dependent reference generation, which can be used to emulate pathologic behavior; 2) all strategies have good tracking and hemodynamic performance; 3) FBL has high sensitivity to its parameter λ, but low sensitivity to fractional-order α (even for $\alpha = 0$, which corresponds to a pure proportional control law, the results do not show large differences); and 4) when reference is independent of the controlled system, the best tracking performance is obtained with fractional controllers.

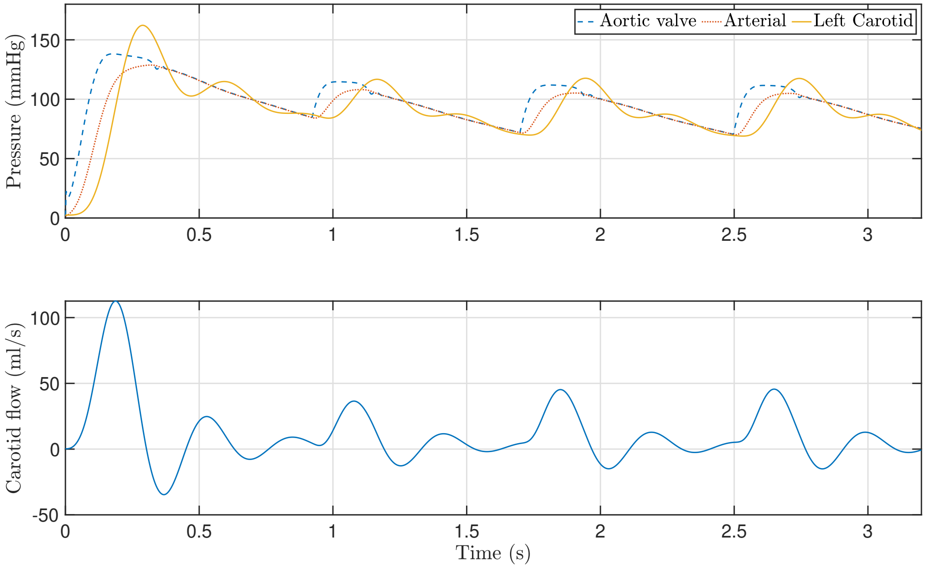

Figure 6.22: Left common carotid artery pressure and flow waveforms.

6.4 Summary

This chapter has presented the results from the two different prototypes and the CVS model and platform.

Firstly, the path following control strategy was analyzed on the 6-rigid link swimming robot. As a control strategy based on nested control loops, each of the internal control loops was verified and evaluated, showing the validity and robustness of the controller for different conditions. Additionally, an analysis of the influence of the beating waveform is performed. The motion analysis states the existence of a strong relationship between the amplitude coefficients of the waveform and the wave propagation velocity with the propulsive velocity of the swimming robot. In this respect, the fractional beating waveform offers the possibility to control the propulsion speed by means of a single parameter, the fractional coefficient. In particular, this coefficient makes it possible to produce equivalent propulsive forces from harmonic motion to linear Carangiform.

Secondly, the flexible 3-link swimming robot dynamics was identified for control purposes through its frequency response. The experiments were performed considering the first segment as actuator and the rest acting as passive flexible links, and the deflection of each of the links was measured. Models consisting of a fractional integrator in series with a resonant system of both fractional-and integer-order were identified in the frequency range $[0.1, 50]$ rad/s for each link. The results showed that both models can be adequate for control purposes. Furthermore, the identification process led to the conclusion that the tip displacement of any IPMC point is characterized by the same dynamics, which remains unchanged along the link with mere variations of the gain for low-frequency applications. From this conclusion, it was also deduced that single actuation of the robot does not allow to produce a nonreciprocal motion, since the dynamics of the second and third links are subject to the dynamics of the first link. There are only differences in the gain and a slight phase lag, which are not sufficient to generate a nonreciprocal motion. In addition, a controller robust to gain variations was designed to control link deflection regardless of link length allowing to address a distributed actuation with the same controller design. It was tuned based on the methodology of the reference model and two control strategies were proposed: a classical PID controller and a noninteger-order integrator. The results showed that the PID offers a better response to tracking control as a consequence of the increased system speed, but does not meet the design specifications. In contrast, the noninteger-order integrator meets the step response specifications but provides worse results for the tracking problem. Finally, the motions of the swimming robot were analyzed to validate that the robot performs a nonreciprocal motion.

Finally, regarding the CVS model presented in the above chapter, it was validated using the main clinical indices, and the cardiovascular waveform was compared with experimental data obtained from clinical trials performed on a pig. Likewise, the model showed consistency despite variations in the preload and afterload factors.

7

CONCLUSIONS & FUTURE WORKS

"An expert is someone who knows some of the worst mistakes that can be made in his subject, and how to avoid them."'

Werner Heisenberg

This Thesis is devoted to modeling and control the locomotion of microrobots, specifically small artificial eukaryotic flagellum-like swimming robots, as well as modeling an experimental platform that emulates the conditions of the cardiovascular system and low *Re* environments for experimentation. Especially, this thesis centers on two differential aspects of microrobotics that have not received that much attention. Firstly, it focuses on autonomous actuation methods, which are less explored than their counterparts, nonautonomous propulsion methods. Secondly, bioinspired strategies are used to achieve the same function and properties as those found in the natural world. Thus, we focus on functionalities found in nature to perfect microrobotics devices and particularly designed applications.

Chapter 1 presented the motivation, objectives, and main contributions of this Thesis. Currently, different research lines are focusing on the locomotion method of microrobots.

A brief a introduction to the field of microrobotics is given in Chapter 2, presenting the most relevant studies since its beginnings in the mid-19th century and discussing the main challenges that this new field must overcome to consolidate and continue to advance. In addition, theoretical foundations in microrobotics are also given, especially for robots that must work in fluid environments.

Analysis and modeling are, in many cases, a prerequisite for controller design, so it is reasonable to study and establish a theoretical model that represents the system's dynamics. Chapter 3 deals with the mathematical model of a planar swimming robot model with N_u flexible links plus the head and driven by $N_u - 1$ actuated joints suitable for medium *Re* environment. The model is particularized to a strictly low *Re* environment, where inertial forces are negligible and brownian effects are not yet present. In the case of the articulated swimming robot, the model highlights the importance of flagellum motion, which is crucial for improving locomotion and performance. For this purpose, a novel beating waveform is presented. It is based on a fractional order power law for amplitude modulation, which makes it possible to preserve the motion properties obtained by applying classical traveling waveforms and to control the stroke and propulsion with a single parameter.

Special attention has been given in this Thesis to the influence of the beating waveform on the propulsion and locomotion control of swimming robots. Chapter 4 analyses and states the existence of a strong relationship between the amplitude coefficients of the waveform and the wave propagation velocity with the propulsive velocity of the swimming robot. Thereunder, the fractional beating waveform offers the possibility to control the propulsion speed employing a single parameter, the fractional coefficient. On the next sections, controllability and observability are studied, generalizing the analysis to N-link swimming robots. The mentioned analysis concludes that it is not possible to state that a swimming robot is controllable in medium *Re* environments. Nevertheless, it is possible to affirm this for swimming robots in low *Re*. Finally, a control strategy for path following was discussed.

Chapter 5 described the two swimming robot prototypes and the experimental platform for swimming robot testing that have been developed in this Thesis as follows. The first prototype consisted of 6 rigid links plus the head from which a simulator was developed in MATLAB®/Simulink® environment. The second prototype consisted of three ionic polymer-metal composite (IPMC) based flexible links. However, unlike the previous one, all the associated electronics were external and the prototype was essentially the flagellum. In addition to prototypes, a novel electrical model of the cardiovasular system (CVS) was presented with two main objectives. The first one was to complete existing cardiovascular models extending the classic Windkessel model to the left common carotid artery. This is useful medically because it allows the model to be validated. The second objective was to build a simulator based on the model of a realizable platform. This platform emulates a low *Re* environment and hemodynamic cardiovascular conditions and serves as a testbed for swimming robots. The model of the simulator was developed using physical modeling tools.

Experimental and simulation results were presented in Chapter 6 to extensively validate the following: the novel beating waveform, the path following control, the beating waveform generation on a flagellum made up of IPMC and the cardiovascular system model proposed in this Thesis.

Firstly, the fractional order approach for the beating waveform propulsion presented improved locomotion for an rigid N-link artificial eukaryotic flagellum swimming robot. The novel beating waveform was based on a fractional order power law for amplitude modulation. It was demonstrated that it confers similar motion properties to the obtained applying classical beating waveforms but presents some benefits in terms of propulsion. Secondly, regarding control strategy based on nested control loops, each of the internal control stages was verified and evaluated, showing the validity and robustness of the controller for different conditions. The first control loop was based on fractional order control was designed with robustness against load variation along the flagellum to improve locomotion. The second control loop was based on line-of-sight (LOS) guidance methodology, a popular method for straight line following applied in maritime vehicles and surface-to-air missiles whose validity was analyzed for this case. The third and last loop, uses waypoint guidance methodology. This methodology divides the given path in straight lines that define the robot's course.

In the third place, a flexible 3-link artificial eukaryotic flagellum swimming robot made up of IPMC was studied for the generation of beating waveform through single and distributed actuation in low *Re* environments. The dynamics was identified for control purposes through its frequency response. A model was identified for each link. The model consisted of a fractional integrator in series with a resonant system of both fractional and integer order for the frequency range $[0.1, 50]$ rad/s. The identification process led to two conclusions: 1) the tip displacement of all IPMC links is characterized by the same dynamics, which remains unchanged along the link with mere variations of the gain for low-frequency applications; and 2) single actuation of the robot does not allow the reproduction of a nonreciprocal motion, since the dynamics of the second and third links are subject to the dynamics of the first link; there are only differences in the gain and a slight phase lag, which are not sufficient to generate a nonreciprocal motion. Consequently, a controller robust to gain variations was designed to control link deflection regardless of link length, allowing distributed actuation with the same controller design. A classical proportional-integral-derivative (PID) controller and a noninteger order integrator were proposed. The control results showed that the PID offers a better response to tracking control due to increased system speed, but does not meet the design specifications. In contrast, the noninteger order integrator meets the step response specifications but provides worse results for the tracking problem. Likewise, the motion of the swimming robot composed of three links of the same length was analyzed to validate. It was concluded that a distributed actuation (active or passive) is necessary to develop a nonreciprocal motion.

Finally, the novel electrical model of the CVS was validated using the leading clinical indices, and the cardiovascular waveform was compared with experimental data obtained from clinical trials performed on a pig. Likewise, the model showed consistency despite preload and afterload factor variations.

Future works will focus on: 1) the fabrication of the robot prototype and testbench platform to validate all these results on the real system; and 2) studying the control approach for a swimming robot with segments of different lengths.

8

BIBLIOGRAPHY

[1] J. E. Hall, *Guyton and Hall textbook of medical physiology*. Elsevier Health Sciences, 2015.

[2] M. B. Bastos, D. Burkhoff, J. Maly, J. Daemen, C. A. den Uil, K. Ameloot, M. Lenzen, F. Mahfoud, F. Zijlstra, J. J. Schreuder *et al.*, "Invasive left ventricle pressure–volume analysis: overview and practical clinical implications," *European Heart Journal*, vol. 41, no. 12, pp. 1286–1297, 2020.

[3] N. Stergiopulos, J.-J. Meister, and N. Westerhof, "Determinants of stroke volume and systolic and diastolic aortic pressure," *American Journal of Physiology-Heart and Circulatory Physiology*, vol. 270, no. 6, pp. H2050–H2059, 1996.

[4] M. A. Simaan, *Rotary Heart Assist Devices*. Berlin, Heidelberg, Germany: Springer Berlin Heidelberg, 2009, pp. 1409–1422.

[5] Y.-C. Yu, J. R. Boston, M. A. Simaan, and J. F. Antaki, "Estimation of systemic vascular bed parameters for artificial heart control," *IEEE Transactions on Automatic Control*, vol. 43, no. 6, pp. 765–778, 1998.

[6] J. E. Traver, C. Nuevo-Gallardo, P. Rodríguez, I. Tejado, and B. M. Vinagre, "Modeling and control of IPMC-based artificial eukaryotic flagellum swimming robot: Distributed actuation," *Algorithms*, vol. 15, no. 6, 2022.

[7] J. E. Traver, C. Nuevo-Gallardo, I. Tejado, J. Fernández-Portales, J. F. Ortega-Morán, J. B. Pagador, and B. M. Vinagre, "Cardiovascular circulatory system and left carotid model: A fractional approach to disease modeling," *Fractal and Fractional*, vol. 6, no. 2, p. 64, 2022.

[8] J. E. Traver, I. Tejado, C. Nuevo-Gallardo, M. A. López, and B. M. Vinagre, "Performance study of propulsion of n-link artificial eukaryotic flagellum swimming microrobot within a fractional order approach: from simulations to hardware-in-the-loop experiments," *European Journal of Control*, vol. 58, pp. 340–356, 2021.

[9] J. E. Traver, C. Nuevo-Gallardo, I. Tejado, and B. M. Vinagre, "Frequency domain modeling of an IPMC-based artificial eukaryotic flagellum swimming robot," in *Proceedings of the International Conference on Fractional Differentiation and its Applications (ICFDA'21)*,

A. Dzielinski, D. Sierociuk, and P. Ostalczyk, Eds. Cham: Springer International Publishing, 2022, pp. 58–64.

[10] J. E. Traver, I. Tejado, C. Nuevo-Gallardo, J. Prieto-Arranz, M. A. López, and B. M. Vinagre, "Evaluating an AEF swimming microrobot using a hardware-in-the-loop testbed," in *Robot 2019: Fourth Iberian Robotics Conference*, M. F. Silva, J. Luís Lima, L. P. Reis, A. Sanfeliu, and D. Tardioli, Eds. Springer International Publishing, 2020, pp. 524–536.

[11] J. E. Traver, I. Tejado, J. Prieto-Arranz, C. Nuevo-Gallardo, M. A. López, and B. M. Vinagre, "Improved locomotion of an AEF swimming robot using fractional order control," in *2019 IEEE International Conference on Systems, Man and Cybernetics (SMC)*, 2019, pp. 2567–2572.

[12] J. E. Traver, I. Tejado, J. Prieto-Arranz, and B. M. Vinagre, "Comparing classical and fractional order control strategies of a cardiovascular circulatory system simulator," *IFAC-PapersOnLine*, vol. 51, no. 4, pp. 48–53, 2018, 3rd IFAC Conference on Advances in Proportional-Integral-Derivative Control PID 2018.

[13] J. E. Traver, J. F. Ortega, I. Tejado, B. Pagador, F. Sun, R. Pérez-Aloe, B. M. Vinagre, and M. F. Margallo, "Simulador cardiovascular para ensayo de robots de navegación autónoma," in *Actas de las XXXVIII Jornadas de Automática*. Servicio de Publicaciones de la Universidad de Oviedo, 2017, pp. 633–640.

[14] J. E. Traver, I. Tejado, and B. M. Vinagre, "A comparative study of planar waveforms for propulsion of a joined artificial bacterial flagella swimming robot," in *Proceedings of the 2017 4th International Conference on Control, Decision and Information Technologies (CoDIT'17)*, 2017, pp. 550–555.

[15] J. E. Traver, B. M. Vinagre, and I. Tejado, "New waveforms for propulsion of planar artificial bacterial flagella microrobots." VI reunión del Capítulo Español de la Sociedad Europea de Biomecánica, 2016.

[16] J. E. Traver, B. M. Vinagre, and I. Tejado, "Robot nadador tipo flagelo bacteriano plano: estudio y simulación del mecanismo de propulsión," in *Actas de las XXXVII Jornadas de Automática*, 2016, pp. 1075–1082.

[17] J. Li, B. E.-F. de Ávila, W. Gao, L. Zhang, and J. Wang, "Micro/nanorobots for biomedicine: Delivery, surgery, sensing, and detoxification," *Science Robotics*, vol. 2, no. 4, 2017.

[18] E. Diller and M. Sitti, "Micro-scale mobile robotics," *Foundations and trends® in robotics*, vol. 2, no. 3, pp. 143–259, 2013.

[19] M. Sitti, *Mobile microrobotics*. Cambridge, Massachusetts: MIT Press, 2017.

[20] D. D. Carlo and L. P. Lee, "Dynamic single-cell analysis for quantitative biology," *Analytical Chemistry*, vol. 78, no. 23, pp. 7918–7925, 12 2006.

[21] X. Liu, Z. Lu, and Y. Sun, "Orientation control of biological cells under inverted microscopy," *IEEE/ASME Transactions on Mechatronics*, vol. 16, no. 5, pp. 918–924, 2011.

[22] C. Dai, Z. Zhang, Y. Lu, G. Shan, X. Wang, Q. Zhao, C. Ru, and Y. Sun, “Robotic manipulation of deformable cells for orientation control,” *IEEE Transactions on Robotics*, vol. 36, no. 1, pp. 271–283, 2020.

[23] Z. Lu, X. Zhang, C. Leung, N. Esfandiari, R. F. Casper, and Y. Sun, “Robotic icsi (intracytoplasmic sperm injection),” *IEEE Transactions on Biomedical Engineering*, vol. 58, no. 7, pp. 2102–2108, 2011.

[24] J. J. Abbott, Z. Nagy, F. Beyeler, and B. J. Nelson, “Robotics in the small, part i: microbotics,” *IEEE Robotics & Automation Magazine*, vol. 14, no. 2, pp. 92–103, 2007.

[25] L. Dong and B. J. Nelson, “Tutorial - robotics in the small part ii: Nanorobotics,” *IEEE Robotics & Automation Magazine*, vol. 14, no. 3, pp. 111–121, 2007.

[26] L. Dong, X. Tao, M. Hamdi, L. Zhang, X. Zhang, A. Ferreira, and B. J. Nelson, “Nanotube fluidic junctions: internanotube attogram mass transport through walls,” *Nano Letters*, vol. 9, no. 1, pp. 210–214, 2009.

[27] B. Wang, K. F. Chan, F. Ji, Q. Wang, P. W. Y. Chiu, Z. Guo, and L. Zhang, “On-demand coalescence and splitting of liquid marbles and their bioapplications,” *Advanced Science*, vol. 6, no. 10, p. 1802033, 2019.

[28] G. Go, S.-G. Jeong, A. Yoo, J. Han, B. Kang, S. Kim, K. T. Nguyen, Z. Jin, C.-S. Kim, Y. R. Seo *et al.*, “Human adipose–derived mesenchymal stem cell–based medical microrobot system for knee cartilage regeneration in vivo,” *Science Robotics*, vol. 5, no. 38, p. eaay6626, 2020.

[29] A. A. Solovev, W. Xi, D. H. Gracias, S. M. Harazim, C. Deneke, S. Sanchez, and O. G. Schmidt, “Self-propelled nanotools,” *Acs Nano*, vol. 6, no. 2, pp. 1751–1756, 2012.

[30] K. T. Nguyen, S.-J. Kim, H.-K. Min, M. C. Hoang, G. Go, B. Kang, J. Kim, E. Choi, A. Hong, J.-O. Park, and C.-S. Kim, “Guide-wired helical microrobot for percutaneous revascularization in chronic total occlusion in-vivo validation,” *IEEE Transactions on Biomedical Engineering*, vol. 68, no. 8, pp. 2490–2498, 2021.

[31] Y. Zhang, L. Zhang, L. Yang, C. I. Vong, K. F. Chan, W. K. Wu, T. N. Kwong, N. W. Lo, M. Ip, S. H. Wong *et al.*, “Real-time tracking of fluorescent magnetic spore–based microrobots for remote detection of c. diff toxins,” *Science advances*, vol. 5, no. 1, p. eaau9650, 2019.

[32] J. Jiang, Z. Yang, A. Ferreira, and L. Zhang, “Control and autonomy of microrobots: Recent progress and perspective,” *Advanced Intelligent Systems*, vol. 4, no. 5, pp. 2 100 279:1–2 100 279:25, 2022.

[33] L. Dekanovsky, B. Khezri, Z. Rottnerova, F. Novotny, J. Plutnar, and M. Pumera, “Chemically programmable microrobots weaving a web from hormones,” *Nature Machine Intelligence*, vol. 2, no. 11, pp. 711–718, 2020.

[34] F. Ji, B. Wang, and L. Zhang, “Light-triggered catalytic performance enhancement using magnetic nanomotor ensembles,” *Research*, vol. 2020, 2020.

[35] J. Li, B. E.-F. de Ávila, W. Gao, L. Zhang, and J. Wang, "Micro/nanorobots for biomedicine: Delivery, surgery, sensing, and detoxification," *Science robotics*, 2017.

[36] B. Wang, K. Kostarelos, B. J. Nelson, and L. Zhang, "Trends in micro-/nanorobotics: materials development, actuation, localization, and system integration for biomedical applications," *Advanced Materials*, vol. 33, no. 4, pp. 2 002 047:1–2 002 047:44, 2021.

[37] S. T. Chang, V. N. Paunov, D. N. Petsev, and O. D. Velev, "Remotely powered self-propelling particles and micropumps based on miniature diodes," *Nature materials*, vol. 6, no. 3, pp. 235–240, 2007.

[38] L. Zhang, J. J. Abbott, L. Dong, B. E. Kratochvil, D. Bell, and B. J. Nelson, "Artificial bacterial flagella: Fabrication and magnetic control," *Applied Physics Letters*, vol. 94, no. 6, p. 064107, 2009.

[39] T. Xu, W. Gao, L.-P. Xu, X. Zhang, and S. Wang, "Fuel-free synthetic micro-/nanomachines," *Advanced Materials*, vol. 29, no. 9, p. 1603250, 2017.

[40] M. Sitti, "Microscale and nanoscale robotics systems: Characteristics, state of the art, and grand challenges," *IEEE Robotics & Automation Magazine*, vol. 14, no. 1, pp. 53–60, 2007.

[41] B. J. Nelson, I. K. Kaliakatsos, and J. J. Abbott, "Microrobots for minimally invasive medicine," *Annual review of biomedical engineering*, vol. 12, pp. 55–85, 2010.

[42] M. Sitti, H. Ceylan, W. Hu, J. Giltinan, M. Turan, S. Yim, and E. Diller, "Biomedical applications of untethered mobile milli/microrobots," *Proceedings of the IEEE*, vol. 103, no. 2, pp. 205–224, 2015.

[43] H. Ceylan, J. Giltinan, K. Kozielski, and M. Sitti, "Mobile microrobots for bioengineering applications," *Lab on a Chip*, vol. 17, no. 10, pp. 1705–1724, 2017.

[44] M. Koleoso, X. Feng, Y. Xue, Q. Li, T. Munshi, and X. Chen, "Micro/nanoscale magnetic robots for biomedical applications," *Materials Today Bio*, vol. 8, p. 100085, 2020.

[45] B. Sun, G. Wood, and S. Miyashita, "Milestones for autonomous in vivo microrobots in medical applications," *Surgery*, vol. 169, no. 4, pp. 755–758, 2021.

[46] T. Wang, Z. Ren, W. Hu, M. Li, and M. Sitti, "Effect of body stiffness distribution on larval fish–like efficient undulatory swimming," *Science Advances*, vol. 7, no. 19, p. eabf7364, 2021.

[47] S. Guo, T. Fukuda, N. Kato, and K. Oguro, "Development of underwater microrobot using icpf actuator," in *Proceedings. 1998 IEEE International Conference on Robotics and Automation (Cat. No. 98CH36146)*, vol. 2. IEEE, 1998, pp. 1829–1834.

[48] G. Laurent and D. Piat, "Efficiency of swimming microrobots using ionic polymer metal composite actuators," in *Proceedings 2001 ICRA. IEEE International Conference on Robotics and Automation (Cat. No. 01CH37164)*, vol. 4. IEEE, 2001, pp. 3914–3919.

[49] B. Kim, D.-H. Kim, J. Jung, and J.-O. Park, "A biomimetic undulatory tadpole robot using ionic polymer–metal composite actuators," *Smart materials and structures*, vol. 14, no. 6, p. 1579, 2005.

[50] R. Dreyfus, J. Baudry, M. L. Roper, M. Fermigier, H. A. Stone, and J. Bibette, "Microscopic artificial swimmers," *Nature*, vol. 437, no. 7060, pp. 862–865, 2005.

[51] T. Honda, K. Arai, and K. Ishiyama, "Micro swimming mechanisms propelled by external magnetic fields," *IEEE Transactions on Magnetics*, vol. 32, no. 5, pp. 5085–5087, 1996.

[52] K. Ishiyama, M. Sendoh, A. Yamazaki, and K. Arai, "Swimming micro-machine driven by magnetic torque," *Sensors and Actuators A: Physical*, vol. 91, no. 1-2, pp. 141–144, 2001.

[53] S. Guo, J. Sawamoto, and Q. Pan, "A novel type of microrobot for biomedical application," in *2005 IEEE/RSJ International Conference on Intelligent Robots and Systems*. IEEE, 2005, pp. 1047–1052.

[54] S. Sudo, S. Segawa, and T. Honda, "Magnetic swimming mechanism in a viscous liquid," *Journal of intelligent material systems and structures*, vol. 17, no. 8-9, pp. 729–736, 2006.

[55] G. Kósa, P. Jakab, N. Hata, F. Jólesz, Z. Neubach, M. Shoham, M. Zaaroor, and G. Székely, "Flagellar swimming for medical micro robots: theory, experiments and application," in *Proceedings of the 2nd IEEE RAS & EMBS International Conference on Biomedical Robotics and Biomechatronics (BioRob 2008)*, 2008, pp. 258–263.

[56] S. Guo, J. Sawamoto, and Q. Pan, "A novel type of microrobot for biomedical application," in *2005 IEEE/RSJ International Conference on Intelligent Robots and Systems*. IEEE, 2005, pp. 1047–1052.

[57] G. Kósa, M. Shoham, and M. Zaaroor, "Analysis of a swimming micro robot," in *The First IEEE/RAS-EMBS International Conference on Biomedical Robotics and Biomechatronics, 2006. BioRob 2006.* IEEE, 2006, pp. 130–134.

[58] S. Guo, Y. Ge, L. Li, and S. Liu, "Underwater swimming micro robot using IPMC actuator," in *2006 International Conference on Mechatronics and Automation*, 2006, pp. 249–254.

[59] B. Behkam and M. Sitti, "Design Methodology for Biomimetic Propulsion of Miniature Swimming Robots," *Journal of Dynamic Systems, Measurement, and Control*, vol. 128, no. 1, pp. 36–43, 09 2005. [Online]. Available: https://doi.org/10.1115/1.2171439

[60] K.-J. Cho, E. Hawkes, C. Quinn, and R. J. Wood, "Design, fabrication and analysis of a body-caudal fin propulsion system for a microrobotic fish," in *2008 IEEE international Conference on Robotics and Automation*. IEEE, 2008, pp. 706–711.

[61] Z. Wang, G. Hang, J. Li, Y. Wang, and K. Xiao, "A micro-robot fish with embedded sma wire actuated flexible biomimetic fin," *Sensors and Actuators A: Physical*, vol. 144, no. 2, pp. 354–360, 2008.

[62] Z. Wang, G. Hang, J. Li, Y. Wang, and K. Xiao, “A micro-robot fish with embedded sma wire actuated flexible biomimetic fin,” *Sensors and Actuators A: Physical*, vol. 144, no. 2, pp. 354–360, 2008.

[63] K. Ishiyama, M. Sendoh, and K. Arai, “Magnetic micromachines for medical applications,” *Journal of Magnetism and Magnetic Materials*, vol. 242, pp. 41–46, 2002.

[64] J. Edd, S. Payen, B. Rubinsky, M. L. Stoller, and M. Sitti, “Biomimetic propulsion for a swimming surgical micro-robot,” in *Proceedings 2003 IEEE/RSJ International Conference on Intelligent Robots and Systems (IROS 2003)(Cat. No. 03CH37453)*, vol. 3. IEEE, 2003, pp. 2583–2588.

[65] B. Behkam and M. Sitti, “Bacterial flagella-based propulsion and on/off motion control of microscale objects,” *Applied Physics Letters*, vol. 90, no. 2, p. 023902, 2007.

[66] H. Li, J. Tan, and M. Zhang, “Dynamics modeling and analysis of a swimming microrobot for controlled drug delivery,” *IEEE Transactions on Automation Science and Engineering*, vol. 6, no. 2, pp. 220–227, 2008.

[67] K. E. Peyer, L. Zhang, B. E. Kratochvil, and B. J. Nelson, “Non-ideal swimming of artificial bacterial flagella near a surface,” in *2010 IEEE International Conference on Robotics and Automation*, 2010, pp. 96–101.

[68] L. Zhang, K. E. Peyer, T. Petit, B. E. Kratochvil, and B. J. Nelson, “Motion control of artificial bacterial flagella,” in *10th IEEE International Conference on Nanotechnology*, 2010, pp. 893–896.

[69] A. Ghosh and P. Fischer, “Controlled propulsion of artificial magnetic nanostructured propellers,” *Nano letters*, vol. 9, no. 6, pp. 2243–2245, 2009.

[70] K. B. Yesin, K. Vollmers, and B. J. Nelson, “Modeling and control of untethered biomicrorobots in a fluidic environment using electromagnetic fields,” *The International Journal of Robotics Research*, vol. 25, no. 5-6, pp. 527–536, 2006.

[71] S. Martel, J.-B. Mathieu, O. Felfoul, A. Chanu, E. Aboussouan, S. Tamaz, P. Pouponneau, L. Yahia, G. Beaudoin, G. Soulez, and M. Mankiewicz, “Automatic navigation of an untethered device in the artery of a living animal using a conventional clinical magnetic resonance imaging system,” *Applied Physics Letters*, vol. 90, no. 11, p. 114105, 2007.

[72] S. Floyd, C. Pawashe, and M. Sitti, “An untethered magnetically actuated micro-robot capable of motion on arbitrary surfaces,” in *2008 IEEE International Conference on Robotics and Automation*, 2008, pp. 419–424.

[73] S. Floyd, C. Pawashe, and M. Sitti, “Two-dimensional contact and noncontact micromanipulation in liquid using an untethered mobile magnetic microrobot,” *IEEE Transactions on Robotics*, vol. 25, no. 6, pp. 1332–1342, 2009.

[74] C. Pawashe, S. Floyd, and M. Sitti, "Modeling and experimental characterization of an untethered magnetic micro-robot," *The International Journal of Robotics Research*, vol. 28, no. 8, pp. 1077–1094, 2009.

[75] S. Martel and M. Mohammadi, "Using a swarm of self-propelled natural microrobots in the form of flagellated bacteria to perform complex micro-assembly tasks," in *2010 IEEE International Conference on Robotics and Automation*, 2010, pp. 500–505.

[76] L. Arcese, M. Fruchard, and A. Ferreira, "Adaptive controller and observer for a magnetic microrobot," *IEEE Transactions on Robotics*, vol. 29, no. 4, pp. 1060–1067, 2013.

[77] B. Donald, C. Levey, C. McGray, I. Paprotny, and D. Rus, "An untethered, electrostatic, globally controllable mems micro-robot," *Journal of Microelectromechanical Systems*, vol. 15, no. 1, pp. 1–15, 2006.

[78] B. R. Donald, C. G. Levey, and I. Paprotny, "Planar microassembly by parallel actuation of mems microrobots," *Journal of Microelectromechanical Systems*, vol. 17, no. 4, pp. 789–808, 2008.

[79] L. Huang, L. Rogowski, M. J. Kim, and A. T. Becker, "Path planning and aggregation for a microrobot swarm in vascular networks using a global input," in *2017 IEEE/RSJ International Conference on Intelligent Robots and Systems (IROS)*. IEEE, 2017, pp. 414–420.

[80] M. Takahashi, I. Hayashi, N. Iwatsuki, K. Suzumori, and N. Ohki, "The development of an in-pipe microrobot applying the motion of an earthworm," in *1994 5th International Symposium on Micro Machine and Human Science Proceedings*, 1994, pp. 35–.

[81] P. Dario, M. Carrozza, L. Lencioni, B. Magnani, and S. D'Attanasio, "A microrobotic system for colonoscopy," in *Proceedings of International Conference on Robotics and Automation*, vol. 2, 1997, pp. 1567–1572 vol.2.

[82] P. Dario, M. Carrozza, C. Stefanini, and S. D'Attanasio, "A mobile microrobot actuated by a new electromagnetic wobble micromotor," *IEEE/ASME Transactions on Mechatronics*, vol. 3, no. 1, pp. 9–16, 1998.

[83] C. Anthierens, C. Libersa, M. Touaibia, M. Betemps, M. Arsicault, and N. Chaillet, "Micro robots dedicated to small diameter canalization exploration," in *Proceedings. 2000 IEEE/RSJ International Conference on Intelligent Robots and Systems (IROS 2000) (Cat. No.00CH37113)*, vol. 1, 2000, pp. 480–485 vol.1.

[84] B. Kim, S. Lee, J. H. Park, and J.-O. Park, "Inchworm-like microrobot for capsule endoscope," in *2004 IEEE International Conference on Robotics and Biomimetics*, 2004, pp. 458–463.

[85] A. Menciassi, S. Gorini, G. Pernorio, and P. Dario, "A sma actuated artificial earthworm," in *IEEE International Conference on Robotics and Automation, 2004. Proceedings. ICRA '04. 2004*, vol. 4, 2004, pp. 3282–3287 Vol.4.

[86] N. Saga and T. Nakamura, “Development of a peristaltic crawling robot using magnetic fluid on the basis of the locomotion mechanism of an earthworm,” in *Smart Structures, Devices, and Systems*, E. C. Harvey, D. Abbott, and V. K. Varadan, Eds., vol. 4935, International Society for Optics and Photonics. SPIE, 2002, pp. 369 – 377. [Online]. Available: https://doi.org/10.1117/12.476128

[87] B. Kim, M. G. Lee, Y. P. Lee, Y. Kim, and G. Lee, “An earthworm-like micro robot using shape memory alloy actuator,” *Sensors and Actuators A: Physical*, vol. 125, no. 2, pp. 429–437, 2006. [Online]. Available: https://www.sciencedirect.com/science/article/pii/S0924424705003067

[88] J. Lim, H. Park, J. An, Y.-S. Hong, B. Kim, and B.-J. Yi, “One pneumatic line based inchworm-like micro robot for half-inch pipe inspection,” *Mechatronics*, vol. 18, no. 7, pp. 315–322, 2008, special Section of Revised Papers from the 8th International IFAC Symposium on Robot Control. [Online]. Available: https://www.sciencedirect.com/science/article/pii/S0957415808000834

[89] C. Pawashe, S. Floyd, and M. Sitti, “Multiple magnetic microrobot control using electrostatic anchoring,” *Applied Physics Letters*, vol. 94, no. 16, p. 164108, 2009.

[90] P. Fischer and A. Ghosh, “Magnetically actuated propulsion at low reynolds numbers: towards nanoscale control,” *Nanoscale*, vol. 3, no. 2, pp. 557–563, 2011.

[91] M. Sitti, H. Ceylan, W. Hu, J. Giltinan, M. Turan, S. Yim, and E. Diller, “Biomedical applications of untethered mobile milli/microrobots,” *Proceedings of the IEEE*, vol. 103, no. 2, pp. 205–224, 2015.

[92] T. Li, J. Li, H. Zhang, X. Chang, W. Song, Y. Hu, G. Shao, E. Sandraz, G. Zhang, L. Li, and J. Wang, “Magnetically propelled fish-like nanoswimmers,” *Small*, vol. 12, no. 44, pp. 6098–6105, 2016.

[93] O. J. Sul, M. R. Falvo, R. M. Taylor, S. Washburn, and R. Superfine, “Thermally actuated untethered impact-driven locomotive microdevices,” *Applied Physics Letters*, vol. 89, no. 20, p. 203512, 2006.

[94] W. Hu, K. S. Ishii, and A. T. Ohta, “Micro-assembly using optically controlled bubble microrobots,” *Applied Physics Letters*, vol. 99, no. 9, p. 094103, 2011.

[95] M. S. Sakar, E. B. Steager, D. H. Kim, A. A. Julius, M. Kim, V. Kumar, and G. J. Pappas, “Modeling, control and experimental characterization of microbiorobots,” *The International Journal of Robotics Research*, vol. 30, no. 6, pp. 647–658, 2011.

[96] A. A. Solovev, Y. Mei, E. Bermúdez Ureña, G. Huang, and O. G. Schmidt, “Catalytic microtubular jet engines self-propelled by accumulated gas bubbles,” *Small*, vol. 5, no. 14, pp. 1688–1692, 2009.

[97] W. Duan, W. Wang, S. Das, V. Yadav, T. E. Mallouk, and A. Sen, “Synthetic nano- and micromachines in analytical chemistry: Sensing, migration, capture, delivery, and separation,” *Annual Review of Analytical Chemistry*, vol. 8, no. 1, pp. 311–333, 2015, pMID: 26132348.

[98] G. Hwang, R. Braive, L. Couraud, A. Cavanna, O. Abdelkarim, I. Robert-Philip, A. Beveratos, I. Sagnes, S. Haliyo, and S. Régnier, "Electro-osmotic propulsion of helical nanobelt swimmers," *The International Journal of Robotics Research*, vol. 30, no. 7, pp. 806–819, 2011.

[99] D. Hyung Kim, P. Seung Soo Kim, A. Agung Julius, and M. Jun Kim, "Three-dimensional control of tetrahymena pyriformis using artificial magnetotaxis," *Applied Physics Letters*, vol. 100, no. 5, p. 053702, 2012.

[100] V. Magdanz, S. Sanchez, and O. G. Schmidt, "Development of a sperm-flagella driven micro-bio-robot," *Advanced Materials*, vol. 25, no. 45, pp. 6581–6588, 2013.

[101] B. J. Williams, S. V. Anand, J. Rajagopalan, and M. T. A. Saif, "A self-propelled biohybrid swimmer at low reynolds number," *Nature communications*, vol. 5, no. 1, pp. 1–8, 2014.

[102] I. Shimoyama, "Scaling in microrobots," in *In Proceedings of the 1995 IEEE/RSJ International Conference on Intelligent Robots and Systems. Human Robot Interaction and Cooperative Robots*, vol. 2. IEEE, 1995, pp. 208–211.

[103] W. Trimmer and R. Jebens, "Actuators for micro robots," in *In Proceedings of the 1989 IEEE International Conference on Robotics and Automation*. IEEE Computer Society, 1989, pp. 1547–1548.

[104] M. Wautelet, "Scaling laws in the macro-, micro-and nanoworlds," *European Journal of Physics*, vol. 22, no. 6, pp. 601–611, 2001.

[105] C. Brennen and H. Winet, "Fluid mechanics of propulsion by cilia and flagella," *Annual Review of Fluid Mechanics*, vol. 9, no. 1, pp. 339–398, 1977.

[106] J. Happel and H. Brenner, *Low Reynolds number hydrodynamics: with special applications to particulate media*, 1st ed. Springer, 2012, vol. 1.

[107] E. Hinch, "Hydrodynamics at low reynolds numbers: a brief and elementary introduction," in *Disorder and mixing*. Springer, 1988, pp. 43–56.

[108] E. Lauga and T. R. Powers, "The hydrodynamics of swimming microorganisms," *Reports on Progress in Physics*, vol. 72, no. 9, pp. 096 601:1–096 601:36, 2009.

[109] G. I. Taylor, "Analysis of the swimming of microscopic organisms," *Proc. R. Soc. Lond. A*, vol. 209, no. 1099, pp. 447–461, 1951.

[110] G. Hancock, "The self-propulsion of microscopic organisms through liquids," *Proceedings of the Royal Society of London. Series A. Mathematical and Physical Sciences*, vol. 217, no. 1128, pp. 96–121, 1953.

[111] J. Gray and G. J. Hancock, "The propulsion of sea-urchin spermatozoa," *Journal of Experimental Biology*, vol. 32, no. 4, pp. 802–814, 1955.

[112] R. G. Cox, "The motion of long slender bodies in a viscous fluid part 1. general theory," *Journal of Fluid Mechanics*, vol. 44, no. 4, p. 791–810, 1970.

[113] J. Lighthill, “Flagellar hydrodynamics,” *SIAM review*, vol. 18, no. 2, pp. 161–230, 1976.

[114] R. Johnson and C. Brokaw, “Flagellar hydrodynamics. a comparison between resistive-force theory and slender-body theory,” *Biophysical journal*, vol. 25, no. 1, pp. 113–127, 1979.

[115] J. Rathore and N. Sharma, “Engineering nanorobots: Chronology of modeling flagellar propulsion,” *Journal of Nanotechnology in Engineering and Medicine*, vol. 1, no. 3, 2010.

[116] B. Liu, K. S. Breuer, and T. R. Powers, “Helical swimming in stokes flow using a novel boundary-element method,” *Physics of Fluids*, vol. 25, no. 6, p. 061902, 2013.

[117] B. Rodenborn, C.-H. Chen, H. L. Swinney, B. Liu, and H. Zhang, “Propulsion of microorganisms by a helical flagellum,” *Proceedings of the National Academy of Sciences*, vol. 110, no. 5, pp. E338–E347, 2013.

[118] E. M. Purcell, “Life at low Reynolds number,” *American Journal of Physics*, vol. 45, no. 1, pp. 3–11, 1977.

[119] E. Mancha, J. E. Traver, I. Tejado, J. Prieto, B. M. Vinagre, and V. Feliu, “Artificial flagellum microrobot. design and simulation in comsol,” in *ROBOT 2017: Third Iberian Robotics Conference*, A. Ollero, A. Sanfeliu, L. Montano, N. Lau, and C. Cardeira, Eds. Cham: Springer International Publishing, 2018, pp. 491–501.

[120] B. Alberts, D. Bray, K. Hopkin, A. D. Johnson, J. Lewis, M. Raff, K. Roberts, and P. Walter, *Essential cell biology*. Garland Science, 2015.

[121] A. Barrientos *et al.*, *Fundamentos de robótica*. Biblioteca Hernán Malo González, 2007.

[122] Shugen, “Analysis of creeping locomotion of a snake-like robot,” *Advanced Robotics*, vol. 15, no. 2, pp. 205–224, 2001.

[123] P. Liljebäck, K. Y. Pettersen, Ø. Stavdahl, and J. T. Gravdahl, *Snake robots: modelling, mechatronics, and control*. Springer, 2013.

[124] K. Y. Pettersen, “Snake robots,” *Annual Reviews in Control*, vol. 44, pp. 19–44, 2017.

[125] R. J. Full, “Invertebrate locomotor systems,” *Comprehensive physiology*, pp. 853–930, 2010.

[126] E. Lauga and C. Eloy, “Shape of optimal active flagella,” *Journal of Fluid Mechanics*, vol. 730, p. R1, 2013.

[127] M. Lighthill, “Note on the swimming of slender fish,” *Journal of fluid Mechanics*, vol. 9, no. 2, pp. 305–317, 1960.

[128] M. Shahinpoor and K. J. Kim, “Ionic polymer metal composites: IV industrial and medical applications,” *Smart Materials and Structures*, vol. 14, no. 1, pp. 197–214, 2004.

[129] S. Nemat-Nasser, “Micromechanics of actuation of ionic polymer-metal composites,” *Journal of Applied Physics*, vol. 92, no. 5, pp. 2899–2915, 2002.

[130] D. Pugal, “Physics based model of ionic polymer metal composite electromechanical and mechanoelectrical transduction,” Ph.D. dissertation, University of Nevada, 2012.

[131] Z. Chen and X. Tan, “A control-oriented and physics-based model for ionic polymer–metal composite actuators,” *IEEE/ASME Transactions on Mechatronics*, vol. 13, no. 5, pp. 519–529, 2008.

[132] R. Caponetto, S. Graziani, F. Sapuppo, and V. Tomasello, “An enhanced fractional order model of ionic polymer-metal composites actuator,” *Advances in Mathematical Physics*, pp. 717 659:1–717 659:6, 2013.

[133] G.-H. Feng and R.-H. Chen, “Universal concept for fabricating arbitrary shaped μIPMC transducers and its application on developing accurately controlled surgical devices,” in *Proceedings of the 2nd IEEE International Conference on Nano/Micro Engineered and Molecular Systems*, 2007, pp. 622–625.

[134] G.-H. Feng and R.-H. Chen, “Improved cost-effective fabrication of arbitrarily shaped μIPMC transducers,” *Journal of Micromechanics and Microengineering*, vol. 18, no. 1, p. 015016, 2008.

[135] S. Tsuchitani, K. Kikuchi, I. Shimizu, T. Taniguchi, and H. Miki, “IPMC actuators fabricated using MEMS technology,” in *Proceedings of the 7th Forum on New Materials - Part A*, vol. 97, 2017, pp. 57–60.

[136] J. Liu, Y. Wang, D. Zhao, C. Zhang, H. Chen, and D. Li, “Design and fabrication of an IPMC-embedded tube for minimally invasive surgery applications,” in *Proceedings of the 2014 Electroactive Polymer Actuators and Devices (EAPAD)*, 2014.

[137] S. Nemat-Nasser and J. Y. Li, “Electromechanical response of ionic polymer-metal composites,” *Journal of Applied Physics*, vol. 87, no. 7, pp. 3321–3331, 2000.

[138] Z. Chen, X. Tan, A. Will, and C. Ziel, “A dynamic model for ionic polymer–metal composite sensors,” *Smart Materials and Structures*, vol. 16, no. 4, p. 1477, 2007.

[139] G. A. Roth, G. A. Mensah, C. O. Johnson, G. Addolorato, E. Ammirati, L. M. Baddour, N. C. Barengo, A. Z. Beaton, E. J. Benjamin, C. P. Benziger *et al.*, “Global burden of cardiovascular diseases and risk factors, 1990–2019: update from the gbd 2019 study,” *Journal of the American College of Cardiology*, vol. 76, no. 25, pp. 2982–3021, 2020.

[140] World Health Organization: Cardiovascular Diseases (CVDs). [Online]. Available: https://www.who.int/news-room/fact-sheets/detail/cardiovascular-diseases-(cvds)

[141] F. Martini, J. Nath, and E. Bartholomew, *Fundamentals of Anatomy & Physiology*. Benjamin-Cummings Publishing Company, 2015.

[142] Texas Heart Institute: Carotid Artery Disease. [Online]. Available: https://www.texasheart.org/heart-health/heart-information-center/topics/carotid-artery-disease/

[143] J. A. Goldstein and M. J. Kern, *Principles of Normal Physiology and Pathophysiology*. New Jersey, USA: John Wiley and Sons, Ltd, 2018, ch. 1, pp. 1–34.

[144] D. U. Silverthorn, W. C. Ober, C. W. Garrison, A. C. Silverthorn, and B. R. Johnson, *Human physiology: an integrated approach*. Pearson/Benjamin Cummings San Francisco, CA, USA:, 2009.

[145] Z. Keshavarz-Motamed, "A diagnostic, monitoring, and predictive tool for patients with complex valvular, vascular and ventricular diseases," *Scientific Reports*, vol. 10, no. 1, pp. 1–19, 2020.

[146] S. S. Simakov, "Lumped parameter heart model with valve dynamics," *Russian Journal of Numerical Analysis and Mathematical Modelling*, vol. 34, no. 5, pp. 289–300, 2019.

[147] S. Bozkurt, "Mathematical modeling of cardiac function to evaluate clinical cases in adults and children," *PloS One*, vol. 14, no. 10, p. e0224663, 2019.

[148] S. Paeme, K. T. Moorhead, J. G. Chase, B. Lambermont, P. Kolh, V. D'orio, L. Pierard, M. Moonen, P. Lancellotti, P. C. Dauby *et al.*, "Mathematical multi-scale model of the cardiovascular system including mitral valve dynamics. application to ischemic mitral insufficiency," *Biomedical Engineering Online*, vol. 10, no. 1, pp. 1–20, 2011.

[149] J. P. Mynard, M. R. Davidson, D. J. Penny, and J. J. Smolich, "A simple, versatile valve model for use in lumped parameter and one-dimensional cardiovascular models," *International Journal for Numerical Methods in Biomedical Engineering*, vol. 28, no. 6-7, pp. 626–641, 2012.

[150] H. Liu, S. Liu, X. Ma, and Y. Zhang, "A numerical model applied to the simulation of cardiovascular hemodynamics and operating condition of continuous-flow left ventricular assist device," *Mathematical Biosciences and Engineering*, vol. 17, no. 6, pp. 7519–7543, 2020.

[151] G. Faragallah and M. A. Simaan, "An engineering analysis of the aortic valve dynamics in patients with rotary left ventricular assist devices," *Journal of Healthcare Engineering*, vol. 4, no. 3, pp. 307–327, 2013.

[152] S. Shimizu, D. Une, T. Kawada, Y. Hayama, A. Kamiya, T. Shishido, and M. Sugimachi, "Lumped parameter model for hemodynamic simulation of congenital heart diseases," *The Journal of Physiological Sciences*, vol. 68, no. 2, pp. 103–111, 2018.

[153] F. Ježek, T. Kulhánek, K. Kalecky̌, and J. Kofránek, "Lumped models of the cardiovascular system of various complexity," *Biocybernetics and Biomedical Engineering*, vol. 37, no. 4, pp. 666–678, 2017.

[154] E. Ortiz-Rangel, G. V. Guerrero-Ramírez, C. D. García-Beltrán, M. Guerrero-Lara, M. Adam-Medina, C. M. Astorga-Zaragoza, J. Reyes-Reyes, and R. Posada-Gómez, "Dynamic modeling and simulation of the human cardiovascular system with pda," *Biomedical Signal Processing and Control*, vol. 71, p. 103151, 2022.

[155] G. Ferrari, A. Di Molfetta, K. Zieliński, and L. Fresiello, “Circulatory modelling as a clinical decision support and an educational tool,” *Biomed Data J*, vol. 1, no. 3, pp. 45–50, 2015.

[156] Y. Wang, N. Loghmanpour, S. Vandenberghe, A. Ferreira, B. Keller, J. Gorcsan, and J. Antaki, “Simulation of dilated heart failure with continuous flow circulatory support,” *PloS one*, vol. 9, no. 1, p. e85234, 2014.

[157] W. Nichols, M. O’Rourke, and C. Vlachopoulos, *McDonald’s Blood Flow in Arteries, Sixth Edition: Theoretical, Experimental and Clinical Principles*. CRC Press, 2011.

[158] Y. Liu, P. Allaire, Y. Wu, H. Wood, and D. Olsen, “Construction of an artificial heart pump performance test system,” *Cardiovascular Engineering*, vol. 6, no. 4, pp. 151–158, 2006.

[159] L. P. Dasi, H. A. Simon, P. Sucosky, and A. P. Yoganathan, “Fluid mechanics of artificial heart valves,” *Clinical and Experimental Pharmacology and Physiology*, vol. 36, no. 2, pp. 225–237, 2009.

[160] V. O. Björk, F. Intonti, and A. Meissl, “A mechanical pulse duplicator for testing prosthetic mitral and aortic valves,” *Thorax*, vol. 17, no. 3, pp. 280–283, 1962.

[161] W. J. Kolff, “Mock circulation to test pumps designed for permanent replacement of damaged hearts.” *Cleveland Clinic Quarterly*, vol. 26, p. 223, 1959.

[162] H. Reul, B. Tesch, J. Schoenmackers, and S. Effert, “Hydromechanical simulation of systemic circulation,” *Medical and Biological Engineering and Computing*, vol. 12, no. 4, pp. 431–436, 1974.

[163] L. Baloa, J. Boston, and J. Antaki, “Elastance-based control of a mock circulatory system,” *Annals of biomedical engineering*, vol. 29, no. 3, pp. 244–251, 2001.

[164] G. Fiore, A. Redaelli, M. Rasponi, and R. Fumero, “Development of a model left ventricle with physiologic-like diastolic behaviour for studying mitral valve surgical correction,” in *Summer Bioengineering Conference, Sonesta Beach Resort in Key Biscayne, Florida June*, 2003.

[165] L. Formaggia, A. Quarteroni, and A. Veneziani, *Cardiovascular Mathematics: Modeling and simulation of the circulatory system*, ser. MS&A. Springer Milan, 2010.

[166] T.-C. Lee, K.-F. Huang, M.-L. Hsiao, S.-T. Tang, and S.-T. Young, “Electrical lumped model for arterial vessel beds,” *Computer methods and programs in biomedicine*, vol. 73, no. 3, pp. 209–219, 2004.

[167] N. Westerhof, F. Bosman, C. J. De Vries, and A. Noordergraaf, “Analog studies of the human systemic arterial tree,” *Journal of biomechanics*, vol. 2, no. 2, pp. 121–143, 1969.

[168] F. Alouges, A. DeSimone, L. Heltai, A. Lefebvre, and B. Merlet, “Optimally swimming Stokesian robots,” *arXiv e-prints*, p. arXiv:1007.4920, jul 2010.

[169] M. Sato, M. Fukaya, and T. Iwasaki, “Serpentine locomotion with robotic snakes,” *IEEE Control Systems Magazine*, vol. 22, no. 1, pp. 64–81, 2002.

[170] F. Alouges, A. DeSimone, L. Giraldi, and M. Zoppello, “Self-propulsion of slender micro-swimmers by curvature control: N-link swimmers,” *International Journal of Non-Linear Mechanics*, vol. 56, pp. 132–141, 2013.

[171] E. Kelasidi, K. Y. Pettersen, and J. T. Gravdahl, “Modeling of underwater snake robots moving in a vertical plane in 3d,” in *2014 IEEE/RSJ International Conference on Intelligent Robots and Systems*, 2014, pp. 266–273.

[172] J. Morison, J. Johnson, and S. Schaaf, “The Force Exerted by Surface Waves on Piles,” *Journal of Petroleum Technology*, vol. 2, no. 05, pp. 149–154, 05 1950. [Online]. Available: https://doi.org/10.2118/950149-G

[173] J. N. Newman, *Marine hydrodynamics*. The MIT press, 2018.

[174] J.-J. E. Slotine, W. Li *et al.*, *Applied nonlinear control*. Prentice hall Englewood Cliffs, NJ, 1991, vol. 199, no. 1.

[175] H. Goldstein, C. Poole, and J. Safko, “Classical mechanics,” 2002.

[176] G. I. Taylor, “Analysis of the swimming of long and narrow animals,” *Proceedings of the Royal Society of London. Series A. Mathematical and Physical Sciences*, vol. 214, no. 1117, pp. 158–183, 1952.

[177] M. S. Triantafyllou, G. Triantafyllou, and D. Yue, “Hydrodynamics of fishlike swimming,” *Annual review of fluid mechanics*, vol. 32, no. 1, pp. 33–53, 2000.

[178] M. S. Triantafyllou, G. Triantafyllou, and D. Yue, “Hydrodynamics of fishlike swimming,” *Annual review of fluid mechanics*, vol. 32, no. 1, pp. 33–53, 2000.

[179] J. Gray, “The mechanism of locomotion in snakes,” *Journal of experimental biology*, vol. 23, no. 2, pp. 101–120, 1946.

[180] S. Hirose, “Biologically inspired robots,” *Snake-Like Locomotors and Manipulators*, 1993.

[181] S. Hirose and H. Yamada, “Snake-like robots [tutorial],” *IEEE Robotics & Automation Magazine*, vol. 16, no. 1, pp. 88–98, 2009.

[182] J. Gray, “Studies in animal locomotion: I. the movement of fish with special reference to the eel,” *Journal of experimental biology*, vol. 10, no. 1, pp. 88–104, 1933.

[183] F. Alouges, A. DeSimone, L. Giraldi, and M. Zoppello, “Self-propulsion of slender micro-swimmers by curvature control: N-link swimmers,” *International Journal of Non-Linear Mechanics*, vol. 56, pp. 132–141, 2013.

[184] T. I. Fossen, *Handbook of marine craft hydrodynamics and motion control*. John Wiley & Sons, 2011.

[185] K. Machin, “Wave propagation along flagella,” *Journal of Experimental Biology*, vol. 35, no. 4, pp. 796–806, 1958.

[186] C. Brokaw, “Non-sinusoidal bending waves of sperm flagella,” *Journal of Experimental Biology*, vol. 43, no. 1, pp. 155–169, 1965.

[187] D. Calvetti, G. Golub, W. Gragg, and L. Reichel, “Computation of gauss-kronrod quadrature rules,” *Mathematics of computation*, vol. 69, no. 231, pp. 1035–1052, 2000.

[188] J.-M. Coron, *Control and nonlinearity*. American Mathematical Soc., 2007, no. 136.

[189] H. J. Sussmann, “A general theorem on local controllability,” *SIAM Journal on Control and Optimization*, vol. 25, no. 1, pp. 158–194, 1987.

[190] R. M. Bianchini and G. Stefani, “Graded approximations and controllability along a trajectory,” *SIAM Journal on Control and Optimization*, vol. 28, no. 4, pp. 903–924, 1990.

[191] H. Nijmeijer and A. J. Van der Schaft, *Nonlinear dynamical control systems*. Springer, 1990, vol. 175.

[192] R. Hermann and A. Krener, “Nonlinear controllability and observability,” *IEEE Transactions on Automatic Control*, vol. 22, no. 5, pp. 728–740, 1977.

[193] E. D. Sontag, “A concept of local observability,” *Systems & Control Letters*, vol. 5, no. 1, pp. 41–47, 1984.

[194] Y. Wang and E. D. Sontag, “On two definitions of observation spaces,” *Systems & control letters*, vol. 13, no. 4, pp. 279–289, 1989.

[195] O. Arrieta and R. Vilanova, “Simple PID tuning rules with guaranteed Ms robustness achievement,” *IFAC Proceedings Volumes*, vol. 44, no. 1, pp. 12 042–12 047, 2011.

[196] Y. Jin, Y. Q. Chen, and D. Xue, “Time-constant robust analysis of a fractional order [proportional derivative] controller,” *IET Control Theory & Applications*, vol. 5, no. 1, pp. 164–172, 2011.

[197] R. S. Barbosa, J. A. T. Machado, and I. M. Ferreira, “Tuning of pid controllers based on bode’s ideal transfer function,” *Nonlinear Dynamics*, vol. 38, no. 1, pp. 305–321, 2004.

[198] F. Otto, “Die grundform des arteriellen pulses,” *Zeitung fur Biologie*, vol. 37, pp. 483–586, 1899.

[199] N. Westerhof, J. Lankhaar, and B. E. Westerhof, “The arterial Windkessel,” *Medical & Biological Engineering & Computing*, vol. 47, no. 2, pp. 131–141, 2009.

[200] D. S. Breitenstein, “Cardiovascular modeling: The mathematical expression of blood circulation,” *Master’s thesis, University of Pittsburgh, PA*, 1993.

[201] H. Suga and K. Sagawa, “Instantaneous pressure-volume relationships and their ratio in the excised, supported canine left ventricle,” *Circulation research*, vol. 35, no. 1, pp. 117–126, 1974.

[202] M. A. A. Pacher and H. Cingolani, “Modelo de ventrículo izquierdo,” Ph.D. dissertation, Universidad Católica de Córdoba, 1997.

[203] L. Sheffer, W. P. Santamore, and O. Barnea, “Cardiovascular simulation toolbox,” *Cardiovascular Engineering*, vol. 7, no. 2, pp. 81–88, 2007.

[204] N. Westerhof, N. Stergiopulos, and M. I. Noble, *Snapshots of hemodynamics: an aid for clinical research and graduate education*. Springer Science & Business Media, 2010.

[205] D. K. Chaturvedi, *Modeling and simulation of systems using MATLAB and Simulink*. CRC Press, 2009.

[206] K.-W. Gwak, H. D. Kim, and C.-W. Kim, “Feedback linearization control of a cardiovascular circulatory simulator,” *IEEE Transactions on Control Systems Technology*, vol. 23, no. 5, pp. 1970–1977, 2015.

[207] K.-W. Gwak, H. D. Kim, S.-G. Lee, S. Park, and C.-W. Kim, “Sliding mode control for the frank–starling response of a piston pump mock ventricle,” *Journal of Process Control*, vol. 25, pp. 70–77, 2015.

[208] K. M. Farinholt, “Modeling and characterization of ionic polymer transducers for sensing and actuation,” Ph.D. dissertation, Virginia Tech, 2005.

[209] R. Caponetto, S. Graziani, F. L. Pappalardo, E. Umana, M. Xibilia, and P. D. Giamberardino, “A scalable fractional model for IPMC actuator,” in *Proceedings of the 7th Vienna International Conference on Mathematical Modelling*, 2012, pp. 593–596.

[210] R. Caponetto, G. Dongola, L. Fortuna, S. Graziani, and S. Strazzeri, “A fractional model for IPMC actuators,” in *In Proceedings of the 2008 IEEE Instrumentation and Measurement Technology Conference*. IEEE, 2008, pp. 2103–2107.

[211] I. Tejado, J. E. Traver, J. Prieto-Arranz, M. Á. López, and B. M. Vinagre, “Frequency domain based fractional order modeling of IPMC actuators for control,” in *Proceedings of the 2019 18th European Control Conference (ECC)*. IEEE, 2019, pp. 4112–4117.

[212] D. Valério and J. Sá da Costa, “Ninteger: a fractional control toolbox for Matlab,” in *In Proceedings of the 1st IFAC Workshop on Fractional Differentiation and its Applications*, 2004, pp. 2103–2107.

[213] M. A. López, J. Prieto, J. E. Traver, I. Tejado, B. M. Vinagre, and I. Petrás, “Testing non reciprocal motion of a swimming flexible small robot with single actuation,” in *Proceedings of the 19th International Carpathian Control Conference (ICCC 2018)*, 2018, pp. 312–317.

[214] C. Monje, Y. Chen, B. Vinagre, D. Xue, and V. Feliu, *Fractional Order Systems and Control - Fundamentals and Applications*. Berlin/Heidelberg, Germany: Springer, 01 2010.

[215] L. Ltd. (2017) Normal hemodynamic parameters. Revised on May 29, 2022. [Online]. Available: http://www.lidco.com/clinical/hemodynamic.php

[216] E. Lifesciences. (2017) Normal hemodynamic parameters and laboratory values. Revised on May 29, 2022. [Online]. Available: http://ht.edwards.com/scin/edwards/sitecollectionimages/edwards/products/presep/ar04313hemodynpocketcard.pdf

[217] H.-J. Priebe and K. Skarvan, *Cardiovascular physiology*. BMJ Publishing Group, 1995.

[218] A. Isidori, E. Sontag, and M. Thoma, *Nonlinear control systems*. Springer, 1995, vol. 3.

[219] S. Sastry, *Nonlinear systems: analysis, stability, and control*. Springer Science & Business Media, 2013, vol. 10.

Appendices

A

N-LINK SWIMMING ROBOT MODEL

Contents

This appendix details the variables used for the description of the model of a flagellum-type articulated eukaryotic swimming robot. In addition, a brief introduction to the differential geometry techniques for the study and analysis of nonlinear systems from the point of view of control theory [191, 218], applied in chapter 4.

A.1 Variables for medium *Re* environment

This section arranges the equations that define the swimming robot dynamics, described in chapter 3, and fully describes the variables that compose it. Starting with Newton's second law, the forces that affect the swimming robot's head dynamics (3.26a) are

$$\begin{aligned} m_n\ddot{q}_x &= f_{v,x,N} + f_{a,x,N} + h_{x,N} = \mathbf{e}^T\Big(\mathbf{F}_{v,x} + \mathbf{F}_{a,x}\Big) \\ m_n\ddot{q}_y &= f_{v,y,N} + f_{a,y,N} + h_{y,N} = \mathbf{e}^T\Big(\mathbf{F}_{v,y} + \mathbf{F}_{a,y}\Big) \end{aligned} \tag{A.1}$$

and the dynamics of the links (3.32) is

$$\begin{aligned} \mathbf{J}\ddot{\boldsymbol{\theta}} =& \mathbf{D}^T\mathbf{Q}\mathbf{U} + \mathbf{T}_v + \mathbf{T}_a - \mathbf{D}^T\mathbf{K}_f\mathbf{D}\boldsymbol{\theta} - \mathbf{D}^T\mathbf{B}_f\mathbf{D}\dot{\boldsymbol{\theta}} \\ &+ \frac{1}{2}\mathbf{L}\mathbf{S}_\theta\mathbf{A}^T\Big(\mathbf{D}\mathbf{M}^{-1}\mathbf{D}^T\Big)^{-1}\Big(\frac{1}{2}\mathbf{A}\mathbf{L}\Big(\mathbf{C}_\theta\dot{\boldsymbol{\theta}}^2 + \mathbf{S}_\theta\ddot{\boldsymbol{\theta}}\Big) - \mathbf{D}\mathbf{M}^{-1}\Big(\mathbf{F}_{v,x} + \mathbf{F}_{a,x}\Big)\Big) \\ &- \frac{1}{2}\mathbf{L}\mathbf{C}_\theta\mathbf{A}^T\Big(\mathbf{D}\mathbf{M}^{-1}\mathbf{D}^T\Big)^{-1}\Big(\frac{1}{2}\mathbf{A}\mathbf{L}\Big(\mathbf{S}_\theta\dot{\boldsymbol{\theta}}^2 - \mathbf{C}_\theta\ddot{\boldsymbol{\theta}}\Big) - \mathbf{D}\mathbf{M}^{-1}\Big(\mathbf{F}_{v,y} + \mathbf{F}_{a,y}\Big)\Big). \end{aligned} \tag{A.2}$$

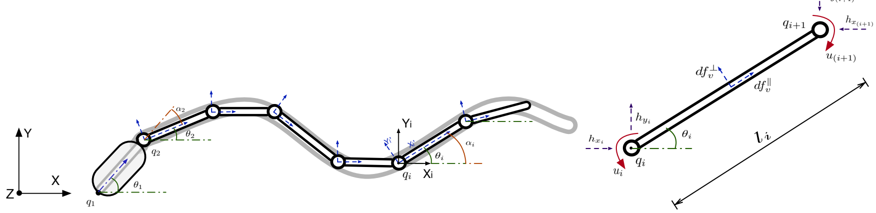

Figure A.1: Free body diagram of articulated artificial eukaryotic flagellum swimming robot

Developing the above expression according to the environment forces and the robot kinematics, the model has the following form:

$$\boldsymbol{\Psi}\begin{bmatrix}\ddot{\boldsymbol{\theta}}\\ \ddot{q}_x\\ \ddot{q}_y\end{bmatrix} = \boldsymbol{\Omega}(\dot{\boldsymbol{\theta}}) + \boldsymbol{\Pi}(\dot{\mathbf{V}}_{f,x}, \dot{\mathbf{V}}_{f,y}) + \mathbf{E}(q_x, q_y, \mathbf{V}_{f,x}, \mathbf{V}_{f,y}) - \mathbf{BU} \tag{A.3}$$

where

$$\begin{gathered}
\boldsymbol{\Psi} = \begin{bmatrix}\mathbf{M}_\theta & -\mathbf{P}_x\mathbf{e} & \mathbf{P}_y\mathbf{e}\\ \mathbf{e}^T\boldsymbol{\sigma}_{x,2} & \mathbf{M}_x + \mathbf{e}^T\boldsymbol{\sigma}_{x,3}\mathbf{e} & -\mathbf{e}^T\boldsymbol{\sigma}_{x,4}\mathbf{e}\\ -\mathbf{e}^T\boldsymbol{\sigma}_{y,2} & -\mathbf{e}^T\boldsymbol{\sigma}_{y,3}\mathbf{e} & \mathbf{M}_y + \mathbf{e}^T\boldsymbol{\sigma}_{y,4}\mathbf{e}\end{bmatrix}, \quad \boldsymbol{\Omega}(\dot{\boldsymbol{\theta}}) = \begin{bmatrix}\omega_\theta\dot{\boldsymbol{\theta}}^2 - \mathbf{V}_\theta\dot{\boldsymbol{\theta}} - \mathbf{D}^T\mathbf{K}_f\mathbf{D}\boldsymbol{\theta}\\ \mathbf{e}^T\boldsymbol{\sigma}_{x,1}\dot{\boldsymbol{\theta}}^2 + \mathbf{e}^T(\boldsymbol{\sigma}_{x,5} - \boldsymbol{\delta}_{x,1})\dot{\boldsymbol{\theta}}\\ \mathbf{e}^T\boldsymbol{\sigma}_{y,1}\dot{\boldsymbol{\theta}}^2 + \mathbf{e}^T(\boldsymbol{\sigma}_{y,5} + \boldsymbol{\delta}_{y,1})\dot{\boldsymbol{\theta}}\end{bmatrix},\\
\mathbf{E}(q_x, q_y, \mathbf{V}_{f,x}, \mathbf{V}_{f,y}) = \begin{bmatrix}\mathbf{N}_x(\mathbf{e}\dot{q}_x - \mathbf{V}_{f,x}) + \mathbf{N}_y(\mathbf{e}\dot{q}_y - \mathbf{V}_{f,y})\\ \mathbf{e}^T(\boldsymbol{\sigma}_{x,6} - \boldsymbol{\delta}_{x,2})(\mathbf{e}\dot{q}_x - \mathbf{V}_{f,x}) + \mathbf{e}^T(\boldsymbol{\delta}_{x,3} - \boldsymbol{\sigma}_{x,7})(\mathbf{e}\dot{q}_y - \mathbf{V}_{f,y})\\ \mathbf{e}^T(\boldsymbol{\sigma}_{y,6} + \boldsymbol{\delta}_{y,2})(\mathbf{e}\dot{q}_x - \mathbf{V}_{f,x}) + \mathbf{e}^T(\boldsymbol{\sigma}_{y,7} - \boldsymbol{\delta}_{y,3})(\mathbf{e}\dot{q}_y - \mathbf{V}_{f,y})\end{bmatrix},\\
\boldsymbol{\Pi}(\dot{\mathbf{V}}_{f,x}, \dot{\mathbf{V}}_{f,y}) = \begin{bmatrix}-\mathbf{P}_x\dot{\mathbf{V}}_{f,x} + \mathbf{P}_y\dot{\mathbf{V}}_{f,y}\\ \mathbf{e}^T\boldsymbol{\sigma}_{x,3}\dot{\mathbf{V}}_{f,x} - \mathbf{e}^T\boldsymbol{\sigma}_{x,4}\dot{\mathbf{V}}_{f,y}\\ \mathbf{e}^T\boldsymbol{\sigma}_{y,4}\dot{\mathbf{V}}_{f,y} - \mathbf{e}^T\boldsymbol{\sigma}_{y,3}\dot{\mathbf{V}}_{f,x}\end{bmatrix}, \quad \mathbf{B} = \begin{bmatrix}\mathbf{D}^T\mathbf{Q}\\ 0\\ 0\end{bmatrix},
\end{gathered} \tag{A.4}$$

$$\begin{aligned}
\mathbf{M}_\theta &= \mathbf{J} + \mathbf{c}_a^\circ + \frac{1}{2}\mathbf{L}(\mathbf{S}_\theta\mathbf{V}\mathbf{S}_\theta + \mathbf{C}_\theta\mathbf{V}\mathbf{C}_\theta) - \frac{1}{2}\mathbf{L}(\mathbf{S}_\theta\mathbf{K}\boldsymbol{\sigma}_{x,2}) - \frac{1}{2}\mathbf{L}(\mathbf{C}_\theta\mathbf{K}\boldsymbol{\sigma}_{y,2}),\\
\mathbf{M}_x &= \mathbf{e}^T\mathbf{M}\mathbf{e},\\
\mathbf{M}_y &= \mathbf{e}^T\mathbf{M}\mathbf{e},\\
\mathbf{V}_\theta &= \mathbf{c}_v^\circ + \mathbf{D}^T\mathbf{B}_f\mathbf{D} - \frac{1}{2}\mathbf{L}\mathbf{S}_\theta\mathbf{K}(\boldsymbol{\delta}_{x,1} - \boldsymbol{\sigma}_{x,5}) - \frac{1}{2}\mathbf{L}\mathbf{C}_\theta\mathbf{K}(\boldsymbol{\delta}_{y,1} + \boldsymbol{\sigma}_{y,5}),\\
\omega_\theta &= \frac{1}{2}\mathbf{L}(\mathbf{C}_\theta\mathbf{V}\mathbf{S}_\theta - \mathbf{S}_\theta\mathbf{V}\mathbf{C}_\theta) - \frac{1}{2}\mathbf{L}\mathbf{S}_\theta\mathbf{K}\boldsymbol{\sigma}_{x,1} + \frac{1}{2}\mathbf{L}\mathbf{C}_\theta\mathbf{K}\boldsymbol{\sigma}_{y,1},\\
\mathbf{P}_x &= \frac{1}{2}\mathbf{L}\mathbf{S}_\theta\mathbf{K}\boldsymbol{\sigma}_{x,3} + \frac{1}{2}\mathbf{L}\mathbf{C}_\theta\mathbf{K}\boldsymbol{\sigma}_{y,3},\\
\mathbf{P}_y &= \frac{1}{2}\mathbf{L}\mathbf{S}_\theta\mathbf{K}\boldsymbol{\sigma}_{x,4} + \frac{1}{2}\mathbf{L}\mathbf{C}_\theta\mathbf{K}\boldsymbol{\sigma}_{y,4},\\
\mathbf{N}_x &= \frac{1}{2}\mathbf{L}\mathbf{S}_\theta\mathbf{K}(\boldsymbol{\delta}_{x,2} + \boldsymbol{\sigma}_{x,6}) - \frac{1}{2}\mathbf{L}\mathbf{C}_\theta\mathbf{K}(\boldsymbol{\delta}_{y,2} + \boldsymbol{\sigma}_{y,6}),\\
\mathbf{N}_y &= \frac{1}{2}\mathbf{L}\mathbf{S}_\theta\mathbf{K}(\boldsymbol{\sigma}_{x,7} - \boldsymbol{\delta}_{x,3}) - \frac{1}{2}\mathbf{L}\mathbf{C}_\theta\mathbf{K}(\boldsymbol{\delta}_{y,3} - \boldsymbol{\sigma}_{y,7}),\\
\mathbf{V} &= \mathbf{A}^T\left(\mathbf{D}\mathbf{M}^{-1}\mathbf{D}^T\right)^{-1}\mathbf{A}\frac{1}{2}\mathbf{L},\\
\mathbf{K} &= \mathbf{A}^T\left(\mathbf{D}\mathbf{M}^{-1}\mathbf{D}^T\right)^{-1}\mathbf{D}\mathbf{M}^{-1},
\end{aligned} \tag{A.5}$$

and the following simplifications correspond to the development of the environment forces:

$$
\begin{aligned}
\boldsymbol{\delta}_{x,1} &= \left(\mathbf{c}_v^{\parallel}(\mathbf{C}_\theta)^2 + \mathbf{c}_v^{\perp}(\mathbf{S}_\theta)^2\right)\frac{1}{2}\mathbf{WLS}_\theta + (\mathbf{c}_v^{\perp} - \mathbf{c}_v^{\parallel})\mathbf{S}_\theta\mathbf{C}_\theta\frac{1}{2}\mathbf{WLC}_\theta,\\
\boldsymbol{\delta}_{y,1} &= \left(\mathbf{c}_v^{\parallel}(\mathbf{S}_\theta)^2 + \mathbf{c}_v^{\perp}(\mathbf{C}_\theta)^2\right)\frac{1}{2}\mathbf{WLC}_\theta + (\mathbf{c}_v^{\perp} - \mathbf{c}_v^{\parallel})\mathbf{S}_\theta\mathbf{C}_\theta\frac{1}{2}\mathbf{WLS}_\theta,\\
\boldsymbol{\delta}_{x,2} &= \mathbf{c}_v^{\parallel}(\mathbf{C}_\theta)^2 + \mathbf{c}_v^{\perp}(\mathbf{S}_\theta)^2,\\
\boldsymbol{\delta}_{y,2} &= \boldsymbol{\delta}_{x,3} = (\mathbf{c}_v^{\perp} - \mathbf{c}_v^{\parallel})\mathbf{S}_\theta\mathbf{C}_\theta,\\
\boldsymbol{\delta}_{y,3} &= \mathbf{c}_v^{\parallel}(\mathbf{S}_\theta)^2 + \mathbf{c}_v^{\perp}(\mathbf{C}_\theta)^2,\\
\boldsymbol{\sigma}_{x,1} &= (\mathbf{c}_a^{\perp} - \mathbf{c}_a^{\parallel})\mathbf{S}_\theta\mathbf{C}_\theta\frac{1}{2}\mathbf{WLS}_\theta - \left(\mathbf{c}_a^{\parallel}(\mathbf{C}_\theta)^2 + \mathbf{c}_a^{\perp}(\mathbf{S}_\theta)^2\right)\frac{1}{2}\mathbf{WLC}_\theta,\\
\boldsymbol{\sigma}_{y,1} &= (\mathbf{c}_a^{\perp} - \mathbf{c}_a^{\parallel})\mathbf{S}_\theta\mathbf{C}_\theta\frac{1}{2}\mathbf{WLC}_\theta - \left(\mathbf{c}_a^{\parallel}(\mathbf{S}_\theta)^2 + \mathbf{c}_a^{\perp}(\mathbf{C}_\theta)^2\right)\frac{1}{2}\mathbf{WLS}_\theta,\\
\boldsymbol{\sigma}_{x,2} &= (\mathbf{c}_a^{\perp} - \mathbf{c}_a^{\parallel})\mathbf{S}_\theta\mathbf{C}_\theta\frac{1}{2}\mathbf{WLC}_\theta + \left(\mathbf{c}_a^{\parallel}(\mathbf{C}_\theta)^2 + \mathbf{c}_a^{\perp}(\mathbf{S}_\theta)^2\right)\frac{1}{2}\mathbf{WLS}_\theta,\\
\boldsymbol{\sigma}_{y,2} &= (\mathbf{c}_a^{\perp} - \mathbf{c}_a^{\parallel})\mathbf{S}_\theta\mathbf{C}_\theta\frac{1}{2}\mathbf{WLS}_\theta + \left(\mathbf{c}_a^{\parallel}(\mathbf{S}_\theta)^2 + \mathbf{c}_a^{\perp}(\mathbf{C}_\theta)^2\right)\frac{1}{2}\mathbf{WLC}_\theta,\\
\boldsymbol{\sigma}_{x,3} &= \mathbf{c}_a^{\parallel}(\mathbf{C}_\theta)^2 + \mathbf{c}_v^{\perp}(\mathbf{S}_\theta)^2\\
\boldsymbol{\sigma}_{y,3} &= \boldsymbol{\sigma}_{x,4} = (\mathbf{c}_a^{\perp} - \mathbf{c}_a^{\parallel})\mathbf{S}_\theta\mathbf{C}_\theta,\\
\boldsymbol{\sigma}_{y,4} &= \left(\mathbf{c}_a^{\parallel}(\mathbf{S}_\theta)^2 + \mathbf{c}_a^{\perp}(\mathbf{C}_\theta)^2\right)\frac{1}{2}\mathbf{WLC}_\theta,\\
\boldsymbol{\sigma}_{x,5} &= (\mathbf{c}_a^{\parallel} - \mathbf{c}_a^{\perp})\mathbf{C}_\theta\mathbf{S}_\theta\dot{\boldsymbol{\theta}}\frac{1}{2}\mathbf{WLS}_\theta + \left(\mathbf{c}_a^{\parallel}(\mathbf{C}_\theta)^2 + \mathbf{c}_a^{\perp}(\mathbf{S}_\theta)^2\right)\dot{\boldsymbol{\theta}}\mathbf{K}^T\frac{1}{2}\mathbf{LC}_\theta,\\
\boldsymbol{\sigma}_{y,5} &= \left(\mathbf{c}_a^{\parallel}(\mathbf{S}_\theta)^2 + \mathbf{c}_a^{\perp}(\mathbf{C}_\theta)^2\right)\dot{\boldsymbol{\theta}}\frac{1}{2}\mathbf{WLS}_\theta - (\mathbf{c}_a^{\parallel} - \mathbf{c}_a^{\perp})\mathbf{C}_\theta\mathbf{S}_\theta\dot{\boldsymbol{\theta}}\frac{1}{2}\mathbf{WLC}_\theta,\\
\boldsymbol{\sigma}_{x,6} &= \boldsymbol{\sigma}_{y,7} = (\mathbf{c}_a^{\parallel} - \mathbf{c}_a^{\perp})\mathbf{C}_\theta\mathbf{S}_\theta\dot{\boldsymbol{\theta}},\\
\boldsymbol{\sigma}_{y,6} &= \left(\mathbf{c}_a^{\parallel}(\mathbf{S}_\theta)^2 + \mathbf{c}_a^{\perp}(\mathbf{C}_\theta)^2\right)\dot{\boldsymbol{\theta}}\\
\boldsymbol{\sigma}_{x,7} &= \left(\mathbf{c}_a^{\parallel}(\mathbf{C}_\theta)^2 + \mathbf{c}_a^{\perp}(\mathbf{S}_\theta)^2\right).
\end{aligned}
\tag{A.6}
$$

A.2 Variables for low *Re* environment

In the case of the model for low *Re*, the model is simplified as described in chapter 3, as well as the variables used. Firstly, the summation of forces on the swimming robot head is equal to zero, according to Newton's law applied for low

Re environment:

$$\begin{aligned} 0 &= f_{v,x,N} + h_{x,N} = \mathbf{e}^T \mathbf{F}_{v,x} \\ 0 &= f_{v,y,N} + h_{y,N} = \mathbf{e}^T \mathbf{F}_{v,y} \end{aligned} \tag{A.7}$$

and the dynamics of the links is reduced to

$$0 = \mathbf{D}^T\mathbf{QU} + \mathbf{T}_v - \mathbf{D}^T\mathbf{K}_f\mathbf{D}\boldsymbol{\theta} - \mathbf{D}^T\mathbf{B}_f\mathbf{D}\dot{\boldsymbol{\theta}} + \frac{1}{2}\mathbf{L}\mathbf{S}_\theta\mathbf{A}^T\mathbf{H}_x - \frac{1}{2}\mathbf{L}\mathbf{C}_\theta\mathbf{A}^T\mathbf{H}_y. \tag{A.8}$$

Both equations define the swimming robot model in a low *Re* as

$$\boldsymbol{\Psi}^\star \begin{bmatrix} \dot{\boldsymbol{\theta}} \\ \dot{q}_x \\ \dot{q}_y \end{bmatrix} = \boldsymbol{\Omega}^\star(\boldsymbol{\theta}, \dot{\boldsymbol{\theta}}) + \mathbf{E}^\star(q_x, q_y, \mathbf{V}_{f,x}, \mathbf{V}_{f,y}) + \mathbf{BU} \tag{A.9}$$

where

$$\begin{aligned} \boldsymbol{\Psi}^\star &= \begin{bmatrix} \mathbf{V}^\star{}_\theta & -\mathbf{N}^\star{}_x\mathbf{e} & \mathbf{N}^\star{}_y\mathbf{e} \\ \mathbf{e}^T\boldsymbol{\delta}_{x,1} & \mathbf{e}^T\boldsymbol{\delta}_{x,2}\mathbf{e} & -\mathbf{e}^T\boldsymbol{\delta}_{x,3}\mathbf{e} \\ -\mathbf{e}^T\boldsymbol{\delta}_{y,1} & -\mathbf{e}^T\boldsymbol{\delta}_{y,2}\mathbf{e} & -\mathbf{e}^T\boldsymbol{\delta}_{y,3}\mathbf{e} \end{bmatrix}, \\ \boldsymbol{\Omega}^\star(\boldsymbol{\theta}, \dot{\boldsymbol{\theta}}) &= \begin{bmatrix} -\mathbf{D}^T\mathbf{K}_f\mathbf{D}\boldsymbol{\theta} \\ 0 \\ 0 \end{bmatrix}, \\ \mathbf{E}^\star(q_x, q_y, \mathbf{V}_{f,x}, \mathbf{V}_{f,y}) &= \begin{bmatrix} -\mathbf{N}^\star{}_x\mathbf{V}_{f,x} + \mathbf{N}^\star{}_y\mathbf{V}_{f,y} \\ \mathbf{e}^T\boldsymbol{\delta}_{x,2}\mathbf{V}_{f,x} - \mathbf{e}^T\boldsymbol{\delta}_{x,3}\mathbf{V}_{f,y} \\ -\mathbf{e}^T\boldsymbol{\delta}_{y,2}\mathbf{V}_{f,x} + \mathbf{e}^T\boldsymbol{\delta}_{y,3}\mathbf{V}_{f,y} \end{bmatrix}, \\ \mathbf{V}^\star{}_\theta &= \mathbf{c}_v^\circ + \mathbf{D}^T\mathbf{B}_f\mathbf{D} - \frac{1}{2}\mathbf{L}\mathbf{S}_\theta\mathbf{K}^\star\boldsymbol{\delta}_{x,1} - \frac{1}{2}\mathbf{L}\mathbf{C}_\theta\mathbf{K}^\star\boldsymbol{\delta}_{y,1}, \\ \mathbf{N}^\star{}_x &= \frac{1}{2}\mathbf{L}\mathbf{S}_\theta\mathbf{K}^\star\boldsymbol{\delta}_{x,2} + \frac{1}{2}\mathbf{L}\mathbf{C}_\theta\mathbf{K}^\star\boldsymbol{\delta}_{y,2}, \\ \mathbf{N}^\star{}_y &= \frac{1}{2}\mathbf{L}\mathbf{S}_\theta\mathbf{K}^\star\boldsymbol{\delta}_{x,3} - \frac{1}{2}\mathbf{L}\mathbf{C}_\theta\mathbf{K}^\star\boldsymbol{\delta}_{y,3} \\ \mathbf{K}^\star &= \mathbf{A}^T\left(\mathbf{D}\mathbf{D}^T\right)^{-1}\mathbf{D}. \end{aligned} \tag{A.10}$$

A.3 Differential geometry tools

This section is only intended to briefly introduce the differential geometry techniques for the study and analysis of nonlinear systems from the point of view of control theory [191, 218]. For a more profound and rigorous explication, the readers are encouraged to consult [174, 188, 191, 218, 219].

The system under consideration is multivariable, nonlinear with m inputs and p outputs, following the form:

$$\begin{aligned} \dot{\mathbf{x}} &= f(\mathbf{x}) + \sum_{i=1}^{m} g_i(\mathbf{x}) u_i \\ \mathbf{y} &= h(\mathbf{x}) \end{aligned} \tag{A.11}$$

The system is properly defined on a state space different from Euclidean space $\Re^n$. Instead, it is defined in a curved n-dimensional subset of $\Re^m$ for some m, called a manifold $\mathcal{M}$, where $\mathbf{x} = [x_1, x_2, \ldots, x_n]^T \in \Re^n$ are local coordinates on $\mathcal{M}$ (it is also known as state vector), $\boldsymbol{u} = [u_1, u_2, \ldots, u_m]^T \in \Re^m$ is the control law vector, and $\mathbf{y} = [y_1, y_2, \ldots, y_p]^T \in \Re^p$ is the the vector of system outputs.

With respect to $f(\mathbf{x}) = [f_1(\mathbf{x}), f_2(\mathbf{x}), \ldots, f_N(\mathbf{x})] \in \Re^n$ and $g_j(\mathbf{x}) = [g_1(\mathbf{x}), g_2(\mathbf{x}), \ldots, g_n(\mathbf{x})]^T \in \Re^n$, with $j = \{1, \ldots, m\}$, are vector fields on $\mathcal{M}$, which assign a tangent vector at $\mathbf{x}_1$ to any point $\mathbf{x}_i$ with $i \in \aleph$ in $\mathcal{M}$. They are also called the system's drift and control vector fields. As for the scalar functions $h(\mathbf{x}) = [h_1(\mathbf{x}), h_2(\mathbf{x}), \ldots, h_p(\mathbf{x})] : \mathcal{M} \longrightarrow \mathcal{Y} = \Re^p$ are the output vectors, that give the system status at a specific point $\mathbf{x}_1$. It is assumed that the vector fields, $\{f, g_1, \ldots, g_m\}$, and the scalar functions h are smooth in their arguments. In other words, all of them are analytic on their domain of definition, that means $\{f, g_1, \ldots, g_m, h\} \in C^\infty$.

A.3.1 Lie derivative and Lie brackets

A nonlinear system can be interpreted as a set of dynamical systems described by the vector fields and parameterized by the control laws. The system's properties depend on the combination of the different dynamical systems corresponding to different control laws. Because the system's dynamics are given by vector fields, this allows performing an algebraic operation to study the interconnections between the different dynamics.

A linear function or operator that is of particular importance is the gradient of a scalar function $f(\mathbf{x}) \in \mathcal{M}$. It is denoted by the operator $\nabla_{\mathbf{x}}$ and is defined as a row vector of $1 \times n$, whose i-th element is the partial derivative of $f(\mathbf{x})$ with respect to x_i, that is:

$$\nabla_{\mathbf{x}} f(\mathbf{x}) = \frac{\partial f}{\partial \mathbf{x}} = \left[\frac{\partial f}{\partial x_1}, \frac{\partial f}{\partial x_2}, \dots, \frac{\partial f}{\partial x_n}\right]. \tag{A.12}$$

From the above definition, two main types of differential operations can be presented: vector fields and the resulting vector from the gradient operation. The first type of operation is the directional derivative along $f(\mathbf{x})$, which is a new vector field from the inner product of a scalar function, $h(\mathbf{x})$, and the gradient vector of function, $\nabla_{\mathbf{x}}$, defined by

$$\langle \nabla_{\mathbf{x}} f(\mathbf{x}), h(\mathbf{x}) \rangle = \frac{\partial h}{\partial \mathbf{x}} f(\mathbf{x}) = \sum_{i=1}^{n} \frac{\partial h}{\partial x_i} f_i(\mathbf{x}). \tag{A.13}$$

This operation is also known as Lie derivative denoted as $\mathcal{L}_f h(\mathbf{x})$, so:

$$\mathcal{L}_f h(\mathbf{x}) = \frac{\partial h}{\partial \mathbf{x}} f(\mathbf{x}). \tag{A.14}$$

Likewise, this operation is possible in a recursive way, for instance, first taking the Lie derivative of $h(\mathbf{x})$ along a vector field $f(\mathbf{x})$ and then along a vector field $g_1(\mathbf{x})$. The recursive Lie derivative is defined as:

$$\mathcal{L}_f^k h(\mathbf{x}) = \mathcal{L}_f\left(\mathcal{L}_f^{k-1} h(\mathbf{x})\right), \tag{A.15}$$

for any $k \geq 1$, and setting $\mathcal{L}_f^0 h(\mathbf{x}) = h(\mathbf{x})$.

The second type of operation is the Lie bracket (or product) of $f(\mathbf{x})$ and $g(\mathbf{x})$. In simple words, the Lie bracket is a measure of the commutation shortage of the flow of vector fields, where the flow is referred to as the general solution that satisfies system (A.11) at time t and with $\mathbf{x}_0$ as initial conditions. The new vector fields are defined as

$$[f, g](\mathbf{x}) = \frac{\partial g}{\partial \mathbf{x}} f(\mathbf{x}) - \frac{\partial f}{\partial \mathbf{x}} g(\mathbf{x}). \tag{A.16}$$

In the same way that the Lie derivative, repeated bracketing of a vector field $g(\mathbf{x})$ with the same vector field $f(\mathbf{x})$ is formulated as:

$$ad_f^k g(\mathbf{x}) = \left[f, ad_f^{k-1} g\right](\mathbf{x}), \tag{A.17}$$

for any $k \geq 1$, and setting $ad_f^0 g(\mathbf{x}) = g(\mathbf{x})$. The advantage of this formulation is that it simplifies the previous notation. It is important to remark that, the Lie product has three basic properties: it is bilinear, skew commutative and satisfies the Jacobi identity.

Another procedure frequently used in the analysis of nonlinear and linear control systems is the change of coordinates in the state space. Although this method was applied in the previous section, it cannot be left unexplained here due to its importance. It is well known that transforming the coordinates in the state space can highlight some system's desired properties or simplify specific control problems. A nonlinear change of coordinates can be formulated as

$$z = \Phi(\mathbf{x}), \tag{A.18}$$

where $\Phi(\mathbf{x})$ is a n-dimensional vector of scalar functions of n-variables. Moreover, the transformation vector field must be nonsingular and analytic, which means that it has an invertible matrix and continuous partial derivatives of any order. The first property ensures the inversion to the original system description, whereas the second ensures that the new system remains smooth. A transformation of this type is usually called a global diffeomorphism on $\Re^n$.

The effects of a change of coordinates in a nonlinear system are analyzed as follows. Differentiating in both sides of the transformation vector field definition with respect to time yields

$$\dot{\mathbf{z}} = \frac{d\mathbf{z}}{dt} = \frac{\partial \Phi}{\partial \mathbf{x}} \frac{d\mathbf{x}}{dt} = \frac{\partial \Phi}{\partial \mathbf{x}} [f(\mathbf{x}) + \sum_{i=1}^{m} g_i(\mathbf{x}) u_i], \tag{A.19}$$

expressing $\mathbf{x} = \Phi^{-1}(\mathbf{z})$, the new description of system (A.11) is now

$$\begin{aligned}\dot{\mathbf{z}} &= \overline{f}(\mathbf{z}) + \sum_{i=1}^{m} \overline{g}_i(\mathbf{z})u_i \\ \mathbf{y} &= \overline{h}(\mathbf{z}),\end{aligned} \tag{A.20}$$

where

$$\begin{aligned}\overline{f}(\mathbf{z}) &= \left[\frac{\partial \Phi}{\partial \mathbf{x}} f(\mathbf{x})\right]_{\mathbf{x}=\Phi^{-1}(\mathbf{z})} = \mathcal{L}_f \Phi\big|_{\mathbf{x}=\Phi^{-1}(\mathbf{z})} \\ \overline{g}_i(\mathbf{z}) &= \left[\frac{\partial \Phi}{\partial \mathbf{x}} g_i(\mathbf{x})\right]_{\mathbf{x}=\Phi^{-1}(\mathbf{z})} = \mathcal{L}_{g_i} \Phi\big|_{\mathbf{x}=\Phi^{-1}(\mathbf{z})} \\ \overline{h}(\mathbf{z}) &= \left[h(\mathbf{x})\right]_{\mathbf{x}=\Phi^{-1}(\mathbf{z})}.\end{aligned} \tag{A.21}$$

Note that if $\Phi(\mathbf{x})$ is linear, it is reduced to $\Phi(\mathbf{x}) = T\mathbf{x}$, where T is the transformation matrix [191, 218].

A.3.2 Distributions

Previously, the vector field concept was introduced, which assigns an n-dimensional vector to each point of $\mathcal{M}$. Now, given a family of smooth vector fields $\{f, g_1, \ldots, g_m\}$ defined in $\mathcal{M}$, the linear subspace spanning at any fixed point $\mathbf{x}_1 \in \mathcal{M}$ is called a distribution. The term span means that another vector field defined in $\mathbf{x}_1$ can be obtained as a linear combination. The notion of distribution is fundamental to the analysis of nonlinear systems and it is denoted by

$$\Delta = \text{span}\Big\{f, g_1, \ldots, g_m\Big\}. \tag{A.22}$$

Since distribution is a linear space, the properties and concepts of linear space (addition, intersection, inclusion) are also related to it [191, 218]. The dimensions of a distribution, Δ, at $\mathbf{x}_1 \in \mathcal{M}$ is the dimension of the subspace. In other words, the number of independent smooth vector fields that form the distribution is equal to its dimension. Therefore, the dimension of Δ at a point $\mathbf{x}_1$ is the rank of the matrix formed by these column vector fields. In addition, if the dimension does not depend on the point, the distribution is called constant dimensional or nonsingular. Associated with the concept of dimension, a distribution is said to be involutive if the Lie bracket $[f, g_i] \in \Delta$, whatever the vector fields f and g_i are on $\mathcal{M}$, that means:

$$f \in \Delta, g_i \in \Delta \longrightarrow [f, g_i] \in \Delta. \tag{A.23}$$

As will be seen later, the involutive property plays a fundamental role in the Frobenius' theorem.

In other instances, instead of distribution, a codistribution is considered. A codistribution is the dual of a distribution. Recalling that a covector field (also known by the name of one-form or linear form), $h(\mathbf{x})$, could be understood as an assignment from any point $\mathbf{x} \in \mathcal{M}$ to an element of the dual space $(\Re^n)^\star$. Similar to the notation used for a distribution, a codistribution is defined as

$$\mathcal{O} = \mathrm{span}\Big\{h_1, g_2, \ldots, g_n\Big\}. \tag{A.24}$$

Because of a codistribution is also a linear space (subspace of $(\Re^n)^\star$), its properties are also applied, as well as the dimension of codistribution at each point $\mathbf{x} \in \mathcal{M}$.

Another way to define a codistribution, $\mathcal{O}$, where $\Delta^\perp$ is the annihilator of Δ and belongs to a subspace of $(\Re^n)^\star$.

starting from a given distribution, Δ, is through the annihilator of $\Delta(\mathbf{x})$ (denoted as $\Delta^\perp$ which belongs to a subspace of $(\Re^n)^\star$), that is, a set of all covectors which annihilate all vectors in $\Delta(\mathbf{x})$:

$$\Delta^\perp = \Big\{h^\star \in (\Re^n)^\star : \langle h^\star, v\rangle = 0 \text{ for all } v \in \Delta(\mathbf{x})\Big\} \tag{A.25}$$

A.3.3 Frobenius' theorem

Frobenius's theorem is a fundamental tool in the analysis and resolution of a n^{th}-order nonlinear system. It provides a necessary and sufficient condition for solving a particular class of partial differential equations. It also establishes a correspondence between the notion of involutive distribution and the existence of local partitions of $\Re^n$ into a manifold $\mathcal{M}$, which allows the study of the concepts of reachable or unreachable systems and observable or unobservable systems.

Frobenius's theorem states that *a nonsingular distribution is completely integrable if and only if it is involutive*. The term completely integrable means that a linear independent set of vector fields $\{f, g_1, \ldots, g_m\} \in \mathfrak{R}^n$ are integrable if and only if there exists $n - (m + 1)$ scalar functions $h(\mathbf{x})$ that satisfy the system of partial differential equations:

$$\sum_{i=1}^{n} \frac{\partial h}{\partial x_i} f_i(\mathbf{x}) = \mathcal{L}_f h(\mathbf{x}) = 0. \tag{A.26}$$

A.3.4 Rashevsky–Chow's theorem

The Rashevsky-Chow's theorem states: let $\mathcal{M}$ be a connect smooth manifold with a set of vector fields $\{g_1, \ldots, g_m\} \in \mathcal{M}$ of a nonlinear system (A.11) and Δ the distribution constructed using the vector fields of the system and all vector fields than can be obtained taking any number of Lie bracket of them. Then, if the distribution Δ is completely nonholonomic (full-rank and bracket-generating):

$$\Delta = T_{\mathbf{x}}\mathcal{M} \qquad \forall\, \mathbf{x} \in \mathcal{M}, \tag{A.27}$$

where $T_{\mathbf{x}}\mathcal{M}$ defines the tangent space to $\mathcal{M}$ at $\mathbf{x}$.

A.4 Particular case: 6-link swimming robot

This section details the variables used in chapter 5 on the description of thee 6-link swimming robot. Recalling model (5.1), the coefficients used are:

$$\begin{aligned}
\Psi_{11} &= \frac{3\pi}{64\cdot 10^3} + 5.72\cdot 10^{-5}, \\
\Psi_{22} &= \frac{13\pi}{64\cdot 10^3} + 5.72\cdot 10^{-5}, \\
\Psi_{33} &= \frac{19\pi}{64\cdot 10^3} + 5.72\cdot 10^{-5}, \\
\Psi_{44} &= \frac{21\pi}{64\cdot 10^3} + 5.72\cdot 10^{-5}, \\
\Psi_{55} &= \frac{19\pi}{64\cdot 10^3} + 5.72\cdot 10^{-5}, \\
\Psi_{66} &= \frac{13\pi}{64\cdot 10^3} + 5.72\cdot 10^{-5}, \\
\Psi_{77} &= \frac{3\pi}{64\cdot 10^3} + 5.72\cdot 10^{-5}, \\
\Psi_{88} &= \frac{7 * pi}{320}, \\
\Psi_{99} &= \frac{7 * pi}{320},
\end{aligned}$$

$$\begin{aligned}
\Psi_{12} &= \frac{11\pi}{128\cdot 10^3}\cos(\theta_1-\theta_2) \\
\Psi_{13} &= \frac{9\pi}{128\cdot 10^3}\cos(\theta_1-\theta_3), \\
\Psi_{14} &= \frac{7\pi}{128\cdot 10^3}\cos(\theta_1-\theta_4), \\
\Psi_{15} &= \frac{\pi}{25.6\cdot 10^3}\cos(\theta_1-\theta_5), \\
\Psi_{16} &= \frac{3\pi}{128\cdot 10^3}\cos(\theta_1-\theta_6), \\
\Psi_{17} &= \frac{\pi}{128\cdot 10^3}\cos(\theta_1-\theta_7), \\
\Psi_{23} &= \frac{27\pi}{128\cdot 10^3}\cos(\theta_2-\theta_3), \\
\Psi_{24} &= \frac{21\pi}{128\cdot 10^3}\cos(\theta_2-\theta_4), \\
\Psi_{25} &= \frac{3\pi}{25.6\cdot 10^3}\cos(\theta_2-\theta_5),
\end{aligned}$$

$$\begin{aligned}
\Psi_{25} &= \frac{3\pi}{25.6\cdot 10^3}\cos(\theta_2-\theta_5), \\
\Psi_{26} &= \frac{9\pi}{128\cdot 10^3}\cos(\theta_2-\theta_6), \\
\Psi_{27} &= \frac{3\pi}{128\cdot 10^3}\cos(\theta_2-\theta_7), \\
\Psi_{34} &= \frac{7\pi}{25.6\cdot 10^3}\cos(\theta_3-\theta_4), \\
\Psi_{35} &= \frac{\pi}{5120}\cos(\theta_3-\theta_5), \\
\Psi_{36} &= \frac{3\pi}{25.6\cdot 10^3}\cos(\theta_3-\theta_6), \\
\Psi_{37} &= \frac{\pi}{25.6\cdot 10^3}\cos(\theta_3-\theta_7), \\
\Psi_{45} &= \frac{7\pi}{25.6\cdot 10^3}\cos(\theta_4-\theta_5), \\
\Psi_{46} &= \frac{21\pi}{128\cdot 10^3}\cos(\theta_4-\theta_6),
\end{aligned}$$

$$\begin{aligned}
\Psi_{47} &= \frac{7\pi}{128\cdot 10^3}\cos(\theta_4-\theta_7), \\
\Psi_{56} &= \frac{27\pi}{128\cdot 10^3}\cos(\theta_5-\theta_6), \\
\Psi_{57} &= \frac{9\pi}{128\cdot 10^3}\cos(\theta_5-\theta_7), \\
\Psi_{67} &= \frac{11\pi}{128\cdot 10^3}\cos(\theta_6-\theta_7).
\end{aligned}$$

$$
\begin{aligned}
\Omega_1 &= -3\cdot 10^{-3}\dot{\theta}_1 + 9.87\cdot 10^{-5}\sum_{j=3}^{6}\sum_{i=2}^{j-1}\cos(\theta_1 - 2\theta_i + \theta_j)\dot{\theta}_j + 4.93\cdot 10^{-5}\sum_{i=2}^{6}\cos(\theta_1 - 2\theta_i + \theta_7)\dot{\theta}_7\\
&- 2.2\cdot 10^{-3}\cos(\theta_1 - \theta_2)\dot{\theta}_2 - 1.9\cdot 10^{-3}\cos(\theta_1 - \theta_3)\dot{\theta}_3 - 1.6\cdot 10^{-3}\cos(\theta_1 - \theta_4)\dot{\theta}_4\\
&- 1.3\cdot 10^{-3}\cos(\theta_1 - \theta_5)\dot{\theta}_5 - 9.87\cdot 10^{-4}\cos(\theta_1 - \theta_6)\dot{\theta}_6 - 4.44\cdot 10^{-4}\cos(\theta_1 - \theta_7)\dot{\theta}_7\\
&- \frac{\pi}{1.28\cdot 10^5} - \Big(11\sin(\theta_1 - \theta_2)\dot{\theta}_2^2 + 9\sin(\theta_1 - \theta_3)\dot{\theta}_3^2 + 7\sin(\theta_1 - \theta_4)\dot{\theta}_4^2 + 5\sin(\theta_1 - \theta_5)\dot{\theta}_5^2 + 3\sin(\theta_1 - \theta_6)\dot{\theta}_6^2\sin(\theta_1 - \theta_7)\dot{\theta}_7^2\Big),\\
\Omega_2 &= -5.9\cdot 10^{-3}\dot{\theta}_2 - 2.2\cdot 10^{-3}\cos(\theta_1 - \theta_2)\dot{\theta}_1) - 1.1\cdot 10^{-3}\cos(2\theta_1 - 2\theta_2)\dot{\theta}_2\\
&- 1.1\cdot 10^{-3}\sum_{i=3}^{6}\cos(\theta_2 - 2\theta_1 + \theta_i)\dot{\theta}_i + 2.96\cdot 10^{-4}\sum_{j=4}^{6}\sum_{i=3}^{j-1}\cos(\theta_2 - 2\theta_i + \theta_j)\dot{\theta}_j - 5.43\cdot 10^{-4}\cos(\theta_2 - 2\theta_1 + \theta_7)\dot{\theta}_7\\
&+ 1.48\cdot 10^{-4}\sum_{i=3}^{6}\cos(\theta_2 - 2\theta_i + \theta_7)\dot{\theta}_7 - 4.2\cdot 10^{-3}\cos(\theta_2 - \theta_3)\dot{\theta}_3 - 3.4\cdot 10^{-3}\cos(\theta_2 - \theta_4)\dot{\theta}_4\\
&- 2.5\cdot 10^{-3}\cos(\theta_2 - \theta_5)\dot{\theta}_5 - 1.6\cdot 10^{-3}\cos(\theta_2 - \theta_6)\dot{\theta}_6 - 6.41\cdot 10^{-4}\cos(\theta_2 - \theta_7)\dot{\theta}_7\\
&- \frac{\pi}{1.28\cdot 10^5}\Big(- 11\sin(\theta_1 - \theta_2)\dot{\theta}_1^2 + 27\sin(\theta_2 - \theta_3)\dot{\theta}_3^2 + 21\sin(\theta_2 - \theta_4)\dot{\theta}_4^2 + 15\sin(\theta_2 - \theta_5)\dot{\theta}_5^2 + 9\sin(\theta_2 - \theta_6)\dot{\theta}_6^2 + 3\sin(\theta_2 - \theta_7)\dot{\theta}_7^2\Big),\\
\Omega_3 &= -7.6\cdot 10^{-3}\dot{\theta}_3 - 8.86\cdot 10^{-4}\Big(\sum_{i=1}^{2}\cos(2\theta_i - 2\theta_3)\dot{\theta}_3) + \sum_{i=1}^{2}\cos(2\theta_i - 2\theta_3)\dot{\theta}_3\\
&+ \cos(\theta_2 - 2\theta_1 + \theta_3)\dot{\theta}_2 + \sum_{j=4}^{6}\sum_{i=1}^{2}\cos(\theta_3 - 2\theta_i + \theta_j)\dot{\theta}_j\Big) - 4.44\cdot 10^{-4}\sum_{i=1}^{2}\cos(2\theta_3 - 2\theta_i + \theta_i)\dot{\theta}_7\\
&+ 4.93\cdot 10^{-4}\Big(+ \cos(\theta_3 - 2\theta_4 + \theta_5)\dot{\theta}_5 + \cos(\theta_3 - 2\theta_4 + \theta_6)\dot{\theta}_6 + \cos(\theta_3 - 2\theta_5 + \theta_6)\dot{\theta}_6\Big)
\end{aligned}
$$

$$
\begin{aligned}
&+ 2.46 \cdot 10^{-4} \sum_{i=4}^{6} \cos(\theta_3 - 2\theta_i + \theta_7)\dot{\theta}_7 - 1.8 \cdot 10^{-3} \cos(\theta_1 - \theta_3)\dot{\theta}_1 - 4.4 \cdot 10^{-3} \cos(\theta_2 - \theta_3)\dot{\theta}_2 - 5.1 \cdot 10^{-3} \cos(\theta_3 - \theta_4)\dot{\theta}_4 \\
&- 3.7 \cdot 10^{-3} \cos(\theta_3 - \theta_5)\dot{\theta}_5 - 2.2 \cdot 10^{-3} \cos(\theta_3 - \theta_6)\dot{\theta}_6 - 8.39 \cdot 10^{-4} \cos(\theta_3 - \theta_7)\dot{\theta}_7 \\
&- \frac{\pi}{1.28 \cdot 10^5}\Big(- 9 \sin(\theta_1 - \theta_3)\dot{\theta}_1^2 - 27 \sin(\theta_2 - \theta_3)\dot{\theta}_2^2 + 35 \sin(\theta_3 - \theta_4)\dot{\theta}_4^2 + 25 \sin(\theta_3 - \theta_5)\dot{\theta}_5^2 + 15 \sin(\theta_3 - \theta_6)\dot{\theta}_6^2 + 5 \sin(\theta_3 - \theta_7)\dot{\theta}_7^2\Big),
\end{aligned}
$$

$$
\begin{aligned}
\Omega_4 = &-8.1 \cdot 10^{-3}\dot{\theta}_4 - 6.91 \cdot 10^{-4}\Big(\sum_{i=1}^{3} \cos(2\theta_i - 2\theta_4)\dot{\theta}_4) \sum_{j=2}^{3} \sum_{i=1}^{j-1} \cos(\theta_j - 2\theta_i + \theta_4)\dot{\theta}_j \\
&\sum_{j=5}^{6} \sum_{i=1}^{3} \cos(\theta_4 - 2\theta_i + \theta_j)\dot{\theta}_j - \cos(\theta_4 - 2\theta_5 + \theta_6)\dot{\theta}_6\Big) - 3.45 \cdot 10^{-4}\Big(\sum_{i=1}^{3} \cos(\theta_4 - 2\theta_i + \theta_7)\dot{\theta}_7 - \sum_{i=5}^{6} \cos(\theta_4 - 2\theta_i + \theta_7)\dot{\theta}_7\Big) \\
&- 1.4 \cdot 10^{-3} \cos(\theta_1 - \theta_4)\dot{\theta}_1 - 3.5 \cdot 10^{-3} \cos(\theta_2 - \theta_4)\dot{\theta}_2 - 5.5 \cdot 10^{-3} \cos(\theta_3 - \theta_4)\dot{\theta}_3 \\
&- 4.8 \cdot 10^{-3} \cos(\theta_4 - \theta_5)\dot{\theta}_5 - 4.8 \cdot 10^{-3} \cos(\theta_4 - \theta_5)\dot{\theta}_5 - 2.8 \cdot 10^{-3} \cos(\theta_4 - \theta_6)\dot{\theta}_6 - 1.0 \cdot 10^{-3} \cos(\theta_4 - \theta_7)\dot{\theta}_7 \\
&+ \frac{\pi}{1.28 \cdot 10^5}\Big(7 \sin(\theta_1 - \theta_4)\dot{\theta}_1^2 + 21 \sin(\theta_2 - \theta_4)\dot{\theta}_2^2 + 7 \sin(\theta_3 - \theta_4)\dot{\theta}_3^2 - 7 \sin(\theta_4 - \theta_5)\dot{\theta}_5^2 - 21 \sin(\theta_4 - \theta_6)\ddot{\theta}_6^2 - 7 \sin(\theta_4 - \theta_7)\dot{\theta}_7^2\Big),
\end{aligned}
$$

$$
\begin{aligned}
\Omega_5 = &-5.5 \cdot 10^{-3}\dot{\theta}_6 - 2.96 \cdot 10^{-4}\Big(\sum_{i=1}^{5} \cos(2\theta_i - 2\theta_6)\dot{\theta}_6) \sum_{j=2}^{5} \sum_{i=1}^{j-1} \cos(\theta_j - 2\theta_i + \theta_6)\dot{\theta}_j\Big) \\
&- 1.48 \cdot 10^{-4} \sum_{i=1}^{5} \cos(\theta_6 - 2\theta_i + \theta_7)\dot{\theta}_7 - 5.92 \cdot 10^{-4} \cos(\theta_1 - \theta_6)\dot{\theta}_1 - 1.5 \cdot 10^{-3} \cos(\theta_2 - \theta_6)\dot{\theta}_2 - 2.4 \cdot 10^{-3} \cos(\theta_3 - \theta_6)\dot{\theta}_3 \\
&- 3.3 \cdot 10^{-3} \cos(\theta_4 - \theta_6)\dot{\theta}_4 - 4.1 \cdot 10^{-3} \cos(\theta_5 - \theta_6)\dot{\theta}_5 - 1.4 \cdot 10^{-3} \cos(\theta_6 - \theta_7)\dot{\theta}_7 \\
&+ \frac{\pi}{1.28 \cdot 10^5}\Big(+ 3 \sin(\theta_1 - \theta_6)\dot{\theta}_1^2 + 9 \sin(\theta_2 - \theta_6)\dot{\theta}_2^2 + 15 \sin(\theta_3 - \theta_6)\dot{\theta}_3^2 + 21 \sin(\theta_4 - \theta_6)\dot{\theta}_4^2 + 27 \sin(\theta_5 - \theta_6)\dot{\theta}_5^2 - 11 \sin(\theta_6 - \theta_7)\dot{\theta}_7^2\Big)
\end{aligned}
$$

$$
\Omega_6 = -5.5 \cdot 10^{-3}\dot{\theta}_6 - 2.96 \cdot 10^{-4}\Big(\sum_{i=1}^{5} \cos(2\theta_i - 2\theta_6)\dot{\theta}_6) \sum_{j=2}^{5} \sum_{i=1}^{j-1} \cos(\theta_j - 2\theta_i + \theta_6)\dot{\theta}_j\Big)
$$

$$
\begin{aligned}
&- 1.48 \cdot 10^{-4} \sum_{i=1}^{5} \cos(\theta_6 - 2\theta_i + \theta_7)\dot{\theta}_7 - 5.92 \cdot 10^{-4} \cos(\theta_1 - \theta_6)\dot{\theta}_1 - 1.5 \cdot 10^{-3} \cos(\theta_2 - \theta_6)\dot{\theta}_2 - 2.4 \cdot 10^{-3} \cos(\theta_3 - \theta_6)\dot{\theta}_3 \\
&- 3.3 \cdot 10^{-3} \cos(\theta_4 - \theta_6)\dot{\theta}_4 - 4.1 \cdot 10^{-3} \cos(\theta_5 - \theta_6)\dot{\theta}_5 - 1.4 \cdot 10^{-3} \cos(\theta_6 - \theta_7)\dot{\theta}_7 \\
&+ \frac{\pi}{1.28 \cdot 10^5}\Big(+ 3\sin(\theta_1 - \theta_6)\dot{\theta}_1^2 + 9\sin(\theta_2 - \theta_6)\dot{\theta}_2^2 + 15\sin(\theta_3 - \theta_6)\dot{\theta}_3^2 + 21\sin(\theta_4 - \theta_6)\dot{\theta}_4^2 + 27\sin(\theta_5 - \theta_6)\dot{\theta}_5^2 - 11\sin(\theta_6 - \theta_7)\dot{\theta}_7^2\Big)
\end{aligned}
$$

$$
\begin{aligned}
\Omega_7 = &-2.7 \cdot 10^{-3}\dot{\theta}_7 - 4.93 \cdot 10^{-5}\Big(\sum_{i=1}^{6} \cos(2\theta_i - 2\theta_7)\dot{\theta}_7\Big) \sum_{j=2}^{6}\sum_{i=1}^{j-1} \cos(\theta_j - 2\theta_i + \theta_7)\dot{\theta}_j\Big) \\
&- 1.97 \cdot 10^{-4} \cos(\theta_1 - \theta_7)\dot{\theta}_1 - 4.93 \cdot 10^{-4} \cos(\theta_2 - \theta_7)\dot{\theta}_2 - 7.89 \cdot 10^{-4} \cos(\theta_3 - \theta_7)\dot{\theta}_3 - 1.1 \cdot 10^{-3} \cos(\theta_4 - \theta_7)\dot{\theta}_4 \\
&- 1.4 \cdot 10^{-3} \cos(\theta_5 - \theta_7)\dot{\theta}_5 - 1.7 \cdot 10^{-3} \cos(\theta_6 - \theta_7)\dot{\theta}_6 \\
&+ \frac{\pi}{1.28 \cdot 10^5}\Big(+ \sin(\theta_1 - \theta_7)\dot{\theta}_1^2 + 3\sin(\theta_2 - \theta_7)\dot{\theta}_2^2 + 5\sin(\theta_3 - \theta_7)\dot{\theta}_3^2 + 7\sin(\theta_4 - \theta_7)\dot{\theta}_4^2 + 9\sin(\theta_5 - \theta_7)\dot{\theta}_5^2 + 11\sin(\theta_6 - \theta_7)\dot{\theta}_6^2\Big),
\end{aligned}
$$

$$
\begin{aligned}
\Omega_8 = &-13.80 \cdot 10^{-3} \sum_{j=1}^{5}\sum_{i=1+j}^{6} \sin(2\theta_j - \theta_i)\theta_i^2 - 6.90 \cdot 10^{-3} \sum_{i=1}^{7} \sin(2\theta_i - \theta_7)\theta_7^2 \\
&- 27.60 \cdot 10^{-3} \sin(\theta_1)\dot{\theta}_1 - 69.10 \cdot 10^{-3} \sin(\theta_2)\dot{\theta}_2 - 0.11\sin(\theta_3)\dot{\theta}_3 - 0.15\sin(\theta_4)\dot{\theta}_4 - 0.19\sin(\theta_5)\dot{\theta}_5 - 0.23\sin(\theta_6)\dot{\theta}_6 - 0.12\sin(\theta_7)\dot{\theta}_7,
\end{aligned}
$$

$$
\begin{aligned}
\Omega_9 = &\ 13.80 \cdot 10^{-3} \sum_{j=1}^{5}\sum_{i=1+j}^{6} \cos(2\theta_j - \theta_i)\theta_i^2 + 6.90 \cdot 10^{-3} \sum_{i=1}^{7} \cos(2\theta_i - \theta_7)\theta_7^2 \\
&+ 27.60 \cdot 10^{-3} \cos(\theta_1)\dot{\theta}_1 + 69.10 \cdot 10^{-3} \cos(\theta_2)\dot{\theta}_2 + 0.11\cos(\theta_3)\dot{\theta}_3 + 0.15\cos(\theta_4)\dot{\theta}_4 + 0.19\cos(\theta_5)\dot{\theta}_5 + 0.23\cos(\theta_6)\dot{\theta}_6 + 0.12\cos(\theta_7)\dot{\theta}_7
\end{aligned}
$$

$$
E_1 = 9.87 \cdot 10^{-4}\Big(- \dot{q}_x\Big(+ 6\sin(\theta_1) + \sum_{i=2}^{7} \sin(\theta_1 - 2\theta_i)\Big) + \dot{q}_y\Big(+ 6\cos(\theta_1) - \sum_{i=2}^{7} \cos(\theta_1 - 2\theta_i)\Big)\Big),
$$

$$
E_2 = 3 \cdot 10^{-3}\Big(- \dot{q}_x\Big(+ 1.31\sin(\theta_2) + 3.62\sin(2\theta_1 - \theta_2) + \sum_{i=3}^{7} \sin(\theta_2 - 2\theta_i)\Big) + \dot{q}_y\Big(+ 1.31\cos(\theta_2) + 3.62\cos(2\theta_1 - \theta_2) - \sum_{i=3}^{7} \cos(\theta_2 - 2\theta_i)\Big)\Big),
$$

$$
E_3 = 4.90 \cdot 10^{-3}\Big(- \dot{q}_x\Big(+ 0.40\sin(\theta_3) + 1.81 \sum_{i=1}^{2} \sin(2\theta_i - \theta_3) + \sum_{i=4}^{7} \sin(\theta_3 - 2\theta_i)\Big) + \dot{q}_y\Big(+ 1.31\cos(\theta_3) + 1.81 \sum_{i=1}^{2} \cos(2\theta_i - \theta_3) - \sum_{i=4}^{7} \cos(\theta_3 - 2\theta_i)\Big)\Big),
$$

$$E_4 = 6.90 \cdot 10^{-3}\Big(- \dot{q}_x\Big(+ \sum_{i=1}^{3} \sin(2\theta_i - \theta_4) + \sum_{i=5}^{7} \sin(\theta_4 - 2\theta_i)\Big) + \dot{q}_y\Big(+ \sum_{i=1}^{3} \cos(2\theta_i - \theta_4) - \sum_{i=5}^{7} \cos(\theta_4 - 2\theta_i)\Big)\Big),$$

$$E_5 = 8.90 \cdot 10^{-3}\Big(- \dot{q}_x\Big(- 0.22 \sin(\theta_5) + 0.55 \sum_{i=1}^{4} \sin(2\theta_i - \theta_5) + \sum_{i=6}^{7} \sin(\theta_5 - 2\theta_i)\Big) + \dot{q}_y\Big(+ 0.22 \cos(\theta_5) + 0.55 \sum_{i=1}^{4} \cos(2\theta_i - \theta_5) - \sum_{i=6}^{7} \cos(\theta_5 - 2\theta_i)\Big)\Big),$$

$$E_6 = 8.90 \cdot 10^{-3}\Big(- \dot{q}_x\Big(- 0.22 \sin(\theta_5) + 0.55 \sum_{i=1}^{4} \sin(2\theta_i - \theta_5) + \sum_{i=6}^{7} \sin(\theta_5 - 2\theta_i)\Big) + \dot{q}_y\Big(+ 0.22 \cos(\theta_5) + 0.55 \sum_{i=1}^{4} \cos(2\theta_i - \theta_5) - \sum_{i=6}^{7} \cos(\theta_5 - 2\theta_i)\Big)\Big),$$

$$E_7 = 10.90 \cdot 10^{-3}\Big(- \dot{q}_x\Big(- 0.36 \sin(\theta_6) + 0.57 \sum_{i=1}^{5} \sin(2\theta_i - \theta_6) + \sin(\theta_6 - 2\theta_7)\Big) + \dot{q}_y\Big(- 0.36 \cos(\theta_6) + 0.27 \sum_{i=1}^{5} \cos(2\theta_i - \theta_6) - \cos(\theta_6 - 2\theta_7)\Big)\Big),$$

$$E_8 = 9.87 \cdot 10^{-4}\Big(- \dot{q}_x\Big(- 6 \sin(\theta_7) + \sum_{i=1}^{6} \sin(2\theta_i - \theta_7)\Big) + \dot{q}_y\Big(- 6 \cos(\theta_7) + \sum_{i=1}^{6} \cos(2\theta_i - \theta_7)\Big)\Big),$$

$$E_9 = 0.1382\Big(\dot{q}_x\Big(\sum_{i=1}^{7} \cos(2\theta_i) - 21.0058\Big) + \dot{q}_y \sum_{i=1}^{7} \sin(2\theta_i)\Big) + 0.1382\Big(\dot{q}_x \sum_{i=1}^{7} \sin(2\theta_i) - \Big(\dot{q}_y \sum_{i=1}^{7} \cos(2\theta_i) + 21.0058\Big)\Big)$$

A.5 Robot simulator

The flagellum is implemented by employing distributed actuators, i.e., a set of segments linked by 1-DOF joints. The set of segments is developed using the basic unit shown in Figure A.2, which is repeated as many times as the desired number of joints. As observed, this basic unit consists of two elements: the actuator, modeled as a DC motor (red frame), and a cylindrical-shaped segment with the corresponding gears (green frame). On the one hand, the inputs of the basic unit are the voltage that governs each joint, the power supply of the electronic circuit and motor, and the bus signal, which simulates the physical communication medium in the prototype and is a common connection between the segments. On the other hand, the output of this basis unit is just the bus signal, whose main signals are: 1) the kinematic variables of the segment (linear and angular velocity, angular position, and the cross displacement); 2) mechanical variables (torque and power developed by the actuator); and 3) the electrical variables (current and voltage applied, and power supplied). It is worth mentioning that the basic unit has two Simscape physical connection ports, namely, ports B (base) and F (follower), which allow the analysis of the model as a complete mechanical system. More details of each element are given below.

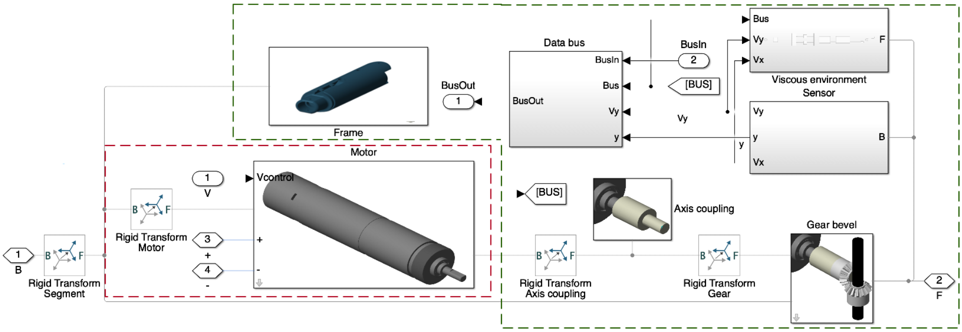

Figure A.2: Block diagram of Simulink of the basic unit of the flagellum of an AEF microrobot.

A.5.1 Actuator model

The actuator is modeled as a DC motor with the corresponding electronics, as shown in Figure A.3. The model's electrical side (blue network) consists of an H-

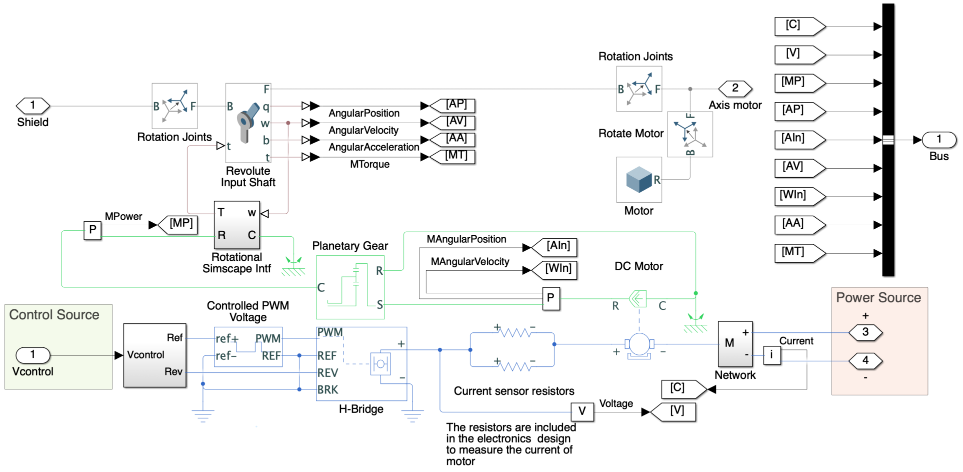

Figure A.3: Details of the actuator of the basic unit of the AEF microrobot simulator.

bridge governed by a logical and PWM signal, which controls the rotation direction and the electrical power supplied to the motor. Furthermore, it incorporates the passive components presented in the real design. The mechanical side (green and red networks) is based on the planetary gearhead coupled at the motor, modeled as a planetary gear block whose gear ratio and efficiency are configurable. Both sides are linked through the electromechanical model of the DC motor. The mechanical power (torque and velocity) developed by the DC motor is transferred to an ideal 1-DOF joint through the interface, enabling the extension of the model from Simscape Driveline to Simscape Multibody 3D and integrating the physical effects modeled on both sides. In this scheme, it should be highlighted that the inertia block is connected in parallel due to the software used for the implementation. Thus, Newton's second law violation during simulation is avoided.

To analyze and study the developed and supplied energy, power sensor blocks are used in the mechanical and electrical sides of the motor to measure the power required, which allows the calculation of the current demanded and the torque exerted by the motor, as well as the voltage that determines the angular velocity.

For its part, the kinematic variables of the motor (angular position, velocity and acceleration) are measured from the ideal joint with respect to a local reference system. These variables, together with the voltage, establish the control strategy and emulate the desired wave. All the measured variables are included in the data bus signal.

A.5.2 Link model

Figure A.4 illustrates the block diagram of the basic unit of one robot segment developed on Simulink, in which three parts can be identified. The first part (red) consists of the solid representing the frame of the motor, a cylinder with a radius d, length L_s, the axis coupling and the bevel gear, which transmit the motion of the motor to the following link allowing to govern its position. The second group of blocks (blue) implements the viscous environment, where the viscous forces are defined according to (3.15) and the measured variables are calculated and exerted over the segment. In the third part (green), similarly to the actuator model, sensor blocks are also used to obtain information about the system.

Particularly, both the normal and tangential velocity are registered, as well as, and the vertical displacement of the segment in four positions ($L_s/4$, $L_s/2$, $3L_s/4$, L_s), with respect to a global reference system placed at the robot head. Finally, all the measured variables are also included in the data bus signal.

A.5.3 Testbed for HIL experiments

It is important to mention that this simulator is prepared to be used as a testbed to perform HIL experiment with the swimming robot so as to validate the designed

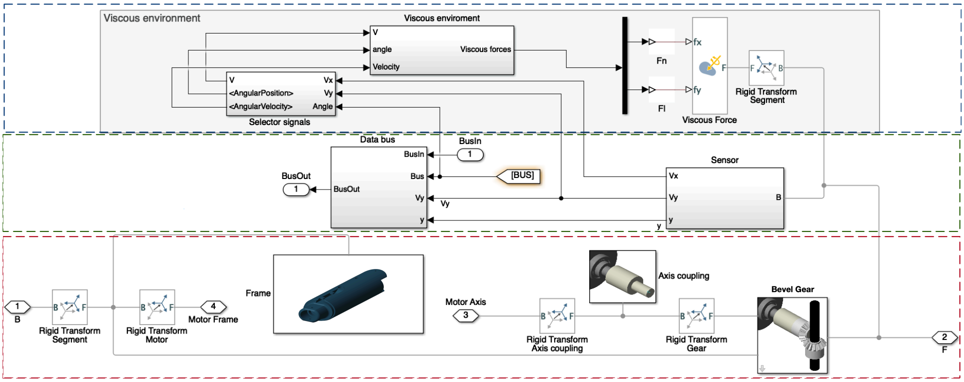

Figure A.4: Details of a segment of the basic unit of the AEF microrobot simulator.

controllers. A scheme of the testbed is illustrate in Figure A.5. As can be seen, it consist of the followign components:

- The simulator of the robot described above, which runs on Macintosh with the following specifications: Intel Core i7 (six core) with a clock speed of 2.2 GHz and 16 Gb DDR4 RAM.
- The robot software. For the control operation requirements, the chosen microcontroller is an Atmel ATmega32u4. It has an architecture of 8 bits, a capability of 16 MIPS at a clock frequency of 16 MHz, and a hardware multiplier that improves the time of arithmetic operations. Its capacity to do the control task in the desired sampling time makes it suitable for this application.

The data interchange between the microcontroller and the computer is done using micro USB port type B through a serial protocol via universal asynchronous receiver-transmitter (UART) configured as follows: BigEndian byte order, 32-bit data, IEEE Standard 754 floating point for data representation, and 250000 baud rate. On the computer side, an *S-Function* was written to receive/send data. As shown in Figure A.5, the simulator sends the position error of each link to the microcontroller, whereas this hardware calculates and sends back the control laws to the computer.

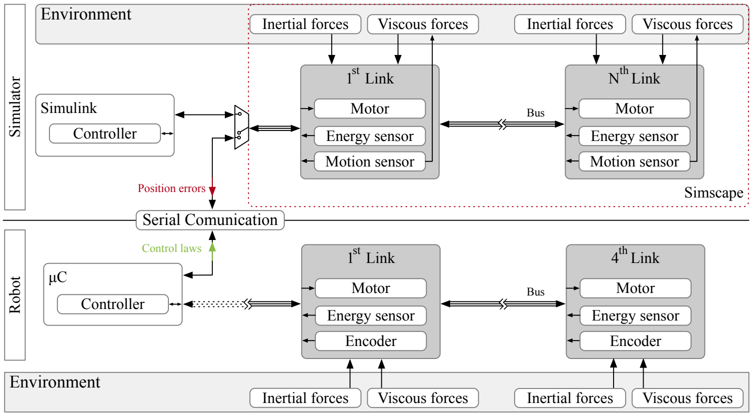

Figure A.5: Connection scheme of the robot testbed to perform HIL experiments.

B

MATHEMATICAL MODEL OF ELECTRICAL EQUIVALENCE OF CARDIOVASCULAR SYSTEM

This appendix details the analysis of the electrical circuit described in chapter 5.

The mathematical description of the circuit is obtained applying the Kirchoff's circuit law to the electrical circuit depicted in Figure 5.7 and taking the state variables given in Table 5.4. With respect to diodes, their behavior is defined by the ramp function:

$$d(x) = \begin{cases} x, & \text{if } x \geq 0 \\ 0, & \text{if } x < 0 \end{cases} \tag{B.1}$$

Then, the dynamic equations of the model are obtained as follows. The state x_1 is described recalling the Frank-Starling's law, which states that:

$$E(t) = \frac{LVP(t)}{LVV(t) - V_0} \tag{B.2}$$

where $LVV(t) = \int (I_M - I_A)dt$ is the charge in the capacitor, being I_M and I_A the currents through the mitral diode D$_M$ and the aortic diode D$_A$, respectively. Therefore, the state x_1 is defined as:

$$x_1 = E(t)\Big(\int (I_M - I_A)dt - V_0\Big) \tag{B.3}$$

Deriving the terms on both sides of the equality and recalling that $E(t) = 1/C(t)$ and $\dot{E}(t) = -\dot{C}(t)/C^2(t)$, the differential equation for x_1 can be written as:

$$\dot{x}_1 = \dot{E}(t)\Big(\int (I_m - I_a)dt - V_0\Big) + E(t)\frac{d}{dt}\int (I_M - I_A)dt \tag{B.4a}$$

$$\dot{x}_1 = \frac{1}{C(t)}\Big(- \dot{C}(t)x_1 + \frac{1}{R_M}d(x_1 - x_2) - \frac{1}{R_A}d(x_4 - x_1)\Big) \tag{B.4b}$$

Applying the Kirchoff's first law to capacitor C$_R$, it results that

$$I_S = I_2 + I_M \tag{B.5}$$

where I_S, I_2 and I_M are the currents through the systemic resistance and return from left common carotid, the capacitor C$_R$ and the mitral diode D$_M$, respectively. Using the Ohm's law, the currents can be expressed as a function of voltage as:

$$\frac{1}{R_S}(x_2 - x_3) + \frac{1}{R_{SLC}}(x_2 - x_3) = C_R\dot{x}_2 + \frac{1}{R_M}d(x_1 - x_2) \tag{B.6}$$

Solving for $\dot{x}_2$, it result:

$$\dot{x}_2 = \frac{1}{C_R}\left(\frac{1}{R_S}d(x_3 - x_2) + \frac{1}{R_{SLC}}(x_6 - x_2) - \frac{1}{R_M}d(x_2 - x_1)\right) \tag{B.7}$$

Similarly, the application of Kirchoff's first law to the node x_3 allows obtaining:

$$x_5 = x_7 + \frac{1}{R_S}(x_3 - x_2) + I_3 \tag{B.8}$$

where I_3 is the current through the capacitor C$_S$. Using the Ohm's law for I_3 and solving for $\dot{x}_3$, it results that:

$$\dot{x}_3 = \frac{1}{C_S}\left(x_5 - x_7 - \frac{1}{R_S}d(x_3 - x_2)\right) \tag{B.9}$$

Doing the same analysis for capacitor C$_A$, the sum of currents is:

$$I_A = I_4 + x_5 \tag{B.10}$$

where I_4 is the current through C$_A$. Applying the Ohm's law and solving for $\dot{x}_4$:

$$\dot{x}_4 = \frac{1}{C_A}\left(\frac{1}{R_A}d(x_4 - x_1) - x_5\right) \tag{B.11}$$

For the differential equation of x_5, the Kirchoff's second law is employed in the $x_4 - x_5 - x_3$ mesh, formulating:

$$x_4 = L\dot{x}_5 + R_C x_5 + x_3 \tag{B.12}$$

Solving for $\dot{x}_5$, the dynamics of the state x_5 is defined by:

$$\dot{x}_5 = \frac{1}{L}(x_4 - x_3 - R_C x_5) \tag{B.13}$$

Recalling again the Kirchoff's first law for the node x_6, the currents involved are:

$$x_7 - \frac{1}{R_{SLC}}(x_6 - x_2) - I_6 = 0 \tag{B.14}$$

where I_6 is the current through capacitor C_{LC}. Applying the Ohm's law and solving for $\dot{x}_6$, it is obtained:

$$\dot{x}_6 = \frac{1}{C_{LC}}\left(\frac{1}{R_{SLC}}(x_2 - x_6) + x_7\right) \tag{B.15}$$

Finally, the differential equation for the state x_7 is solved using the Kirchoff's second law for the mesh corresponding to $x_3 - x_6 - x_7$:

$$x_3 = L_{LC}\dot{x}_7 + R_{LC}x_7 + x_6 \tag{B.16}$$

Solving for $\dot{x}_7$, the state equation for $\dot{x}_7$ is defined by:

$$\dot{x}_7 = \frac{1}{L_{LC}}\left(x_3 - x_6 - R_{LC}x_7\right) \tag{B.17}$$